Estimation of Serum Potassium and Calcium Concentrations from Electrocardiographic Depolarization and Repolarization Waveforms

Syed Hassaan Ahmed Bukhari

université de BORDEAUX

Ph.D. Thesis

Estimation of Serum Potassium and Calcium Concentrations from Electrocardiographic Depolarization and Repolarization Waveforms

Syed Hassaan Ahmed Bukhari

Supervisors:

Prof. Esther Pueyo, Dr. Mark Potse, Dr. Carlos Sánchez

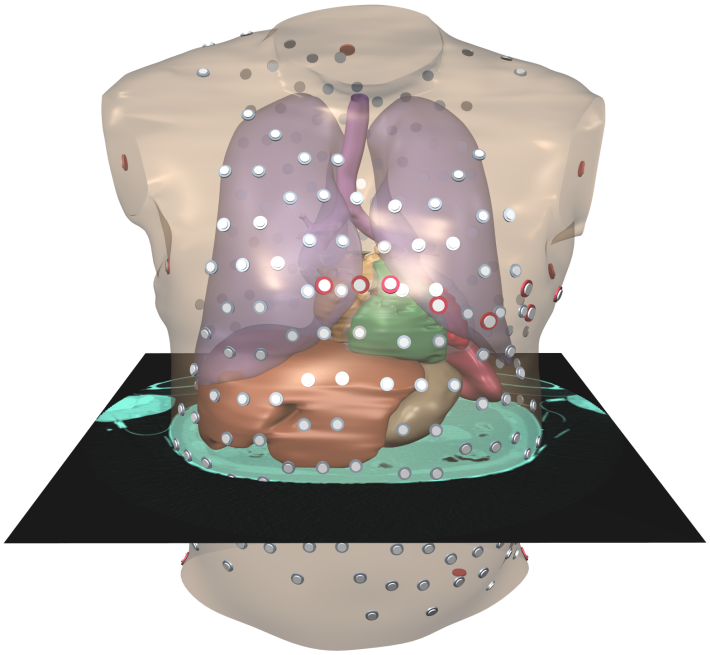

University of Zaragoza, Spain & University of Bordeaux, France

March 2023

université de BORDEAUX

Ph.D. Thesis

Estimation of Serum Potassium and Calcium Concentrations from Electrocardiographic Depolarization and Repolarization Waveforms

Syed Hassaan Ahmed Bukhari

I3A Institute, University of Zaragoza, IIS Aragón, Zaragoza, Spain
Carmen team, Inria Bordeaux Sud-Ouest, Talence, France
Univ. Bordeaux, IMB, UMR 5251, Talence, France

Supervisors:

Director: **Dr. Mark Potse** Research Professor, University of Bordeaux, France
Co-director: **Prof. Esther Pueyo** Associate Professor, University of Zaragoza, Spain
Co-director: **Dr. Carlos Sánchez** Assistant Professor, University of Zaragoza, Spain

Jury members:

Prof. José María Ferrero	Polytechnic University of Valencia, Spain	President
Prof. Vaidotas Marozas	University of Kaunas, Lithuania	Examiner
Dr. Juan Ignacio Pérez	University of Zaragoza, Spain	Examiner
Dr. Ana Mincholé	University of Zaragoza, Spain	Examiner
Dr. Chiara Bartolucci	University of Bologna, Italy	Examiner, Reviewer
Dr. Massimo Rivolta	Polytechnic University of Milan, Italy	Reviewer

Defended on March 2, 2023

Abstract

Chronic kidney disease (CKD), a condition defined by a gradual decline in kidney function over time, has become a global health concern affecting between 11 and 13% of the world population [1]. As renal function declines, CKD patients gradually lose their ability to maintain normal values of potassium concentration ($[K^+]$) in their blood. Elevated serum $[K^+]$, known as hyperkalemia, increases the risk for life-threatening arrhythmias and sudden cardiac death [2].

An increase in serum $[K^+]$ outside the physiological range is commonly silent and is only detected when hyperkalemia is already very severe or when a blood test is performed. Maintenance and monitoring of $[K^+]$ in the blood is an important component in the treatment of CKD patients because therapies for hyperkalemia management in CKD patients are designed to prevent arrhythmias and to immediately lower serum $[K^+]$ to safe ranges. However, this is currently only possible by taking a blood sample and is associated with a long analysis time. Therefore it is useful to have a simple, noninvasive method to estimate serum $[K^+]$, particularly using the electrocardiogram (ECG). Indeed, variations in serum electrolyte levels have been shown to alter the electrical behavior of the heart and to induce changes in the ECG [3–6]. However, large inter-individual variability exists in the relationship between ion concentrations and ECG features. Previous attempts to estimate serum $[K^+]$ from the ECG have therefore shown limitations [7–9], such as not being applicable to some common types of ECG waveforms or relying on specific ECG characteristics that may present large variations not necessarily associated with hyperkalemia.

The aim of this thesis is to develop novel estimates of serum $[K^+]$ that are robust enough to detect hypokalemia (reduced $[K^+]$) or hyperkalemia in a timely manner to provide life-saving treatment. Additionally, the effect of changes in other electrolyte levels, like calcium concentration ($[Ca^{2+}]$), and in heart rate are investigated. These aims are achieved by combining novel ECG signal processing techniques with *in silico* modeling and simulation of cardiac electrophysiology.

The specific objectives are:

1. Characterization of hypokalemia or hyperkalemia and hypocalcemia (reduced $[Ca^{2+}]$) or hypercalcemia (elevated $[Ca^{2+}]$)-induced changes in ventricular repolarization from ECGs (T wave) of CKD patients. This is addressed in chapter 3 and

chapter 4. In these chapters, we describe how T waves are extracted from ECGs and how we characterize changes in T waves at varying potassium, calcium and heart rate using analyses based on time warping and Lyapunov exponents. Next, univariable and multivariable regression models including markers of T wave nonlinear dynamics in combination with warping-based markers of T wave morphology are built and their performance for $[K^+]$ estimation is assessed.

2. Characterization of hypo- or hyperkalemia and hypo- or hypercalcemia-induced changes in ventricular depolarization from the QRS complex of CKD patients. This is reported in chapter 5. In this chapter, we present how QRS complexes from ECGs of CKD patients are processed and how we measure changes at varying $[K^+]$, $[Ca^{2+}]$ and heart rate. Univariate and multivariate regression analyses including novel QRS morphological markers in combination with T wave morphological markers are performed to assess the contribution of depolarization and repolarization features for electrolyte monitoring in CKD patients.

3. Identification of potential sources underlying inter-individual variability in ECG markers in response to changes in $[K^+]$ and $[Ca^{2+}]$. *In silico* investigations of cardiac electrophysiology are conducted and ECG features are computed. Simulation results are compared with patient data. This is explained in chapter 3 using one-dimensional (1D) fibers and in chapter 6 using three-dimensional (3D) human heart-torso models. Chapter 6 includes the development of a population of realistic computational models of human ventricular electrophysiology, based on human anatomy and electrophysiology, to better understand how changes in individual characteristics influence the ECG (QRS and T wave) markers that we introduced in previous chapters. ECG waveforms are characterized by their amplitude, duration and morphology. Simulations are performed with the most realistic available techniques to model the electrophysiology of the heart and the resulting ECG. We establish mechanisms that contribute to inter-individual differences in the characterized ECG features.

In conclusion, we identify several markers of ECG morphology, including depolarization and repolarization features, that are highly correlated with serum electrolyte (potassium and calcium) concentrations. ECG morphological variability markers vary significantly with $[K^+]$ and $[Ca^{2+}]$ in both simulated and measured ECGs, with a wide range of patterns observed for such relationships. The proportions of endocardial, midmyocardial and epicardial cells have a large impact on ECG markers, particularly for serum electrolyte concentrations out of their physiological levels. This suggests that transmural heterogeneities can modulate ECG responses to changes in electrolyte concentrations in CKD patients. Agreement between actual potassium and calcium levels and their estimates derived from the ECG is promising, with lower average errors than previously

proposed markers in the literature. These findings can have major relevance for noninvasive monitoring of serum electrolyte levels and prediction of arrhythmic events in these patients.

Resumen y conclusiones

La enfermedad renal crónica (ERC), una afección definida por una disminución gradual de la función renal a lo largo del tiempo, se ha convertido en un problema de salud mundial que afecta a entre el 11 y el 13% de la población mundial [1]. A medida que disminuye la función renal, los pacientes con ERC pierden gradualmente su capacidad para mantener valores normales de concentración de potasio ($[K^+]$) en la sangre. La $[K^+]$ sérica elevada, conocida como hiperpotasemia, aumenta el riesgo de arritmias potencialmente mortales y muerte cardíaca súbita [2].

Un aumento de la $[K^+]$ sérica fuera del rango fisiológico suele ser silencioso y solo se detecta cuando la hiperpotasemia ya es muy grave o cuando se realiza un análisis de sangre. El mantenimiento y monitoreo de $[K^+]$ en la sangre es un componente importante en el tratamiento de pacientes con CKD porque las terapias para el control de la hiperpotasemia en pacientes con CKD están diseñadas para prevenir arritmias y para reducir inmediatamente el $[K^+]$ sérico a rangos seguros. Sin embargo, actualmente esto solo es posible tomando una muestra de sangre y está asociado con un tiempo de análisis prolongado. Por lo tanto, es útil contar con un método simple y no invasivo para estimar $[K^+]$ sérico, en particular mediante electrocardiograma (ECG). De hecho, se ha demostrado que las variaciones en los niveles de electrolitos séricos alteran el comportamiento eléctrico del corazón e inducen cambios en el ECG [3–6]. Sin embargo, existe una gran variabilidad interindividual en la relación entre las concentraciones de iones y las características del ECG. Por lo tanto, los intentos anteriores de estimar $[K^+]$ en suero a partir del ECG han mostrado limitaciones [7–9], como no ser aplicable a algunos tipos comunes de formas de onda del ECG o depender de características específicas del ECG que pueden presentar grandes variaciones no necesariamente asociadas con hiperpotasemia.

El objetivo de esta tesis es desarrollar estimadores novedosos de $[K^+]$ en suero que sean lo suficientemente robustos para detectar hipopotasemia ($[K^+]$ reducido) o hiperpotasemia en el momento oportuno para proporcionar tratamientos que puedan salvar vidas. Se investigan además los efectos de cambios en otros electrolitos, como la concentración de calcio ($[Ca^{2+}]$), y en la frecuencia cardíaca. Estos objetivos se logran mediante la combinación de nuevas técnicas de procesamiento de señales electrocardiográficas con el modelado *in silico* y la simulación de electrofisiología cardíaca.

Los objetivos específicos son:

1. Caracterización de cambios inducidos por hipopotasemia o hiperpotasemia e hipocalcemia ($[Ca^{2+}]$ reducido) o hipercalcemia ($[Ca^{2+}]$ elevado) en la repolarización ventricular a partir de ECG (onda T) de pacientes con ERC. Esto se aborda en el capítulo 3 y el capítulo 4. En ellos describimos cómo se extraen las ondas T del ECG y cómo caracterizamos los cambios en las ondas T a niveles variables de potasio, calcio y frecuencia cardíaca utilizando análisis basados en la distorsión del tiempo y en los exponentes Lyapunov. A continuación, se construyen modelos de regresión univariables y multivariables que incluyen marcadores de dinámica no lineal de ondas T en combinación con marcadores basados en la deformación de la morfología de ondas T y se evalúa su rendimiento para la estimación de $[K^+]$.

2. Caracterización de hipo o hiperpotasemia y cambios inducidos por hipo o hipercalcemia en la despolarización ventricular del complejo QRS de pacientes con ERC. Esto se describe en el capítulo 5. En este capítulo, presentamos cómo se procesan los complejos QRS de los ECG de pacientes con ERC y cómo medimos los cambios frente a variaciones en $[K^+]$, $[Ca^{2+}]$ y frecuencia cardiaca. Se realizan análisis de regresión univariante y multivariante que incluyen nuevos marcadores morfológicos del QRS en combinación con marcadores morfológicos de la onda T para evaluar la contribución de las características extraídas de la despolarización y repolarización cardíacas para el control de electrolitos en pacientes con ERC.

3. Identificación de fuentes potenciales subyacentes a la variabilidad interindividual en los marcadores de ECG en respuesta a cambios en $[K^+]$ y $[Ca^{2+}]$. Mediante la utilización de modelos computacionales se llevan a cabo investigaciones de electrofisiología cardíaca y se obtienen las características del ECG. Los resultados de las simulaciones se comparan con los datos de los pacientes. Esto se explica en el capítulo 3, en el que se emplean fibras unidimensionales (1D), y en el capítulo 6, en el que se usan modelos tridimensionales (3D) de corazón-torso humano. Además, el capítulo 6 incluye el desarrollo de una población de modelos computacionales realistas de ventrículo humano, basados en la anatomía y la electrofisiología humanas, para comprender mejor cómo los cambios en las características individuales influyen en los marcadores de ECG (QRS y onda T) que presentamos en los capítulos anteriores. Las formas de onda del ECG se caracterizan por su amplitud, duración y morfología. Las simulaciones se realizan con las técnicas más realistas disponibles para modelar la electrofisiología del corazón y el ECG resultante. Partiendo de dichas simulaciones, se establecen los mecanismos que contribuyen a las diferencias interindividuales en las características del ECG analizadas.

En conclusión, identificamos varios marcadores de la morfología del ECG, incluidas las características de despolarización y repolarización, que están altamente correlacionados con las concentraciones de electrolitos séricos (potasio y calcio). Los marcadores de variabilidad morfológica de ECG varían significativamente con $[K^+]$ y $[Ca^{2+}]$ tanto en ECG

simulados como medidos, con una amplia gama de patrones observados para tales relaciones. Las proporciones de células endocárdicas, miocárdicas medias y epicárdicas tienen un gran impacto en los marcadores de ECG, particularmente para las concentraciones de electrolitos séricos fuera de sus niveles fisiológicos. Esto sugiere que las heterogeneidades transmurales pueden modular las respuestas del ECG a los cambios en las concentraciones de electrolitos en pacientes con ERC. La concordancia entre los niveles reales de potasio y calcio y sus estimaciones derivadas del ECG es prometedora, con errores promedio más bajos que los marcadores propuestos previamente en la literatura. Estos hallazgos pueden tener una gran relevancia para la monitorización no invasiva de los niveles de electrolitos séricos y la predicción de eventos arrítmicos en estos pacientes.

Résumé

L'insuffisance rénale chronique (IRC), caractérisée par un déclin graduel de la fonction rénale, est devenu un problème sanitaire important, affectant entre 11 et 13% de la population mondiale [1]. Lorsque leur fonction rénale décline, les patients affectées d'IRC perdent graduellement leur capacité de maintenir une concentrations sanguine de potassium ($[K^+]$) normale. Une $[K^+]$ sanguine élevée, nommée hyperkaliémie, augmente le risque d'arythmie cardiaque engageant le pronostic vital et de mort subite cardiaque [2].

Une augmentation de la $[K^+]$ sanguine hors de sa plage physiologique reste le plus souvent inaperçue et n'est détectée que si elle est très sévère ou si un prélèvement sanguin est effectué. La maintenance et la surveillance de la $[K^+]$ sanguine est un élément important de la prise en charge des patients affectés d'IRC, les thérapies pour la maîtrise de l'hyperkaliémie dans ces patients visant la prévention des arythmies et la réduction immédiate de la $[K^+]$ vers des valeurs inoffensives. Cependant, de nos jours une telle surveillance n'est possible que par des prélèvements sanguins associées avec un temps d'analyse long. Il serait donc utile d'avoir une méthode simple et noninvasive pour l'estimation de la $[K^+]$, notamment en utilisant l'électrocardiogramme (ECG). En effet, il a été démontré que les variations des niveaux d'électrolytes dans le sérum sanguin modifient le comportement électrique du cœur et donc l'ECG [3–6]. Malheureusement, la rélation entre les concentrations d'électrolytes et les caractéristiques de l'ECG est très variable d'une personne à l'autre. Des travaux antérieurs [7–9] ont donc montré des limitations, tels que l'exclusion de certains types d'ECG ou la dépendance sur des caractéristiques présentant une variabilité large et non nécessairement corrélée avec l'hyperkaliémie.

L'objectif de cette thèse est de développer des nouveaux marqueurs de la $[K^+]$ sanguine suffisamment robustes pour détecter l'hypokaliémie ($[K^+]$ anormalement bas) et l'hyperkaliémie assez rapidement pour permettre des interventions potentiellement salvateures. En plus, les effets de changements d'autres concentrations d'électrolytes, tels que le calcium ($[Ca^{2+}]$) et de la fréquence cardiaque sont étudiés. Ces objectifs sont atteints en combinant des nouvelles techniques de traitement de signal avec la modélisation *in silico* de l'électrophysiologie cardiaque.

Les objectifs spécifique sont les suivantes.

1. Caractérisation des effets de l'hypokaliémie, de l'hyperkaliémie, de l'hypocalcémie

($[Ca^{2+}]$ réduit) et de l'hypercalcémie ($[Ca^{2+}]$ élevé) sur la repolarisation cardiaque, observés dans l'onde T de l'ECG chez des patients atteints d'IRC. C'est l'objet des chapitres 3 et 4. Dans ces chapitres, nous décrivons comment les ondes T sont extraits des ECGs et comment nous caractérisons les changements dans les ondes T dues à la variation de $[K^+]$, $[Ca^{2+}]$, et la fréquence cardiaque, en utilisant des analyses basées sur la distorsion du signal dans le temps et sur les exposants de Liapounov. Ensuite, des modèles de régression linéaire simples et multiples incluant des marqueurs de la dynamique nonlinéaire de l'onde T combinés aux marqueurs basées sur la distorsion dans le temps sont construits et leur capacité à estimer la $[K^+]$ est évaluée.

2. Caractérisation des effets de l'hypokaliémie, de l'hyperkaliémie, de l'hypocalcémie et de l'hypercalcémie sur la dépolarisation ventriculaire, observés dans le complexe QRS de l'ECG chez des patients atteints d'IRC. C'est l'objet du chapitre 5. Dans ce chapitre, nous présentons comment le complexe QRS est traité et comment nous mesurons les changements dus à la variation de $[K^+]$, de $[Ca^{2+}]$, et de la fréquence cardiaque. Des modèles de régression linéaire simples et multiples incluant des nouveaux marqueurs morphologiques du complexe QRS combinés aux marqueurs morphologiques de l'onde T sont mis en œuvre afin d'analyser la contribution des marqueurs de dépolarisation et repolarisation à la surveillance des concentrations d'électrolytes chez des patients atteints d'IRC.

3. Identification des sources potentielles de la variabilité inter-individuelle de la réponse des marqueurs électrocardiographiques aux changements de $[K^+]$ et $[Ca^{2+}]$. Des études *in silico* sont conduites et des marqueurs électrocardiographiques sont calculés. Les résultats sont comparés avec des données issues de patients. Ces travaux sont décrits dans le chapitre 3, concernant des fibres unidimensionnelles, et dans le chapitre 6, concernant des modèles cœur-torse tridimensionnels. Ce dernier chapitre inclut le développement d'une population de modèles réalistes, basées sur l'anatomie et électrophysiologie humaine, afin de mieux comprendre comment les changements de caractéristiques individuelles influencent les marqueurs (du complexe QRS et de l'onde T) de l'ECG introduits dans les chapitres précédents. Les composants des ECGs sont caractérisés par leur amplitude, durée et morphologie. Des simulations sont conduites utilisant les techniques les plus réalistes pour la modélisation de l'électrophysiologie cardiaque et de l'ECG. Nous établissons des mécanismes contribuant aux différences inter-individuelles des marqueurs électrocardiographiques.

En conclusion, nous identifions plusieurs marqueurs morphologiques de l'ECG, incluant des caractéristiques de dépolarisation et de repolarisation, qui sont fortement corrélées avec $[K^+]$ et $[Ca^{2+}]$. Cette corrélation est présente aussi bien dans les ECGs simulées que

dans les ECGs mesurées, avec une gamme de morphologies telle qu'observée chez les patients. Les proportions de cellules de type endocardique, mi-myocardique, et épicardique ont un effet important sur les marqueurs de l'ECG, particulièrement pour des concentrations électrolytiques hors de leurs plages physiologiques. Cette observation suggère que ces hétérogénéités peuvent moduler la réponse de l'ECG aux changements des concentrations électrolytiques chez des patients atteints d'IRC. La concordance entre les concentrations estimées et celles mesurées est prometteuse, avec des erreurs moyennes moins grands que celles obtenues avec les méthodes de la littérature. Ces résultats peuvent avoir une grande importance pour la surveillance noninvasive des concentrations d'électrolytes dans le sang et pour la prévision d'arythmies chez les patients atteints d'IRC.

Contents

List of Figures

List of Tables

Acronyms

CKD Chronic Kidney Disease

ESRD End Stage Renal Disease

HD Hemodialysis

HUCZ Hospital Clínico Universitario de Zaragoza

ECG Electrocardiogram

MWTW Mean Warped T wave

MWQRS Mean Warped QRS complex

HR Heart Rate

AP Action Potential

APD Action Potential Duration

IQR Interquartile Range

PC Principal Component

PCA Principal Component Analysis

SCD Sudden Cardiac Death

SNR Signal-to-noise Ratio

SRSF Square-root Slope Function

Std Standard Deviation

MSE Mean Square Error

RMSE Root Mean Square Error

MAE Mean Absolute Error

1D one-Dimensional

3D three-Dimensional

Endo Endocardial

Mid Midmyocardial

Epi Epicardial

WT Wavelet Transform

pECG Pseudo-ECG

MCS Morphology Combination Score

CL Cycle Length

LE Lyapunov Exponent

MLE Maximal Lyapunov Exponent

S Stage-specific Estimator

P Patient-specific Estimator

G Global Estimator

Chapter 1

Introduction

1.1 Motivation

Chronic kidney disease (CKD) includes a gradual decrease in kidney function over time, which leads to kidney failure when kidneys stop working, i.e. when they lose the ability to filter waste from the blood. CKD involves high associated economic cost, increased mortality risk and decreased quality of life for affected patients [1]. Sudden cardiac death, myocardial infarction and other types of cardiac arrhythmias are the main causes of mortality among CKD patients undergoing hemodialysis (HD), all together accounting for 43% of deaths [10]. Most of these deaths correspond to end-stage CKD patients and are associated with elevated serum potassium, i.e. hyperkalemia [2]. As renal function declines, CKD patients present with an increasingly impaired ability to maintain potassium homeostasis, thus increasing the risk for life-threatening arrhythmias and sudden cardiac death. Therapies for hyperkalemia management in CKD patients are designed to target prevention of arrhythmias and to immediately lower serum potassium levels to safe ranges.

Since elevation in serum potassium outside the physiological range is commonly silent, it is only detected when a blood test is performed. Therefore the possibility of having a simple, noninvasive method to estimate serum potassium before the patient presents with serious consequences is of major importance. Previous attempts to estimate serum potassium levels from the electrocardiogram (ECG) have been made. Although promising, those attempts present limitations, such as not being applicable to some common types of ECG waveforms or relying on specific ECG characteristics that may present large variations not necessarily associated with hyperkalemia.

1.2 Thesis aim

Variations in serum electrolyte levels, mainly potassium, $[K^+]$, and calcium, $[Ca^{2+}]$, have been shown to alter ventricular depolarization and repolarization in the ECG [3–5], sug-

gesting that it could indeed be possible to infer $[K^+]$ and $[Ca^{2+}]$ from the ECG. However, large inter-individual variability exists in the relationship between $[K^+]$ or $[Ca^{2+}]$ and ECG manifestations.

The aim of this PhD thesis is to propose and assess ECG-based estimators of serum $[K^+]$ and $[Ca^{2+}]$ that are robust enough to detect hypokalemia (reduced $[K^+]$) or hyperkalemia (elevated $[K^+]$) and hypocalcemia (reduced $[Ca^{2+}]$) or hypercalcemia (elevated $[Ca^{2+}]$) in a timely manner to provide lifesaving treatment. Additionally, the effects of changes in heart rate (HR) on ECG ventricular depolarization and repolarization are investigated. These aims are achieved by combining ECG signal processing techniques with *in silico* modeling and simulation of cardiac electrophysiology. Specifically, we process 12-lead ECGs of CKD patients undergoing HD, we evaluate ECG characteristics related to $[K^+]$ and $[Ca^{2+}]$ and we conduct *in silico* simulations using developed models of human cardiac electrical activity to uncover sources of inter-individual variability in ECG response to serum electrolyte variations. This investigation could help in improving current therapies and risk stratification tools for CKD patients.

1.3 The heart

1.3.1 Anatomy

The heart is a fist-sized organ that pumps blood throughout the body. Anatomically, the heart is divided into different parts, walls, chambers, valves, blood vessels and the electrical conduction system. Heart walls have three layers, endocardium (inner layer), midmyocardium (middle layer) and epicardium (outer layer), which contract and relax. The heart consists of four chambers. The upper chambers (right and left atria) receive incoming blood and the lower chambers (right and left ventricles) pump blood out of the heart. The heart has four valves named the tricuspid, mitral, aortic and pulmonary valve, which prevent blood from flowing backwards when the chambers contract. The tricuspid valve opens so that blood flows from the right atrium to the right ventricle. The mitral valve opens to allow blood flow from the left atrium to the left ventricle. The aortic valve opens to pump blood out of the left ventricle to the aorta, which carries blood to the body. The pulmonary valve opens to allow blood pumping from the right ventricle to pulmonary arteries, which carry blood to the lungs. Blood vessels include arteries, veins and capillaries, whose main function is to deliver and carry back blood to the organs and tissues throughout the body.

The electrical conduction system mainly includes the sinoatrial (SA) and atrioventricular (AV) nodes, bundle of His (left and right bundle branch) and Purkinje fibers. The SA node generates electrical impulses, thereby setting the normal heartbeat (sinus rhythm). The AV node carries electrical signals from the atria to the ventricles. The bundle of His serves to transmit electrical impulses from the AV node to the Purkinje fibers that carry

cardiac impulses to the ventricles of the heart and cause them to contract, where the left bundle branch carries electrical impulses to the left ventricle and the right bundle branch carries signals to the right ventricle [11, 12] (see Figure 1.1 for the anatomy of heart).

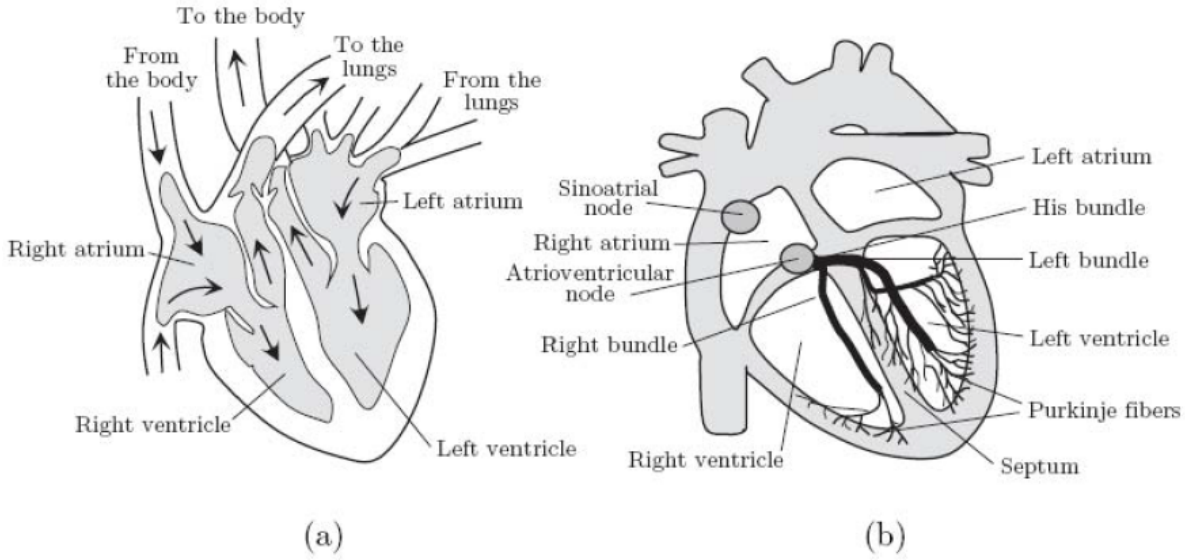

Figure 1.1: Anatomy of the heart. Adapted from [13].

1.3.2 Electrophysiology

The wall of the heart is called the myocardium, and is composed of muscle cells (myocytes) that control the contraction and relaxation of the heart. The heart is surrounded by a double-layered membrane (pericardium), which lubricates the heart to protect it from friction with tissues around it. Each cardiac myocyte is bounded by a thin phospholipid membrane or sarcolemma, which acts as a barrier between the extracellular and intracellular parts of the muscle cells. The intracellular space is encapsulated in this membrane and the space that lies outside the sarcolemma is called extracellular space.

The voltage difference between inside and outside of the myocardial cell is called the membrane potential. It is negative at resting state (when the cell is not electrically excited). The main ions in the intracellular and extracellular spaces are calcium (Ca^{2+}), chloride (Cl^{-}) and sodium (Na^{+}), whereas potassium (K^{+}) is mainly found inside the cell. The movement of ions across the cell membrane is responsible for the opening and closing of ion channels (protein complexes in the membranes of individual cells). These ions are primarily involved in the generation of cardiac action potential (AP), which represents the electrical activity of a single cell, where the shape and duration of each AP are determined by the activity of ion channel [14].

The cardiac AP has five phases (phase 0–4) as follows (see Figure 1.2):

1. Phase 0 refers to “rapid depolarization”, which is due to the opening of the fast

inward Na^+ channels that allow rapid influx of Na^+ ions into the cell.

2. Phase 1 relates with "early repolarization", which occurs with the inactivation of the fast Na^+ channels. The transient outward K^+ current contributes to it and is also responsible for the "notch" in some AP morphologies.

3. Phase 2 corresponds to the "plateau" phase of the cardiac AP, which is sustained by a balance between inward movement of calcium Ca^{2+} through L-type calcium channels and outward movement of K^+ through the slow delayed rectifier potassium channels. The "plateau" pattern is produced because the voltage-sensitive Ca^{2+} channels are opened to facilitate the influx of positively-charged Ca^{2+} ions to activate the contraction mechanism.

4. Phase 3 is the "rapid repolarization" phase, which occurs with the closing of the L-type Ca^{2+} channels while the slow delayed rectifier K^+ channels are still open. This ensures a net outward current, corresponding to a negative change in membrane potential, thus allowing more types of K^+ channels to open. These are primarily the rapid delayed rectifier K^+ channels and the inwardly rectifying K^+ current. The inwardly rectifying K^+ current remains conducting throughout phase 4 to set the resting membrane potential. However, the delayed rectifier K^+ channels close when the membrane potential is restored to about -80 to -85 mV.

5. Phase 4 is the "slow diastolic depolarization or resting" phase, and occurs when the cell is at rest. The resting membrane potential is stable due to the balanced ions (ions flowed into, e.g. Na^+, and out, e.g. K^+ and Cl^-, of the cell are perfectly balanced). This process prepares the cell for the next AP cycle.

1.3.3 The electrocardiogram

The electrocardiogram (ECG) is a signal that represents the electrical events of the cardiac cycle and is measured on the body surface by placing electrodes on the chest. ECGs can be used to monitor and diagnose conditions affecting the heart, particularly to identify arrhythmias, myocardial ischemia, myocardial infarction, pericarditis, hypertrophy, drug toxicity and electrolyte disturbances, i.e. hypokalemia or hyperkalemia and hypocalcemia or hypercalcemia.

ECG leads ECG leads are used to measure the difference in electrical potential between two points. They are divided into bipolar, difference between two points on the body, and unipolar leads, which measure the difference in electrical potential with one point on the body and another point on a virtual reference point, i.e. Wilson's Central Terminal.

The standard 12-lead (see Figure 1.3) ECG consists of 3 standard limb leads (I, II, III), 3 augmented limb leads (aVF, aVR, aVL) and 6 precordial leads (V1–V6). The 12

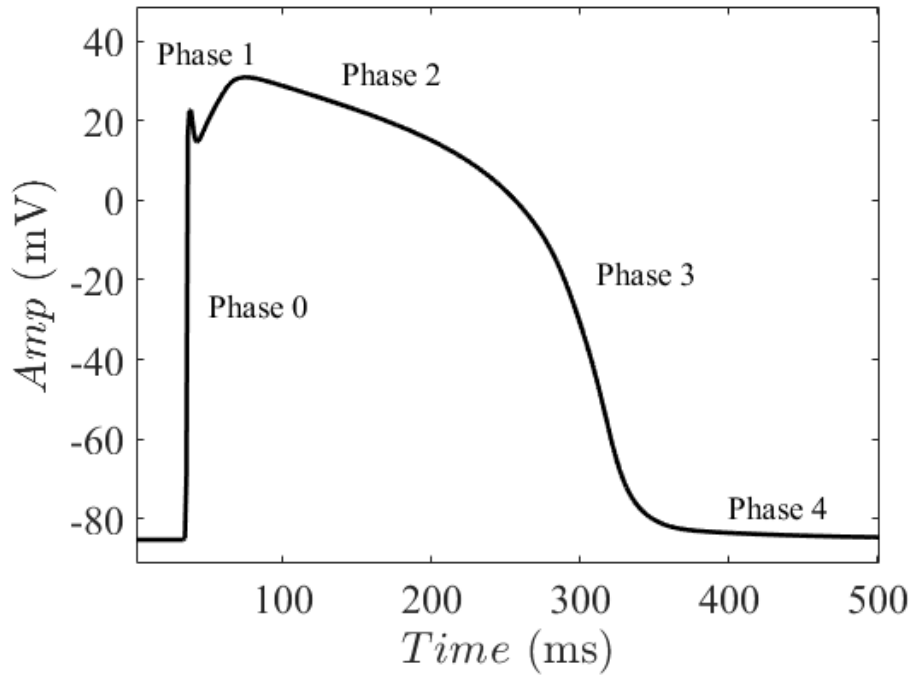

Figure 1.2: Phases (0–4) of cardiac AP. Phase 0, rapid depolarization; Phase 1, early repolarization; Phase 2, plateau; Phase 3, rapid repolarization; Phase 4, slow diastolic depolarization or resting phase.

leads of the ECG can be divided intro two groups of six leads based on the plane that is used to analyze the electrical events in the heart. The six chest leads, also referred to as the precordial leads, V1 to V6, examine these electrical events in the horizontal or transverse plane (Figure 1.3 (right)), while the remaining six frontal leads (I, II, III, aVF, aVR and aVL) examine the flow of depolarization and repolarization through the heart in the vertical, or frontal, plane (Figure 1.3 (left)) [13].

Among the twelve standard leads, it would be enough to consider only eight leads (two limb and six precordial leads) to represent all the information that can be extracted from them [13].

ECG waves The deflections from "isoelectric line", which is a flat line with no net current flowing in its direction, are named with letters in an alphabetical order [15]. The depolarizing wavefront moving towards the positive terminal of the lead produces a positive deflection on the ECG signal above the isoelectric line, while the depolarizing wavefront moving away from the the positive terminal of the lead produces a negative deflection below the isoelectric line. The repolarizing wavefront has the opposite polarity to the depolarizing wavefront [13].

The atrial depolarization wavefront produces a positive deflection on the ECG signal because it moves towards the chest leads, which is the P wave of the ECG, and the atria are completely depolarized when the P wave ends. The ECG signal then returns

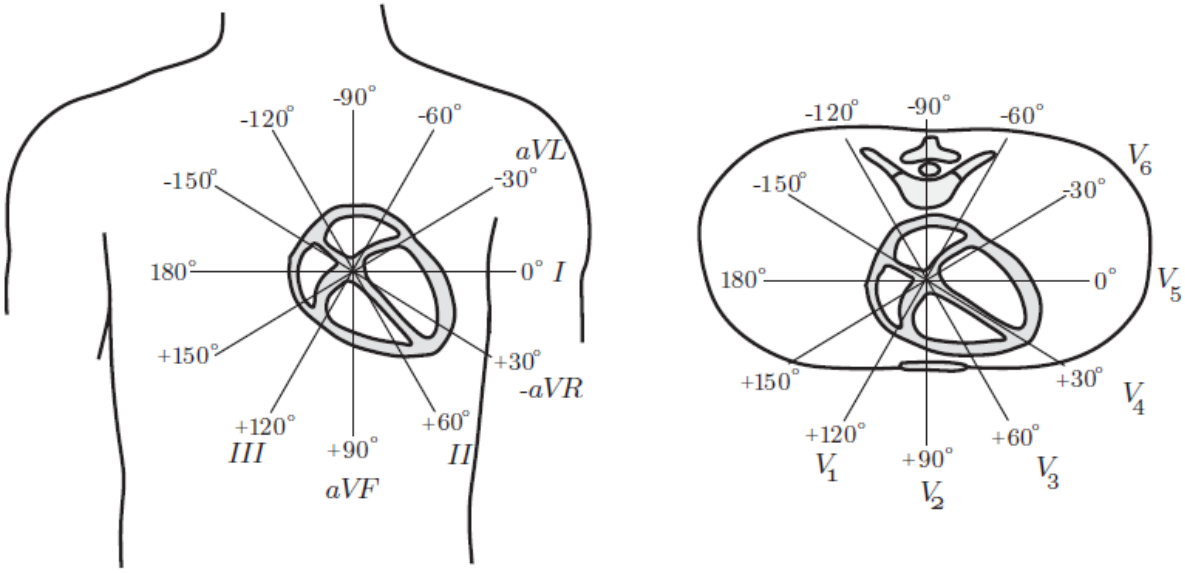

Figure 1.3: Three-dimensional representation of cardiac electrical activity. Adapted from [13].

to baseline and an AP spreads to the AV node and bundle of His where it triggers the ventricular depolarization. Thus, the right and left ventricles begin to depolarize, resulting in what is called the QRS complex, with Q (first negative deflection), R (large positive deflection) and S (negative deflection after R wave) waves. The atria repolarize simultaneously with the QRS complex.

After the completion of ventricular depolarization, the onset of ventricular repolarization begins. The deflection produced by the ventricular repolarization is termed the T wave, which has a very different morphology than the QRS complex.

ECG intervals and segments The notable regions in the ECG waveform consists of PQ interval, PR interval, RR interval (inverse of instantaneous HR), QT interval, PR and ST segments. The PQ or PR intervals are measured from the onset of the P wave to the onset of the QRS complex when its first deflection is, respectively, negative or positive. The RR interval is the time interval measured between two successive R waves. The QT interval is measured from the onset of QRS complex to the end of the T wave. The PR segment corresponds to the region from the end of the P wave to the beginning of the QRS complex. The ST segment refers to the region between the end of the S wave and the beginning of the T wave (see Figure 1.4).

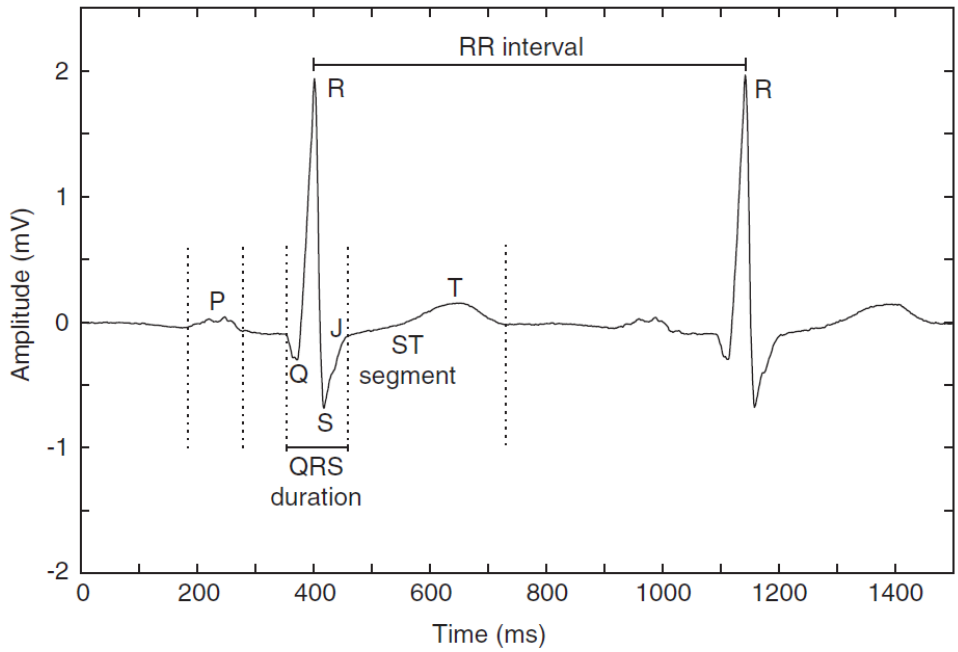

Figure 1.4: ECG signal for two beats with their waves and time intervals. Adapted from [13].

1.4 Chronic kidney disease

1.4.1 Definition

The function of the kidneys is to purify the blood from waste products, ensuring electrolyte levels are normal and regulating the overall amount of water. To measure how well the kidneys are filtering, Glomerular filtration rate (GFR) is used, which is normal if greater than 90 mL/min/1.73m^2, but it might decrease with age or by kidney disease. When kidneys are damaged (with an GFR of less than 60 mL/min/1.73m^2 [16]) for more than 3 months and unable to properly filter blood the way they should, CKD may be caused. A dialysis or a kidney transplant may be required at a very low GFR. All stages of this disease, but particularly the late, most severe ones, so called end-stage renal disease (ESRD), are associated with increased mortality risk and decreased quality of life, thus involving high economic costs [1, 17]. An estimated 843.6 million individuals worldwide (approximately 1 in 10) may have CKD, among which all-age mortality rate attributed to CKD increased by 41.5% between 1990 and 2017 [18]. Millions of people die each year because they do not have access to affordable treatment [19]. Between five and seven million ESRD patients need renal replacement therapy worldwide [17].

1.4.2 Stages of CKD

There are five stages of CKD [20, 21], which can be determined by GFR (see Table 1.1).

Table 1.1: Stages of CKD.

Stage	GFR (mL/min/1.73m^2)	Description
1	> 90	Normal kidney or with very mild damage
2	$60 - 89$	Mild decrease in kidney function but kidneys remain healthy
3	$30 - 59$	Moderate decrease in kidney function and some damage to kidneys, which do not properly filter waste, toxins and fluids
4	$15 - 29$	Severe decrease in kidney function and severely damaged kidneys, cause to build up waste, toxins, and fluids in the body
5	< 15	Kidney failure, with buildup of waste and toxins becoming life threatening. It is termed as ESRD

1.4.3 Hemodialysis

Hemodialysis (HD) is also called "artificial kidney", which is used to remove waste products from the blood through a process called dialysis. HD cleans the patient's blood outside the body when the kidneys are not able to do this work. The blood is routed through a dialyzer (filter) to clean it and then returned to the patient. The whole process is controlled by a HD machine, which also removes fluid excess using anticoagulants and regulates the entire cleaning process (see Figure 1.5).

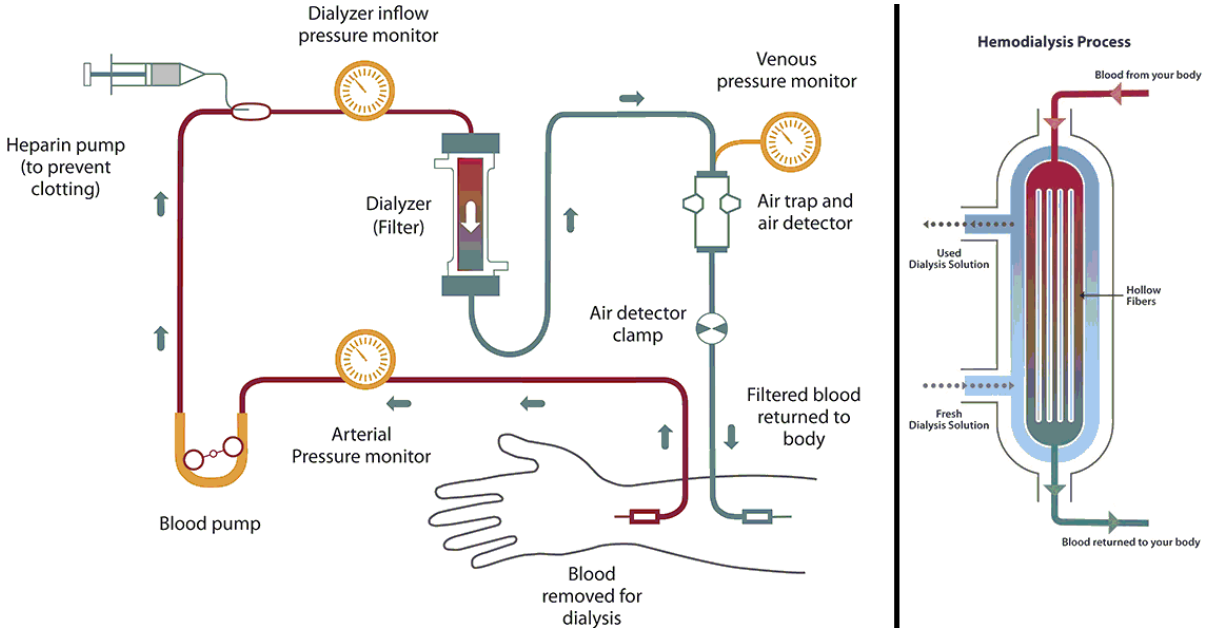

Figure 1.5: Diagram of the complete hemodialysis process. Adapted from [22].

HD is a common treatment for patients in whom the disease has progressed to ESRD. The main causes of death among ESRD patients undergoing HD are cardiovascular diseases, all together accounting for 43% of mortality [10]. Many of these deaths are due to ventricular arrhythmias and sudden cardiac death (SCD) [2].

1.5 ECG waveforms and electrolyte variations

ESRD patients show impaired ability to maintain electrolyte balance in the bloodstream. Serum potassium ($[K^+]$) and calcium ($[Ca^{2+}]$) levels outside normal ranges, in the form of hypo- or hyperkalemia and hypo- or hypercalcemia, are known to increase the risk for life-threatening arrhythmias [6, 23–25]. HD can even enhance arrhythmic risk due to changes in volume and electrolyte concentrations associated with the intermittent nature of the treatment [26]. ESRD patients undergoing HD frequently have serum electrolyte levels outside normal ranges, which can increase the risk for life-threatening arrhythmias and SCD [6, 23–25]. Non-invasive ambulatory monitoring of these electrolyte levels can be useful for risk prediction and triggering of early warnings.

Electrolyte levels can be monitored using blood tests, but their ambulatory measurement is currently not feasible. Therefore, the use of alternative techniques that can provide information on serum concentration electrolyte levels becomes necessary. Changes in the concentration level of electrolytes cause visible variations on the ECG, making it a suitable tool for extracting the required information (see Figure 1.6).

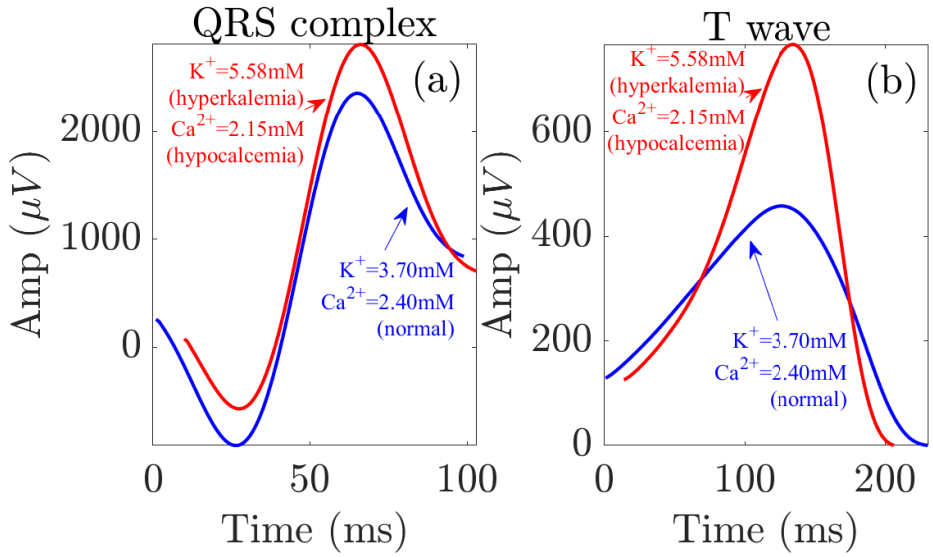

Figure 1.6: Processed average ECG signals before (red) and after HD (blue). Panel (a) shows the waveforms related to the electrical activation of the heart ventricular muscle (the 'QRS complex' of the ECG) and panel (b) the signals related to the subsequent electrical relaxation ('T wave' of the ECG). Due to the applied signal processing, the traces are smoother than the original ECGs.

Changes in $[K^+]$ and $[Ca^{2+}]$ affect cardiac electrical activity and are reflected in the ECG, both in ventricular depolarization (QRS complex) and repolarization (T wave) [3–6, 23, 27]. Because of its noninvasive nature and ease of use, markers derived from the ECG are useful tools for continuous monitoring of $[K^+]$ and $[Ca^{2+}]$ and, thus, for risk assessment and triggering early-warning alerts, which could facilitate timely therapies for ESRD patients.

1.5.1 ECG changes induced by electrolyte variations

Several markers have previously been published in the literature to characterize ECG changes induced by $[K^+]$ and $[Ca^{2+}]$ variations, but there are some limitations in terms of sensitivity and specificity, as discussed below:

Width of T wave. The T wave width, T_w, is the time from T wave onset to T wave end [28]. Although T_w shows high correlation with $[K^+]$ or $[Ca^{2+}]$, the correlation is remarkably diminished after controlling for additional effects occurring during HD [29].

Amplitude of T wave. The amplitude of the T wave is computed as the difference in millivolts between the T wave peak and end. Previous studies have described that ECGs recorded under hyperkalemic conditions commonly have more peaked T waves than those recorded under normal levels of $[K^+]$ [4, 23, 25, 30]. Also, some studies have reported a moderate or strong relationship between $[K^+]$ and the T wave amplitude in simulated ECGs [7]. However, a change in the T wave amplitude with variations in $[K^+]$ could not be consistently measured in all patients due to large inter-individual variability in the relationship between $[K^+]$ and T wave amplitude.

Slope of T wave. Some studies have computed the final slope of the T wave as the mean first derivative of the T wave from its peak to its end [8]. A tight relationship between $[K^+]$ and T wave slope has been shown in simulated ECGs [7]. Nevertheless, the trend in the relationship between this marker and $[K^+]$ was not consistent in different ECG databases.

Slope-to-amplitude ratio of T wave ($T_{S/A}$). $T_{S/A}$ represents the ratio between the maximal downward slope (in absolute value) and the amplitude of the T wave, expressed in 1/ms [9, 31]. A strong correlation has been reported between $T_{S/A}$ and $[K^+]$, but the correlation was reduced after removing other covariates during HD [29].

Slope-to-square root of amplitude of T wave ($T_{S/\sqrt{A}}$). $T_{S/\sqrt{A}}$ represents the ratio between the maximal downward slope (in absolute value) and the square root of the amplitude of the T wave [32]. The reported high association between $T_{S/\sqrt{A}}$ and $[K^+]$ was remarkably reduced after controlling for additional effects occurring during HD [29].

T wave amplitude-to-R wave amplitude ratio (T/R). T/R is the ratio between the amplitude of the T wave and the amplitude of the R wave. It has been reported to present high association with $[K^+]$ [8].

Morphology Combination Score (MCS) of T wave. Regarding the analysis of the T wave shape, a morphology combination score (MCS) based on T wave asymmetry,

flatness and notching has been used to analyze its relationship with [K^+] in a primary care population [33–36]. A clear association between MCS and [K^+] could only be found among individuals with [K^+] in the range 2–4.1 mM, but not among those with [K^+] in the range 4.2–6 mM [36].

Width of QRS complex. The QRS complex width, QRS_{w}, represents QRS duration calculated from QRS onset to end [28]. QRS complex duration has rendered inconsistent results, with some works reporting widened QRS complex [23, 37] and others reporting narrowed QRS complex at high [K^+] [6, 38].

Amplitude of QRS complex. The QRS complex amplitude, QRS_{a}, represents QRS amplitude calculated from maximum to minimum values of the QRS complex. QRS_{a} has been described to be strongly negatively correlated with [K^+], i.e. QRS_{a} increases with decreasing [K^+] [38].

Slope of QRS complex. The upward slope, I_{US}, and the downward slope, I_{DS}, are defined as the maximum (between Q wave and R wave) and minimum (between R wave and S wave) values of the QRS complex derivative, respectively [39, 40]. Both markers have been found to be strongly correlated with [K^+] and [Ca^{2+}] [41].

QT interval. The QT interval is the time interval from the start of the Q wave (QRS onset) to the end of the T wave (T end). Although the QT interval has long been used to monitor CKD patients during HD [42–47], contradictory findings have been presented, with many studies reporting QT prolongation [44, 45, 47–49] and others showing QT shortening or no effects on QT with electrolyte variations along HD [50, 51].

1.5.2 Estimation of electrolyte levels from the ECG

A large number of studies have been proposed in the literature to estimate [K^+] and [Ca^{2+}] from ECG, as discussed below:

1. In [32], a single-lead ECG estimator of [K^+] based on the ratio of the T wave downward slope and the square root of T wave amplitude was proposed and validated in 19 HD patients, yielding a mean absolute error of 0.36±0.34 mM. The proposed method was also applied to data from a handheld device by the same group [52]. ECG was obtained using a commercially available ECG electrode system measuring the signal between two fingertips of both hands, yielding an error of 0.38±0.32 mM.

2. On a similar basis, a multi-lead ECG estimator of [K^+] based on the ratio of the downward slope and amplitude of the T wave was proposed and validated in 45 HD patients [9, 31, 53] using leave-one-patient-out cross validation, yielding a mean absolute error of 0.46±0.39 mM.

3. In [54], an ECG-based $[K^+]$ estimator was designed using QRS duration in addition to T wave markers, but QRS duration was found not to be highly correlated with $[K^+]$, in agreement with our present results for QRS_w.

4. Pilia et al. [27] reviewed a large number of studies evaluating QRS amplitude and width features, but no improved serum electrolyte prediction by incorporating these features into repolarization-based estimators was provided.

5. In a deep learning-based study, Lin et al. [55] proposed a deep learning model, ECG12Net, based on 66321 ECGs with a $[K^+]$ measurement within one hour before and after ECG recording, from different ECG features such as P wave axis, RS wave axis, T wave axis, HR, PR, QRS, QT intervals and QTc, yielding a mean absolute error of 0.531 mM.

1.5.3 Limitations of previously proposed ECG markers

Although the above mentioned studies suggest that it is possible to monitor changes in $[K^+]$ and $[Ca^{2+}]$ based on ECG analysis, further investigation is needed to demonstrate the feasibility of such approach. On the one hand, most of the proposed ECG markers rely on only one specific ECG interval duration or wave amplitude that may present large variations not necessarily associated with electrolyte levels. Also, some of the proposed ECG markers cannot always be robustly measured due to difficulties in the delineation of low amplitude waves, which could hinder their use for ambulatory monitoring. Importantly, the physiological underpinnings of changes in the proposed ECG markers in association with electrolyte variations have not been well established.

Another main limitation of these ECG markers is that, even if some of them may show a high degree of correlation with the level of $[K^+]$, their changes cannot be exclusively attributed to $[K^+]$ variations, as confirmed in our study by including additional confounders like variations in $[Ca^{2+}]$ or HR [29]. Some of them were strongly correlated with $[K^+]$ but not in a wide range of values. Some of these features are very sensitive to T wave or QRS complex delineation and thus could be more prone to errors when measured in ambulatory recordings.

Some recent studies have investigated changes in markers of sympathetic activity-related T wave instability along HD [56] and in model-based descriptors of T wave morphology along the interdialytic interval [57], but these studies either have not been able to establish a clear correlation between the values of the evaluated indices and $[K^+]$ or have reported moderate correlation coefficients, thus limiting ambulatory $[K^+]$ monitoring.

Assessment of the whole morphology of ventricular depolarization and repolarization for serum electrolyte estimation has been less explored. Similarly to QT studies, research on QRS complex duration has rendered inconsistent results. Other works have assessed the time voltage area, amplitude and sine wave shape of the QRS complex, but limitations

in terms of their significance or their dependence on blood volume have been acknowledged [27, 58–60].

In this thesis, we evaluated markers accounting for the whole T wave and QRS complex morphology that can more robustly characterize repolarization and depolarization changes associated with different $[K^+]$ and $[Ca^{2+}]$ and, thus, be better suited for noninvasive electrolyte estimation.

1.6 Computational modeling of cardiac electrophysiology

1.6.1 Why cardiac modeling

Cardiovascular diseases are the leading cause of death in the world, taking an estimated 17.9 million lives each year, representing 32%, of all global deaths [61]. It causes death of one person in every 36 seconds in the United States (source: Centers for Disease Control and Prevention. Underlying Cause of Death, 1999–2018). In spite of intense research efforts in the past years, the mechanisms underlying the initiation and maintenance of a number of cardiovascular diseases remain yet to be fully elucidated. In the last decades, mathematical modeling and simulation of cardiac activity has proved to be a powerful approach to describe heart function in health and disease and understand the mechanisms involved in cardiac pathologies.

Although *in vitro* and *in vivo* analyses are being used to shed light on biophysical and biochemical processes involved in cardiac activity, there are several practical and ethical limitations and restrictions when performing experimental and clinical investigations in humans and animal species. Because of this, computational models have become fundamental tools to understand the function of the heart, the commonly observed inter-patient variability and the underlying mechanisms, in all cases without any ethical constraint. In particular, computational models of the human heart are being used to aid in the detection and treatment of cardiac arrhythmias [62].

The electrical activity of the heart (cellular to tissue or whole heart levels) can be simulated using cardiac electrophysiological models, which could further ease to enhance knowledge on cardiac electrophysiology, assist in decision making and reduce animal experimentation.

1.6.2 Electrophysiological models of human ventricular electrophysiology

1.6.2.1 First electrophysiological model

Alan L. Hodgkin and Andrew F. Huxley (HH) proposed the first computational model of the AP [63], which described the electrical activity of the squid giant axon obtained using the voltage clamp technique. In this model, the cell was described as an electrical circuit in which the cell membrane acts as a capacitor while ionic currents flow through ion channels, which are modeled as resistors. Figure 1.7 shows the equivalent circuit of the Hodgkin-Huxley model, comprising four ionic currents (sodium current, I_{Na}, potassium current, I_K, leak current, I_L, and capacitive current). Here, leak current refers to the current generated by other ions different from sodium and potassium. Most of the electrophysiological models developed after that of Hodgkin and Huxley, including cardiac models, include the formalism introduced by them [63].

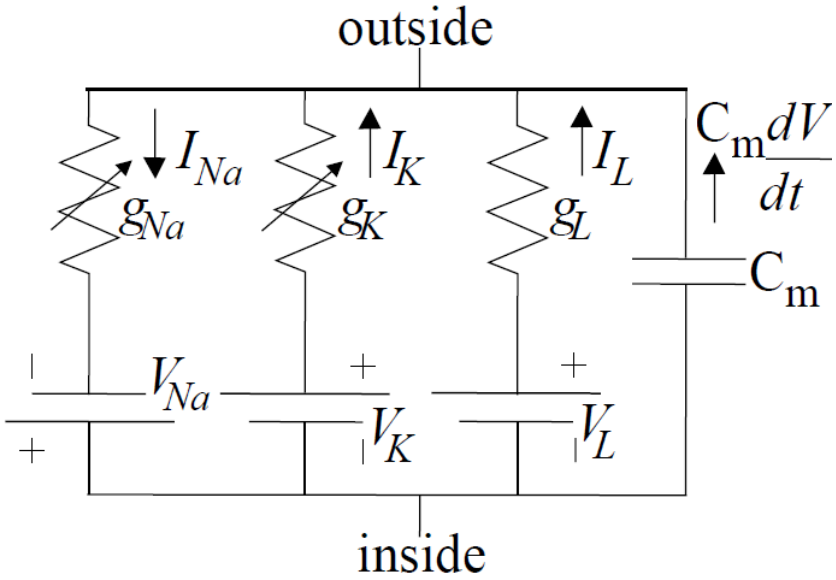

Figure 1.7: The equivalent circuit of the Hodgkin-Huxley model representing cell membrane, with voltage sources (V_{Na}, V_K, V_L), membrane capacitance (C_m) and conductances of sodium (g_{Na}), potassium (g_K) and the rest of ions (g_L). Adapted from [64].

Ionic movements across the cell membrane are mainly due to electrical and diffusion forces. The ion is in equilibrium when these two forces are equal in magnitude but opposite in sign. The Nernst potential, equilibrium potential of an ion, is defined as follows [64]:

$$V_k = -\frac{RT}{z_k F} \log(\frac{[k]_i}{[k]_o}), \tag{1.1}$$

where V_k is the Nernst potential for a specific ion k, T is the absolute temperature, R is the ideal gas constant, z_k is the valence of ion k, F is Faraday's constant, k_i is the

intracellular concentration of ion k and k_o is the extracellular concentration of ion k.

Using Ohm's law, the conductance per unit area, g_k, for a specific ion k, can be computed as:

$$g_k = \frac{I_k}{V_m - V_k}, \tag{1.2}$$

where V_m is the transmembrane potential and I_k is the electric current carried by ion k per unit area.

According to HH formulation, each type of ion passes through channels that are specifically selective for that particular ion type. In the HH model, sodium channels are comprised of one inactivation (h type) and three activation (m type) gates, whereas potassium channels are composed of four equal activation (n type) gates. On the one hand, the activation gates open when transmembrane potential increases, while they remain closed at resting AP phase. On the other hand, the inactivation gates are open at resting AP phase and they close at increased transmembrane potential. Therefore, I_{Na} and I_K can be computed as follows:

$$I_{Na} = g_{Na}(V_m - V_{Na}) = g_{Na_{max}} m^3 h (V_m - V_{Na}), \tag{1.3}$$

$$I_K = g_K(V_m - V_K) = g_{K_{max}} n^4 (V_m - V_K), \tag{1.4}$$

where $g_{Na_{max}}$ and $g_{K_{max}}$ are the maximal conductances of sodium and potassium channels, respectively. The variables m, h and n are the gates of each ionic channel. The ionic conductance is equal to the maximal ionic conductance when all the gates are in the open state for a specific ion channel.

The values of the gate variables m, h and n are calculated by the following ODE:

$$\frac{dx}{dt} = \alpha_x(1 - x) - \beta_x x, \tag{1.5}$$

where x refers to the m, h or n gates of ion channels and α and β are transfer rate coefficients from closed to open state and open to closed state, respectively.

Therefore, following the HH methodology, the total current across the cell membrane can be computed as the sum of all ionic currents as follows:

$$I_{tot} = C_m \frac{dV_m}{dt} + I_{Na} + I_K + I_L. \tag{1.6}$$

1.6.2.2 Main ionic currents

As stated in the previous section, a cardiac electrophysiological model represents, among other aspects, all the different currents that pass through the cell membrane. These currents are generated by the flow of ions through different channels, exchangers and pumps, which connect intracellular and extracellular media [65]. Potassium, calcium and sodium are the most relevant ions that play a role in the human ventricular AP models.

The main ionic currents associated with these ions are: Potassium currents (transient outward potassium current, I_{to}, rapidly activating delayed rectifier potassium current, I_{Kr}, slowly activating delayed rectifier potassium current, I_{Ks}, and inward rectifier potassium current, I_{K1}), calcium currents (L-type calcium current, I_{CaL}) and sodium currents (fast sodium current, I_{Na}, and late sodium current, I_{NaL}). These ionic currents do not have requirements for energy consumption, in general. However, there are also currents that are associated with pumps (which force the movement of ions against gradient and require ATP consumption) and exchangers (which force ions to pass in the direction of the ion concentration gradients and may change the ion flux direction) that require energy and/or do not work as the rest of ion channels, such as the sodium-potassium pump current, I_{NaK}, and the sodium-calcium exchanger current, I_{ncx}.

1.6.2.3 Propagation models of electrical activity

The electrical activity in the human heart depends not only on cellular electrophysiology but also on the electrical propagation between cells. In this thesis, 1D models representing cardiac fibers and 3D models representing cardiac tissues of human ventricles have been simulated.

The electrical activity of cardiac tissue is simulated by a coupled system of partial differential equations (PDEs) and ordinary differential equations (ODEs). PDEs are used to simulate electrical wavefront propagation and ODEs are used to simulate single cell electrophysiological activity [66]. A scheme of a tissue model is illustrated in Figure 1.8.

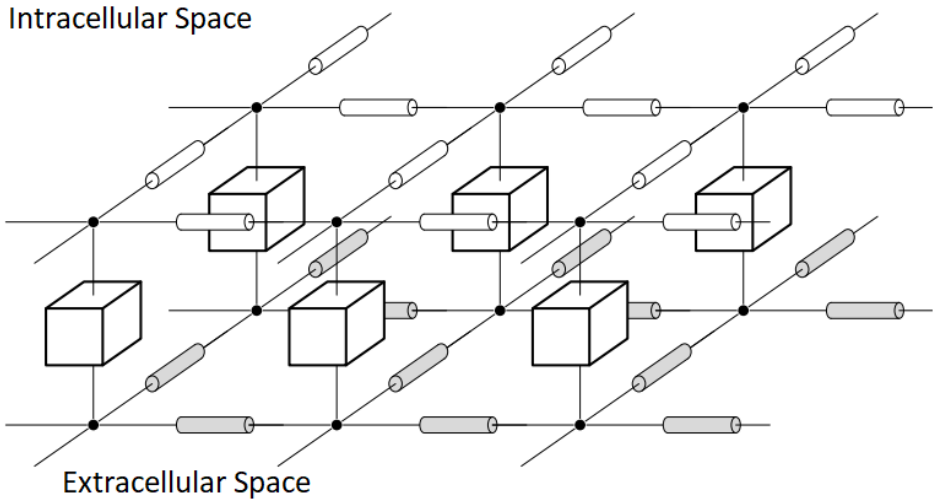

Figure 1.8: Tissue model used in propagation models, where the membranes of the cells (boxes) are connected to each other with resistances in both intracellular (white cylinders) and extracellular (grey cylinders) space. Adapted and modified from [67].

The monodomain and bidomain equations have been used to simulate cardiac electrical propagation. The monodomain equation consists of a parabolic PDE coupled to

a system of ODEs and the bidomain equations consists of a parabolic PDE, an elliptic PDE and a system of ODEs [68].

The bidomain equations are:

$$\beta(C_{\mathrm{m}}\frac{\partial V_{\mathrm{m}}}{\partial t} + I_{\mathrm{ion}}) - \nabla \cdot (\sigma_i \nabla (V_{\mathrm{m}} + \phi_e)) = I_{\mathrm{s_i}}, \tag{1.7}$$

$$\nabla \cdot ((\sigma_i + \sigma_e)\nabla \phi_e + \sigma_i \nabla V_{\mathrm{m}}) = I_{\mathrm{s_e}}, \tag{1.8}$$

where V_{m} is the transmembrane potential, C_{m} is the membrane capacitance, β is the membrane surface-to-volume ratio (the amount of membrane found in a given volume of tissue), I_{ion} is the sum of all transmembrane ionic currents, ϕ_e is the extracellular potential, σ_i and σ_e represent the intracellular and extracellular conductivity tensor fields, respectively, and $I_{\mathrm{s_i}}$ and $I_{\mathrm{s_e}}$ represent the external stimuli applied to the intracellular and extracellular spaces, respectively.

After simplifying equations 1.7 and 1.8 by considering proportionality between the conductivity tensor matrices σ_i and σ_e, i.e. $\sigma_i = \alpha\sigma_e$, the monodomain equation is expressed as follows:

$$\beta(C_{\mathrm{m}}\frac{\partial V_{\mathrm{m}}}{\partial t} + I_{\mathrm{ion}}) = \nabla \cdot (\sigma \nabla V_{\mathrm{m}}), \tag{1.9}$$

where σ is a conductivity tensor as described by $\sigma = \sigma_i(\sigma_i + \sigma_e)^{-1}\sigma_e$ [68].

In this thesis, ventricular electrical propagation was simulated with the monodomain reaction-diffusion model since, for our investigations, the accuracy with respect to the bidomain model is similar, but its computational cost is lower [66].

1.6.2.4 Electrophysiological models of human ventricular electrophysiology: recent developments

Several mathematical models of electrical and ionic homeostasis in human ventricular myocytes have been proposed in recent years [65]. Among all, the most studied human model is proposed by Ten Tusscher and Panfilov (TP06) [69], which is an improved version of the Ten Tusscher-Noble-Noble-Panfilov (TNNP04) model [70]. In this model, the slow delayed rectifier potassium current, the L-type calcium current and the calcium dynamics were reformulated. Both the TNNP04 and the TP06 models were based on experimental human data for most of the main ionic currents. The TP06 model can more accurately reproduce restitution of the APD than previously proposed human ventricular models. Another human ventricular model was proposed by Iyer et al. (IMW04) [71], which includes a description of calcium homeostasis and reproduces diverse aspects of the excitation-contraction coupling (ECC). A more recent model of the human ventricular AP was proposed by Grandi et al. (GPB) [72], which includes new definitions of kinetics and ionic current densities according to experimental data on human myocytes. The GPB model relies on the framework of the rabbit ECC model proposed by Shannon et

al. [73].

Based on the GPB model, a new model was proposed by Carro et al. (CRLP) [74] including modifications and reformulations of various currents based on human data. Then, O'Hara et al. proposed the O'Hara-Rudy dynamic (ORd) model [75], which is based on an extensive dataset of undiseased human cells to characterize the steady-state rate dependence and restitution of the ventricular AP. This model also incorporates the effects of Ca^{2+}/calmodulin-dependent protein kinase II (CAMKII) on ionic currents. Subsequently, Himeno et al. [76] proposed a human ventricular membrane excitation contraction model, which includes a more detailed description of the ECC than previously described models and was proved to reproduce calcium-induced calcium release and membrane excitation characteristics.

In the last years, a large number of studies have been published to include the formalism of previously proposed human ventricular AP models and to modify them based on specific requirements. In Dutta et al. [77], the authors assessed the ability of four human ventricular AP models (TP06, GPB, CRLP and ORd) to simulate key electrophysiological consequences of acute myocardial ischemia in single cell and tissue simulations. They observed that these models, particularly GPB and ORd, have limitations with respect to the simulation of hyperkalemic effects in tissues, as these models do not reproduce propagation of excitation for $[K^+]$, especially for values larger than 6 mM. Therefore, the authors modified the intracellular potassium concentration in the GPB model and the sodium current in the ORd model to reproduce the electrophysiological alterations in repolarization, refractoriness and conduction velocity caused by acute myocardial ischemia. They also concluded that the TP06 and ORd models showed the closest agreement to experimental data.

Based on that, we first considered using the modified version of the ORd model [75] proposed by Dutta et al. [77], but we observed this model was not able to reproduce the inverse relationship between APD and $[Ca^{2+}]$ described in several *in vitro* and *in vivo* studies [78–80]. Even a more recently proposed modified version of the ORd model by Tomek et al. [81] was not able to reproduce a physiological APD-$[Ca^{2+}]$ relationship. Therefore, to adequately represent the relationship between APD and $[Ca^{2+}]$, we considered the Ten Tusscher-Panfilov model in which we incorporated the updates published by Severi et al. [82]. These included modifications in the formulation of two L-type calcium current gates: an inactivation gate dependent on voltage, f_2, and an inactivation gate dependent on the calcium concentration in the dyadic space f_{Cass}. Another recently proposed model, by Bartolucci et al. (BPS2020) [83], which is a modification of the ORd model [75], can reproduce APD-$[Ca^{2+}]$ relationship, but this model still needs to be tested in 3D tissues. They mainly changed the description of L-type calcium current inactivation, sarcoplasmic reticulum and calcium release. In future studies, the BPS2020 model could be a good option, considering its ability to reproduce a physiological APD-$[Ca^{2+}]$ relationship. In this thesis, we used the modified version of TP06 model proposed by

Severi et al. [82] because it was already available when we started our research, it can reproduce a physiological APD-[Ca^{2+}] relationship and it allows running cell and tissue simulations at an affordable computational time.

1.6.3 *In silico* analysis to assess electrolyte variations

Computational modeling has particularly been used to assess the effects of changes in [K^+], [Ca^{2+}] and sodium concentration ([Na^+]) on simulated APs and ECGs [7,84,85]. A strong relationship between [K^+] and [Ca^{2+}] with simulated ECG intervals, particularly QT and RT intervals, has been reported, with negligible effects of [Na^+] changes on those intervals [84]. In [85], prolongation of the RT interval has been shown in response to increased [K^+], which is acknowledged by the authors to be in contrast with clinical data and possibly explained by factors other than [K^+]. In some other studies using ventricular electrophysiology models [9, 84, 86, 86, 87], reductions in QT interval and T_{w} have been observed by increasing [K^+] and [Ca^{2+}], respectively.

The above discussed results show that *in silico* modeling and simulation can help to gain insight into the ECG changes observed in response to electrolyte abnormalities. Simulation of ECGs from a set of human ventricular tissue models representing potential inter-patient differences could help to explain inter-patient variability in ECG response to [K^+] and [Ca^{2+}] and could be used to shed light on the inter-individual differences in the relationships between ECG markers and [K^+] or [Ca^{2+}].

1.7 Objectives, outline and publications derived from the thesis

The main objective of this work is to characterize changes in T wave and QRS complex morphology, both in the time and amplitude domains, and in nonlinear dynamics in relation to [K^+] and [Ca^{2+}] variations in ESRD patients and human-specific computational ventricular models. Since HR may play a role in those relationships, the effects of its variations are also assessed in this thesis.

The specific objectives of this PhD research are:

1. Characterization of hypo- or hyperkalemia and hypo- or hypercalcemia-induced changes in ventricular depolarization and repolarization from ECGs of ESRD patients.

2. Proposal of a method for noninvasive estimation of serum potassium and calcium levels based on ECG ventricular depolarization and repolarization features.

3. Establishment of sources explaining inter-individual differences in the characterized ECG features using *in silico* ventricular electrophysiology models.

The contents of the thesis are organized as follows:

Chapter 2. In this chapter, general materials and methods used in the following chapters are described. In particular, we present details of the patient population, ECG signal processing, methodology for time-warping markers and statistical analysis.

Chapter 3. In this chapter, we characterize changes in T wave amplitude, duration and morphology, the latter both in the time and amplitude domains, during HD in relation to $[K^+]$, $[Ca^{2+}]$ and HR variations in patients and simulated ECGs. We discuss new proposed T wave markers and compare them with previously proposed markers. The following publications are based on the results described in this chapter:

- H. A. Bukhari, F. Palmieri, D. Ferreira, M. Potse, J. Ramírez, P. Laguna, C. Sánchez, E. Pueyo. Transmural Ventricular Heterogeneities Play a Major Role in Determining T-Wave Morphology at Different Extracellular Potassium Levels. Computing in Cardiology, 2019, article no. 404.

- H. A. Bukhari, F. Palmieri, J. Ramírez, P. Laguna, J. E. Ruiz, D. Ferreira, M. Potse, C. Sánchez, E. Pueyo. Characterization of T Wave Amplitude, Duration and Morphology Changes During Hemodialysis: Relationship With Serum Electrolyte Levels and Heart Rate. IEEE Transactions on Biomedical Engineering, vol. 68, no. 8, pp. 2467-2478, 2021.

- F. Palmieri, P. Gomis, D. Ferreira, JE. Ruiz, B. Bergasa, A. Martín-Yebra, H. A. Bukhari, E. Pueyo, J. P. Martínez, J. Ramírez, P. Laguna. T-Wave Morphology Changes as Surrogate for Blood Potassium Concentration in Hemodialysis Patients. Computing in Cardiology, 2019, article no. 109.

- F. Palmieri, P. Gomis, D. Ferreira, JE. Ruiz, B. Bergasa, A. Martín-Yebra, H. A. Bukhari, E. Pueyo, J. P. Martínez, J. Ramírez, P. Laguna. Monitoring blood potassium concentration in hemodialysis patients by quantifying T-wave morphology dynamics. Scientific Reports, vol. 11, no. 1, 2021.

Chapter 4. Multivariable prediction of serum potassium in ESRD patients using nonlinear dynamics and T wave morphology markers are presented in this chapter. T wave nonlinear dynamics markers are proposed and evaluated to assess the extent to which they provide information that is complementary to the already evaluated T wave amplitude, duration and morphology markers (explored in chapter 3). In particular, the nonlinear dynamics markers are used to analyze physiological beat-to-beat repolarization variability at varying $[K^+]$ in ESRD patients. A synthetic analysis is also performed to further explore the key concepts behind its functionality. The following publications are based on the research described in this chapter:

- S. Srinivasan, HA. Bukhari, P. Laguna, C. Sánchez and E. Pueyo. Analysis of T Wave Nonlinear Dynamics for Serum Potassium Monitoring in End-Stage Renal Disease Patients. Computing in Cardiology, 2020, article no. 461.

- HA. Bukhari, C. Sánchez, S. Srinivasan, F. Palmieri, M. Potse, P. Laguna and E. Pueyo. Estimation of potassium levels in hemodialysis patients by T wave nonlinear dynamics and morphology markers. Computers in Biology and Medicine, vol. 143, 2022.

Chapter 5. Ambulatory monitoring of serum potassium and calcium levels in ESRD patients by ECG depolarization morphology analysis is discussed in this chapter. The aim of this chapter is to quantify changes in the QRS amplitude, duration and morphology, the latter both in the time and amplitude domains, at varying $[K^+]$, $[Ca^{2+}]$ and HR in ESRD patients. Furthermore, univariable and multivariable $[K^+]$ and $[Ca^{2+}]$ estimators, including novel QRS morphological markers in combination with already proposed T wave markers, are devised and the contribution of depolarization analysis to $[K^+]$ and $[Ca^{2+}]$ monitoring is assessed.

The following publications are based on the research described in this chapter:

- HA. Bukhari, P. Laguna, M. Potse, C. Sánchez and E. Pueyo. QRS Slopes for Potassium and Calcium Monitoring in End-Stage Renal Disease Patients. Computing in Cardiology, 2021, article no. 221.

- HA. Bukhari, C. Sánchez, M. Potse, P. Laguna and E. Pueyo. Estimación del nivel de potasio en sangre mediante las pendientes del QRS del electrocardiograma en pacientes renales crónicos. X Jornada de Jóvenes Investigadores e Investigadoras del I3A, vol. 9, 2021.

- HA. Bukhari, C. Sánchez, JE. Ruiz, M. Potse, P. Laguna, E. Pueyo. Monitoring of Serum Potassium and Calcium Levels in End-Stage Renal Disease Patients by ECG Depolarization Morphology Analysis. Sensors, vol. 22, no. 8, 2022.

Chapter 6. A 3D torso model based analysis is performed in this chapter using a realistic anatomy. The aim of this chapter is to characterize ECG features, including several markers for $[K^+]$ and $[Ca^{2+}]$, in models with different proportions of endocardial, midmyocardial and epicardial myocytes at varying $[K^+]$ and $[Ca^{2+}]$, and compare the results to measurements in 29 ESRD patients. In addition to that, a sensitivity analysis is performed to investigate the extent to which different proportions of endocardial, midmyocardial and epicardial cells contribute to explain inter-individual differences in QRS complex and the T wave amplitude, time and morphology, particularly for $[K^+]$ and $[Ca^{2+}]$ values outside normal ranges.

The following publications are based on the research described in this chapter:

- HA. Bukhari, P. Laguna, M. Potse, C. Sánchez and E. Pueyo. Inter-individual differences in cell composition across the ventricular wall may explain variability in ECG response to serum potassium and calcium variations. Computing in Cardiology, 2022, article no. 166.

- HA. Bukhari, C. Sánchez, M. Potse and E. Pueyo. Accelerating stabilization of whole-heart models after changes in cycle length. Computing in Cardiology, 2022, article no. 388.

- HA. Bukhari, C. Sánchez, P. Laguna, M. Potse, and E. Pueyo. Differences in ventricular wall composition contribute to explain inter-patient variability in the ECG response to variations in serum potassium and calcium. Under review in Frontiers in Physiology, 2023.

Chapter 7. This chapter contains the main achievements, limitations, possible future work and the main conclusions of this PhD thesis.

1.8 Collaborations and research secondments

All the research presented in this thesis was conducted within the cotutelle Ph.D. program in Biomedical Engineering at University of Zaragoza, Spain and Mathematics & Computer Sciences at University of Bordeaux, France, under the supervision of Prof. Esther Pueyo, Dr. Carlos Sánchez and Dr. Mark Potse. Moreover, we collaborated with researchers and clinicians from other institutions for data collection and interpretation, including Dr. Julia Ramírez (Queen Mary University of London, UK and currently at University of Zaragoza, Spain), D. José Esteban Ruiz and Dr. Beatriz Bergasa (Nephrology Ward, Hospital Clínico Universitario Lozano Blesa, Zaragoza, Spain).

During my progress review meetings, I learned from the suggestions of different researchers such as Prof. Pablo Laguna, Prof. Juan Pablo Martínez and Dr. Alba Martín (University of Zaragoza, Spain), Prof. Pedro Gomis (Universitat Politécnica de Catalunya, Barcelona, Spain), Prof. Blanca Rodriguez (external expert from Oxford University, UK), Prof. Pablo Lamata (external mentor from King's College London, UK), Prof. Jean-Marc Couveignes and Dr. Afaf Bouharguane (monitoring committee members from University of Bordeaux, France).

During my stays in the CARMEN team at the Inria center in Bordeaux, I learnt new computational methodologies to simulate the electrical behavior of the human heart with realistic 3D models of the torso, which was used to compute ECG features in a more realistic way, so that they can be compared with patient data, under the supervision of Dr. Mark Potse.

Chapter 2

General Materials and Methods

In this chapter, general materials and methods used in following chapters are presented. The materials section includes the patient population and clinical measurements, whereas the methods section includes ECG signal processing, methodology for the quantification of T wave and QRS complex morphological descriptors, and statistical analysis. All those methods will be further discussed in each chapter with respect to the specific applications.

2.1 Materials

48-hour 12-lead ECGs, with 3.75 μV resolution and 1 kHz sampling frequency (H12+, Mortara Instruments, Milwaukee, WI, USA), were collected from 29 ESRD patients undergoing HD at Hospital Clínico Universitario de Zaragoza (HCUZ). Concurrently, six blood samples were taken, five during the HD session and one 48 hours after HD start, with patients in supine position. The first blood sample was taken at the HD onset (h_0) and the next three samples (h_1, h_2 and h_3), every hour during the HD session (Fig. 2.1 in red). The fifth sample (h_4) was taken at the end of the session (minute 215 or 245, depending on the patient) and the sixth sample, 48 hours after the start, immediately before the next session (h_{48}). $[K^+]$ and $[Ca^{2+}]$ were measured from the extracted blood samples using a Cobas 6000 c501 analyzer (Roche Diagnostic, Germany) by an indirect ion selective electrode method. The Research Ethics Committee of Aragón approved the study protocol (*CEICA*, ref. PI18/003) on February 14, 2018, and all patients gave signed informed consent. Table 2.1 shows demographic population characteristics, $[K^+]$ and $[Ca^{2+}]$ values, as well as HD duration and dialysate composition.

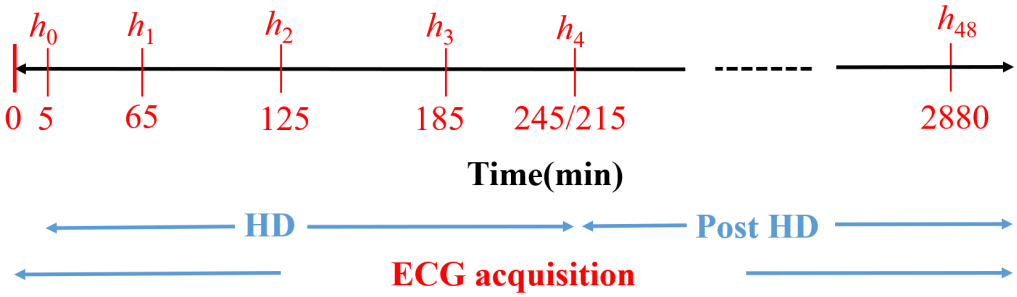

Figure 2.1: Diagram of the study protocol. h_0 to h_4 and h_{48} are the time stages corresponding to blood sample extraction, with indication of the time in minutes from the start of the ECG acquisition.

Table 2.1: Characteristics of the ESRD study population. Values are expressed as number (%) for categorical variables and median (interquartile range) for continuous variables.

Characteristics	Quantity
Age [years]	75 (12)
Gender [male/female]	20 (69%) / 9 (31%)
Electrolyte concentrations	
$[K^+]$ [Pre HD] (mM)	5.05 (1.57)
$[K^+]$ [End HD] (mM)	3.35 (0.62)
$[Ca^{2+}]$ [Pre HD] (mM)	2.15 (0.18)
$[Ca^{2+}]$ [End HD] (mM)	2.32 (0.20)
	#Patients (%)
HD session duration	
240 min	26 (90%)
210 min	3 (10%)
Dialysate composition	
Potassium (1.5 mM)	21 (73%)
Potassium (3 mM)	5 (17%)
Potassium (variable mM)	3 (10%)
Calcium (3 mg/dL)	8 (28%)
Calcium (2.5 mg/dL)	21 (72%)

2.2 Methods

2.2.1 ECG pre-processing

ECG signals were filtered to remove baseline wander, powerline interference and muscular noise for subsequent ECG waveform analysis. A detailed analysis to perform ECG preprocessing can be found in [13]:

Baseline wander Baseline wander is a narrow band low-frequency component in the ECG which may be caused by respiration, body movements and poor electrode contact. It may affect the ECG signal analysis. In this thesis, baseline wander was removed

with a high-pass, forward-backward 6-th order Butterworth filter with 0.5 Hz cut-off frequency [88].

Powerline interference and muscular noise Powerline interference is a common noise source in the ECG that can be characterized by 50 or 60 Hz sinusoidal interference, possibly accompanied by a number of harmonics. Powerline interference increases the difficulty in analyzing and interpreting the ECG, which may result in poor delineation of low-amplitude waveforms [88]. Muscle activity is another source of noise that is more challenging to handle because of the substantial spectral overlap between the muscle noise and ECG as briefly described in [88]. A low-pass 6-th order Butterworth filter with 40 Hz cut-off frequency was applied to remove powerline interference and muscular noise.

2.2.2 ECG waveform detection and delineation

QRS detection and wave delineation were performed in each ECG lead using a wavelet-based delineation method as fully described in [28, 89]. The wavelet transform (WT) decomposed the signal in the time-scale domain, allowing its representation at different resolutions [89].

In the method used here, the discrete dyadic WT [28, 89] is implemented. The detection of the fiducial points is carried out across the adequate WT scales, depending on their frequency content. For Q, R and S waves, the scales 2^1–2^2 are considered, while for the T and P waves the scales 2^4 or 2^5 are used [28,89]. ECG maximum slopes correspond to maxima and minima of the WT and ECG wave peaks correspond to zero crossings in the WT. A wave morphology is assigned and boundaries are located using threshold-based criteria, depending on the number and polarity of the slopes found. The onset of a wave occurs before the first significant slope and the end occurs after the last significant slope associated with the wave [28, 89].

2.2.3 Spatial principal component analysis

A lead space reduction by principal component analysis (PCA) was performed. PCA is a robust spatial transformation that emphasizes waveform signal-to-noise ratio (SNR) [90, 91].

In this thesis, to highlight the T waves (RS complexes, respectively) spatial principal components (PCs) were derived from the T waves (or QRS complexes) of 8 independent leads [90, 91] in a stable 10-minute ECG segment at the end of the HD session. This segment was selected because it corresponded to the time when the patient was discharged from hospital with restored serum $[K^+]$ or $[Ca^{2+}]$. PCA was spatially applied over the T waves (or QRS complexes) of the 8 independent leads, and resulting in 8 PCs or transformed leads. The coefficients defining the PCA transformation were obtained from

the eigenvectors of the 8×8 interlead auto-correlation matrix computed over the T-waves (QRS complexes) in a 10-minute window at the end of the HD session [91, 92].

The full ECG recording was then projected onto the direction of the first PC (PC1) and used for further analysis that involves evaluation of different segments along the recording. The onset, peak and end of the waves were delineated on the projection onto the PC1 using the same wavelet-based delineation method [28] and the obtained delineation marks were used in all subsequent analysis. Figure 2.2 shows an example of some standard ECG leads from a recording and the first PC that highlights the T waves.

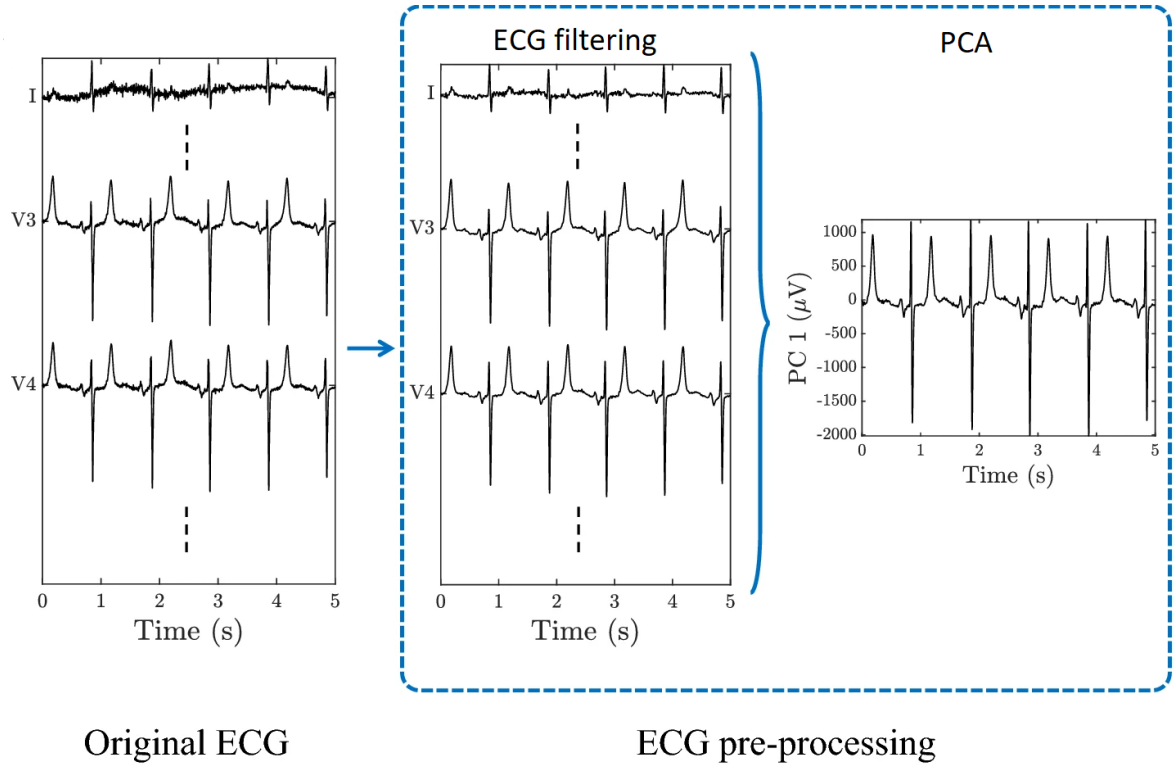

Figure 2.2: Illustration of original ECG signal from three leads (I, V3 and V4), selected from the 12 standard leads, followed by a filtering step as described in section 2.2.1 before spatial PCA analysis (PC1) from 8 independent leads is applied to highlight T waves. Adapted from [91].

2.2.4 Time, amplitude and morphology-based T wave and QRS complex descriptors

2.2.4.1 T wave and QRS complex markers based on morphological characteristics

Morphology-based T wave and QRS complex descriptors were computed using the time-warping methodology described previously [92, 93]. For the patients' ECGs, reference T waves and QRS complexes were calculated from the mean warped T wave (MWTW) and mean warped QRS complex (MWQRS), respectively, at the end of the HD session,

as this is the time when the patient was discharged from hospital with restored serum ion levels, thus being an acceptable reference for ambulatory monitoring. To obtain a MWTW or MWQRS, which is an optimal representative average both in temporal and amplitude domains [93], two-minute ECG segments at the end of each HD hour were analyzed. The two-minute ECG segment was short enough to maintain the assumption of stability for both electrolyte and HR values [89]. Predominant T wave and QRS complex polarities were defined as the most frequent in the analyzed two-minute window. T waves and QRS complexes having the predominant polarity were aligned with respect to their center of gravity so that the calculated MWTW and MWQRS were not affected by potential outlier T wave or QRS complex polarities and morphologies, respectively [93], and used to compute an initial MWTW [93] or MWQRS [92]. After removing outliers from the selected T waves and QRS complexes, the remaining T waves and QRS complexes presenting strong correlation (Spearman's correlation coefficient > 0.98) with the initially calculated MWTW and MWQRS, respectively, were considered to compute the final MWTW and MWQRS.

As mentioned above, the QRS complexes and T waves in each analyzed two-minute window that presented the dominant polarity were considered for MWQRS and MWTW calculation, with the polarity defined as:

$$p_0 = \begin{cases} 1, & \text{if } \max_n\{|f(n)|\} = \max_n\{f(n)\} \\ -1, & \text{if } \max_n\{|f(n)|\} = -\min_n\{f(n)\}, \end{cases} \tag{2.1}$$

where $f(n)$ represents the QRS complex or T wave under analysis. An average of 92% of QRS complexes and 90% of T waves in each analyzed two-minute ECG segment were found to present such dominant polarity (see Fig. 2.3).

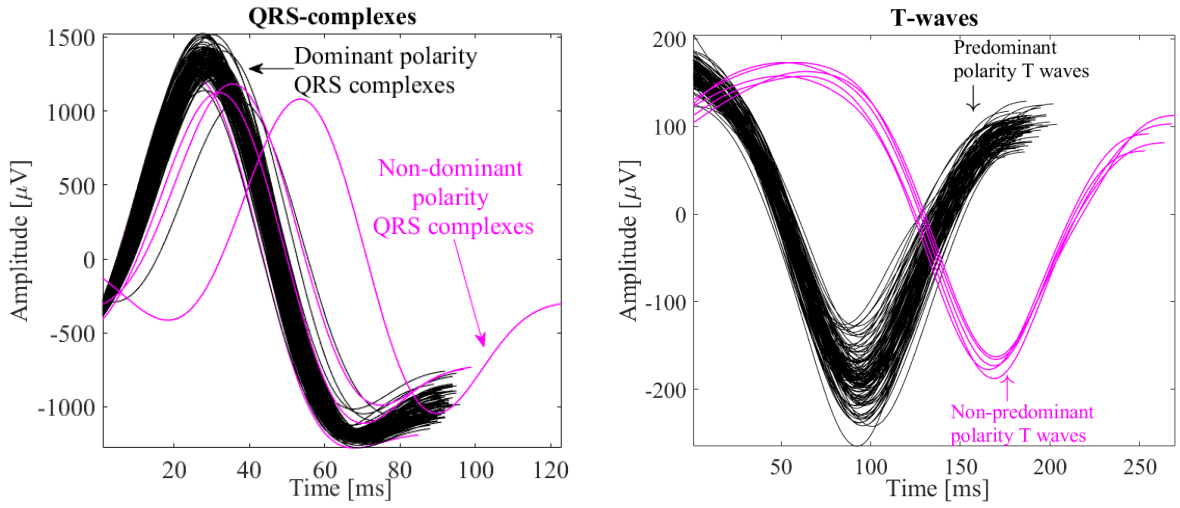

Figure 2.3: QRS complexes (left panel) and T waves (right panel), including selected dominant and non-dominant polarity QRS complexes and T waves from a particular patient at a particular time.

The T wave (QRS complex, respectively) for a given HD time point from a patient's ECG was expressed as $\mathbf{f}^s(\mathbf{t}^s) = [f^s(t^s(1)), ..., f^s(t^s(N_s))]^\top$, and the reference T wave (or QRS complex) as $\mathbf{f}^r(\mathbf{t}^r) = [f^r(t^r(1)), ..., f^r(t^r(N_r))]^\top$, where $\mathbf{t}^r = [t^r(1), ..., t^r(N_r)]^\top$, $\mathbf{t}^s = [t^s(1), ..., t^s(N_s)]^\top$ and N_r and N_s are the total durations of $\mathbf{t}^r$ and $\mathbf{t}^s$, which are the uniformly sampled time vectors corresponding to the T waves (QRS complexes) $\mathbf{f}^s$ and $\mathbf{f}^r$, respectively. Fig. 2.4 (a) shows T waves $\mathbf{f}^r$ and $\mathbf{f}^s$, with their respective time domains, $\mathbf{t}^r$ and $\mathbf{t}^s$. Let $\gamma(\mathbf{t}^r)$ be the warping function that relates $\mathbf{t}^r$ and $\mathbf{t}^s$, such that $\mathbf{f}^s(\gamma(\mathbf{t}^r))$ denotes the time-domain warping of $\mathbf{f}^s(\mathbf{t}^s)$ using $\gamma(\mathbf{t}^r)$. The square-root slope function (SRSF) transformation was used to find the optimal warping function by warping the SRSFs of the original T waves or QRS complexes [93]. This transformation is defined as:

$$\mathbf{q}_f(\mathbf{t}) = \text{sign}(\dot{\mathbf{f}}(\mathbf{t}))|\dot{\mathbf{f}}(\mathbf{t})|^{\frac{1}{2}}. \tag{2.2}$$

The optimal warping function was determined as the one minimizing the SRSF amplitude difference:

$$\gamma^*(\mathbf{t}^r) = \underset{\gamma(\mathbf{t}^r)}{\arg\min}\left(\left\|\mathbf{q}_{f^r}(\mathbf{t}^r) - \mathbf{q}_{f^s}(\gamma(\mathbf{t}^r))\sqrt{\dot{\gamma}(\mathbf{t}^r)}\right\|\right). \tag{2.3}$$

A dynamic programming algorithm was used to obtain the function $\gamma^*(\mathbf{t}^r)$ that optimally warps $\mathbf{f}^r(\mathbf{t}^r)$ into $\mathbf{f}^s(\mathbf{t}^s)$. This function is shown in Fig. 2.4 (d). The warped T wave, $\mathbf{f}^s(\gamma^*(\mathbf{t}^r))$, is shown in Fig. 2.4 (b), together with the reference T wave, $\mathbf{f}^r(\mathbf{t}^r)$.

The T wave descriptor, $d^{\text{u}}_{\text{w,T}}$, shown in Fig. 2.4 (d), was used to quantify the level of warping required to optimally align the T waves $\mathbf{f}^s(\mathbf{t}^s)$ and $\mathbf{f}^r(\mathbf{t}^r)$:

$$d^{\text{u}}_{\text{w,T}} = \frac{1}{N_r}\sum_{n=1}^{N_r}|\gamma^*(t^r(n)) - t^r(n)|. \tag{2.4}$$

where u stands for unsigned.

For the signed version of $d^{\text{u}}_{\text{w,T}}$, the descriptor $d_{\text{w,T}}$ [91] was computed as:

$$d_{\text{w,T}} = \left(\frac{s_d}{|s_d|}\right)\frac{1}{N_r}\sum_{n=1}^{N_r}|\gamma^*(t^r(n)) - t^r(n)|, \tag{2.5}$$

where $s_d = \sum_{n=1}^{N_r^u}(\gamma^*(t^r(n)) - t^r(n)) + \sum_{n=N_r^u+1}^{N_r}(t^r(n) - \gamma^*(t^r(n)))$ is used to account for the sign, with N_r^u denoting the number of samples in the T wave upslope. Similarly, $d^{\text{u}}_{\text{w,Q}}$ was quantified from QRS complexes (see Fig. 2.5).

The T wave amplitude descriptor, $d_{\text{a,T}}$, was computed from the area contained between $\mathbf{f}^r(\mathbf{t}^r)$ and $\mathbf{f}^s(\gamma^*(\mathbf{t}^r))$ normalized by the L2-norm of $\mathbf{f}^r(\mathbf{t}^r)$, thus quantifying amplitude differences after time warping the two T waves:

$$d_{\text{a,T}} = \frac{s_a}{|s_a|}\frac{\|\mathbf{f}^s(\gamma^*(\mathbf{t}^r)) - \mathbf{f}^r(\mathbf{t}^r)\|}{\|\mathbf{f}^r(\mathbf{t}^r)\|} \times 100, \tag{2.6}$$

where $s_a = \sum_{n=1}^{N_r}(f^s(\gamma^*(t^r(n))) - f^r(t^r(n)))$ is used to account for the sign.

The QRS complex amplitude descriptor, $d_{\mathrm{a,Q}}$, was computed from the area contained between $\mathbf{f}^r(\mathbf{t}^r)$ and $\mathbf{f}^s(\gamma^*(\mathbf{t}^r))$ normalized by the L2-norm of $\mathbf{f}^r(\mathbf{t}^r)$, thus quantifying amplitude differences after time warping the two QRS complexes:

$$d_{\mathrm{a,Q}} = p_0 \frac{s_a}{|s_a|} \frac{\|\mathbf{f}^s(\gamma^*(\mathbf{t}^r)) - \mathbf{f}^r(\mathbf{t}^r)\|}{\|\mathbf{f}^r(\mathbf{t}^r)\|} \times 100, \tag{2.7}$$

with only QRS complexes in each analyzed case that presented the dominant polarity being considered for the calculation, with the polarity as defined in Eq. 2.1.

The marker $d^{\mathrm{u}}_{\mathrm{w,T}}$ incorporates information from the linear and non-linear warping required to fit the two T waves in the time domain. The non-linear component of $d^{\mathrm{u}}_{\mathrm{w,T}}$ can be quantified as:

$$d^{\mathrm{NL}}_{\mathrm{w,T}} = \frac{1}{N_r} \sum_{n=1}^{N_r} |\gamma^*(t^r(n)) - \gamma^*_l(t^r(n))|, \tag{2.8}$$

where $\gamma^*_l(t^r)$ (black line in Fig. 2.4 (d)) was derived by linearly fitting $\gamma^*(t^r)$ through the least absolute residual method.

The marker $d^{\mathrm{NL}}_{a,T}$ was defined by computing the L_2 norm of the difference between L_2-normalized versions of $\mathbf{f}^r(\mathbf{t}^r)$ and $\mathbf{f}^s(\gamma^*(\mathbf{t}^r))$:

$$d^{\mathrm{NL}}_{\mathrm{a,T}} = \left\| \frac{\mathbf{f}^r(\mathbf{t}^r)}{\|\mathbf{f}^r(\mathbf{t}^r)\|} - \frac{\mathbf{f}^s(\gamma^*(\mathbf{t}^r))}{\|\mathbf{f}^s(\gamma^*(\mathbf{t}^r))\|} \right\| \times 100. \tag{2.9}$$

Analogously, $d^{\mathrm{NL}}_{\mathrm{w,Q}}$ and $d^{\mathrm{NL}}_{\mathrm{a,Q}}$ were computed from QRS complexes. Fig. 2.5 shows linear and non-linear time warping for QRS complexes.

The set of all morphology-based T wave and QRS complex markers analyzed in this thesis included:

- $d^{\mathrm{u}}_{\mathrm{w,T}}$, representing temporal variations in T wave morphology (expressed in ms),
- $d_{\mathrm{w,T}}$, representing signed version of temporal variations in T wave morphology (expressed in ms),
- $d_{\mathrm{a,T}}$, representing amplitude variations in T wave morphology (expressed as a percentage),
- $d^{\mathrm{NL}}_{\mathrm{w,T}}$, representing non-linear temporal variations in T wave morphology (expressed in ms),
- $d^{\mathrm{NL}}_{\mathrm{a,T}}$, representing non-linear amplitude variations in T wave morphology (expressed as a percentage).
- $d^{\mathrm{u}}_{\mathrm{w,Q}}$, representing temporal variations in QRS morphology (expressed in ms),

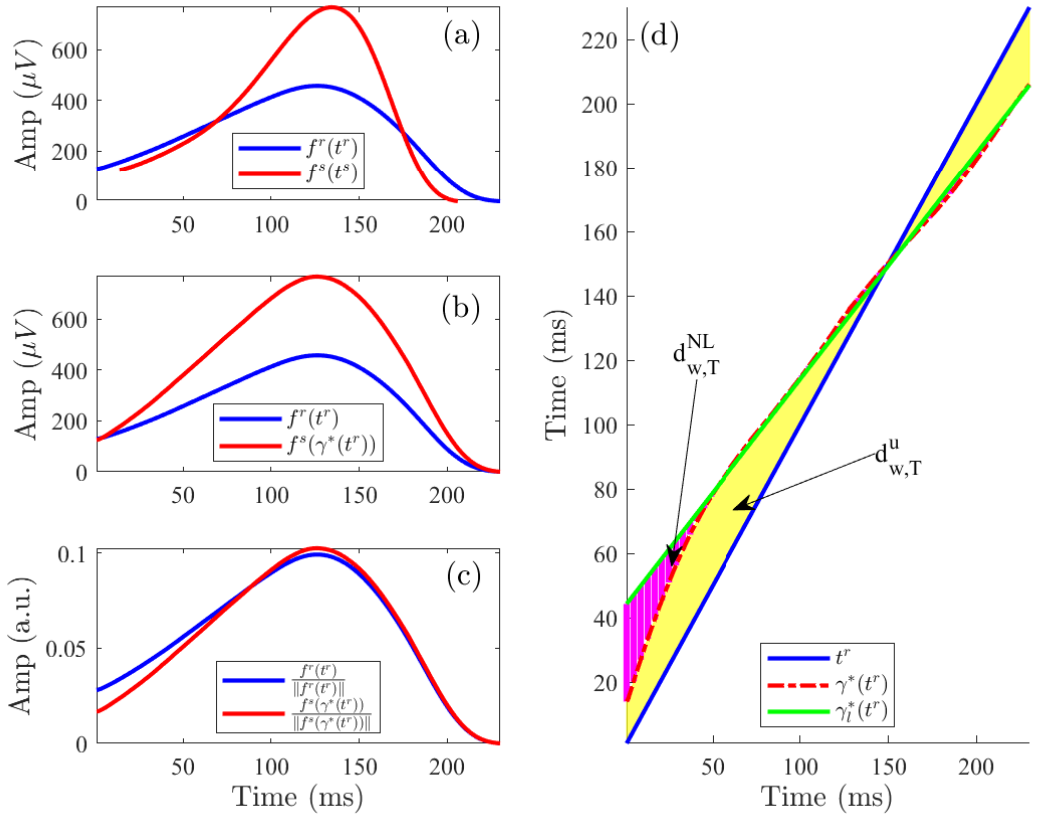

Figure 2.4: Linear and non-linear time warping of T waves from a patient. Panel (a) shows reference (blue) and investigated (red) T waves obtained from an ECG segment during HD. Panel (b) shows the warped T waves, which have the same duration while keeping the original amplitude. Panel (c) depicts the warped T waves after normalization by their L2-norms. The area (yellow region) between both T waves in panel (d) represents $d^{u}_{w,T}$, which quantifies the total amount of warping. The green solid line is the linear regression function $\gamma_l^*(t^r)$ best fitted to $\gamma^*(t^r)$. The marker $d^{NL}_{w,T}$ quantifies the non-linear warping by computing the area of the dashed magenta region between $\gamma^*(t^r)$ and $\gamma_l^*(t^r)$.

- $d_{a,Q}$, representing amplitude variations in QRS morphology (expressed as a percentage),
- $d^{NL}_{w,Q}$, representing nonlinear temporal variations in QRS morphology (expressed in ms),
- $d^{NL}_{a,Q}$, representing nonlinear amplitude variations in QRS morphology (expressed as a percentage).

It should be noted that the warping parameter $d_{w,T}$ has a positive sign if the analyzed T wave is globally widened during the warping procedure to fit the reference T wave, and a negative sign if the T wave is compressed. In the amplitude domain, $d_{a,T}$ is positive if the warped T wave has larger amplitude than the reference T wave, and negative if the T wave has smaller amplitude.

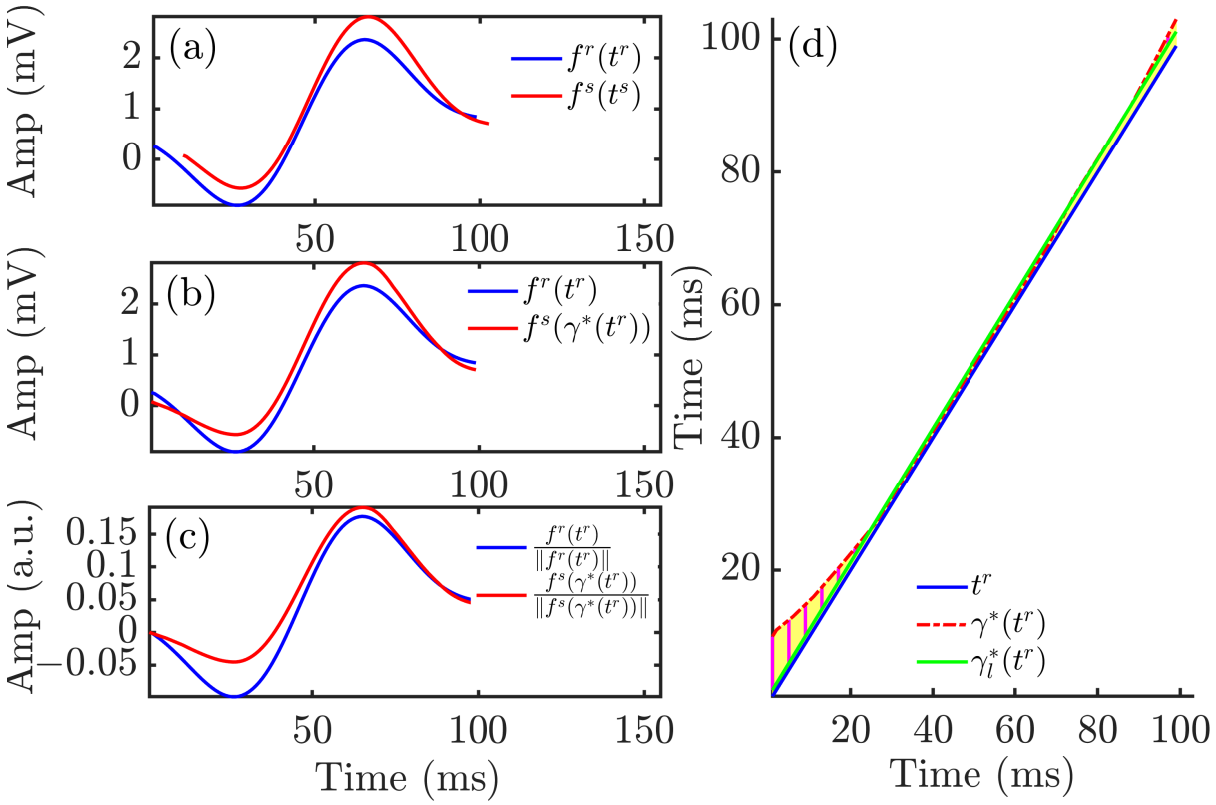

Figure 2.5: Time warping of QRS complexes from a patient. Panel (**a**) shows the reference (blue) and investigated (red) QRS complexes obtained from an ECG segment during HD. Panel (**b**) shows the warped QRS complexes, which had the same duration whilst keeping the original amplitude. Panel (**c**) depicts the warped QRS complexes after normalization by their L2-norms. The yellow area in panel (**d**) represents $d_{\mathrm{w,Q}}^{\mathrm{u}}$, which quantified the total amount of warping. The green solid line is the linear regression function $\gamma_l^*(t^r)$ best fitted to $\gamma^*(t^r)$. The marker $d_{\mathrm{w,Q}}^{\mathrm{NL}}$ quantifies the non-linear warping by computing the area between $\gamma^*(t^r)$ and $\gamma_l^*(t^r)$.

2.2.4.2 Time and amplitude T wave markers

Time- and amplitude-based T wave descriptors computed from MWTWs included:

- T_{w}, representing T wave width calculated from T wave onset to T wave end (expressed in ms) [28].
- $T_{\mathrm{S/A}}$, representing the ratio between the maximal downward slope (in absolute value) and the amplitude of the T wave (expressed in 1/ms) [9, 31].
- $T_{\mathrm{S}/\sqrt{A}}$, representing the ratio between the maximal downward slope (in absolute value) and the square root of the amplitude of the T wave [32].

2.2.4.3 T wave nonlinear dynamics markers

T wave nonlinear dynamics were characterized by computing markers based on maximum Lyapunov exponents computed using Rosenstein's method [94] and another divergence-related marker, as follows.

Lyapunov exponent-based markers λ^t and λ^{wt}. Let's consider 2-minute ECG segments as defined above for each analyzed patient and HD stage. The sequence of concatenated T waves for each of these segments, after having tilted the waves to make their onset and end have zero amplitude, is denoted by:

$$\mathbf{f} = [\mathbf{f}_1^\top, \mathbf{f}_2^\top, \ldots, \mathbf{f}_B^\top]^\top = [f(1), f(2), \ldots, f(N)]^\top \tag{2.10}$$

with $\mathbf{f}_k$=$[f_k(1), f_k(2), \ldots, f_k(N_k)]^\top$ denoting the k-th T wave of N_k samples (i.e. of duration N_k ms, since the sampling frequency is 1 kHz), B the number of beats in the segment and N=$\sum_{k=1}^{B} N_k$ the number of samples of sequence $\mathbf{f}$. Fig. 2.6, panels (a)–(c), shows T waves in three analyzed segments of an ECG recording.

The reconstructed trajectories for delay values of τ were represented by vectors

$$\mathbf{f}^{(\tau)}(j) = [f(j), f(j+\tau), \ldots, f(j+(m-1)\tau)]^\top \tag{2.11}$$

with $j \in \{1, 2, ..., M\}$ and $M = N-(m-1)\tau$, where m is the embedding dimension, here set to 30, and τ the delay in ms, here set to $\lceil N_1/(m-1) \rceil$, where N_1 is the duration of the first T wave, in ms. For each $\mathbf{f}^{(\tau)}(j)$, its nearest neighbor $\mathbf{f}^{(\tau)}(\hat{\jmath})$ was searched for by minimizing

$$d_j(0) = \min_{\mathbf{f}^{(\tau)}(\hat{\jmath})} \left|\left|\mathbf{f}^{(\tau)}(j) - \mathbf{f}^{(\tau)}(\hat{\jmath})\right|\right|, \tag{2.12}$$

with $|j - \hat{\jmath}| > p$, and p set to 25. The notation $||\cdot||$ represents the L2 norm.

Next, the distance between the nearest neighbors $\mathbf{f}^{(\tau)}(j)$ and $\mathbf{f}^{(\tau)}(\hat{\jmath})$ was computed after i steps as:

$$d_j(i) = \left|\left|\mathbf{f}^{(\tau)}(j+i) - \mathbf{f}^{(\tau)}(\hat{\jmath}+i)\right|\right|, \tag{2.13}$$

where $i = 1, 2, \ldots, I$, and $I = \lceil N/5 \rceil$.

For each value of i, the average $y(i)$ of the logarithm of the functions $d_j(i)$ for $j = 1, 2, \ldots, M-I$, was computed as:

$$y(i) = \frac{1}{M-I} \sum_{j=1}^{M-I} \ln(d_j(i)). \tag{2.14}$$

The largest Lyapunov exponent λ^t was estimated as the slope of the least-squares fit to the initial linear portion of $y(i)$, $i = 1, \ldots, c_p$, with c_p being the point where the signal changes most rapidly in mean and slope [95]. Despite being computed from the

linear portion of $y(i)$, this index accounts for nonlinear dynamics of the T wave, as can be observed from equations (2.10)–(2.14).

Figure 2.6, panels (d)–(f), shows λ^t from a patient at three different HD stages (h_0, h_1, h_{48}) and the corresponding functions $y(i)$ for varying i together with its linear fit for $i = 1, \ldots, c_p$.

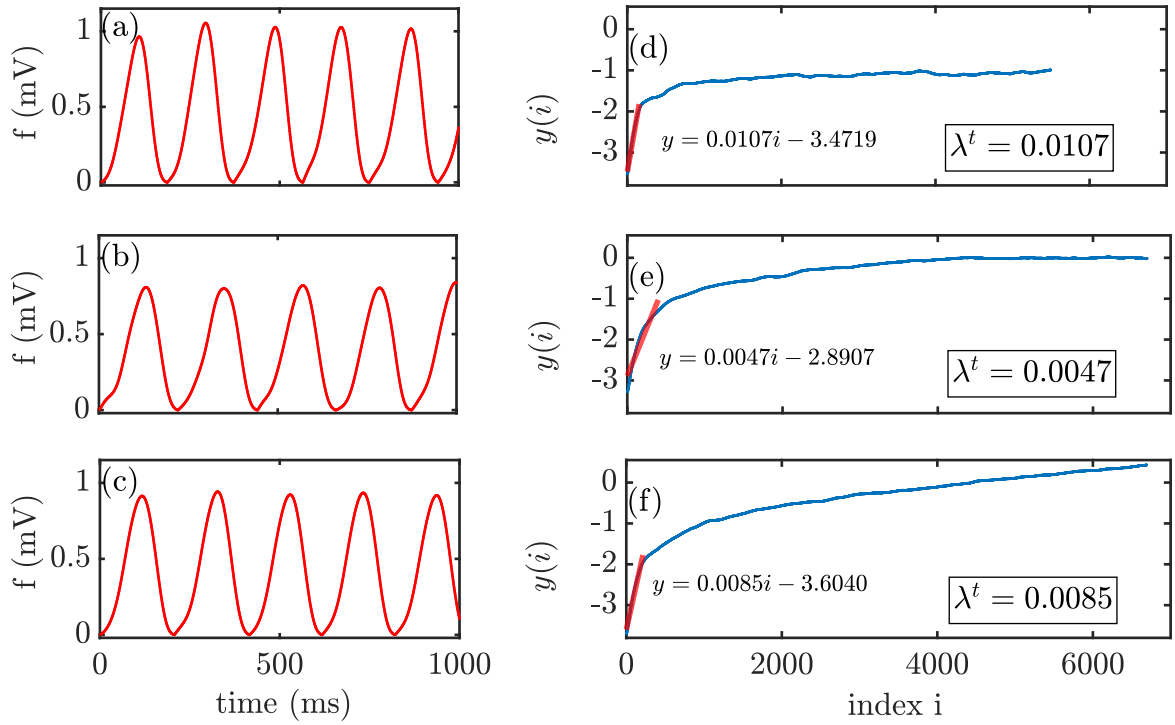

Figure 2.6: Panels a–c: A few T waves from 2-minute ECG segments for a particular patient at different HD stages (h_0, h_1, h_{48}). Panels d–f: $y(i)$ versus index i varying from 1 to I as described in the text. Values of λ^t obtained as the slope of $y(i)$ are shown for each HD time point.

Additionally, another marker, denoted by λ^{wt}, was estimated from the same sequence of T waves in the analyzed 2-minute segments but after warping. The procedure used to calculate λ^{wt} was the same as above but with $\mathbf{f}$ representing the sequence of concatenated warped T waves in the 2-minute segment. The calculation of λ^{wt} and its comparison with λ^t serves to analyze the contribution of amplitude variability, separately from time variability, to the maximum Lyapunov exponent.

Divergence-related marker η. T wave nonlinear dynamics were further evaluated by computing the marker η based on the divergence of trajectories from the inter-MWTW difference defined in equation (2.15) and shown in Fig. 2.7. The figure shows warped T waves for a patient, with reference $\mathbf{f}^r(\mathbf{t}^r)$ (blue) and investigated $\mathbf{f}^s(\gamma^*(\mathbf{t}^r))$ (red) T waves obtained from an ECG segment during HD. The signal shown in black was computed as the difference between the MWTW $\mathbf{f}^s(\gamma^*(\mathbf{t}^r))$ and the reference $\mathbf{f}^r(\mathbf{t}^r)$:

$$\mathbf{f}^d(\mathbf{t}^r) = \mathbf{f}^s(\gamma^*(\mathbf{t}^r)) - \mathbf{f}^r(\mathbf{t}^r). \tag{2.15}$$

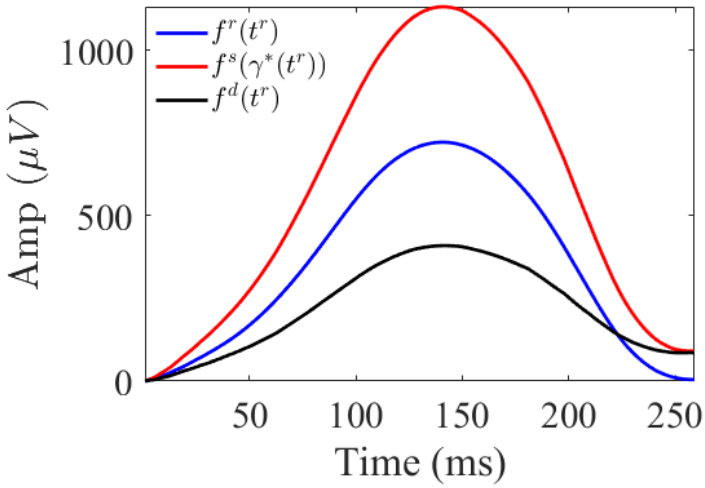

Figure 2.7: Warped T waves (reference $\mathbf{f}^r(\mathbf{t}^r)$ (blue) and investigated $\mathbf{f}^s(\gamma^*(\mathbf{t}^r))$ (red)), which have the same duration while keeping the original amplitude, and the difference between them (black) for a patient.

Specifically, η was computed by averaging $y_d(i)$ from $i = c_p + 1$ to $i = I$:

$$\eta = \frac{1}{I - c_p} \sum_{i=c_p+1}^{I} y_d(i), \tag{2.16}$$

where $y_d(i)$ was computed as $y(i)$ in (2.14) but for the inter-MWTW $\mathbf{f}^d$ rather than for $\mathbf{f}$. In the calculation of $y_d(i)$, $M = N - (m-1)\tau$, where $m = 22$, $\tau = 3$ ms and $p = 25$, with N the duration of the inter-MWTW $\mathbf{f}^d$ in ms.

Fig. 2.8 shows η for inter-MWTW $\mathbf{f}^d$ from a patient at different HD stages (h_0, h_1, h_{48}) as well as the corresponding functions $y_d(i)$ for varying i.

For calculation of η, inter-MWTW at h_4 was computed by taking the difference between the reference T wave and a MWTW computed from the 2-minute ECG segment just before the segment taken at the end of the HD session.

2.2.4.4 QRS slope markers

From each MWQRS (see section 2.2.4.1 for the computation of MWQRS), the upward slope, I_{US}, and the downward slope, I_{DS}, were computed [39, 40]. I_{US} and I_{DS} were defined as the maximum and minimum value of the MWQRS complex derivative denoted by $x'_{\text{QRS}}(n)$, respectively:

$$I_{\text{US}} = \max_n \{x'_{\text{QRS}}(n)\}, \quad n \in \{Q+1, ..., R-1\}, \tag{2.17}$$

$$I_{\text{DS}} = \min_n \{x'_{\text{QRS}}(n)\}, \quad n \in \{R+1, ..., S-1\}, \tag{2.18}$$

with

$$x'_{\text{QRS}}(n) = 0.5 \cdot (x_{\text{QRS}}(n+1) - x_{\text{QRS}}(n-1)), \tag{2.19}$$

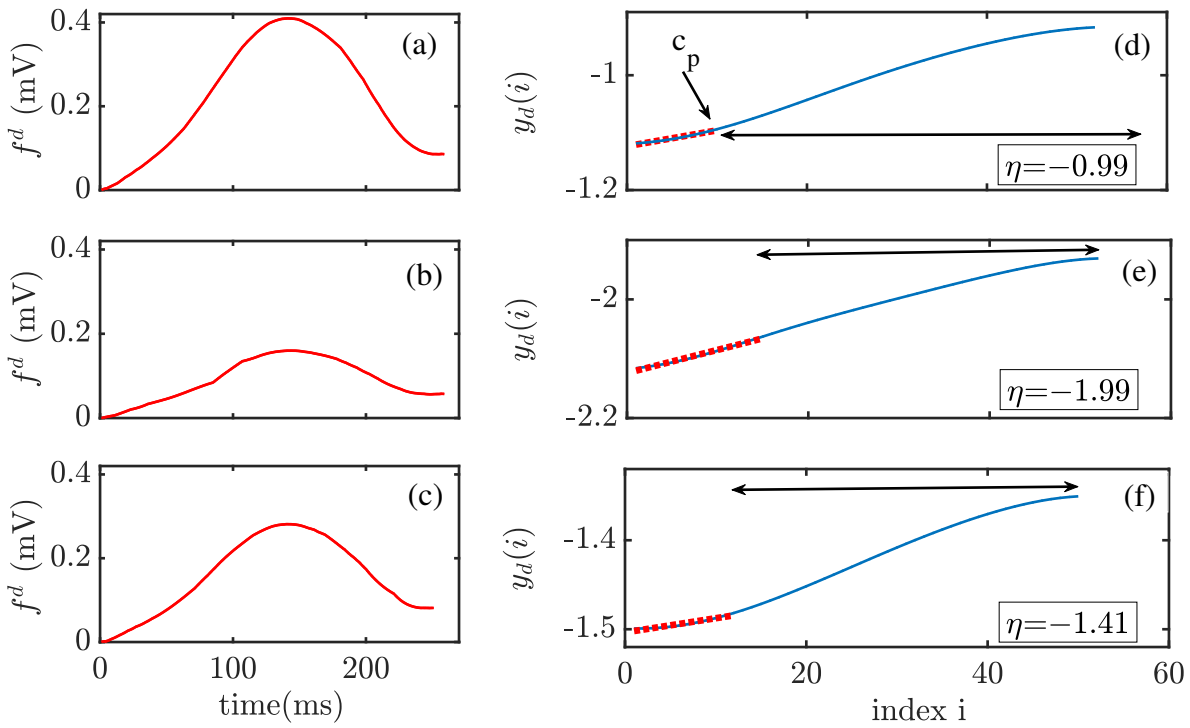

Figure 2.8: Panels a–c: Inter-MWTWs from a particular patient at different HD stages (h_0, h_1, h_{48}). Panels d–f: $y_d(i)$ computed as described in the text, with indication of the corresponding η values from $i = c_p + 1$ to $i = I$ as denoted by double-arrows.

and Q, R and S being the sample locations of the onset, peak and end of the MWQRS, respectively (see Figure 2.9). For time samples n at the limits of the QRS upward and downward intervals, the derivative computation in equation (2.19) requires values outside the interval. In such cases, those values are replaced with the ones at the interval limit. Both slopes are expressed in mV/ms.

From the values of I_{US} and I_{DS} along HD, we quantified the change in QRS slopes with respect to the end of the HD session (h_4) and we denoted them as ΔI_{US} and ΔI_{DS}.

2.2.4.5 QRS duration and amplitude markers

For each MWQRS, the following descriptors were computed:

- QRS_{w}, which represented the QRS width calculated from QRS onset to end (expressed in ms) [28].
- QRS_{a}, which represented the QRS amplitude calculated from the minimum to maximum amplitude of the QRS complex (expressed in mV).

2.2.5 Statistical analysis

To assess the effects of $[K^+]$, $[Ca^{2+}]$ and RR on each investigated T wave or QRS complex marker at different time points during and after HD, linear correlation analysis was

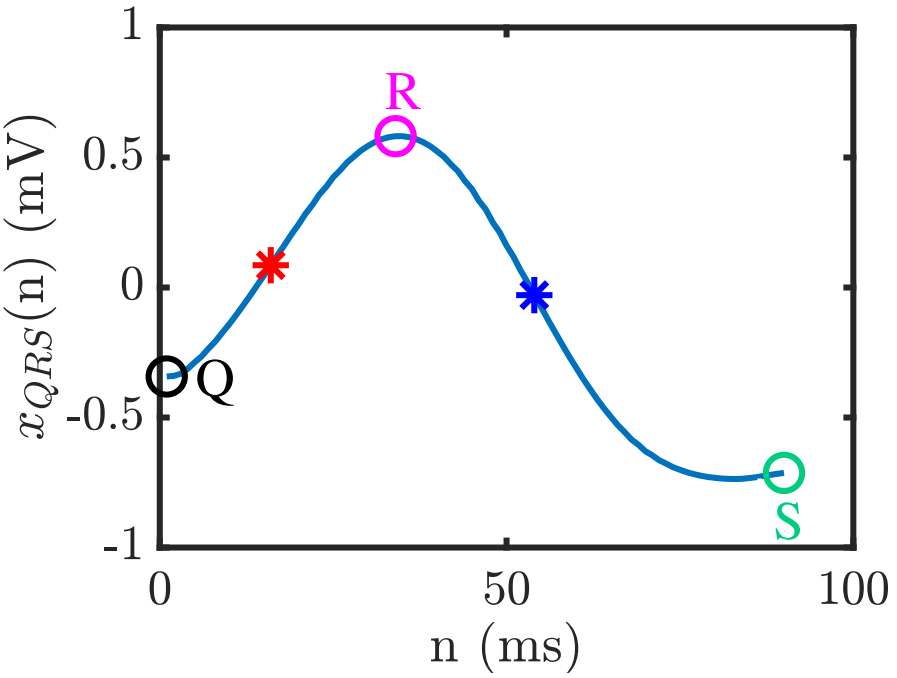

Figure 2.9: MWQRS from a patient's ECG at the start of HD (h_0). Locations of Q (onset of MWQRS), R (peak of MWQRS) and S (end of MWQRS) waves are marked, as well as the locations of maximum and minimum QRS complex derivative (red and blue asterisks, respectively).

performed [96,97]. Let X represent $[K^+]$, $[Ca^{2+}]$ or RR and let Y be one of the markers. The correlation coefficient between X and Y was then computed as:

$$\rho_{XY} = \frac{\sum(X-\bar{X})(Y-\bar{Y})}{\sqrt{\sum(X-\bar{X})^2 \cdot \sum(Y-\bar{Y})^2}}. \tag{2.20}$$

where $\bar{X}$ and $\bar{Y}$ are the sample means.

To independently quantify the effects of $[K^+]$, $[Ca^{2+}]$ and RR on each T wave or QRS marker, linear partial correlation analysis was performed [98, 99]. The correlation coefficient after removing the effects of Z in both X and Y was calculated as:

$$\rho_{XY\cdot Z} = \frac{\rho_{XY} - \rho_{XZ}\rho_{YZ}}{\sqrt{(1-\rho_{XZ}^2)\cdot(1-\rho_{YZ}^2)}}. \tag{2.21}$$

The correlation coefficient between X and Y after removing the effects of two variables Z_0 and Z_1 was calculated as:

$$\rho_{XY\cdot Z_0 Z_1} = \frac{\rho_{XY\cdot Z_0} - (\rho_{XZ_1\cdot Z_0})\cdot(\rho_{YZ_1\cdot Z_0})}{\sqrt{(1-\rho_{XZ_1\cdot Z_0}^2)\cdot(1-\rho_{YZ_1\cdot Z_0}^2)}}, \tag{2.22}$$

where $Z_0, Z_1 \in \{[K^+], [Ca^{2+}], RR\}$.

To test for significant differences in $[K^+]$, $[Ca^{2+}]$, RR, and each marker at different HD time points, Wilcoxon signed-rank tests were performed [100] and p-values (p) were

computed. The use of a non-parametric statistical test was based on the lack of normality of the data distributions according to Shapiro-Wilk test.

Also, to test whether Pearson correlation between each T wave or QRS complex marker and $[K^+]$, $[Ca^{2+}]$ or RR was significantly different from 0 in mean over the population, Student's t-test was performed after converting the statistical distribution of ρ into a normal distribution by application of Fisher's z transform [101].

All statistical analyses were performed using MATLAB version R2020b for Windows (MathWorks Inc., MI, USA).

Chapter 3

Characterization of T Wave Amplitude, Duration and Morphology Changes During Hemodialysis: Relationship with Serum Electrolyte Levels and Heart Rate

This chapter is partially based on the paper published by Bukhari et al., IEEE Transactions on Biomedical Engineering, 2021, 68(8):2467-2478.; 2021.
doi:10.1109/TBME.2020.3043844

3.1 Introduction

As discussed in section 1.5, $[K^+]$ and $[Ca^{2+}]$ variations are known to influence the ECG [3–6]. In a recent large-scale study on unselected individuals, shorter QT intervals were associated with higher $[K^+]$ and $[Ca^{2+}]$ [6]. In [32], a single-lead ECG estimator of $[K^+]$ based on the ratio of the T wave downward slope and the square root of T wave amplitude was proposed and validated in 19 HD patients. On a similar basis, a multi-lead ECG estimator of $[K^+]$ based on the ratio of the downward slope and amplitude of the T wave was proposed and validated in 45 HD patients [9, 31, 53].

As explained in section 1.6, computational modeling has also been used to assess the effects of changes in $[K^+]$, $[Ca^{2+}]$ and sodium ($[Na^+]$) concentrations on simulated APs and ECGs [7, 84, 85]. An inverse relationship between $[K^+]$ and $[Ca^{2+}]$, on the one hand, and simulated QT and RT intervals, on the other, was reported, with negligible effects of $[Na^+]$ changes on those intervals. These *in silico* studies were, however, based on a single

ventricular model not accounting for potential inter-individual variability.

Although the mentioned studies suggest that it is possible to monitor changes in $[K^+]$ and $[Ca^{2+}]$ based on ECG analysis, further investigation is needed to demonstrate the feasibility of such approach. On the one hand, most of the proposed markers rely on only one specific ECG interval duration or wave amplitude that may present large variations not necessarily associated with electrolyte levels. On the other hand, some of the proposed ECG markers cannot always be robustly measured due to difficulties in the delineation of low-amplitude waves, which could hinder their use for ambulatory monitoring. Importantly, the physiological underpinnings of changes in the proposed ECG markers in association with electrolyte variations have not been well established. We hypothesize that markers accounting for the whole T wave morphology can more robustly characterize repolarization changes associated with different $[K^+]$ and $[Ca^{2+}]$ levels and, thus, be better suited for non-invasive electrolyte estimation. Additionally, simulation of ECGs from a set of human ventricular tissue models representing potential inter-patient differences can help in the interpretation of the obtained results.

In this chapter, we characterize changes in T wave amplitude, duration and morphology, the latter both in the time and amplitude domains using the time warping analysis as fully described in section 2.2.4.1, during HD in relation to $[K^+]$ and $[Ca^{2+}]$ variations. Since HR may play a role in those relationships, its effects are also assessed. To uncover potential cellular mechanisms underlying differential T wave responses to variations in $[K^+]$, $[Ca^{2+}]$ and RR, a set of transmural ventricular fibers covering a wide range of cellular heterogeneities is simulated and pseudo-ECGs (pECGs) are computed. A sensitivity analysis is performed to investigate the extent to which different proportions of endocardial, midmyocardial and epicardial cells contribute to explain inter-individual differences in T wave amplitude, time and morphology, particularly for $[K^+]$ and $[Ca^{2+}]$ values outside normal ranges.

3.2 Materials and Methods

3.2.1 Study population and ECG pre-processing

In this chapter, the study population included 20 ESRD patients from HCUZ out of the 29 patients of the study population described in section 2.1. 48-hour 12-lead ECGs were acquired as fully briefly described in 2.1.

Pre-processing of ECG signals from ESRD patients was performed as described in section 2.2.1. A wavelet-based single-lead delineation method was used for QRS detection and wave delineation of each of the twelve leads [28] as briefly described in section 2.2.2.

As described in section 2.2.3, the first PC was computed in a stable ECG segment at the end of the HD session and the full ECG recording was projected onto that direction and used for subsequent ECG analysis. This was based on the fact that it is the

transformed lead where the T waves have maximal energy, thus allowing better morphological characterization. The T waves in the first PC were delineated using the single-lead delineation algorithm described in [28]. The onset, peak and end of the T waves were determined [28] and used for subsequent computation of T wave markers, as fully described in section 2.2.3.

3.2.2 Time, amplitude and morphology-based T wave descriptors

Time and amplitude-based T wave descriptors, T_{w} and $T_{\mathrm{S/A}}$, were computed from MWTWs as fully described in section 2.2.4.2.

Morphology-based T wave descriptors were computed using the time-warping methodology described previously [93] as fully described in section 2.2.4.1. For the patients' ECGs, reference T waves were calculated from the MWTW at the end of the HD session, as this is the time when the patient was discharged from hospital with restored serum ion levels, thus being an acceptable reference for ambulatory monitoring. Fig. 2.4 shows reference, $\mathbf{f}^r$, and studied, $\mathbf{f}^s$, T waves from a patient, with their respective time domains, $\mathbf{t}^r$ and $\mathbf{t}^s$. The linear and nonlinear time and amplitude morphological descriptors, $d_{\mathrm{w,T}}$, $d_{\mathrm{a,T}}$, $d^{\mathrm{NL}}_{\mathrm{w,T}}$ and $d^{\mathrm{NL}}_{\mathrm{a,T}}$, were computed as described in section 2.2.4.1.

3.2.3 Relationship between T wave markers and $[K^+]$, $[Ca^{2+}]$ and HR variations

To assess and quantify the effects of $[K^+]$, $[Ca^{2+}]$ and RR on each investigated T wave marker at different time points during HD, linear correlation and linear partial correlation analysis was performed [96–99] as described in section 2.2.5. For partial correlation, the correlation coefficient was computed after removing the effects of other covariates.

To test for significant differences in $[K^+]$, $[Ca^{2+}]$, RR, T_{w}, $T_{\mathrm{S/A}}$, $d_{\mathrm{w,T}}$, $d_{\mathrm{a,T}}$, $d^{\mathrm{NL}}_{\mathrm{w,T}}$ and $d^{\mathrm{NL}}_{\mathrm{a,T}}$ at different HD time points, Wilcoxon signed-rank tests were performed [100] and p-values (p) were computed.

Student's t-test was performed to test the significance of Pearson correlation between each T wave marker and $[K^+]$, $[Ca^{2+}]$ or RR as described in section 2.2.5.

3.2.4 *In silico* population of human ventricular fibers

In this chapter, transmural electrical propagation from ventricular endocardium to epicardium was simulated using one-dimensional fibers of 1.65 cm in length [9,102]. Cellular electrophysiology was represented by the human ventricular AP model proposed by Ten Tusscher and Panfilov [69]. To adequately represent the relationship between APD and $[Ca^{2+}]$, the updates to the Ten Tusscher-Panfilov model published in [82] were incorpo-

rated. The L-type calcium current was described as:

$$I_{\mathrm{CaL}} = G_{\mathrm{CaL}}\, d\, f\, f_2\, f_{\mathrm{Cass}}\, 4\, \frac{(V_{\mathrm{m}} - 15)F^2}{RT}\, \frac{[\mathrm{Ca}^{2+}] - 0.25\,[\mathrm{Ca}^{2+}]_{\mathrm{ss}}\, e^{2(V_{\mathrm{m}}-15)F/(RT)}}{1 - e^{2(V_{\mathrm{m}}-15)F/(RT)}}, \tag{3.1}$$

where G_{CaL} is the maximal I_{CaL} conductance, d is a voltage-dependent activation gate, f and f_2 are voltage-dependent inactivation gates, f_{Cass} is an inactivation gate dependent on the calcium concentration in the dyadic space (in mM), denoted by $[\mathrm{Ca}^{2+}]_{\mathrm{ss}}$, F is the Faraday constant, R is the gas constant, T is the temperature and V_{m} is the transmembrane potential (in mV). The updated formulations for f_2 and f_{Cass} of [82] read

$$\frac{df_{\mathrm{Cass}}}{dt} = k\frac{f_{\mathrm{Cass,inf}} - f_{\mathrm{Cass}}}{\tau_{f_{\mathrm{Cass}}}}, \tag{3.2}$$

where $k = 0$ if $f_{\mathrm{Cass,inf}} > f_{\mathrm{Cass}}$ and $V > -60$ mV, and $k = 1$ otherwise,

$$f_{\mathrm{Cass,inf}} = \frac{0.9}{1 + \exp\left(\dfrac{[\mathrm{Ca}^{2+}]_{\mathrm{ss}} - 1.95}{0.15}\right)} + 0.1, \tag{3.3}$$

$$\tau_{f_{\mathrm{Cass}}} = \frac{80}{1 + \left(\dfrac{[\mathrm{Ca}^{2+}]_{\mathrm{ss}}}{0.05}\right)^2} + 1, \tag{3.4}$$

and

$$f_{2,\mathrm{inf}} = \frac{0.3}{1 + e^{\left(\frac{V_{\mathrm{m}}+35}{7}\right)}} + 0.7. \tag{3.5}$$

Different proportions of endocardial, midmyocardial and epicardial cells were simulated in a total of 22 combinations with 10% variations in the proportion of each cell type: endocardial layer ranging from 10% to 50%, midmyocardial layer from 10% to 50% and epicardial layer from 20% to 80%. We used the notation Cuvw, where C stands for the word "case" and u, v and w denote the first digit of the proportions of endocardial, midmyocardial and epicardial cells, respectively (e.g. C334 represents the case with 30%, 30% and 40% of endocardial, midmyocardial and epicardial cells, respectively). The combinations of transmural heterogeneities used in this study are shown in Table 3.1.

Table 3.1: Simulated transmural distributions of cell types.

% Endo\Epi	20	30	40	50	60	70	80
10			C154	C145	C136	C127	C118
20		C253	C244	C235	C226	C217	
30	C352	C343	C334	C325	C316		
40	C442	C433	C424	C415			
50	C532	C523	C514				

A train of 10 stimuli was applied to the first cell of each fiber with a basic cycle length of 1000 ms and amplitude equal to 1.5 times the diastolic threshold. The initial state for each simulation was pre-calculated from a single cell simulation, where the values of the model state variables after 1000 paced beats were considered as representative of the cell at steady state. To compute electrical propagation, a finite element-based software [103] was used with a time step of 0.01 ms and space discretization of 0.01 cm.

Unipolar pECGs were computed as described in previous studies [102] using the expression:

$$V_{\mathrm{e}}(x', y', z') = \epsilon \int \frac{\partial V_{\mathrm{m}}(x, y, z)}{\partial x} \left(\frac{\partial}{\partial x} \left(\frac{1}{r(x, y, z)} \right) \right) dx, \tag{3.6}$$

where ϵ is a constant proportional to the ratio of intracellular and extracellular conductivities, $V_{\mathrm{m}}(x, y, z)$ is the transmembrane potential and $r(x, y, z)$ is the distance between each source point (x, y, z) in the 1D fiber and the virtual electrode (x', y', z') located, in this study, 2 cm away from the epicardium in the fiber direction: $r(x, y, z) = \left((x - x')^2 + (y - y')^2 + (z - z')^2\right)^{1/2}$, where $y = y'$ and $z = z'$ are constant.

3.2.5 Effects of $[K^+]$, $[Ca^{2+}]$ and HR variations on simulated T waves

To assess the extent of the contribution of each investigated factor, i.e. $[K^+]$, $[Ca^{2+}]$ and RR, to T wave characteristics, simulations were conducted for each ventricular fiber under varying values of those factors and the corresponding pECGs were computed. The range of simulated $[K^+]$ values included the default level in the Ten Tusscher-Panfilov model, i.e. $[K^+] = 5.4$ mM, as well as other levels below and above it: $[K^+] \in \{3, 4, 5.4, 6.2\}$ mM. In the case of $[Ca^{2+}]$, the range of simulated values included the default level of 2 mM, and values around it: $[Ca^{2+}] \in \{1.4, 2, 2.6, 3.2\}$ mM. For RR, the variations were in accordance to the range measured from the ECGs of the patients: RR $\in \{0.6, 0.8, 1, 1.2\}$ s. In the following, the notation $\mathcal{F}\{[K^+], [Ca^{2+}]\ , \mathrm{RR}\}$ is used to represent simulated cases with varying $[K^+]$, $[Ca^{2+}]$ and RR.

The last pECG beat of each simulated condition was delineated using the same delineation method mentioned above [28]. The time-, amplitude- and morphology-based T wave descriptors of section 6.2.3 were measured over those pECGs. For warping-based markers, reference T waves were calculated from the simulated beats generated for minimum $[K^+]$ (3 mM) and maximum $[Ca^{2+}]$ (3.2 mM) and RR (1.2 s), that is $\mathcal{F}\{3\ \mathrm{mM}; 3.2\ \mathrm{mM}; 1.2\ \mathrm{s}\}$.

3.2.6 Sensitivity analysis for assessment of inter-individual variability

Sensitivity analysis was performed to assess how the proportion, a, of endocardial, mid-myocardial and epicardial cell layers, c, modulated T wave or QRS complex morphology

descriptors, Y, at different [K^+], [Ca^{2+}] or RR levels. For each T wave descriptor at each given concentration of [K^+] ([Ca^{2+}] or RR, respectively), the percentage of change ($D_{Y;c;a_i}$) and its sensitivity ($S_{Y;c;a1,a2}$) to changes in the proportion of cells of each ventricular layer were computed as follows [104]:

$$D_{Y;c;a_i} = \left(\frac{Y_{c;a_i} - Y_{C334}}{Y_{C334}} \right) \cdot 100, \quad i \in \{1, 2\} \tag{3.7}$$

$$S_{Y;c;a_1,a_2} = \frac{(D_{Y;c;a_2} - D_{Y;c;a_1})100}{a_2 - a_1} = \frac{(Y_{c;a_2} - Y_{c;a_1})100^2}{Y_{C334}\ (a_2 - a_1)}, \tag{3.8}$$

where $Y_{c;a}$ is the average value of the T wave marker Y from all possible combinations Cuvw sharing a proportion a, at the c layer of endocardial, midmyocardial or epicardial cells, $c \in \{\text{Endo}, \text{Mid}, \text{Epi}\}$, with respect to case C334, which was used as a reference [105]. The values of a_1 and a_2 were taken as the minimum and maximum proportions of cells in each layer, respectively: 10% and 50% for endocardial and midmyocardial cells, and 20% and 80% for epicardial cells.

Y_{C334} is the value of the T wave descriptor for reference case C334. Thus, $D_{Y;c;a_i}$ measures the mean percentage of change in the T wave marker Y when varying the proportion of cells in layer c to a percentage a_i, $i \in \{1, 2\}$, with respect to that in C334. $S_{Y;c;a_1,a_2}$ measures the sensitivity of Y when varying the proportion of cells in layer c from a_1 to a_2.

3.3 Results

3.3.1 Characterization of T wave changes during HD

Fig. 3.1, panels (a–f), presents the results for all the T wave markers during the HD session for the 20 analyzed patients, while panels (g–i) present the evolution of [K^+], [Ca^{2+}] and RR during the session. In all these panels, significant differences between consecutive HD time points are indicated. The bottom panels illustrate variations in T waves for one patient during the session, with the reference T wave at the end of the HD session shown in blue and each investigated T wave shown in red. [K^+] and [Ca^{2+}] vary strongly during the session, whereas the RR interval varies much less.

A decreasing trend of $T_{S/A}$, $d_{w,T}$, $d^{NL}_{w,T}$ $d_{a,T}$ and $d^{NL}_{a,T}$ and an increasing trend of T_w during the HD session can be observed, with significantly different values along time. In the bottom panels, significant changes in the T wave morphology are seen to accompany the fluctuations of [K^+], [Ca^{2+}] and RR during the session. In the example shown in the bottom panels of Fig. 3.1 for a particular patient, tall and narrow peaked PCA-transformed T waves are observed at the start of the HD session (h_0) corresponding to maximal [K^+].

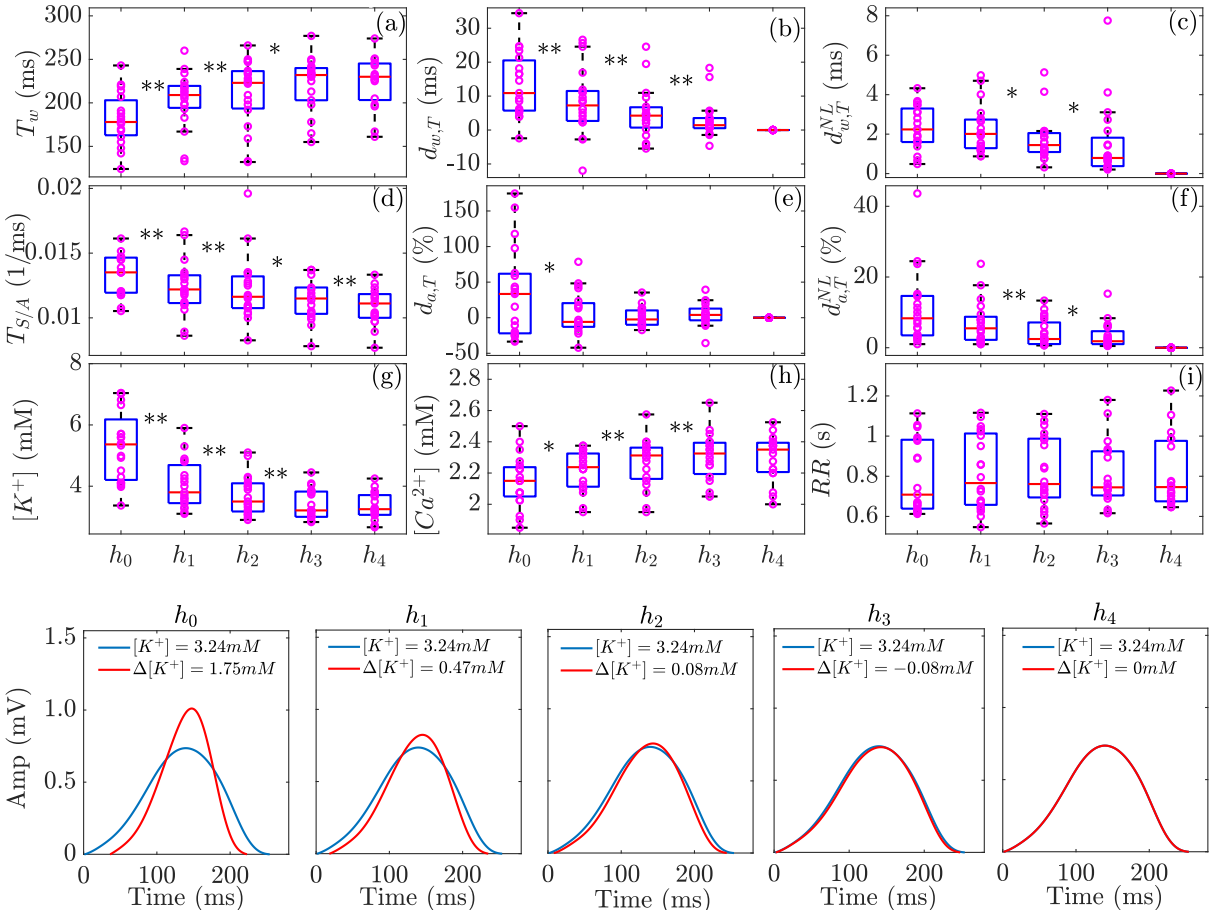

Figure 3.1: Panels a-f: Dynamics of T_{w}, $T_{\mathrm{S/A}}$, $d_{\mathrm{w,T}}$, $d_{\mathrm{a,T}}$, $d^{\mathrm{NL}}_{\mathrm{w,T}}$ and $d^{\mathrm{NL}}_{\mathrm{a,T}}$ during the HD session. Panels g-i: Evolution of [K^+], [Ca^{2+}] and RR during the session. In panels a-i, * indicates $p < 0.05$ and ** indicates $p < 0.01$ in the comparison of each marker between consecutive time points. In each panel, the central line (red) indicates the median, whereas bottom and top edges show the 25th and 75th percentiles, respectively. Each purple dot corresponds to an individual patient. In the bottom panels, red T waves illustrate the PCA-transformed T waves of a patient from the start to the end of the HD session, with Δ denoting the change in [K^+] with respect to the end of the HD session (h_4). The blue line indicates the reference T wave at the end of the HD session used in the computation of time-warping markers.

3.3.2 *In silico* assessment of T wave changes due to [K^+] variations

T wave markers computed from simulated pECGs at varying [K^+] are shown in Fig. 3.2. Panels (a-d) show the simulated APs along the 1-D fiber for the simulated case C154 and $\mathcal{F}\{[\mathrm{K}^+]; 2.0\ \mathrm{mM}; 1.0\ \mathrm{s}\}$ when [K^+] is varied from 6.2 mM to 3 mM. The range of simulated [K^+] values approximately corresponds to the maximum and minimum [K^+] range calculated from the patients' blood data. The corresponding changes in the simulated pECGs are shown in panels (e-h). It can be observed from the figure that a variation in [K^+] causes AP shortening or prolongation in endocardial, midmyocardial and epicardial cells and therefore shorter or longer QT intervals as well as variations in the width,

amplitude and morphology of the T wave.

T wave markers computed from the simulated pECGs are presented in panels (i-n) for the different levels of $[K^+]$. All T wave markers present clear variations with $[K^+]$, reproducing the behavior observed in the patients (Fig. 3.1). A decreasing trend of $d_{w,T}$ and $d_{a,T}^{NL}$ from the maximum to the minimum level of $[K^+]$ was observed in all the simulated cases (panels j and n). Monotonic trends of T_w, $T_{S/A}$, $d_{a,T}$ and $d_{w,T}^{NL}$ were observed in most of the simulated cases (panels i, l, m and n).

The bottom panels in Fig. 3.2 illustrate variations in T waves for simulated fiber C154 from the maximum to the minimum level of $[K^+]$ corresponding to the average value of $[K^+]$ during HD in the analyzed patients, with the reference T wave (blue) and each investigated T wave (red) being displayed. More peaked T waves with varying width and morphology are observed with increasing $[K^+]$ levels for the case shown.

3.3.3 *In silico* assessment of T wave changes due to $[Ca^{2+}]$ and HR variations

APs and T wave markers computed from pECGs at varying $[Ca^{2+}]$ and RR are shown in Fig. 3.3. Panels (a and b) illustrate changes in APs for simulated case C154 and $\mathcal{F}\{5.4\text{mM}; [Ca^{2+}]; 1.0\text{s}\}$ under varying $[Ca^{2+}]$ while panels (e and f) present APs for $\mathcal{F}\{5.4\text{mM}; 2.0\text{mM}; \text{RR}\}$ under varying RR for endocardial (black), midmyocardial (green) and epicardial (red) cells of a simulated fiber. Simulated pECGs, and specifically T waves, are presented for varying $[Ca^{2+}]$ and RR in panels (c, d, g, h, i and j).

From panels (a-d), it can be observed that lower $[Ca^{2+}]$ causes AP prolongation in all the cell types and, consequently, longer QT intervals. Panel (i) shows that the width and amplitude of the T wave increase with decreasing $[Ca^{2+}]$ and the morphology varies too. From panels (e-h) it can be seen that an increase in the RR interval causes AP prolongation and, thus, longer QT intervals (panels e-h). In the middle panel (j), the width and amplitude of the T wave are shown to increase with increasing RR, which is accompanied by changes in the T wave shape.

Changes in the T wave markers when varying $[Ca^{2+}]$, $\mathcal{F}\{5.4\text{mM}; [Ca^{2+}]; 1.0\text{ s}\}$ (red bar), and when varying RR, $\mathcal{F}\{5.4\text{mM}; 2.0\text{mM}; \text{RR}\}$ (green bar), are presented for the 22 simulated cases in panels (k-p) and compared with the changes measured after varying $[K^+]$ $\mathcal{F}\{[K^+]; 2.0\text{mM}; 1.0\text{s}\}$ (blue bar). A monotonic rise in $d_{w,T}$ and $d_{w,T}^{NL}$ (panels l and m) as well as decreasing trends in $d_{a,T}$ and $d_{a,T}^{NL}$ (panels o and p) are observed from the minimum to the maximum levels of $[Ca^{2+}]$. However, T_w and $T_{S/A}$ do not show a clear trend at varying levels of $[Ca^{2+}]$ (panels k and n). As for the effects of increasing RR, trends towards lower $T_{S/A}$, $d_{w,T}$, $d_{w,T}^{NL}$ and $d_{a,T}^{NL}$ can be observed (panels l, m, n and p). Similarly, an increasing trend of $d_{a,T}$ and a monotonic rise in T_w at increasing RR (panels k and o) are shown.

It can be noted from the figure that T wave markers, particularly morphology-based

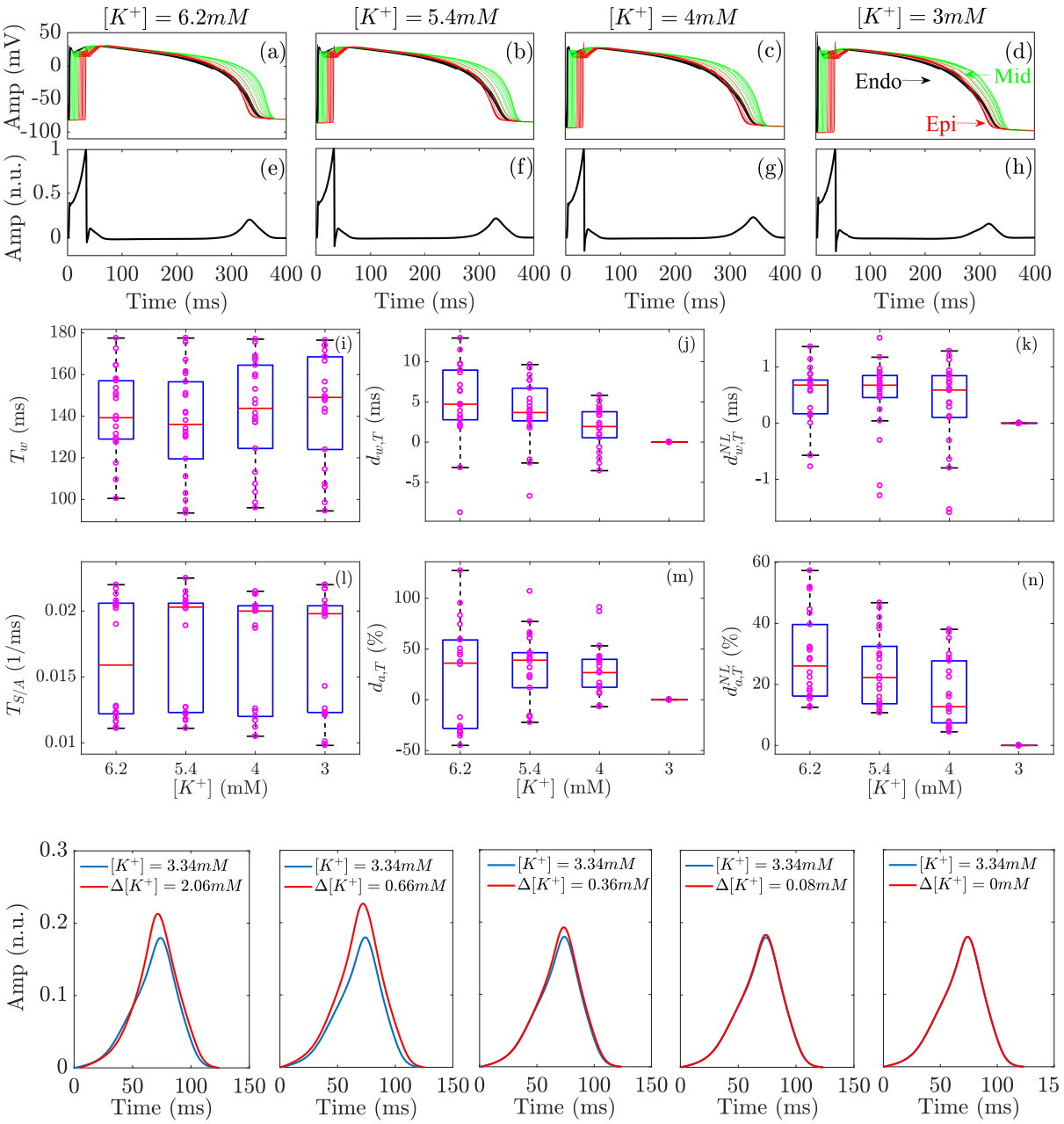

Figure 3.2: Panels a-d: Simulated endocardial (black), midmyocardial (green) and epicardial (red) APs for simulated fiber C154, and $\mathcal{F}\{[\mathrm{K}^+]; 2.0\ \mathrm{mM}; 1.0\ \mathrm{s}\}$. Panels e-h: ECGs for varying $[\mathrm{K}^+]$. Panels i-n: Changes in T_w, $T_{\mathrm{S/A}}$, $d_{\mathrm{w,T}}$, $d_{\mathrm{a,T}}$, $d^{\mathrm{NL}}_{\mathrm{w,T}}$ and $d^{\mathrm{NL}}_{\mathrm{a,T}}$ for simulated fibers when varying $[\mathrm{K}^+]$. Central red lines indicate the median, whereas bottom and top edges show the 25th and 75th percentiles, respectively. Each purple dot corresponds to an individual simulated fiber. In the bottom panels, red traces indicate the T waves of a simulated fiber from an initial (maximum) to a final (minimum) value of $[\mathrm{K}^+]$ corresponding to average $[\mathrm{K}^+]$ values in the analyzed patients. The blue line indicates the reference T wave used when computing time-warping markers.

ones, show remarkable variations at varying $[\mathrm{K}^+]$, $[\mathrm{Ca}^{2+}]$ and RR. However, $[\mathrm{K}^+]$-induced variations are more visible than those induced by $[\mathrm{Ca}^{2+}]$ and RR.

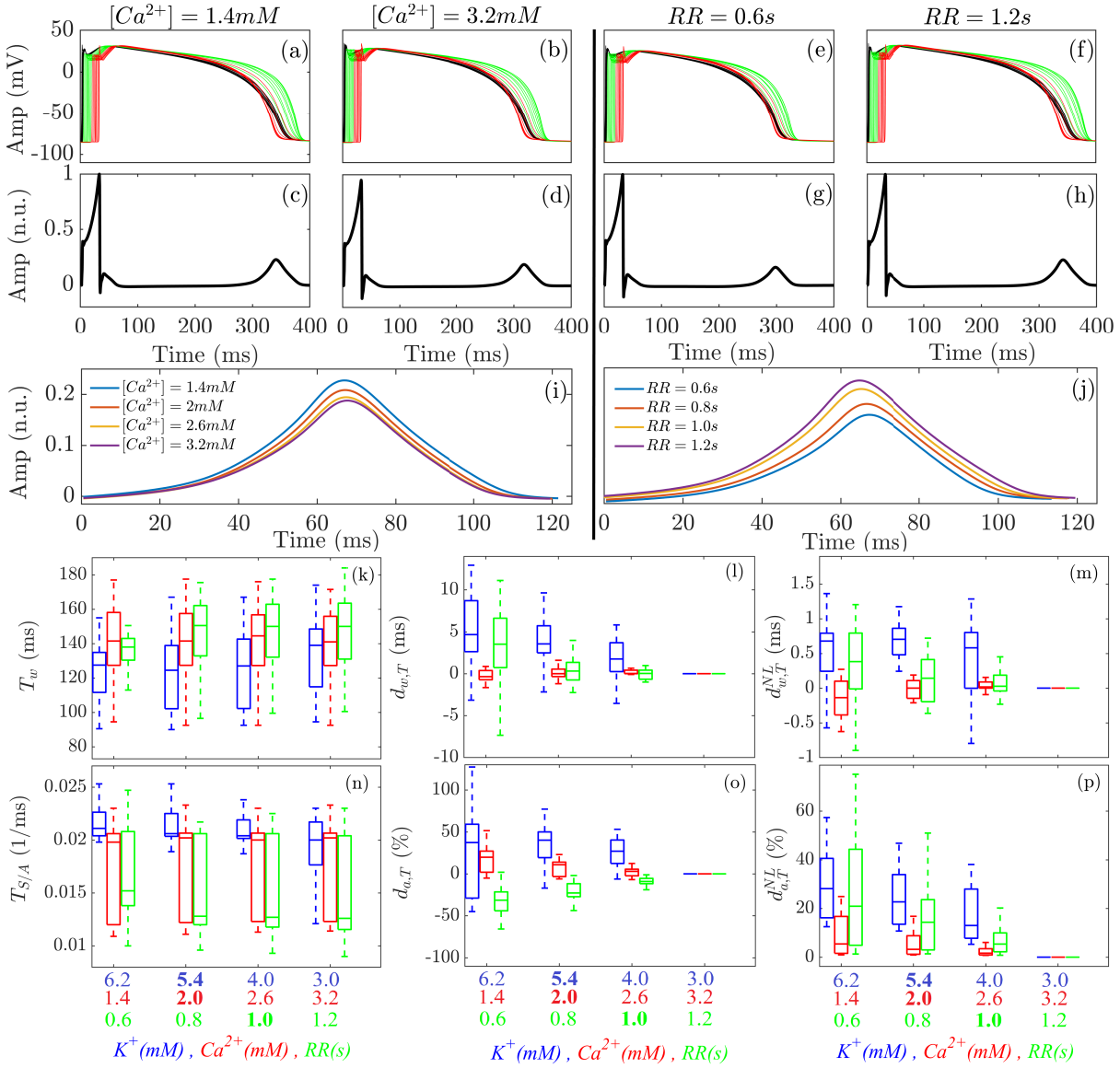

Figure 3.3: Panels a, b: Simulated endocardial (black), midmyocardial (green) and epicardial (red) APs for simulated fiber C154, $\mathcal{F}\{5.4\text{mM}; [\text{Ca}^{2+}]; 1.0\text{ s}\}$ under varying $[\text{Ca}^{2+}]$. Panels c, d, i: ECGs and T waves for $[\text{Ca}^{2+}]$ variations. Panels e, f: Simulated endocardial (black), midmyocardial (green) and epicardial (red) APs for simulated fiber C154, $\mathcal{F}\{5.4\text{mM}; 2.0\text{mM}; \text{RR}\}$, under varying RR. Panels g, h, j: ECGs and T waves for RR variations. Panels k-p: Changes in T_{w}, $T_{\text{S/A}}$, $d_{\text{w,T}}$, $d_{\text{a,T}}$, $d^{\text{NL}}_{\text{w,T}}$ and $d^{\text{NL}}_{\text{a,T}}$ for varying $[\text{K}^+]$, $\mathcal{F}\{[\text{K}^+]; 2.0\text{mM}; 1.0\text{ s}\}$ (blue boxplots), $[\text{Ca}^{2+}]$, $\mathcal{F}\{5.4\text{mM}; [\text{Ca}^{2+}]; 1.0\text{ s}\}$ (red boxplots), and RR, $\mathcal{F}\{5.4\text{mM}; 2.0\text{mM}; \text{RR}\}$ (green boxplots), in the horizontal axis for the 22 simulated fibers. Central lines indicate the median, whereas bottom and top edges show the 25th and 75th percentiles, respectively. Values of $[\text{K}^+] \in \{3.0, 4.0, 5.4, 6.2\}$ mM, $[\text{Ca}^{2+}] \in \{1.4, 2.0, 2.6, 3.2\}$ mM, and RR $\in \{0.6, 0.8, 1.0, 1.2\}$ s are used.

3.3.4 Contribution of $[K^+]$, $[Ca^{2+}]$ and HR variations to T wave changes *in vivo* and *in silico*

To assess the relationship between electrolyte or RR variations and the corresponding changes in T wave markers, a correlation analysis was performed, both for ECG recordings from the patients and simulated pECGs. Results are presented in Fig. 3.4. The three graphics in panel (a) illustrate the linear correlation coefficients ρ between $[K^+]$, $[Ca^{2+}]$ or RR and each of the analyzed T wave markers computed from the patients' ECGs. Panel (b) shows the corresponding linear partial correlation coefficients after removing the effects of the other two covariates ($[K^+]$, $[Ca^{2+}]$ or RR). Panel (c) shows the linear correlation coefficients in the simulated cases at varying $[K^+]$, $[Ca^{2+}]$ and RR.

Most of the analyzed T wave markers strongly correlated with $[K^+]$. T_{w}, $T_{\mathrm{S/A}}$, $d_{\mathrm{w,T}}$ and $d_{\mathrm{a,T}}^{\mathrm{NL}}$ were the most highly correlated ones, with median ρ of -0.94, 0.87, 0.88 and 0.80, respectively, in the patients, and -0.97, 0.86, 0.97 and 0.95, respectively, in the simulations. However, only $d_{\mathrm{a,T}}^{\mathrm{NL}}$ was strongly correlated with $[K^+]$ when the effects of $[Ca^{2+}]$ and RR in the patient's data were removed (median value of partial correlation coefficient of 0.75).

Similarly, T_{w}, $T_{\mathrm{S/A}}$, $d_{\mathrm{w,T}}$ and $d_{\mathrm{a,T}}^{\mathrm{NL}}$ were strongly correlated with $[Ca^{2+}]$ (median value of ρ of 0.79, -0.82, -0.80 and -0.74, respectively, in the patients, and -0.75, 0.91, 0.42 and -0.99, respectively, in the simulations). In this case, only $d_{\mathrm{w,T}}$ was strongly correlated with $[Ca^{2+}]$ when removing the effects of $[K^+]$ and RR (median value of partial correlation coefficient of -0.74) in the patients' data.

As for the relationship between T wave markers and RR, only $d_{\mathrm{a,T}}$ presented a strong correlation in both patients' and simulated ECGs (median ρ of -0.67 for Pearson correlation and -0.90 for partial correlation in the patients, and of 0.99 for Pearson correlation in the simulations).

Table 3.2 shows the p-values from the Student's t-test applied to assess the statistical significance of non-zero mean Fisher's z-transformed Pearson correlation coefficients between T wave markers and each of $[K^+]$, $[Ca^{2+}]$ and RR in the patient population. As can be seen from the table, all the analyzed T wave markers, except for $d_{\mathrm{a,T}}$, correlated strongly with $[K^+]$ and $[Ca^{2+}]$. On the other hand, only $d_{\mathrm{a,T}}$ correlated strongly with RR.

3.3.5 Mechanisms for inter-individual differences in the effects of $[K^+]$, $[Ca^{2+}]$ and RR on T wave changes

The results of the linear regression analysis performed to investigate how different proportions of endocardial, midmyocardial and epicardial cells contribute to explain individual T wave responses when varying $[K^+]$ are presented in Fig. 3.5 for a commonly used T wave marker, T_{w}, and a morphology-based marker, $d_{\mathrm{a,T}}^{\mathrm{NL}}$. Cell proportions are represented in the x-axis, with solid lines showing fitted linear regression models for T_{w} and $d_{\mathrm{a,T}}^{\mathrm{NL}}$ for all simulated cases.

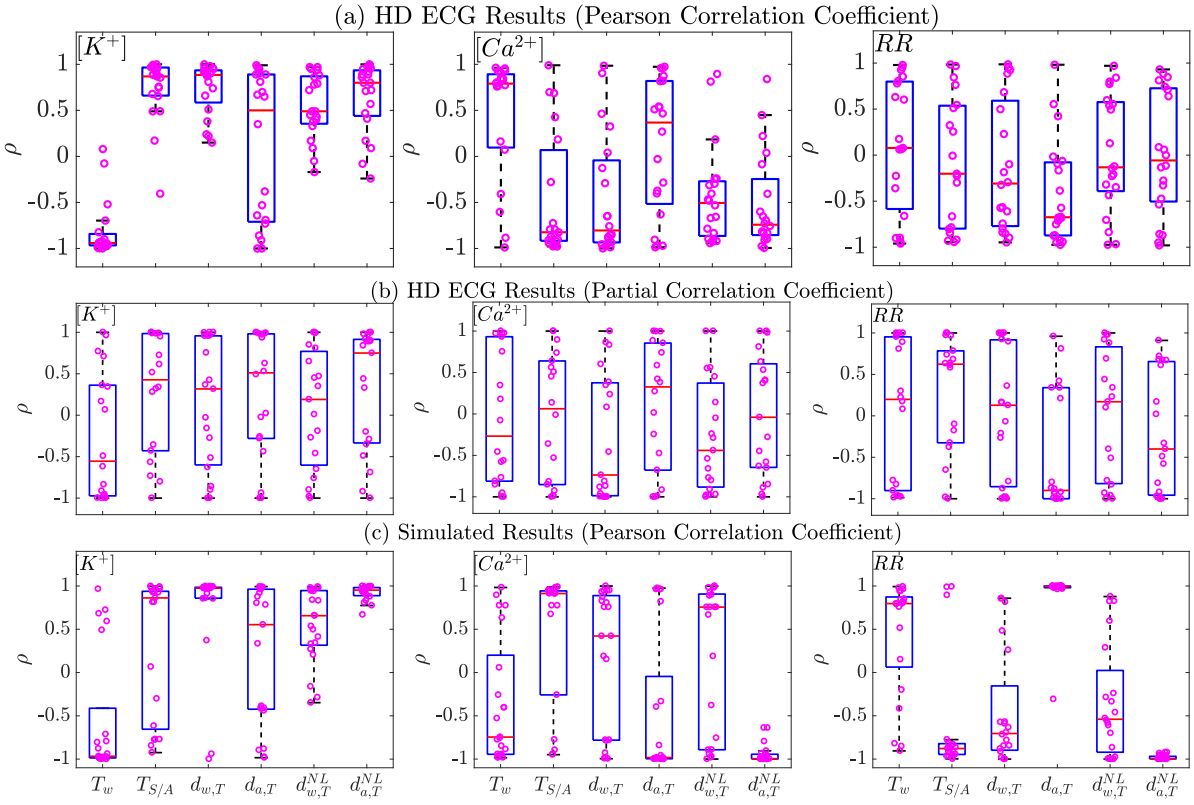

Figure 3.4: Panel a: Pearson correlation coefficients between each T wave marker (T_{w}, $T_{\mathrm{S/A}}$, $d_{\mathrm{w,T}}$, $d_{\mathrm{a,T}}$, $d^{\mathrm{NL}}_{\mathrm{w,T}}$ and $d^{\mathrm{NL}}_{\mathrm{a,T}}$) and [$K^+$] (left), [$Ca^{2+}$] (middle) or RR (right) for the analyzed patients. Panel b: Partial correlation coefficients between each T wave marker (T_{w}, $T_{\mathrm{S/A}}$, $d_{\mathrm{w,T}}$, $d_{\mathrm{a,T}}$, $d^{\mathrm{NL}}_{\mathrm{w,T}}$ and $d^{\mathrm{NL}}_{\mathrm{a,T}}$) and [$K^+$] (left), [$Ca^{2+}$] (middle) or RR (right) for the analyzed patients after removing the effects of the other two variables among [K^+], [Ca^{2+}] and RR. Panel c: Pearson correlation coefficients between each T wave marker (T_{w}, $T_{\mathrm{S/A}}$, $d_{\mathrm{w,T}}$, $d_{\mathrm{a,T}}$, $d^{\mathrm{NL}}_{\mathrm{w,T}}$ and $d^{\mathrm{NL}}_{\mathrm{a,T}}$) and [$K^+$] (left), [$Ca^{2+}$] (middle) or RR (right) for the simulated fibers under varying [K^+], $\mathcal{F}\{[K^+]; 2.0\mathrm{mM}; 1.0\ \mathrm{s}\}$ (left), [Ca^{2+}], $\mathcal{F}\{5.4\mathrm{mM}; [Ca^{2+}]; 1.0\ \mathrm{s}\}$ (middle) and RR, $\mathcal{F}\{5.4\mathrm{mM}; 2.0\mathrm{mM}; \mathrm{RR}\}$ (right). Each purple dot represents the correlation coefficient for an individual patient or simulated fiber. Central red lines indicate the median, whereas bottom and top edges show the 25th and 75th percentiles, respectively.

Both T_{w} and $d^{\mathrm{NL}}_{\mathrm{a,T}}$ present clear relationships with transmural heterogeneities, being such relationships more or less accentuated depending on the [K^+] level. The highest sensitivities, shown in Table 3.3, and coefficients of determination, R^2 shown in Fig. 3.5, of the time-based marker T_{w} are with respect to variations in the proportion of endocardial (positive correlation) and midmyocardial cells (negative correlation), with a more notable dependence for low [K^+] values. In the case of the morphology-based marker $d^{\mathrm{NL}}_{\mathrm{a,T}}$, the highest sensitivity and R^2 are observed for midmyocardial (positive correlation) and epicardial (negative correlation) variations, particularly under high [K^+] values. Sensitivity results for all the analyzed T wave markers at varying [Ca^{2+}] and RR are presented in Tables 3.4 and 3.5.

Table 3.2: P-values from Student's t-test to evaluate statistical significance of non-zero mean Fisher's z-transformed Pearson correlation coefficient between T wave markers and each of $[K^+]$, $[Ca^{2+}]$ and RR in the patient population.

p-values	T_w	$T_{S/A}$	$d_{w,T}$	$d_{a,T}$	$d_{w,T}^{NL}$	$d_{a,T}^{NL}$
ρ	ms	1/ms	ms	%	ms	%
$[K^+]$	< 0.01	< 0.01	< 0.01	0.25	< 0.01	< 0.01
$[Ca^{2+}]$	0.03	0.01	0.01	0.73	0.01	< 0.01
RR	0.59	0.79	0.75	0.02	0.98	0.92

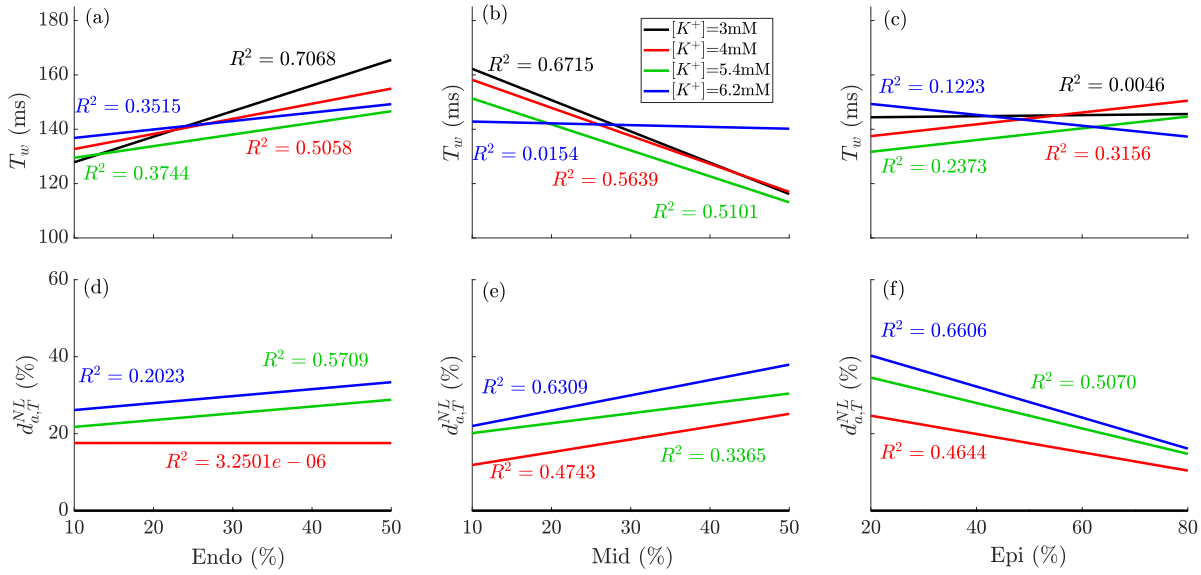

Figure 3.5: Panels a-c: Fitted regression lines for the average values of T_w for all simulated cases sharing the same proportion of endocardial, midmyocardial or epicardial cells at different $[K^+]$ levels. Panels d-f: Fitted regression lines for the average values of $d_{a,T}^{NL}$ for all simulated cases sharing the same proportion of endocardial, midmyocardial or epicardial cells at different $[K^+]$, with the reference value for $[K^+] = 3$ mM. Coefficients of determination (R^2), estimated as the square of the linear correlation coefficient between the analyzed T wave markers and each cell type (endocardial, midmyocardial or epicardial), are indicated.

Table 3.3: Results of the sensitivity analysis, $S_{Y;c;a_1,a_2}$, for different values of $[K^+]$, when varying cell proportions in layer c from a_1 to a_2.

$S_{Y;c;a_1,a_2}$	Y	T_{w}	$T_{\mathrm{S/A}}$	$d_{\mathrm{w,T}}$	$d_{\mathrm{a,T}}$	$d_{\mathrm{w,T}}^{\mathrm{NL}}$	$d_{\mathrm{a,T}}^{\mathrm{NL}}$
c, a_1, a_2	$[K^+]$ (mM)	%	%	%	%	%	%
Endo, 10, 50	4.0	2.9	7.2	108.3	21.9	97.7	0.4
	6.2	2.2	7.2	78.7	16.2	3.1	9.7
Mid, 10, 50	4.0	4.5	1.4	41.5	43.5	9.2	10.9
	6.2	0.3	11.1	10.7	53.7	8.2	11.8
Epi, 20, 80	4.0	1.3	8.2	102.3	16.7	86.1	10.1
	6.2	1.1	12.4	41.6	36.8	2.6	17.2

Table 3.4: Results of the sensitivity analysis, $S_{Y;c;a_1,a_2}$, for different values of $[Ca^{2+}]$, when varying cell proportions in layer c from a_1 to a_2.

$S_{Y;c;a_1,a_2}$	Y	T_{w}	$T_{\mathrm{S/A}}$	$d_{\mathrm{w,T}}$	$d_{\mathrm{a,T}}$	$d_{\mathrm{w,T}}^{\mathrm{NL}}$	$d_{\mathrm{a,T}}^{\mathrm{NL}}$
c, a_1, a_2	$[Ca^{2+}]$ (mM)	%	%	%	%	%	%
Endo, 10, 50	1.4	4.5	−11.4	45.0	−22.2	34.2	10.4
	2.6	4.5	−11.6	7.5	−3.9	1.5	10.9
Mid, 10, 50	1.4	0.3	−12.3	39.0	42.3	−11.7	14.1
	2.6	−0.2	−10.4	9.0	63.6	11.2	16.2
Epi, 20, 80	1.4	−0.8	12.7	−84.3	−21.7	−26.5	−19.3
	2.6	0.2	11.1	−14.4	−25.6	−7.0	−25.6

Table 3.5: Results of the sensitivity analysis, $S_{Y;c;a_1,a_2}$, for different values of RR, when varying cell proportions in layer c from a_1 to a_2.

$S_{Y;c;a_1,a_2}$	Y	T_{w}	$T_{\mathrm{S/A}}$	$d_{\mathrm{w,T}}$	$d_{\mathrm{a,T}}$	$d_{\mathrm{w,T}}^{\mathrm{NL}}$	$d_{\mathrm{a,T}}^{\mathrm{NL}}$
c, a_1, a_2	RR (s)	%	%	%	%	%	%
Endo, 10, 50	0.6	0.5	−0.8	−7.3	−8.4	50.5	4.6
	1.0	0.1	−1.7	−76.7	−11.6	−40.6	−11.1
Mid, 10, 50	0.6	−2.7	−5.2	19.6	32.6	82.2	26.6
	1.0	0.1	−11.3	−29.0	20.6	−1.9	8.7
Epi, 20, 80	0.6	0.3	7.5	−9.3	−16.2	−13.5	−29.9
	1.0	−0.9	12.2	65.7	−7.9	32.6	−14.8

3.4 Discussion

Serum $[K^+]$ and $[Ca^{2+}]$ levels outside the normal range are associated with increased mortality [2,4,106–110]. The availability of non-invasive tools to monitor serum $[K^+]$ and $[Ca^{2+}]$ concentrations, particularly in ESRD patients, might have a significant impact on clinical practice. In this chapter, we characterized changes in ECG markers measuring duration, amplitude and morphology of the T wave during HD in ESRD patients and we assessed their relationship with $[K^+]$, $[Ca^{2+}]$ and HR variations. In addition, we simulated human transmural ventricular fibers to unravel potential underpinnings of the high inter-individual differences in T wave responses observed in the patients in response to electrolyte and heart rate variations.

3.4.1 T wave analysis in ESRD patients during HD

We evaluated commonly used markers describing T wave time and amplitude characteristics, like its width (T_{w}) and its downward slope-to-amplitude ratio ($T_{\mathrm{S/A}}$), as well as more recently proposed markers describing morphological characteristics computed by warping-based techniques ($d_{\mathrm{w,T}}$, $d_{\mathrm{a,T}}$, $d^{\mathrm{NL}}_{\mathrm{w,T}}$ and $d^{\mathrm{NL}}_{\mathrm{a,T}}$). Those markers were measured at sequential time points during HD because large changes in serum electrolyte concentrations can be expected during this period. We showed that such an analysis indeed allows to provide a characterization of T wave changes for a wide range of $[K^+]$, $[Ca^{2+}]$ and HR variations, with $d^{\mathrm{NL}}_{\mathrm{a,T}}$, $d_{\mathrm{w,T}}$ and $d_{\mathrm{a,T}}$ being the markers most strongly correlated with $[K^+]$, $[Ca^{2+}]$ and RR, respectively, after removing the effects of the other covariates. These results emphasize the importance of considering more complex markers to fully characterize the ECG repolarization response during HD.

Variations in serum electrolyte levels, mainly $[K^+]$ and $[Ca^{2+}]$, have been shown to alter ventricular properties in the ECG [4–6, 111, 112]. In particular, previous studies have described that ECGs recorded under hyperkalemic conditions commonly have more peaked T waves than those recorded under normal levels of $[K^+]$ [4, 23, 25, 30]. In this study, we could observe such behavior in some of the ESRD patients' recordings, as illustrated in the bottom panels of Fig. 3.1. However, a decrease in T wave amplitude could not be consistently measured for all patients, but large inter-individual variability was noted in the relationship between $[K^+]$ and T wave amplitude. Other studies have analyzed the effects of $[K^+]$ changes on the width, slope and amplitude-to-slope ratio of the T wave as well as the ratio of the T wave amplitude to the R wave amplitude [7–9, 31, 113]. The main limitation of these descriptors is that, even if some of them may show a high degree of correlation with the level of $[K^+]$, their changes cannot be exclusively attributed to $[K^+]$ variations, as confirmed in our study by including in the analysis additional confounders like variations in $[Ca^{2+}]$ or HR.

Regarding the analysis of the T wave shape, a MCS based on T wave asymmetry, flatness and notching [33–35] has been used to analyze its relationship with $[K^+]$ in a

primary care population [36]. A clear association between MCS and $[K^+]$ could only be found among individuals with $[K^+]$ in the range 2–4.1 mM, but not among those with $[K^+]$ in the range 4.2–6 mM. In ESRD patients, we found that morphological variability, specifically quantified by our analyzed T wave marker $d_{a,T}^{NL}$ was closely related to serum $[K^+]$ in a wide range of values, covering both hyper- and hypokalemic values.

As for the effects of $[Ca^{2+}]$ variations on the ECG, a recent large-scale study has found that low $[Ca^{2+}]$ values are associated with clinically relevant QT prolongation in the general population [6]. In chronic patients undergoing HD, changes in $[Ca^{2+}]$ have been found to be negatively correlated with changes in the last part of the ECG repolarization measured by the T-peak to T-end interval [50]. In this chapter, we showed that the full repolarization duration measured by T_w indeed presents an inverse relationship with $[Ca^{2+}]$ after removing the effects of other confounders. Nevertheless, such a relationship between T_w and $[Ca^{2+}]$ was not as strong as that of other markers like $d_{w,T}$ reflecting temporal variations in T wave morphology. The values of $[Ca^{2+}]$ in our study were in the ranges reported in other studies [6, 57, 114–117]. It should be noted that these are serum calcium concentration values. Ionized calcium concentrations would be lower.

3.4.2 T wave analysis in simulated ventricular tissues at varying $[K^+]$, $[Ca^{2+}]$ and HR

All the T wave markers analyzed in this chapter showed a diversity of patterns in their relationship with electrolyte variations during HD. Both the general trend of such relationships and the high inter-individual variability were well reproduced by our simulated ventricular fibers for most of the markers. This can be explained by the fact that we simulated 22 different transmural fibers accounting for proportions of endocardial, mid-myocardial and epicardial cells varying within plausible limits, as reported in previous studies [87,102,105,118]. We are not aware of other *in silico* studies investigating morphological variability in the T wave of the ECG in relation to electrolyte variations such as those occurring during HD, but there are different *in silico* studies characterizing T wave duration and amplitude as a function of electrolyte concentrations [9, 84].

In agreement with our ECG data, an increase in $[K^+]$ led to shortening of the repolarization time quantified by T_w in our transmural fibers. Other computational studies have shown divergent results in this regard. In [85], prolongation of the RT interval has been reported in response to increased $[K^+]$, which is acknowledged by the authors to be in contrast with clinical data but possibly explained by factors other than $[K^+]$. In [9, 86], a simulated increase in $[K^+]$ has been shown to lead to QT shortening, which would be in line with our results. Our results on T_w reduction with increasing $[Ca^{2+}]$ are concordant with the shortening of the repolarization time reported by others [84, 86, 87]. Also, our results at the cellular level are aligned with those obtained with the human ventricular AP model recently proposed by Bartolucci et al. [83], which, in contrast to

most AP models, is able to reproduce a physiological APD-$[Ca^{2+}]$ relationship. For the simulations, we considered the default $[Ca^{2+}]$ value of 2 mM defined in the Ten Tusscher-Panfilov model [69], which we used as a basis for our study with subsequent modifications to properly represent the relationship between $[Ca^{2+}]$ and APD [82]. Other human ventricular cell models have used 2 mM as the default $[Ca^{2+}]$ value too [71, 119]. A lower value of 1.8 mM has been used in yet other human ventricular cell models [72, 75, 76, 83].

Moreover, in our simulations, the marker $T_{S/A}$ quantifying the T wave slope-to-amplitude ratio was shown to correlate strongly with $[K^+]$ and $[Ca^{2+}]$. These results are in agreement with previous studies [9, 31], in which $T_{S/A}$ was proposed as an index to monitor $[K^+]$ during HD and a cause-effect sequence for the observed decrease in $T_{S/A}$ was provided through computational simulations.

The above discussed results show that *in silico* modeling and simulation can help to gain insight into the ECG changes observed in response to electrolyte abnormalities. In contrast to other computational studies, which used one single cell or tissue electrophysiological model, we simulated a population of human ventricular tissue fibers, which can be used to shed light on the highly inter-individual relationships between ECG markers and $[K^+]$ or $[Ca^{2+}]$.

3.4.3 Potential mechanisms for inter-individual T wave responses to electrolyte and HR variations

We computed T wave marker sensitivities to explain how different transmural heterogeneities can contribute to explain distinct T wave responses to variations in $[K^+]$, $[Ca^{2+}]$ and HR. The morphological descriptors $d_{w,T}$, $d^{NL}_{w,T}$, $d_{a,T}$ and $d^{NL}_{a,T}$ generally showed higher sensitivity to variations in the proportions of the ventricular layers than the time and amplitude markers T_w and $T_{S/A}$. Previous experimental and theoretical studies have described how cell distributions across the ventricular wall affect ECG repolarization and, in particular, T wave morphology [93, 120–125]. Our study, in this chapter, confirms these observations on the impact of transmural heterogeneities on T wave width, amplitude and shape characteristics, not only at physiological electrolyte concentrations but also at high and low $[K^+]$ and $[Ca^{2+}]$ levels and at different heart rates. Even if transmural heterogeneities can contribute to inter-individual differences in the T wave response to electrolyte and HR variations, other ventricular heterogeneities, like interventricular, apicobasal or anteroposterior, may play a relevant role, which should be assessed in further studies.

Our results on the sensitivity of T wave morphological markers with respect to variations in transmural heterogeneities, and more specifically to the proportion of epicardial cells within the ventricular wall, are aligned with computational findings presented by Janusek et al. [120], which demonstrated the influence of epicardial cells on the development of T wave alternans, a form of repolarization variability [120]. The contribution of

variations in the midmyocardial layer to T wave morphology has been shown in a recent study too [122].

3.4.4 Study limitations and future research

In this chapter, 20 ECG recordings of ESRD patients during an HD session, with 5 blood samples available along HD, are investigated. Future studies should investigate the application of the proposed methods to larger numbers of patients and, if possible, with more available blood samples during the full 48-hour ECG recording. This would allow more robust assessment of the relationship between changes in T wave markers and specific variations in $[K^+]$, $[Ca^{2+}]$ or HR, potentially using nonlinear regression statistical techniques [126, 127]. In chapters 4 and 5, we included a few more patients with an additional HD point 48 hours after the start of the HD.

In this chapter, electrophysiological simulations were performed for human transmural ventricular 1D fibers. In chapter 6, we extended the investigations of the present study to include simulations in bi-ventricular models embedded in patient-specific torso models, from which more realistic ECGs can be computed. This research could additionally allow exploring the role of other types of ventricular heterogeneities, on top of transmural ones, on the T wave response to electrolyte and HR variations.

3.5 Conclusions

We showed that descriptors of T wave width (T_{w}), slope-to-amplitude ratio ($T_{\mathrm{S/A}}$) and morphological variability ($d_{\mathrm{w,T}}$, $d_{\mathrm{a,T}}$, $d^{\mathrm{NL}}_{\mathrm{w,T}}$ and $d^{\mathrm{NL}}_{\mathrm{a,T}}$) vary remarkably with varying $[K^+]$, $[Ca^{2+}]$ and HR, but a wide range of patterns is observed for such relationships. Among the proposed descriptors, $d^{\mathrm{NL}}_{\mathrm{a,T}}$ $d_{\mathrm{w,T}}$ and $d_{\mathrm{a,T}}$ are the ones that best correlate with $[K^+]$, $[Ca^{2+}]$ and HR, respectively. The proportion of midmyocardial and epicardial cells has a large impact on T wave markers, particularly for serum electrolyte concentrations and HR out of their physiological levels. This suggests that transmural heterogeneities can modulate patient-dependent T wave responses to changes in electrolyte concentrations and HR in ESRD patients. These findings can have major relevance for non-invasive monitoring and prediction of arrhythmic events in these patients.

Chapter 4

Estimation of Potassium Levels in Hemodialysis Patients by T wave Nonlinear Dynamics and Morphology Markers

This chapter is partially based on the paper published by Bukhari et al., Computers in Biology and Medicine, 2022, 143:105304.; 2022.
doi:10.1016/j.compbiomed.2022.105304

4.1 Introduction

In chapter 3, T wave morphology markers derived from the ECG, obtained by applying time warping analysis, were used to characterize ECG repolarization changes during HD in ESRD patients and to relate them with variations in $[K^+]$, $[Ca^{2+}]$ and HR. In this chapter, we propose to characterize nonlinear dynamics of the T wave using markers based on maximum Lyapunov exponents and a divergence-related marker. We hypothesize that elevated $[K^+]$ at the start of HD and 48 hours later is associated with higher variability in the form of dynamical instabilities, which will be reflected in larger values of the quantified nonlinear dynamics markers [128, 129]. In particular, larger repolarization variability at elevated $[K^+]$ would be expected to lead to larger rates of divergence of phase space trajectories associated with T waves and, consequently, higher Lyapunov exponents. This type of $[K^+]$-related changes in nonlinear dynamics could be complementary to other types of T wave morphology, duration and amplitude changes previously described in chapter 3.

Next, in this chapter, we evaluate the degree of correlation between each of the analyzed markers and $[K^+]$ in ESRD patients during and after HD. Univariable and multivariable regression models including markers of T wave nonlinear dynamics in combination with warping-based markers of T wave morphology are built and their performance for

[K^+] estimation is assessed.

4.2 Methods

4.2.1 Study population and ECG pre-processing

In this chapter, 48-hour 12-lead ECGs were collected from 29 ESRD patients undergoing HD at HCUZ as fully described in section 2.2.1.

ECG signals were pre-processed as described in section 2.2.1. The onset, peak and end of the T waves were delineated [28] as described in section 2.2.2.

A flow chart from ECG pre-processing to the determination of the estimators is shown in Fig. 4.1.

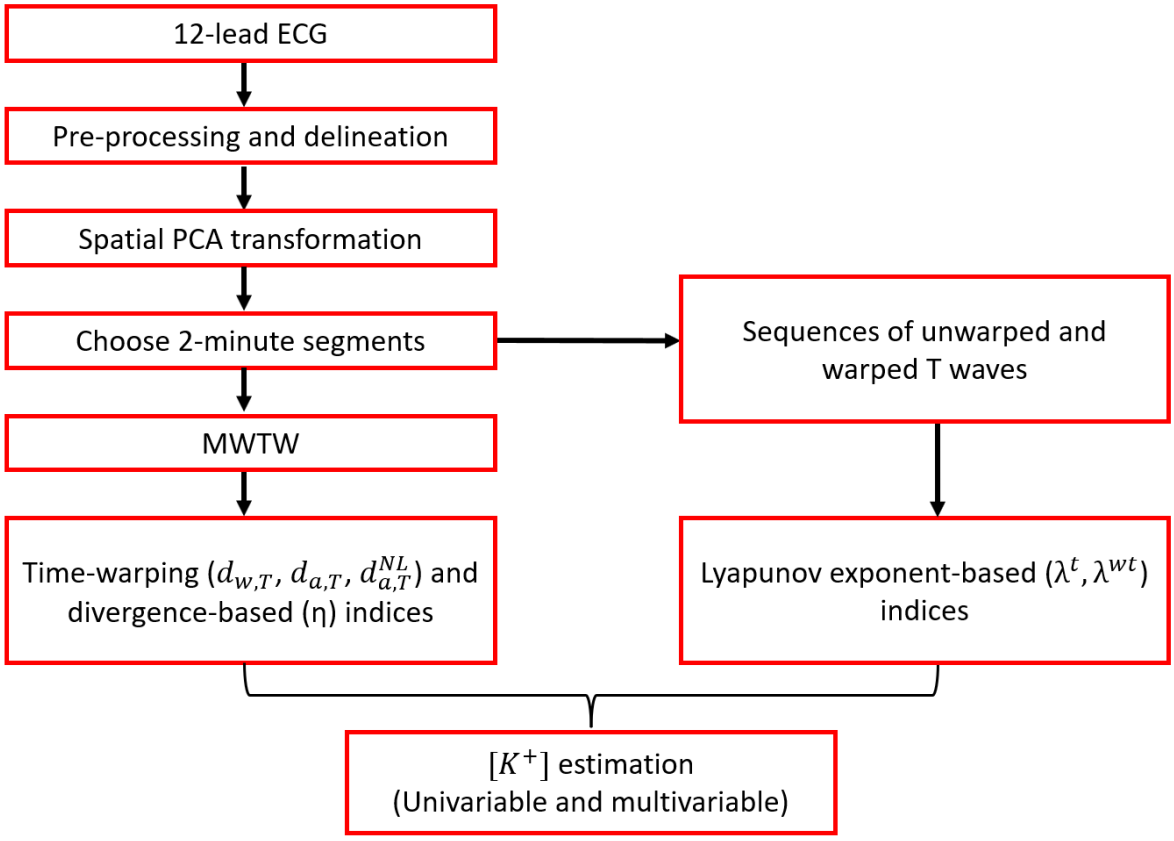

Figure 4.1: Flow chart showing the ECG processing steps performed in this study, from the collection of raw ECGs to the estimation of [K^+].

4.2.2 T wave morphology and nonlinear dynamics markers

Two-minute ECG segments at the HD start (h_0), at the end of each HD hour (h_1 to h_4) and at 48 hours (h_{48}) were analyzed to compute MWTWs, which are optimal representative averages obtained after time-warping all the T waves in the analyzed segment [93],

which was fully described in section 3.2.2. The predominant T wave polarity was identified as the most frequent polarity in the analyzed 2-minute window, with an average of 90% of T waves in each analyzed segment found to present such predominant polarity [29, 91] (see Fig. 2.3). For MWTW computation, only the T waves having the predominant polarity were considered after alignment with respect to their center of gravity [93] so that the calculated MWTW was not affected by potential outlier T waves.

In this chapter, $d_{\mathrm{w,T}}$, $d_{\mathrm{a,T}}$ and $d^{\mathrm{NL}}_{\mathrm{a,T}}$ based T wave morphological descriptors and λ^t, λ^{wt} and η based T wave nonlinear dynamics markers were calculated, as described in section 2.2.4.

4.2.3 Synthetically generated T waves

In this chapter, the ability of nonlinear dynamics markers, λ^t, λ^{wt} η, and time-warping markers, $d_{\mathrm{w,T}}$, $d_{\mathrm{a,T}}$ and $d^{\mathrm{NL}}_{\mathrm{a,T}}$, to capture gradual linear and nonlinear T wave time and amplitude variations along time, both in the absence and presence of temporal inter-beat variability, was assessed by generating sets of synthetic T waves in which changes were simulated according to specifically defined functions, as described in the following.

4.2.3.1 Simulation of T wave duration and amplitude changes

We considered a pre-processed PCA-transformed T wave obtained from a particular patient as a reference T wave, $\mathbf{f}^r(\mathbf{t}^r)$. We defined nonlinear T wave amplitude changes by:

$$\mathbf{f}^k_{\mathrm{NL}}(\mathbf{t}^r) = \mathbf{f}^r(\mathbf{t}^r) + c(k)\sin\left(2\pi\frac{1}{4N_r}\mathbf{t}^r\right), \tag{4.1}$$

where $c(k) = 25\,\sin\left[\pi(B_{\mathrm{T}}+k)/(2B_{\mathrm{T}})\right]$ being $k = 1,\ldots,B_{\mathrm{T}}$ the index of a T wave and B_{T} the total number of simulated beats, which was set to the number of beats during the whole HD session in the patient from whom the reference T wave was selected. The simulated T waves in the first 2-minute segment were identified as representative of h_0, while the simulated T waves for beats in 2-minute segments at the end of the first, second, third and fourth hours were taken as representative of h_1, h_2, h_3 and h_4, respectively.

Additional linear T wave amplitude changes were generated on top of the nonlinear amplitude changes:

$$\mathbf{f}^k_l(\mathbf{t}^r) = \mathbf{f}^k_{\mathrm{NL}}(\mathbf{t}^r)b(k) \tag{4.2}$$

where $b(k) = 1 + 0.25\,\sin(\pi(B_{\mathrm{T}}+k)/(2B_{\mathrm{T}}))$.

Nonlinear T wave duration changes were generated as follows:

$$\mathbf{t}^k_{\mathrm{NL}} = \mathbf{t}^r + g(k)\frac{N_r}{N_k}\sin\left(2\pi\frac{1}{N_r}\mathbf{t}^r\right), \tag{4.3}$$

where $g(k) = 10\frac{k-1}{B_{\mathrm{T}}-1} - 10$.

Additional linear T wave duration changes were simulated on top of the nonlinear duration changes:

$$\mathbf{t}_l^k = \gamma_k(\mathbf{t}_{\mathrm{NL}}^k), \tag{4.4}$$

where $\gamma_k(\mathbf{t}_{\mathrm{NL}}^k)$ stretches $\mathbf{t}_{\mathrm{NL}}^k$ according to a downsampling factor $a(k) = 0.25\frac{k-1}{B_{\mathrm{T}}-1} + 0.75$.

Combined simulated T wave duration and amplitude changes were defined according to:

$$\mathbf{f}_{\mathrm{S}}^k(\mathbf{t}^k) = \mathbf{f}_l^k(\mathbf{t}_l^k). \tag{4.5}$$

In this study, we used six different cases, $C\#$, which corresponded to linear and nonlinear duration and amplitude changes in the T waves:

- $C1$ considered the reference T wave and maintained its duration and amplitude along the whole simulation
- $C2$, defined by nonlinear amplitude changes,
- $C3$, defined by linear amplitude changes on top of nonlinear amplitude ones,
- $C4$, defined by nonlinear duration changes,
- $C5$, defined by linear duration changes on top of nonlinear duration ones, and
- $C6$, corresponding to the combined effects of linear and nonlinear amplitude and duration modulations in the T waves.

4.2.3.2 Simulation of temporal inter-beat variability

Realistic variability signals were obtained from an ESRD patient, with index q_0, for each 2-minute segment representative of each stage during and after HD. Variability signals were defined as the difference of each individual aligned T wave and the corresponding average in the 2-minute window:

$$\mathbf{f}_v^k = \mathbf{f}_{v,q_0}^k = \mathbf{f}^k - \frac{1}{B}\sum_{k=1}^{B}\mathbf{f}^k. \tag{4.6}$$

To make the magnitude of temporal inter-beat variability be representative of the averaged variability over patients rather than representative of an individual patient, the following factors were computed for each patient in a 2-minute window around each HD stage point and the median over all patients was calculated. Two different approaches were used to compute the factors associated with variability modulation in each patient. On the one hand, inter-beat variability factors at a given HD stage were defined for each

patient q as:

$$\alpha_{v,q}^{\text{Inter}} = \frac{1}{N^{\text{Inter}}} \sum_{n=1}^{N^{\text{Inter}}} f_{\text{IQR}_{v,q}}^{\text{Inter}}(n), \tag{4.7}$$

$$f_{\text{IQR}_{v,q}}^{\text{Inter}}(n) = \text{IQR}\{f_{v,q}^{1}(n), f_{v,q}^{2}(n), \ldots, f_{v,q}^{B}(n)\}, \tag{4.8}$$

where IQR represents the interquartile range operation, B is the number of beats in the 2-minute segment and N^{Inter} is the number of samples in the $\mathbf{f}_{\text{IQR}_v}^{\text{Inter}}$.

Similarly, intra-beat variability factors at a given HD stage were defined for each patient q as:

$$\alpha_{v,q}^{\text{Intra}} = \frac{1}{B} \sum_{k=1}^{B} f_{\text{IQR}_{v,q}}^{k}, \tag{4.9}$$

$$f_{\text{IQR}_{v,q}}^{k} = \text{IQR}\{f_{v,q}^{k}(1), f_{v,q}^{k}(2), \ldots, f_{v,q}^{k}(N_k)\}. \tag{4.10}$$

Representative scaling factors accounting for information from all patients, denoted by $\widetilde{\alpha}_v^{\text{Inter}}$ and $\widetilde{\alpha}_v^{\text{Intra}}$, were calculated by taking the median of the variability factors $\alpha_{v,q}^{\text{Inter}}$ and $\alpha_{v,q}^{\text{Intra}}$ over all patients. The calculated factors were applied to the variability signal, $\mathbf{f}_v^k$, and added to the synthetic T wave, $\mathbf{f}_{\text{S}}^k$, obtained as described in section 4.2.3.1, to have representative variability in the simulation:

$$\mathbf{f}_{\text{S}+v_{\text{Inter}}}^{k} = \frac{\widetilde{\alpha}_v^{\text{Inter}}}{\alpha_{v,q_0}^{\text{Inter}}} \cdot \mathbf{f}_{v,q_0}^{k} + \mathbf{f}_{\text{S}}^{k}, \tag{4.11}$$

and

$$\mathbf{f}_{\text{S}+v_{\text{Intra}}}^{k} = \frac{\widetilde{\alpha}_v^{\text{Intra}}}{\alpha_{v,q_0}^{\text{Intra}}} \cdot \mathbf{f}_{v,q_0}^{k} + \mathbf{f}_{\text{S}}^{k}, \tag{4.12}$$

where $\alpha_{v,q_0}^{\text{Inter}}$ and $\alpha_{v,q_0}^{\text{Intra}}$ were computed from the variability signals of the particular patient q_0.

For each analyzed HD stage, the generated T waves with added variability, i.e. $\mathbf{f}_{\text{S}+v_{\text{Inter}}}^{k}$ and $\mathbf{f}_{\text{S}+v_{\text{Intra}}}^{k}$, were concatenated for all simulated beats $k = 1, 2, \ldots, B$.

Additionally, MWTWs and inter-MWTWs were computed from simulated T waves in 2-minute segments to assess the response of $d_{\text{w,T}}$, $d_{\text{a,T}}$, $d_{\text{a,T}}^{\text{NL}}$ and η to the simulated duration and amplitude changes, both with and without additional scaled intra-beat variability. Inter-beat variability was used to assess the performance of λ^t and λ^{wt}.

4.2.4 Correlation analysis and statistical comparisons

To assess the relationship between each investigated T wave marker and $[\text{K}^+]$ during and after HD, Pearson, Spearman and linear partial correlation analyses (the latter to account for the influence of other factors affecting the T wave) were performed for each patient as described in section 2.2.5.

The duration of the ECG recordings was 48 hours for all patients, except for a few that ended some minutes earlier, mainly due to electrode detachment or battery exhaustion. However, given the small expected drift of $[K^+]$ in this short time period, we assumed that the end of the ECG recording corresponded to the blood sample taken at 48 hours. For this reason, correlation coefficients were computed using the six values of $[K^+]$ at HD stages h_i, $i \in \{0, 1, 2, 3, 4, 48\}$.

Wilcoxon signed-rank tests were performed to test for significant differences in λ^t, λ^{wt}, η, $d_{\mathrm{w,T}}$, $d_{\mathrm{a,T}}$ and $d^{\mathrm{NL}}_{\mathrm{a,T}}$ at different time stages during and after HD and Student's t-test was applied to test the significance of Pearson correlation coefficient r between each T wave marker and $[K^+]$ as fully described in section 2.2.5.

The performance of our investigated T wave markers was compared with that of the previously proposed T wave markers $T_{\mathrm{S/A}}$ [9, 31] and $T_{\mathrm{S}/\sqrt{A}}$ [32], which were computed from MWTWs at time points h_0, h_1, h_2, h_3, h_4 and h_{48} during and after HD as described in section 2.2.4.2.

4.2.5 Univariable and multivariable estimation of $[K^+]$

To estimate $[K^+]$ from the analyzed T wave markers, univariable and multivariable linear regression models were built. The univariable models included either η or $d_{\mathrm{w,T}}$ and the multivariable model included both.

The univariable estimators $[K^+]^{d_{w,T}}$ and $[K^+]^{\eta}$ and the multivariable estimator $[K^+]^{\mathrm{m}}$ were defined as:

$$[K^+]^{\eta} = \beta_0^{\eta} + \beta_1^{\eta} \cdot \eta \ , \tag{4.13}$$

$$[K^+]^{d_{w,T}} = \beta_0^{d_{w,T}} + \beta_1^{d_{w,T}} \cdot d_{\mathrm{w,T}} \ , \tag{4.14}$$

$$[K^+]^{\mathrm{m}} = \beta_0^{\mathrm{m}} + \beta_1^{\mathrm{m}} \cdot \eta \ + \beta_2^{\mathrm{m}} \cdot d_{\mathrm{w,T}} \ . \tag{4.15}$$

For the univariable models, the coefficients $\boldsymbol{\beta} = \begin{bmatrix} \beta_0^{\eta} & \beta_1^{\eta} \end{bmatrix}^T$ or $\boldsymbol{\beta} = \begin{bmatrix} \beta_0^{d_{w,T}} & \beta_1^{d_{w,T}} \end{bmatrix}^T$ were computed as:

$$\hat{\boldsymbol{\beta}} = (\mathbf{X}^T\mathbf{X})^{-1}\mathbf{X}^T\mathbf{y}^T, \tag{4.16}$$

with $\mathbf{X} = \begin{bmatrix} \mathbf{j}^T & \mathbf{x}_b^T \end{bmatrix}$. The definition of $\mathbf{j}^T$, $\mathbf{x}_b^T$ and $\mathbf{y}$ is different for time- and patient-specific estimators, as described in the following.

For a given HD stage i, the stage-specific estimator $\hat{\boldsymbol{\beta}}$ was calculated from equation (4.16) by considering $\mathbf{j} = [1, 1, \ldots, 1]$ of dimension $1 \times Q$, with Q the number of patients. The vector $\mathbf{x}_b = [b_{i,1}, b_{i,2}, \ldots, b_{i,Q}]$ contained the values of the marker b, being either η or $d_{\mathrm{w,T}}$, at the considered HD stage i from all the patients $q = 1, \ldots, Q$. The vector $\mathbf{y} = [[K^+]_{i,1}, [K^+]_{i,2}, \ldots, [K^+]_{i,Q}]$, contained the measured values of $[K^+]$ at the HD stage i for all patients.

For a given patient q, the patient-specific estimator $\hat{\boldsymbol{\beta}}$ was calculated by considering $\mathbf{j} = [1, 1, \ldots, 1]$ of dimension 1×6. The vector $\mathbf{x}_b = [b_{0,q}, b_{1,q}, b_{2,q}, b_{3,q}, b_{4,q}, b_{48,q}]$ contained

the values of b, either η or $d_{\mathrm{w,T}}$, for patient q at all HD stages $i = 0, 1, 2, 3, 4, 48$. The vector $\mathbf{y} = [[\mathrm{K}^+]_{0,q}, [\mathrm{K}^+]_{1,q}, [\mathrm{K}^+]_{2,q}, [\mathrm{K}^+]_{3,q}, [\mathrm{K}^+]_{4,q}, [\mathrm{K}^+]_{48,q}]$ contained the measured values of $[\mathrm{K}^+]$ values for patient q at all HD stages i.

For the multivariable model, $\boldsymbol{\beta} = [\beta_0^{\mathrm{m}}, \beta_1^{\mathrm{m}}, \beta_2^{\mathrm{m}}]^T$ was calculated from equation (4.16), now using $\mathbf{X} = [\mathbf{j}^T, \mathbf{x}_{b^{(1)}}^T, \mathbf{x}_{b^{(2)}}^T]$, with $\mathbf{x}_{b^{(1)}}$ containing the values of η and $\mathbf{x}_{b^{(2)}}$ containing the values of $d_{\mathrm{w,T}}$ and defined as described above for either HD-stage- or patient-specific estimators.

Leave-one-out cross validation was used to assess the performance of the $[\mathrm{K}^+]$ estimators:

- *Stage-specific estimators:* The estimator was trained with $Q-1$ patients for each HD stage individually and then tested for the Q-th patient. This process was repeated for all HD stages.

- *Patient-specific estimators:* The estimator was trained with five HD stage points for each patient individually and tested for the 6th stage. This process was repeated for all patients.

The error ϵ between measured and estimated $[\mathrm{K}^+]$ values was computed as

$$\epsilon = [\mathrm{K}^+]_a - [\mathrm{K}^+]_e, \tag{4.17}$$

where $[\mathrm{K}^+]_a$ is $[\mathrm{K}^+]$ measured from blood test and $[\mathrm{K}^+]_e$ is the estimated $[\mathrm{K}^+]$. The relative error R_v was computed as

$$R_v = \frac{[\mathrm{K}^+]_a - [\mathrm{K}^+]_e}{[\mathrm{K}^+]_{\mathcal{D}}}, \tag{4.18}$$

where $[\mathrm{K}^+]_{\mathcal{D}}$ was defined, for each patient, as the difference between maximum and minimum $[\mathrm{K}^+]_a$ values across HD stage. The relative error R_r was computed as

$$R_r = \frac{[\mathrm{K}^+]_a - [\mathrm{K}^+]_e}{[\mathrm{K}^+]_{\mathcal{R}}}, \tag{4.19}$$

where $[\mathrm{K}^+]_{\mathcal{R}}$ was defined as the difference between maximum 75th and minimum 25th percentiles of $[\mathrm{K}^+]$ across patients at each HD stage.

To assess the agreement between actual and estimated $[\mathrm{K}^+]$ values, Bland-Altman analysis was performed [130] to show the difference vs the mean of actual and estimated $[\mathrm{K}^+]$ for all patients at all HD time points.

It should be noted that a $[\mathrm{K}^+]$ estimator was not computed at the end of the HD session (h_4) since the morphological T wave marker $d_{\mathrm{w,T}}$ was zero by definition, as the reference was taken at that time stage.

4.3 Results

4.3.1 Robust calculation of T wave nonlinear dynamics markers

Fig. 4.2 shows λ^t, λ^{wt} and η for variations in the values of the parameters p, τ and m around their default values so as to assess the sensitivity of these markers to their parameters. The individual T waves in a 2-minute window from a particular patient at a given HD stage were used for the computation of $\lambda^t$and λ^{wt}, whereas the corresponding inter-MWTW was used for the computation of η. Thus, the default values of the parameters p, τ and m were different for λ^t and λ^{wt} than for η, as described in section 2.2.4.3. As can be seen from Fig. 4.2, λ^t and λ^{wt} were more sensitive to τ and m than to p but they tended to be stable around the values $\tau = 6$ and $m = 30$ employed here. The marker η, computed from inter-MWTW, was almost stable around the chosen values $p = 25$, $\tau = 3$ and $m = 22$.

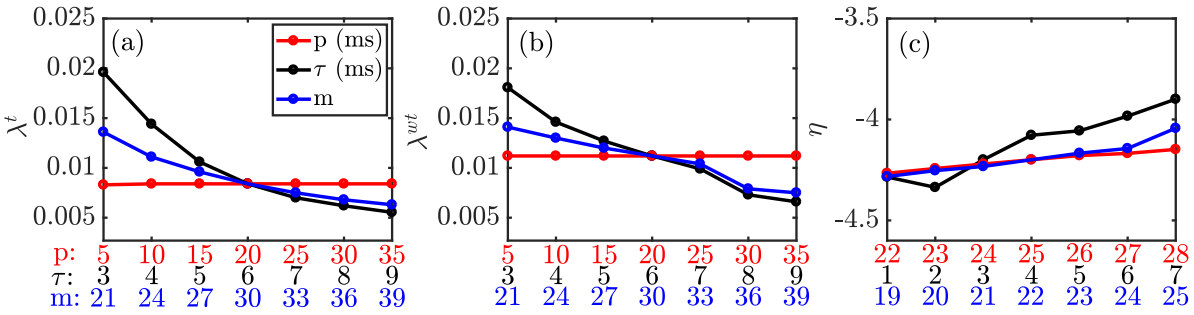

Figure 4.2: Panels a–c: Sensitivity of λ^t (left), λ^{wt} (middle) and η (right) for different values of the parameters representing the period (p), delay (τ) and embedding dimension (m) calculated from unwarped and warped T waves in a 2-minute window and inter-MWTW of a patient at a particular HD stage (h_4). Note that the default values of p, τ and m used in the calculation of λ^t and λ^{wt} are different from the ones used in the calculation of η, which explains differences in the x-axis of panels (a) and (b) with respect to panel (c).

4.3.2 Simulation of changes in T wave amplitude, duration and temporal inter-beat variability

Fig. 4.3, top panels, shows T waves under simulated linear and nonlinear duration and amplitude changes. Each panel shows the last T wave ($\mathbf{f}_S^k$) in a simulated 2-minute segment representing an HD stage. The bottom panels show the variability signals ($\mathbf{f}_v^k$) added to the T waves. Tall and narrow T waves are observed at h_0, representing the situation at the HD start, with a subsequent amplitude decrease and duration increase along time to represent variations during HD.

Fig. 4.4 shows the evolution of T wave markers (λ^t, η, $d_{\mathrm{w,T}}$, $d_{\mathrm{a,T}}$ and $d_{\mathrm{a,T}}^{\mathrm{NL}}$) for simulated linear and nonlinear variations in duration and amplitude ($C2$ to $C6$), with (panels f–j)

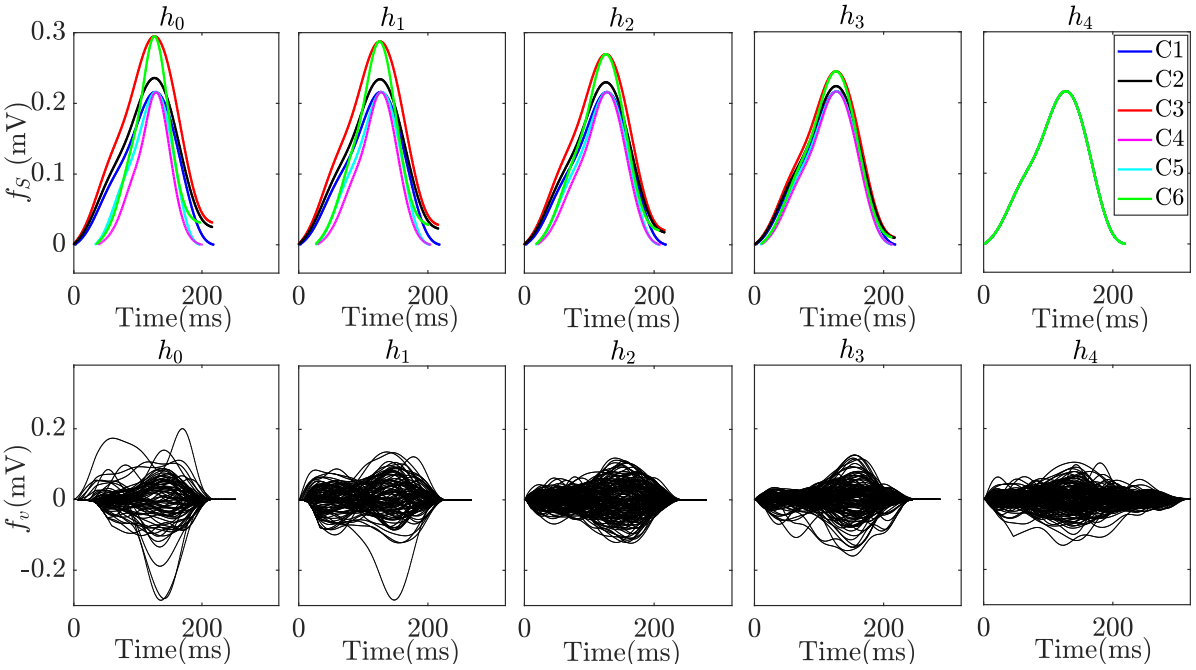

Figure 4.3: Simulated (last) T wave from a sequence of 2 minute T waves ($\mathbf{f}_{\mathrm{S}}^{k}$) in linear and nonlinear duration and amplitude domain (top panels) and the variability ($\mathbf{f}_{\mathrm{v}}^{k}$) in 2 minute T waves (bottom panels) during HD. Solid black and red T waves correspond to nonlinear and linear amplitude modulation ($C2$, $C3$), solid cyan and magenta T waves correspond to nonlinear and linear duration modulation ($C4$, $C5$), and solid green T wave includes both time and amplitude modulation ($C6$). Blue T wave corresponds to the reference T wave ($C1$).

and without (panels a–e) added variability to T waves. As can be seen from the figure, the Lyapunov exponent-based marker λ^t reflects temporal inter-beat variability in the T wave well, while the divergence marker η and morphology-based markers $d_{\mathrm{w,T}}$, $d_{\mathrm{a,T}}$ and $d_{\mathrm{a,T}}^{\mathrm{NL}}$ are able to describe linear and nonlinear duration or amplitude changes. The markers $d_{\mathrm{w,T}}$ and η are the ones best reflecting simulated time changes and combined time and amplitude changes in the T wave, respectively. Results for λ^{wt} were similar to those obtained for λ^t, although the decreasing trend along simulated time was less clear.

4.3.3 Characterization of T wave changes during and after HD

Fig. 4.5, panels a–f, shows the changes in the analyzed T wave markers (λ^t, λ^{wt}, η, $d_{\mathrm{w,T}}$, $d_{\mathrm{a,T}}$ and $d_{\mathrm{a,T}}^{\mathrm{NL}}$) together with [$\mathrm{K}^+$] changes during and after the HD session for the analyzed ESRD patients' recordings. Illustrative T waves for a patient are shown in the bottom panels g–h, presenting the reference T wave (blue), each investigated T wave (red) and inter-MWTW (black) during and after the HD session, both before (panel g) and after (panel h) warping and averaging.

A decreasing trend in all markers (right y-axis, in red) with decreasing [K^+] (left y-axis, in blue) was observed during HD, from h_0 (HD start) to h_4 (HD end). The marker values increased with increasing [K^+] from the HD end to the 48-th hour after the HD

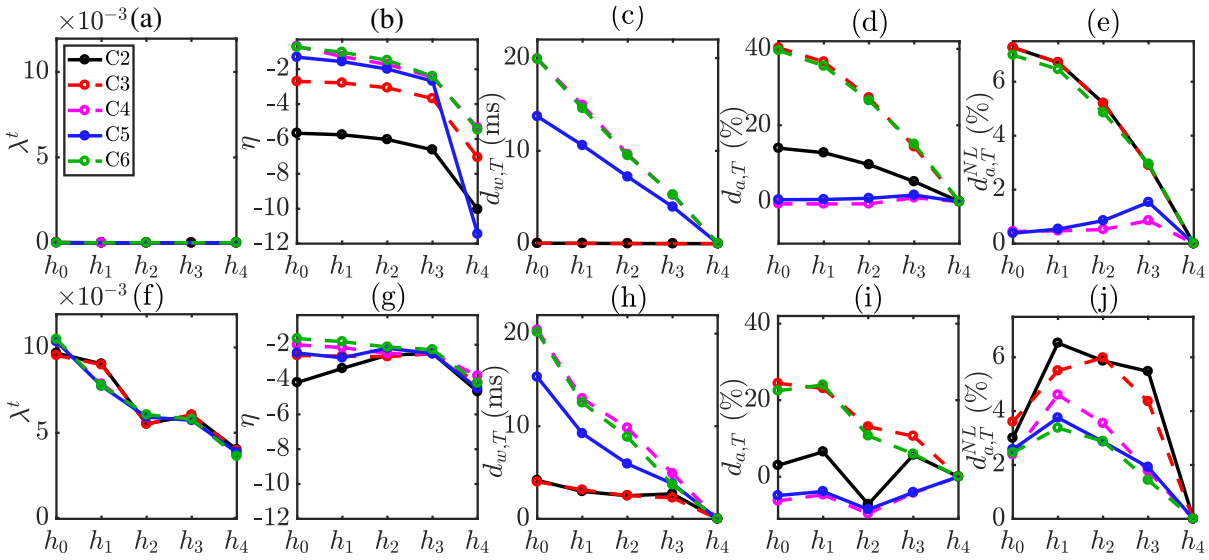

Figure 4.4: Panels a–j: T wave markers (λ, η, $d_{\mathrm{w,T}}$, $d_{\mathrm{a,T}}$ and $d^{\mathrm{NL}}_{\mathrm{a,T}}$) in linear and nonlinear duration and amplitude simulations during HD, with (bottom panels f–j) and without (top panels a–e) adding scaled variability's. Solid black and dotted red results correspond to nonlinear and combined nonlinear and linear amplitude modulation ($C2$, $C3$), dotted cyan and solid blue results correspond to nonlinear and combined nonlinear and linear duration modulation ($C4$, $C5$), and dotted green results includes both time and amplitude modulations ($C6$).

start. Particularly remarkable changes can be seen for the morphology marker $d_{\mathrm{w,T}}$ and for the nonlinear dynamics marker η. Since we took the end of the HD session (h_4) as reference for computation of $d_{\mathrm{w,T}}$, $d_{\mathrm{a,T}}$ and $d^{\mathrm{NL}}_{\mathrm{a,T}}$, these markers take zero value at this HD stage. From the bottom panels of Fig. 4.5, tall and narrow T waves can be observed before (h_0) and 48 hours after HD (h_{48}), corresponding to the highest [K^+] values.

4.3.4 Correlation between T wave markers and [K^+]

Fig. 4.6 shows the results of the correlation analysis. The linear correlation coefficients between [K^+] and each of the T wave markers are shown in black and the partial linear correlation coefficients after removing the effects of RR and [Ca^{2+}] are shown in red and blue, respectively. The markers $d_{\mathrm{w,T}}$, η, $d^{\mathrm{NL}}_{\mathrm{a,T}}$ and λ^t were the most highly linearly correlated with [K^+], with median Pearson r over patients presented in Table 4.2. λ^{wt} and $d_{\mathrm{a,T}}$ poorly correlated with [K^+]. Also, $d_{\mathrm{w,T}}$ and η were the most strongly correlated with [K^+] after removing the effects of RR and these two indices, together with $d_{\mathrm{a,T}}$ and $d^{\mathrm{NL}}_{\mathrm{a,T}}$, were the most strongly correlated with [K^+] after removing the effects of [Ca^{2+}]. Results obtained for Pearson and Spearman correlation coefficients between [K^+] and each the T wave markers investigated in this study are presented in Table 4.1, with the highest values obtained for $d_{\mathrm{w,T}}$, η and $T_{\mathrm{S/A}}$.

Table 4.2 also shows the p-values from Student's t-test to assess the statistical significance of non-zero mean Fisher's z-transformed Pearson correlation coefficients between

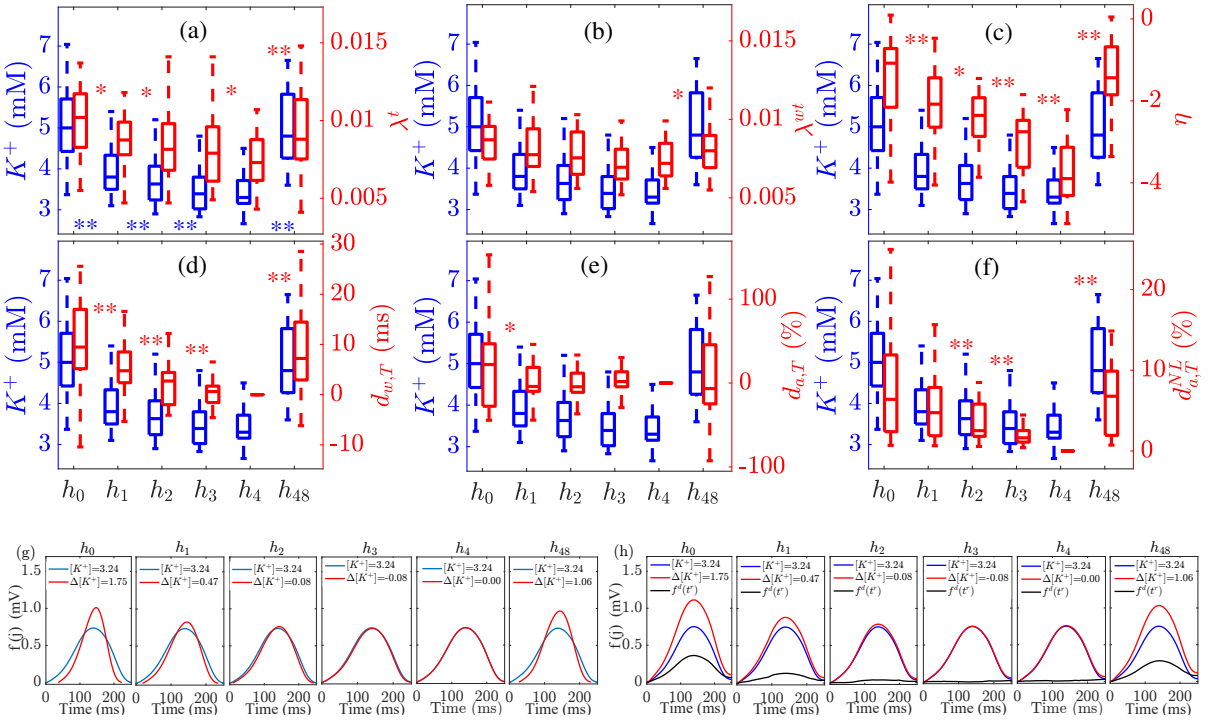

Figure 4.5: Panels a–f: Changes in λ^t, λ^{wt}, η, $d_{\mathrm{w,T}}$, $d_{\mathrm{a,T}}$ and $d^{\mathrm{NL}}_{\mathrm{a,T}}$ with [K^+] variations for the analyzed patients' recordings during and after HD. In panels a–f, * indicates $p < 0.05$ and ** indicates $p < 0.01$ in the comparison of each marker between consecutive time stages. The central line indicates the median, whereas top and bottom edges show the 25^{th} and 75^{th} percentiles, respectively. Panel g: T waves of a patient during and after HD. Panel h: Warped T waves of a patient during and after HD, with the reference T wave (blue), each analyzed T wave (red) and inter-MWTW (black) being displayed. Δ denotes the change in [K^+] with respect to the end of the HD session and the units in the legends of panels (g) and (h) are mM.

Table 4.1: Intra-patient Pearson's (r) and Spearman's (ρ) correlation coefficients between [K^+] and the T wave markers.

Parameter	r	ρ
λ^t	0.63 (0.47)	0.62 (0.69)
λ^{wt}	0.32 (0.89)	0.43 (0.78)
η	0.78 (0.38)	0.79 (0.51)
$d_{\mathrm{w,T}}$	0.83 (0.50)	0.78 (0.63)
$d_{\mathrm{a,T}}$	0.29 (1.35)	0.18 (0.95)
$d^{\mathrm{NL}}_{\mathrm{a,T}}$	0.66 (0.32)	0.66 (0.29)
$T_{\mathrm{S/A}}$	0.78 (0.39)	0.80 (0.36)
$T_{\mathrm{S}/\sqrt{A}}$	0.68 (0.77)	0.53 (0.74)

*Values are expressed as median (IQR)

T wave markers and [K^+]. As can be seen from the table, all the analyzed T wave markers, except for $d_{\mathrm{a,T}}$ and λ^{wt}, correlated significantly with [K^+].

To confirm that T wave nonlinear dynamics markers (λ^t, λ^{wt} and η) provided com-

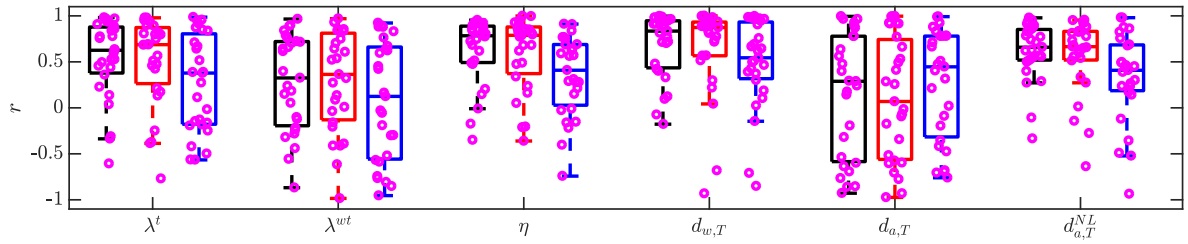

Figure 4.6: Correlation coefficients between T wave markers (λ^t, λ^{wt}, η, $d_{\mathrm{w,T}}$, $d_{\mathrm{a,T}}$, and $d_{\mathrm{a,T}}^{\mathrm{NL}}$) and [$K^+$] from patients' ECGs. Black boxplots: Pearson correlation coefficients. Red boxplots: Partial linear correlation coefficients after removing the effects of RR. Blue boxplots: Partial linear correlation coefficients after removing the effects of [Ca^{2+}]. Each purple dot represents the correlation coefficient for an individual patient. The central line indicates the median, whereas top and bottom edges show the 25^{th} and 75^{th} percentiles, respectively.

Table 4.2: Median Pearson r and partial correlation coefficients after removing the effects of RR (r_{RR}) and [Ca^{2+}] ($r_{[Ca^{2+}]}$), and p-values from Student's t-test to evaluate statistical significance of non-zero mean Fisher's z-transformed Pearson correlation coefficient between T wave markers and [K^+].

[K^+]	λ^t	λ^{wt}	η	$d_{\mathrm{w,T}}$	$d_{\mathrm{a,T}}$	$d_{\mathrm{a,T}}^{\mathrm{NL}}$
r	0.63	0.32	0.78	0.83	0.29	0.66
r_{RR}	0.69	0.36	0.79	0.87	0.07	0.66
$r_{[Ca^{2+}]}$	0.38	0.12	0.41	0.54	0.45	0.41
p-values	<0.01	0.01	<0.01	<0.01	0.18	<0.01

plementary information to morphological markers ($d_{\mathrm{w,T}}$, $d_{\mathrm{a,T}}$ and $d_{\mathrm{a,T}}^{\mathrm{NL}}$), linear correlation analysis was performed and results are shown in Table 4.3. As can be observed, the markers $d_{\mathrm{a,T}}^{\mathrm{NL}}$ and η correlated strongly.

Table 4.3: Intra-patient Pearson correlation coefficients (r) between morphological and nonlinear dynamics T wave markers.

Parameter	λ^t	λ^{wt}	η
$d_{\mathrm{w,T}}$	0.66 (0.43)	0.42 (0.58)	0.55 (0.73)
$d_{\mathrm{a,T}}$	0.29 (1.25)	0.05 (0.95)	−0.12 (1.62)
$d_{\mathrm{a,T}}^{\mathrm{NL}}$	0.57 (0.42)	0.21 (0.60)	0.72 (0.25)

*Values are expressed as median (IQR)

4.3.5 ECG-based estimation of $[K^+]$

Fig. 4.7 shows the error ϵ for univariable and multivariable $[K^+]$ estimators for all ESRD patients at each HD stage using both stage-specific and patient-specific approaches. Particularly for the multivariable estimator, Table 4.4 shows the estimated $[K^+]_e^m$ values using stage-specific, $[K^+]_e^{m,S}$, and patient-specific, $[K^+]_e^{m,P}$, approaches and compares them with the measured $[K^+]_a$ values.

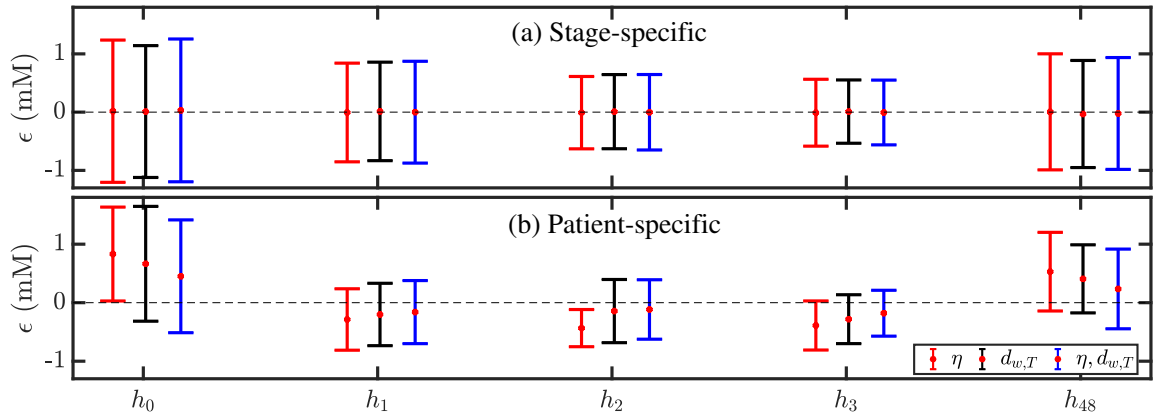

Figure 4.7: Error ϵ between estimated and actual $[K^+]$ for all ESRD patients during and after HD using univariable (η or $d_{w,T}$) and multivariable (η and $d_{w,T}$) estimators with stage-specific (panel (a)) or patient-specific (panel (b)) approaches. The central red dot represents the mean of the errors, whereas top and bottom edges show the standard deviation (SD) for all the patients. The central black dotted horizontal line represents a reference at '0'.

Table 4.4: Results for the multivariable $[K^+]_e^m$ estimator at each HD stage. $[K^+]_e^{m,S}$: estimated $[K^+]$ using stage-specific approach; $[K^+]_e^{m,P}$: estimated $[K^+]$ using patient-specific approach.

Actual vs Estimated $[K^+]$	h_0	h_1	h_2	h_3	h_{48}
$[K^+]_a$	5.23±1.10	4.05±0.78	3.70±0.58	3.48±0.52	5.01±0.93
$[K^+]_e^{m,S}$	5.20±0.33	4.05±0.20	3.70±0.16	3.46±0.14	5.04±0.31
$[K^+]_e^{m,P}$	4.78±1.45	4.21±0.68	3.82±0.76	3.63±0.73	4.78±1.26

*Values are expressed as mean ± standard deviation and the units are mM

Tables 4.5 and 4.6 show the relative errors R_v and R_r between actual and estimated $[K^+]$ at each HD stage for the multivariable estimator using stage-specific and patient-specific approaches.

Table 4.7 shows the median and IQR values of intra-patient Pearson correlation coefficient between actual and estimated $[K^+]$ for univariable and multivariable estimators using stage-specific and patient-specific approaches.

Bland-Altman plots in Figures 4.8-4.12 show the difference vs the mean of actual and estimated $[K^+]$ for $T_{S/A}$, $T_{S/\sqrt{A}}$, $d_{w,T}$, η and the combination of $d_{w,T}$ and η using stage and

Table 4.5: Relative errors R_v using stage-specific (S) and patient-specific (P) approaches for the multivariable estimator.

R_v	h_0	h_1	h_2	h_3	h_{48}
S	−0.20±0.68	−0.13±0.45	−0.10±0.35	−0.07±0.29	−0.17±0.57
P	0.30±0.61	−0.11±0.28	−0.09±0.26	−0.09±0.20	0.18±0.38

*Values are expressed as mean ± standard deviation

Table 4.6: Relative errors R_r using stage-specific (S) and patient-specific (P) approaches for the multivariable estimator.

R_r	h_0	h_1	h_2	h_3	h_{48}
S	0.011±0.442	0.000±0.315	−0.001±0.234	−0.002±0.201	−0.008±0.347
P	0.163±0.348	−0.058±0.194	−0.042±0.184	−0.065±0.142	0.085±0.246

*Values are expressed as mean ± standard deviation

Table 4.7: Intra-patient Pearson correlation coefficients (r) between actual and estimated $[K^+]$ ($r_{[K^+],[K^+]_e}$) using stage-specific (S) and patient-specific (P) approaches for univariable and multivariable estimators.

$r_{[K^+],[K^+]_e}$	η	$d_{w,T}$	η, $d_{w,T}$
S	0.98 (0.03)	0.97 (0.06)	0.97 (0.05)
P	0.32 (1.29)	0.65 (1.07)	0.77 (0.88)

*Values are expressed as median (IQR)

patient-specific approach.

A comparison between estimation errors obtained for T wave markers analyzed in the present study and in previous studies is presented in Tables 4.8–4.9.

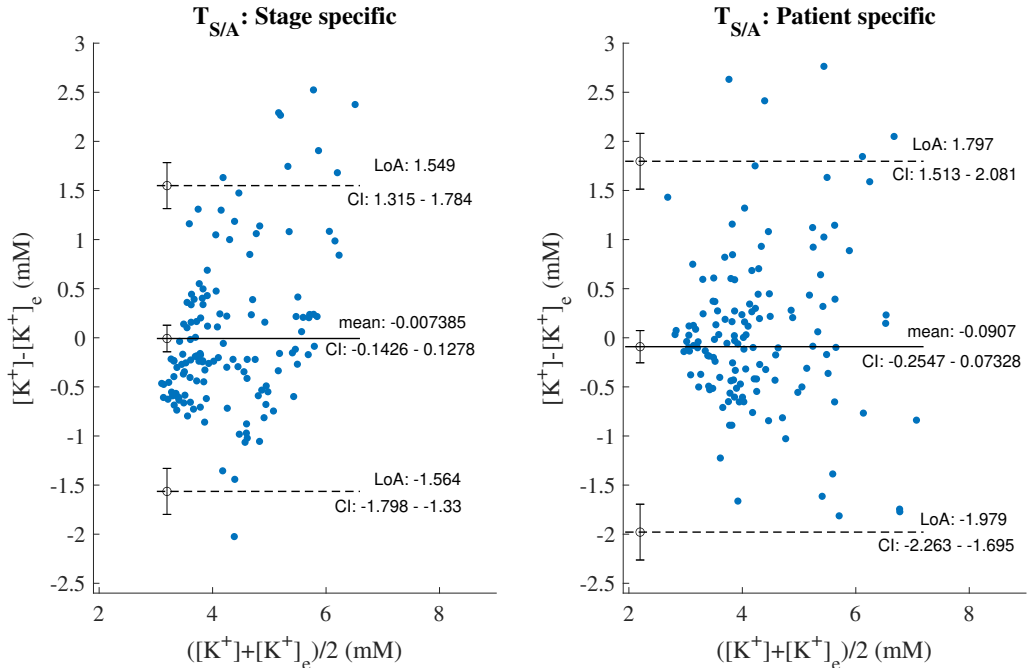

Figure 4.8: Left Panel: Bland-Altman plot between actual and estimated $[K^+]$ for $T_{S/A}$ using stage-specific approach. Right Panel: Bland-Altman plot using patient-specific approach.

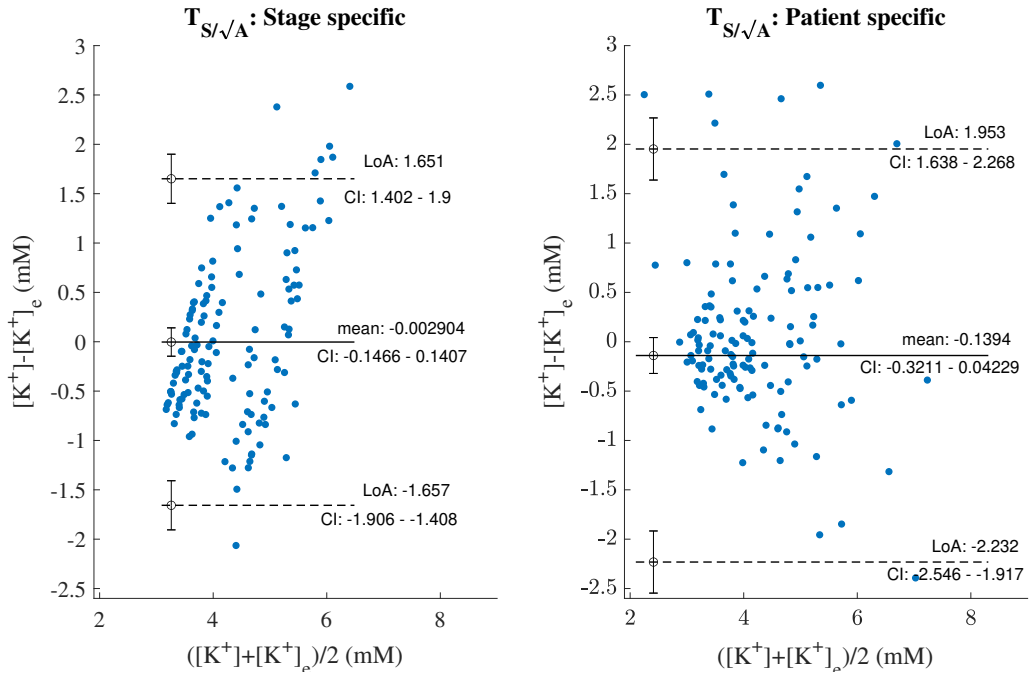

Figure 4.9: Left Panel: Bland-Altman plot between actual and estimated $[K^+]$ for $T_{S/\sqrt{A}}$ using stage-specific approach. Right Panel: Bland-Altman plot using patient-specific approach.

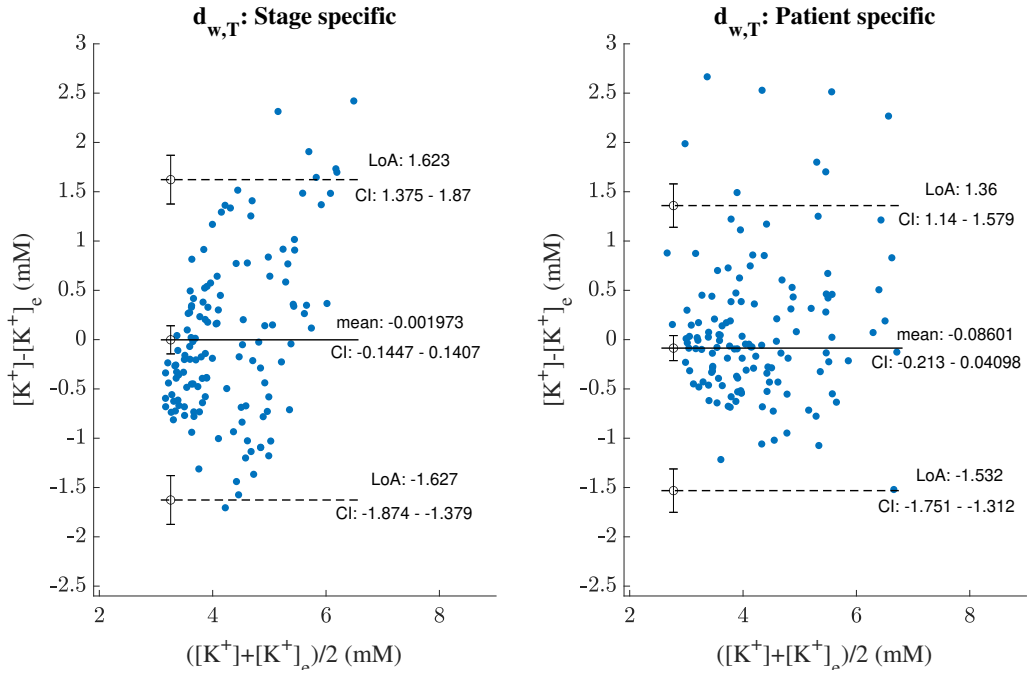

Figure 4.10: Left Panel: Bland-Altman plot between actual and estimated $[K^+]$ for $d_{w,T}$ using stage-specific approach. Right Panel: Bland-Altman plot using patient-specific approach.

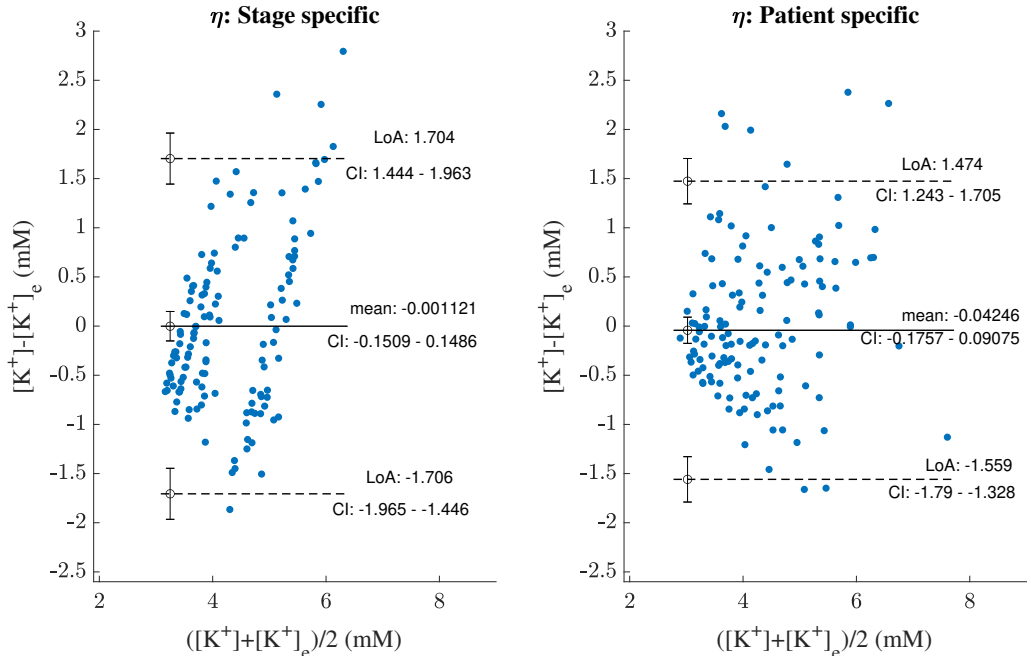

Figure 4.11: Left Panel: Bland-Altman plot between actual and estimated $[K^+]$ for η using stage-specific approach. Right Panel: Bland-Altman plot using patient-specific approach.

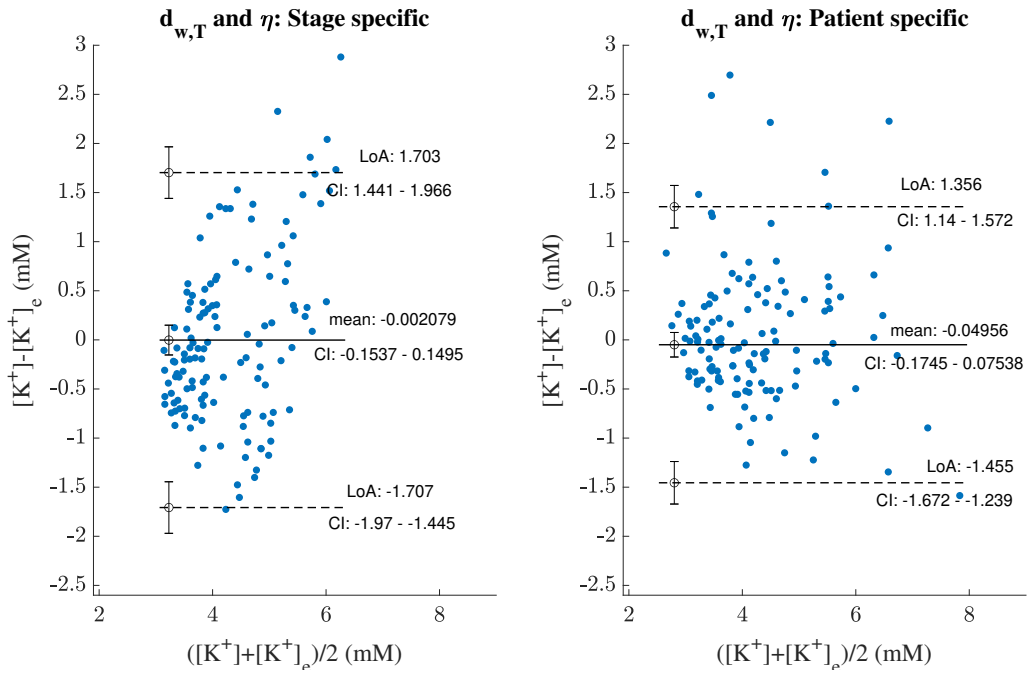

Figure 4.12: Left Panel: Bland-Altman plot between actual and estimated $[K^+]$ for $d_{w,T}$ and η using stage-specific approach. Right Panel: Bland-Altman plot using patient-specific approach.

4.4 Discussion

In this chapter, we analyzed the T waves of the ECG in ESRD patients during and after HD by novel nonlinear dynamics and morphology markers as described in chapter 3. Three nonlinear dynamics markers were evaluated: the first two, λ^t and λ^{wt}, assessed repolarization instabilities and temporal inter-beat variability by computing the maximum Lyapunov exponent from T wave sequences before and after warping, respectively; the third one, η, was proposed in this study to measure intra-beat differences in an averaged representative T wave after subtraction of a reference wave. Additionally, three warping-based markers were evaluated to assess morphological variability in the time domain ($d_{w,T}$) and amplitude domain ($d_{a,T}$ and $d^{NL}_{a,T}$). A comparison between our investigated markers and previously proposed markers, $T_{S/A}$ [9, 31] and $T_{S/\sqrt{A}}$ [32], was performed. The correlation between the analyzed T wave markers and serum $[K^+]$ during and after HD was found to be particularly strong for η and $d_{w,T}$. ECG estimators of $[K^+]$ were built based on individual and combined values of these two markers. We found a tight relationship between actual and estimated $[K^+]$ values, especially when the estimation used population ECG data evaluated at the same time stage after the start of an HD session. Our results can be used for noninvasive monitoring of $[K^+]$ in ESRD patients to anticipate arrhythmic risk associated with hypo- or hyperkalemia.

4.4.1 T wave variations during and after HD

This chapter investigated maximum Lyapunov exponent-based markers to characterize changes in the T wave of the ECG and their association with serum electrolyte levels. Previous studies have investigated indices of repolarization instability in patients undergoing HD, including T wave alternans [131], beat-to-beat QT interval variability [43] or T wave periodic repolarization dynamics [56]. However, most of these studies either have not been able to establish a clear correlation between the values of the evaluated indices and serum potassium levels or have reported moderate correlation coefficients, thus limiting their possibilities for ambulatory $[K^+]$ monitoring. We assessed whether nonlinear dynamics of the T wave could help in capturing relevant information on the changes in repolarization characteristics during and after HD. Also, on the basis of recent studies where we measured T wave morphological variability by time warping-based techniques and we showed its tight relationship with $[K^+]$, we investigated the combination of nonlinear dynamics and morphology descriptors to improve their individual performances for $[K^+]$ monitoring.

To characterize nonlinear dynamics we evaluated the maximum Lyapunov exponent from 2-minute sequences of T waves taken every hour from the start of HD and 48 hours after it. Lyapunov exponents quantify the sensitivity of a dynamical system to the initial conditions by measuring how a small change in the system variables at a certain time affects the behavior of the system at a future time [94]. Here, we calculated λ^t and λ^{wt}, representing the maximum Lyapunov exponent from unwarped and warped T wave sequences, respectively, and we found them to take positive values at all evaluated stages during and after HD. These results would indicate chaotic behavior in the form of local repolarization instabilities, which are significantly larger at the onset of the HD sessions when $[K^+]$ is elevated.

Also, we investigated a novel marker, η, evaluated from inter-MWTWs computed during and after HD to describe intra-beat dissimilarities and their variations with $[K^+]$. We found η to take higher values at the beginning of HD sessions, which would point to larger intra-beat differences in repolarization associated with raised $[K^+]$. This is concordant with the fact that T wave amplitude increases with $[K^+]$ and so does its difference with respect to the reference T wave.

To confirm the robustness of our calculations, we varied the values of the parameters used in the definition of λ^t, λ^{wt} and η and found relatively modest effects around the default parameter values as compared to changes measured during HD, particularly for η. To assess the specific information captured by the investigated nonlinear dynamics markers, we generated synthetic T waves and showed that λ^t and λ^{wt} mainly reflected temporal inter-beat variability while η was more sensitive to simulated amplitude and duration modulations.

4.4.2 Correlation of T wave changes markers to $[K^+]$

The correlation with $[K^+]$ was particularly strong for the nonlinear dynamics marker η and the time-domain morphological variability marker $d_{w,T}$, with median Pearson correlation coefficients across patients above 0.78. Importantly, the relationship between each of these two markers and $[K^+]$ remained tight even after removal of the effects of covariates like heart rate, with partial linear correlation coefficients still above 0.78. Such a relationship was, however, weaker when the effects of $[Ca^{2+}]$ were removed. This could be explained by $[K^+]$ and $[Ca^{2+}]$ exerting concurrent changes in the T wave during HD.

Previous works have shown that the T wave of the ECG is altered by variations in $[K^+]$ [4–6, 27], with narrow and peaked T waves recorded under high levels of $[K^+]$ [4, 23, 25, 30], in agreement with our observations. The effects of $[K^+]$ on specific T wave features like width, amplitude, slope, slope-to-amplitude or amplitude-to-slope ratio have been quantified [7–9, 31, 113]. Some of these features are very sensitive to T wave delineation and thus could be more prone to errors when measured in ambulatory recordings. Other markers, like the slope-to-amplitude, were tested in chapter 3 and were found to present changes that were as strongly correlated to $[K^+]$ variations as the time-domain morphology marker $d_{w,T}$, both with and without removing the effects of other covariates like heart rate and $[Ca^{2+}]$ [29].

Morphological characteristics of the T wave have been evaluated in previous studies, as recently reviewed [27]. In particular, a MCS based on T wave asymmetry, flatness and notching [33, 35] has been used to analyze the relationship between changes in the T wave shape and $[K^+]$ variations in large scale populations [36]. A strong correlation was found between MCS and $[K^+]$ when the latter varied in the range 2-4.1 mM but not in the range 4.2-6 mM. Our proposed markers of T wave morphological variability were strongly correlated with $[K^+]$ in a wide range of values, including both hypo- and hyperkalemic values. For some of our morphology markers, such a relationship was better represented by a nonlinear function than by a linear one [132], which agrees with previous studies describing nonlinear relationships between T wave markers like the slope-to-amplitude ratio and $[K^+]$ [9] and could help to explain the lower linear correlations found in other studies investigating $[K^+]$-induced alterations in ECG repolarization.

Mathematical modeling and numerical simulation have been used as tools to provide mechanistic understanding of ECG changes elicited in response to electrolyte variations and to improve the processing methods used to derive ECG markers with capacity for $[K^+]$ monitoring [9, 27, 84, 133]. In the case of T wave morphology markers, *in silico* analysis has been used to explain the high inter-individual variation in patterns measured in ESRD patients with varying $[K^+]$ [29, 134]. Differences in transmural distributions of endocardial, midmyocardial and epicardial cells contributed to explain the inter-individual variability in the T wave response to $[K^+]$ variations. In the case of T wave nonlinear dynamics, this is the first study investigating the markers λ^t, λ^{wt} and η and their relationship to $[K^+]$. Similarly to the morphological markers, we observed large inter-individual

Table 4.8: Estimation errors (ϵ) for T wave markers and their combinations using stage-specific (S) estimators.

$\epsilon(S)$	h_0	h_1	h_2	h_3	h_{48}
$T_{\mathrm{S/A}}$	0.019±1.159	0.620±0.517	0.003±0.630	0.004±0.559	0.007±0.730
$T_{\mathrm{S}/\sqrt{A}}$	0.009±1.180	−0.001±0.825	0.003±0.627	0.001±0.554	0.003±0.947
$d_{\mathrm{w,T}}$	0.010±1.132	0.012±0.845	0.008±0.636	0.009±0.543	−0.032±0.919
η	0.016±1.221	−0.006±0.847	−0.009±0.621	−0.010±0.574	0.005±0.996
$d_{\mathrm{w,T}}$ and η	0.030±1.225	−0.001±0.874	−0.002±0.648	−0.006±0.556	−0.023±0.960

*Values are expressed as mean ± standard deviation and the units are mM

differences in nonlinear dynamics characteristics. Our work on synthetic T waves simulating linear and nonlinear amplitude and duration changes served to establish the effects captured by these indices, with different levels of temporal inter-beat variability having a direct effect on their magnitudes, as discussed in the previous section.

4.4.3 Estimation of $[K^+]$ from T wave markers

Taking the two markers presenting the highest correlation with $[K^+]$, i.e. η and $d_{\mathrm{w,T}}$, we designed ECG-based $[K^+]$ estimators. On top of univariable estimators using one of these two markers, we built multivariable estimators based on their combination. For each of the constructed estimators, we considered both stage-specific and patient-specific approaches, with the first approach estimating $[K^+]$ for a patient at a given HD stage based on population data measured at the same stage with respect to the start of an HD session and the second approach estimating $[K^+]$ for a patient at a given time stage based on data from the same patient measured at different time stages. The stage-specific approach rendered results that were unbiased in mean and median over patients. However, the dispersion was generally larger than for the patient-specific approach. The combination of the two markers η and $d_{\mathrm{w,T}}$ led to overall improvements in terms of reduced estimation errors (Fig. 4.7 and Table 4.9). Multivariable $[K^+]$ estimates also correlated significantly better with actual $[K^+]$ than univariable estimates in the patient-specific approach. Agreement between actual and estimated $[K^+]$ was promising using our proposed T wave markers as compared to previously proposed T wave markers [9,31,32], which was confirmed by Bland-Altman analysis and calculation of estimation errors. The estimation errors over patients and HD stages using the patient-specific approach were 0.046 ± 0.69 mM for the combination of η and $d_{\mathrm{w,T}}$ while they were 0.091 ± 0.96 mM for $T_{\mathrm{S/A}}$ and 0.139 ± 1.07 mM for $T_{\mathrm{S}/\sqrt{A}}$. Also, we confirmed the suitability of $[K^+]$ estimation based on our ECG proposed markers under synthetic noisy scenarios, in which we took the ECG signal of a patient and we added noise at signal-to-noise ratio (SNR) values down to 5 dB. Estimation errors (ϵ) based on $d_{\mathrm{w,T}}$ and η were, in median over HD points, always below 0.4 mM, while these reached 0.73 mM for $T_{\mathrm{S/A}}$ at the lowest SNRs (Fig. 4.13).

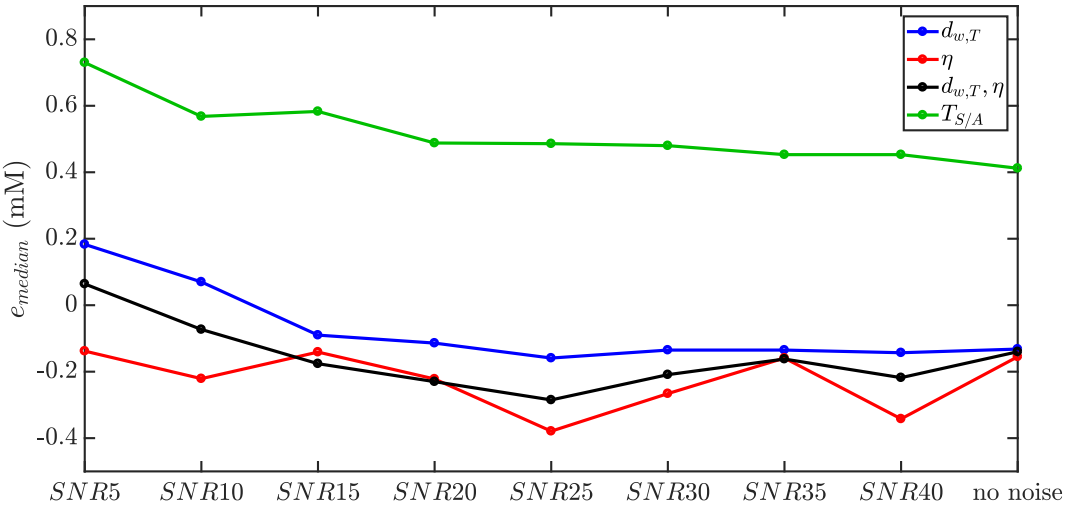

Figure 4.13: Estimation errors (e) based on $d_{\mathrm{w,T}}$, η and $T_{\mathrm{S/A}}$, in median over HD points, at different levels of SNR ($5-40$ dB).

Table 4.9: Estimation errors (ϵ) for T wave markers and their combinations using patient-specific (P) estimators.

$\epsilon(P)$	h_0	h_1	h_2	h_3	h_{48}
$T_{\mathrm{S/A}}$	0.967±0.729	0.479±0.455	0.357±0.350	0.381±0.409	0.922±1.192
$T_{\mathrm{S}/\sqrt{A}}$	0.904±1.413	0.022±0.827	−0.248±0.299	−0.333±0.402	0.353±1.373
$d_{\mathrm{w,T}}$	0.665±0.981	−0.202±0.533	−0.143±0.540	−0.282±0.418	0.407±0.582
η	0.831±0.802	−0.287±0.525	−0.435±0.318	−0.390±0.419	0.530±0.672
$d_{\mathrm{w,T}}$ and η	0.451±0.964	−0.161±0.539	−0.116±0.508	−0.180±0.392	0.235±0.681

*Values are expressed as mean ± standard deviation and the units are mM

The highest estimation errors were obtained at the start of the HD session (h_0) and 48 hours after it (h_{48}), corresponding to the highest [K^+] values. The reason for this could lie in the fact that these HD stages are associated with [K^+] values well apart from the ones measured at h_1, h_2, h_3 and h_4, which translates into large differences in the T wave markers at h_0 and h_{48} as compared to other HD points. In the learning phase, the estimators are fitted to all the available values along and after HD, with large relevance of the high number of HD stages corresponding to lower [K^+], which would explain the lower performance of the estimators at h_0 and h_{48}. Future research could be designed so as to have more available [K^+] measurements during the time period from the end of the HD session to the start of a new session 48 hours later, or during the first hour of the HD. This would allow improved learning of the estimators, which could also be designed to account for nonlinear relationships between the investigated repolarization markers and [K^+]. Previous studies have shown the relevance of accounting for such nonlinearities in the design of the estimators [9, 132], which we discarded in the present study due to the

limited number of sampled HD stages per patient.

The above discussed results suggest that T wave nonlinear dynamics and warping-based morphology markers can be valuable for $[K^+]$ monitoring during inter-dialytic periods in ESRD patients.

4.4.4 Study limitations and future research

We focused our research on the effects of $[K^+]$ on ventricular repolarization. The impact of other electrolytes like $[Ca^{2+}]$ and $[Mg^{2+}]$ could also be analyzed and univariable and multivariable estimators could be derived from ECGs. While some reports have already described alterations in T wave morphology in response to variations in $[Ca^{2+}]$ and $[Mg^{2+}]$ [6,50,135–137], the impact on T wave markers remains unknown. Therefore, we performed extensive analysis to estimate $[Ca^{2+}]$ with $[K^+]$, not only from T waves but also from QRS complexes, in following chapter (chapter 5). $[Mg^{2+}]$ was not explored because $[Mg^{2+}]$ measurements were not available for the present study.

Other multivariable estimators including indices reported in previous studies [9, 31, 32, 52, 53] could be tested to analyze its potential for improved noninvasive monitoring of $[K^+]$.

The present work could be extended to include deep learning-based approaches for serum electrolyte estimation provided large data sets of ECG recordings and concomitant blood samples were available for the analysis, in line with studies already addressing hypo- and hyperkalemia screening from the ECG using deep learning methods [55, 138, 139].

4.5 Conclusions

In this chapter, we showed that noninvasive monitoring of $[K^+]$ in ESRD patients based on combined T wave nonlinear dynamics and morphological variability markers is feasible. The proposed methods can find application in hypo- and hyperkalemia screening, which can be of major relevance to anticipate arrhythmic events in these patients.

Chapter 5

Monitoring of Serum Potassium and Calcium Levels in End-stage Renal Disease Patients by ECG Depolarization Morphology Analysis

This chapter is partially based on the paper published by Bukhari et al., Sensors, 2022, 22(8):2951.; 2022.
doi:10.3390/s22082951

5.1 Introduction

In chapters 3 and 4, we used time-warping and nonlinear dynamics techniques to characterize changes in the whole morphology of T wave at varying $[K^+]$ and $[Ca^{2+}]$ in patients and simulated ECGs [29, 89, 129, 132, 134, 140]. We found a strong relationship between $[K^+]$ and T wave linear and nonlinear features. These T wave markers could be used for the continuous monitoring of these two electrolyte levels, which could facilitate timely therapies for ESRD patients.

Assessment of ventricular depolarization for serum electrolyte estimation has been less explored in the literature. Similarly to QT studies, research on QRS complex duration has rendered inconsistent results, with some works reporting widened QRS complexes [23, 37] and others reporting narrowed QRS complexes at high $[K^+]$ [6, 38]. Other works have assessed the time voltage area, amplitude and sine wave shape of the QRS complex, but limitations in terms of their significance or their dependence on blood volume have been acknowledged [27, 58–60]. None of these studies have, however, quantitatively characterized overall variations in the morphology of the QRS complex during HD. We hypothesized that QRS morphology could provide complementary information on $[K^+]$ and $[Ca^{2+}]$, in addition to that provided by repolarization.

In this chapter, we quantify changes in the QRS amplitude, duration and morphology, the latter both in the time and amplitude domains using time-warping analysis as fully explained in section 2.2.4.1, at varying $[K^+]$, $[Ca^{2+}]$ and HR in ESRD patients. Univariable and multivariable electrolyte estimators, including novel QRS morphological markers in combination with already proposed T wave markers [29, 89, 93, 134], as discussed in chapters 3 and 4, were devised. The contribution of depolarization analysis to $[K^+]$ and $[Ca^{2+}]$ monitoring was assessed.

5.2 Materials

In this chapter, forty-eight-hour 12-lead ECGs were acquired from 29 ESRD patients of HCUZ as fully described in section 2.2.1. In this chapter, we defined another time point for ECG analysis, corresponding to a segment taken two minutes before the end of HD (minute 213 or 243, depending on the patient), which we denoted by h_4^-. The $[K^+]$ and $[Ca^{2+}]$ values at h_4^- were assumed to be the same as at h_4, as the time difference between these two segments was just two minutes.

5.3 Methods

A flow chart showing all the stages of the signal processing starting with 12-lead ECG pre-processing, followed by PCA transformation, computation of MWQRS (see section 2.2.4.1 for the computation of MWQRS) and QRS morphological markers (see section 2.2.4.1 for the computation of QRS markers), and finishing with the estimation of $[K^+]$ and $[Ca^{2+}]$ is shown in Figure 5.1.

5.3.1 ECG pre-processing and QRS descriptors

In this chapter, ECG pre-processing was performed as described in previous chapters but here we focused on QRS complex rather than T wave. Baseline wander, muscular noise and powerline interference were removed from the ECG signals by the pre-processing described in section 2.2.1. As described in section 2.2.3, the first PC was computed in a stable ECG segment at the end of the HD session and this segment corresponded to the time when the patient was discharged from hospital with restored serum $[K^+]$ and $[Ca^{2+}]$. The QRS complexes from each time point in the first PC were delineated [28] to mark their onsets, peaks and ends.

The linear and nonlinear time and amplitude morphological QRS descriptors ($d^{\mathrm{u}}_{\mathrm{w,Q}}$, $d_{\mathrm{a,Q}}$, $d^{\mathrm{NL}}_{\mathrm{w,Q}}$ and $d^{\mathrm{NL}}_{\mathrm{a,Q}}$), QRS slopes markers ($I_{\mathrm{US}}$ and I_{DS}) and QRS duration and amplitude markers (QRS_{w} and QRS_{a}), were computed as fully described in section 2.2.4.1.

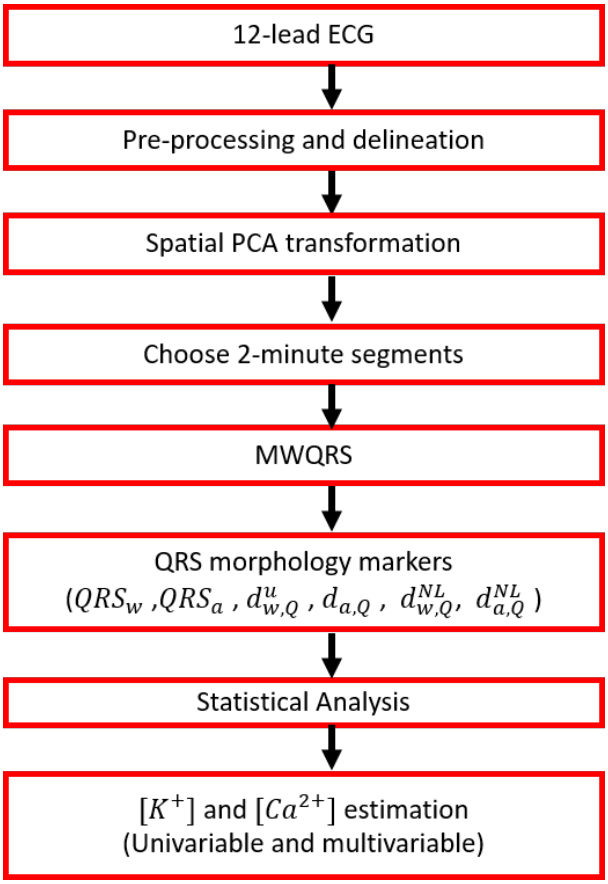

Figure 5.1: Flow chart showing the ECG processing steps performed in this study, from the collection of raw ECGs to the estimation of $[K^+]$ and $[Ca^{2+}]$.

5.3.2 Uni- and multivariable estimation of $[K^+]$ and $[Ca^{2+}]$

Pearson correlation coefficients (r), Wilcoxon signed-rank test and a Student's t-test were performed for $[K^+]$, $[Ca^{2+}]$, RR, QRS_w, QRS_a, $d^u_{w,Q}$, $d_{a,Q}$, $d^{NL}_{w,Q}$ and $d^{NL}_{a,Q}$ as described in section 2.2.5.

To estimate $[K^+]$ and $[Ca^{2+}]$, univariable and multivariable estimators were developed in this chapter. Of all the analyzed QRS descriptors, $d^u_{w,Q}$ was selected to build univariable estimators because it presented high median absolute Pearson correlation with $[K^+]$ and $[Ca^{2+}]$ and a relatively low IQR range, particularly for $[K^+]$. Univariable estimators were additionally built using the repolarization descriptor $d^u_{w,T}$, which had shown strong correlation with electrolyte levels [29, 89]. $d^u_{w,T}$ was calculated analogously to $d^u_{w,Q}$ but for the T wave instead of the QRS complex in chapter 3. Multivariable estimators were tested using both $d^u_{w,Q}$ and $d^u_{w,T}$.

The univariable $[\hat{K}^+]_u$ ($[\hat{Ca}^{2+}]_u$, respectively) and multivariable $[\hat{K}^+]_m$ ($[\hat{Ca}^{2+}]_m$, respectively) estimators were computed, as fully described in section 4.2.5, but using $d^u_{w,Q}$ and $d^u_{w,T}$. The performance of the estimators was tested by using the leave-one-out cross-validation approach for both $[K^+]$ and $[Ca^{2+}]$.

Three different types of estimators were considered, namely stage-specific, patient-

specific and global estimators, as described in the following paragraphs. The definition of $\mathbf{j}^T$, $\mathbf{x}_b^T$ and $\mathbf{y}$ was different for each type of estimator:

- For an HD stage-specific (S) estimator, which estimates the electrolyte level ($[K^+]$ or $[Ca^{2+}]$) at stage h_i of a given patient q from the marker's values of the remaining patients at that stage as fully explained in section 4.2.5 .

- For a patient-specific (P) estimator, which estimates the electrolyte level at stage h_i of a given patient q from the marker's values at the remaining stages for that same patient as described in section 4.2.5 but the vector $\hat{\boldsymbol{\beta}}$ was calculated from the vector $\mathbf{j} = \begin{bmatrix} 1 & 1 & \cdots & 1 & 1 \end{bmatrix}$ of dimension 1×6 (if h_i was h_0 or h_{48}) or 1×7 (if h_i was different from h_0 or h_{48}), $\mathbf{x}_b = \begin{bmatrix} b_{0,q} & b_{0,q} & b_{1,q} & \cdots b_{4^-,q} & b_{48,q} & b_{48,q} \end{bmatrix}$ containing the values of the marker $b = d^{\mathrm{u}}_{\mathrm{w,Q}}$ or $d^{\mathrm{u}}_{\mathrm{w,T}}$ for patient q at the different time points except for h_i, with h_0 and h_{48} being duplicated. The vector $\mathbf{y}$ was defined as $\mathbf{y} = [[K^+]_{0,q}\,[K^+]_{0,q}\,[K^+]_{1,q} \cdots [K^+]_{4^-,q}\,[K^+]_{48,q}\,[K^+]_{48,q}]$ containing the measured $[K^+]$ values for patient q at all time points except for h_i. An analogous definition of vector $\mathbf{y}$ was applied for $[Ca^{2+}]$. This process was repeated for each patient individually.

- For a global (G) estimator, which estimates the electrolyte level at stage h_i of a given patient q from the marker values at all other time points from all other patients, the vector $\hat{\boldsymbol{\beta}}$ was calculated by defining vectors $\mathbf{x}_b$ and $\mathbf{y}$ to contain the marker values and the electrolyte measures from all patients at all stages except for patient q at time i.

For the multivariable estimators, $\boldsymbol{\beta} = \begin{bmatrix} \beta_0^{\mathrm{m}} & \beta_1^{\mathrm{m}} & \beta_2^{\mathrm{m}} \end{bmatrix}^T$ was estimated as described in section 4.2.5, depending on the type of estimator (stage-specific, patient-specific or global).

The estimated error, e, and the relative error, e_r, with respect to the range of electrolyte measurements, between actual $[K^+]$ (or $[Ca^{2+}]$) and estimated $[\hat{K}^+]$ (or $[\hat{Ca}^{2+}]$) was computed as briefly described in section 4.2.5.

The relative error, e_v, with respect to the actual electrolyte measurement $[K^+]$ for each patient at each HD stage (analogously for $[Ca^{2+}]$) was computed as

$$e_v = \frac{[K^+] - [\hat{K}^+]}{[K^+]}. \tag{5.1}$$

The mean absolute error was computed by averaging the absolute value of e defined in Equation (4.17). The root mean square error was computed by taking the root mean square of e defined in Equation (4.17).

To assess the agreement between actual and estimated $[K^+]$ and $[Ca^{2+}]$ values, Bland–Altman analysis was performed [130], in which the differences between the actual and

estimated [K^+] and [Ca^{2+}] were plotted as a function of their averages, for all patients at all HD time points. [K^+] and [Ca^{2+}] estimation accuracy using our investigated markers was also compared with those of the previously proposed markers $T_{S/A}$ [9,31] and $T_{S/\sqrt{A}}$ [32] as described in section 4.2.4.

In this chapter, it should be noted that estimations of [K^+] and [Ca^{2+}] could not be performed at the end of the HD session (h_4) since the morphological QRS complex and T wave markers were zero by definition due to the fact that the reference was taken at that time stage. Therefore, we defined an extra time point h_4^-, as described in section 5.2, just before the HD end (reference) so as to improve the estimation accuracy based on one additional HD point.

5.4 Results

5.4.1 Characterization of QRS complex changes during and after HD

Figure 5.2 shows the relationship between ΔI_{US} (ΔI_{DS}, respectively) and Δ[K^+] for the 29 patients (panels a-b). ΔI_{US} and ΔI_{DS} took the smallest and largest values at the beginning of the HD session, corresponding to the highest [K^+] values, respectively. In the bottom panels of Figure 5.2, significant changes in the morphology of the QRS complex can be observed during HD. Both QRS slope markers significantly varied with decreasing [K^+] during HD, in all the ESRD patients. As shown in the figure, QRS slope changes in ESRD patients were related to both amplitude and duration of the QRS complex.

The top panels in Figure 5.3 show the results for the QRS markers (QRS_w, QRS_a, $d^u_{w,Q}$, $d_{a,Q}$, $d^{NL}_{w,Q}$ and $d^{NL}_{a,Q}$) together with [K^+], [Ca^{2+}] and RR variations during and after HD for all patients. Statistically significant differences between consecutive HD stages were found for QRS_a, $d^u_{w,Q}$, $d_{a,Q}$, $d^{NL}_{w,Q}$ and $d^{NL}_{a,Q}$ as well as for [K^+] and [Ca^{2+}] variations, but not for RR.

The bottom panels of Figure 5.3 show MWQRS during and after HD (red) compared to the reference MWQRS (blue) computed at the end of HD. Lower QRS_a values could be observed at h_0 and h_{48}, corresponding to the highest [K^+] and the lowest [Ca^{2+}].

5.4.2 Contribution of [K^+], [Ca^{2+}] and HR variations to QRS complex changes

Figure 5.4 shows the strong linear Pearson correlation of ΔI_{US} and ΔI_{DS} with Δ[K^+] (median value of -0.84 and 0.88) and with Δ[Ca^{2+}] (median value of 0.78 and -0.91). However, a poor association was found between both QRS slope markers and ΔRR, possibly because the RR interval varies much less than [K^+] and [Ca^{2+}] during HD in the analyzed ESRD patients. Here, Δ[K^+], Δ[Ca^{2+}] or ΔRR variations represent changes in

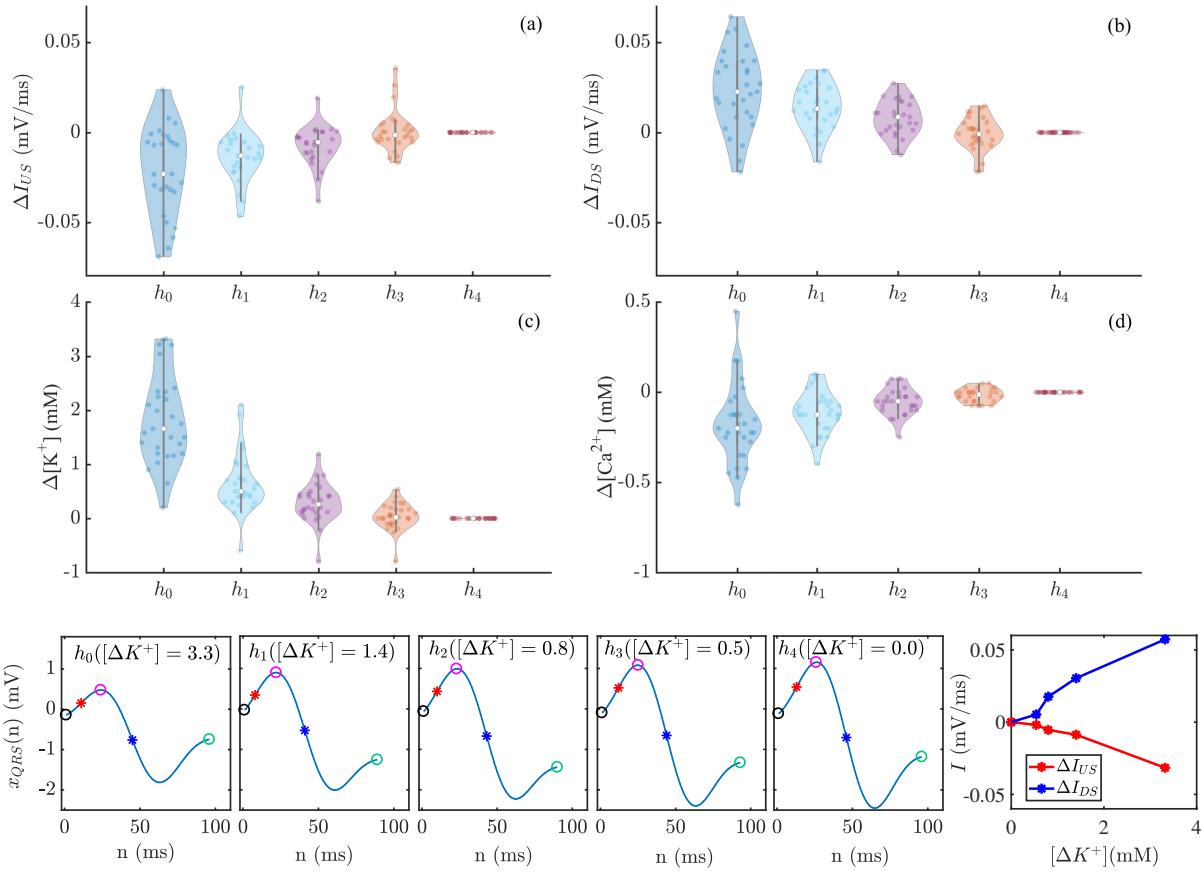

Figure 5.2: Panels a–d: Violin plots of ΔI_{US} (panel a), ΔI_{DS} (panel b), $\Delta[\mathrm{K}^+]$ (panel c) and $\Delta[\mathrm{Ca}^{2+}]$ (panel d) from MWQRS of 29 ESRD patients showing their values during HD stages. In each panel, the central white dot indicates the median. Each dot corresponds to an individual patient. Bottom panels show the MWQRS complexes and QRS slopes variations during HD with $\Delta[\mathrm{K}^+]$ for a patient. Location of Q, R and S waves were marked by black, purple and green circles, respectively. Red and blue asterisks show the locations associated with I_{US} and I_{DS} in the QRS complex, respectively. Δ denotes change with respect to the end of HD session (h_4).

$[\mathrm{K}^+]$, $[\mathrm{Ca}^{2+}]$ and RR with respect to the values at the end of HD end.

Figure 5.5 shows the Pearson correlation coefficient, r, between QRS markers (QRS_{w}, QRS_{a}, $d^{\mathrm{u}}_{\mathrm{w,Q}}$, $d_{\mathrm{a,Q}}$, $d^{\mathrm{NL}}_{\mathrm{w,Q}}$ and $d^{\mathrm{NL}}_{\mathrm{a,Q}}$) and $[\mathrm{K}^+]$ (black), $[\mathrm{Ca}^{2+}]$ (red) and RR (blue). QRS_{a}, $d^{\mathrm{u}}_{\mathrm{w,Q}}$, $d_{\mathrm{a,Q}}$, $d^{\mathrm{NL}}_{\mathrm{w,Q}}$ and $d^{\mathrm{NL}}_{\mathrm{a,Q}}$ were the most highly correlated, in median, with $[\mathrm{K}^+]$ (median r being -0.87, 0.78, -0.80, 0.73 and 0.81, respectively) and $[\mathrm{Ca}^{2+}]$ (0.76, -0.61, 0.63, -0.70 and -0.75, respectively). The IQR of r was the lowest for $d^{\mathrm{u}}_{\mathrm{w,Q}}$ when the correlation with $[\mathrm{K}^+]$ was analyzed, and for QRS_{a} in the case of $[\mathrm{Ca}^{2+}]$. Poor association between all the analyzed markers and RR was found.

Table 5.1 shows the p-values from the Student's t-test used to determine the statistical significance of non-zero mean Fisher z-transformed Pearson correlation coefficients between QRS markers and each of $[\mathrm{K}^+]$, $[\mathrm{Ca}^{2+}]$ and RR in the patient population, during and after HD. All the analyzed QRS markers showed significant association with $[\mathrm{K}^+]$ and most of them (all but QRS_{w}) with $[\mathrm{Ca}^{2+}]$. On the other hand, no marker presented

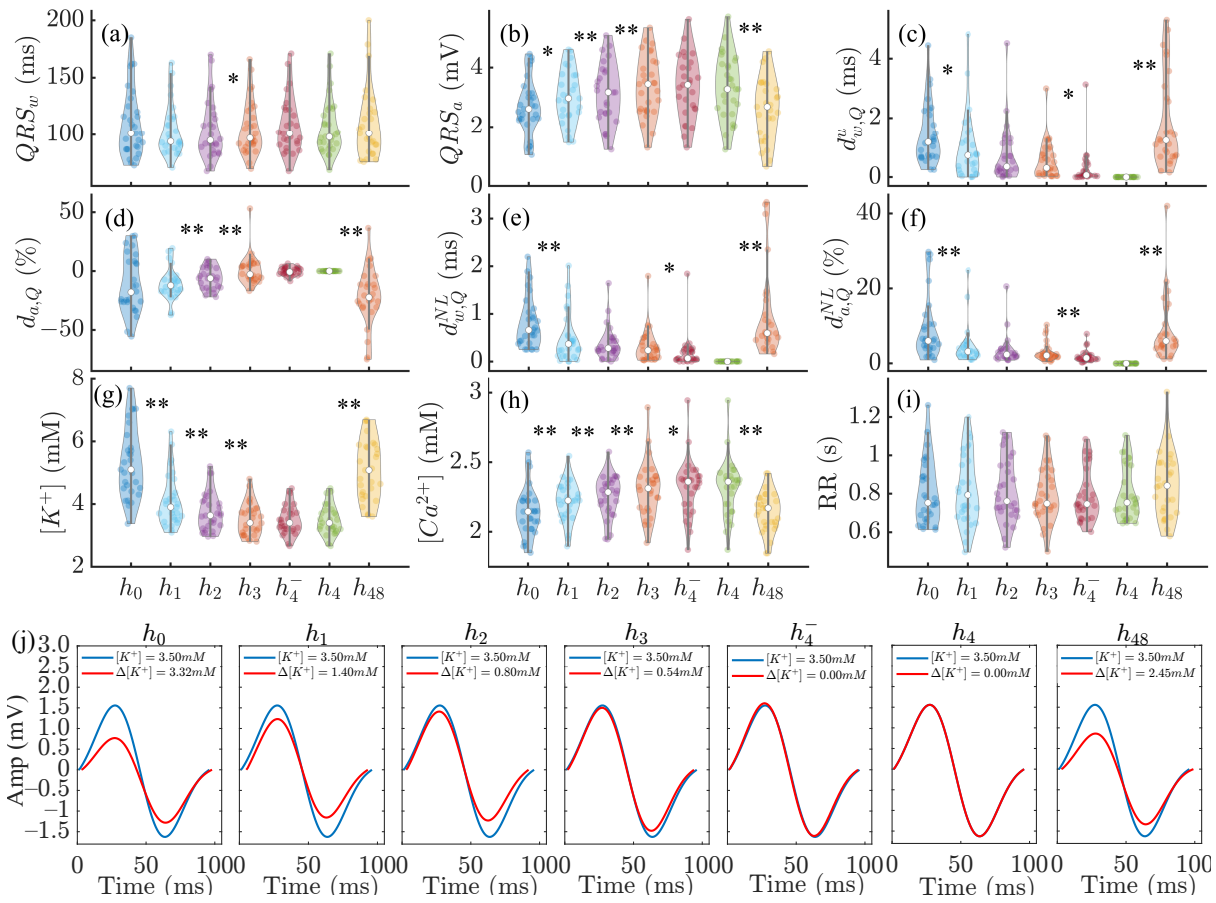

Figure 5.3: Panels (**a**–**f**): changes in QRS_{w}, QRS_{a}, $d^{\mathrm{u}}_{\mathrm{w,Q}}$, $d_{\mathrm{a,Q}}$, $d^{\mathrm{NL}}_{\mathrm{w,Q}}$ and $d^{\mathrm{NL}}_{\mathrm{a,Q}}$ during HD stages. Panels (**g**–**i**): corresponding variations in [K$^+$], [Ca^{2+}] and RR. In panels (**a**–**i**), * denotes $p < 0.05$ and ** denotes $p < 0.01$. In each panel, the central white dot indicates the median. Each dot corresponds to an individual patient. Panel (**j**): MWQRS (red) of a patient at different HD stages and reference MWQRS (blue). Δ denotes the change in [K$^+$] with respect to the end of HD (h_4).

Table 5.1: p-values from the parametric test (t-test) to evaluate statistical significance of non-zero mean Fisher z-transformed Pearson correlation coefficients between QRS markers and [K$^+$], [Ca^{2+}] and RR.

***p*-Values**	$\boldsymbol{QRS_{\mathrm{w}}}$	$\boldsymbol{QRS_{\mathrm{a}}}$	$\boldsymbol{d^{\mathrm{u}}_{\mathrm{w,Q}}}$	$\boldsymbol{d_{\mathrm{a,Q}}}$	$\boldsymbol{d^{\mathrm{NL}}_{\mathrm{w,Q}}}$	$\boldsymbol{d^{\mathrm{NL}}_{\mathrm{a,Q}}}$	$\boldsymbol{\Delta I_{\mathrm{US}}}$	$\boldsymbol{\Delta I_{\mathrm{DS}}}$
[K$^+$]	0.01	< 0.01	< 0.01	< 0.01	< 0.01	< 0.01	< 0.01	< 0.01
[Ca^{2+}]	0.09	< 0.01	< 0.01	0.02	< 0.01	< 0.01	< 0.01	< 0.01
RR	0.37	0.94	0.48	0.12	0.23	0.60	0.88	0.43

significant association with RR.

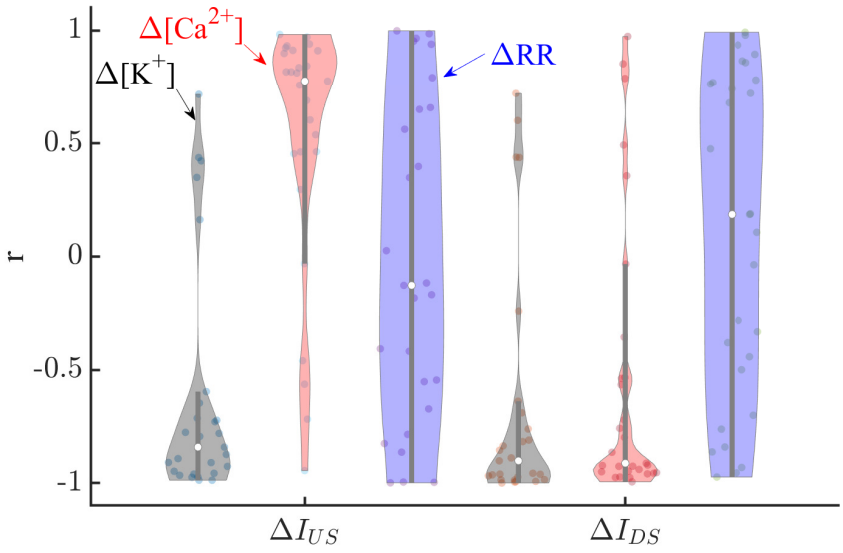

Figure 5.4: Pearson correlation coefficients between QRS slope markers (ΔI_{US} and ΔI_{DS}) and $\Delta[\mathrm{K}^+]$ (black), $\Delta[\mathrm{Ca}^{2+}]$ (red) and $\Delta\mathrm{RR}$ (blue) for all patients. The central white dot indicates the median. Each dot corresponds to an individual patient.

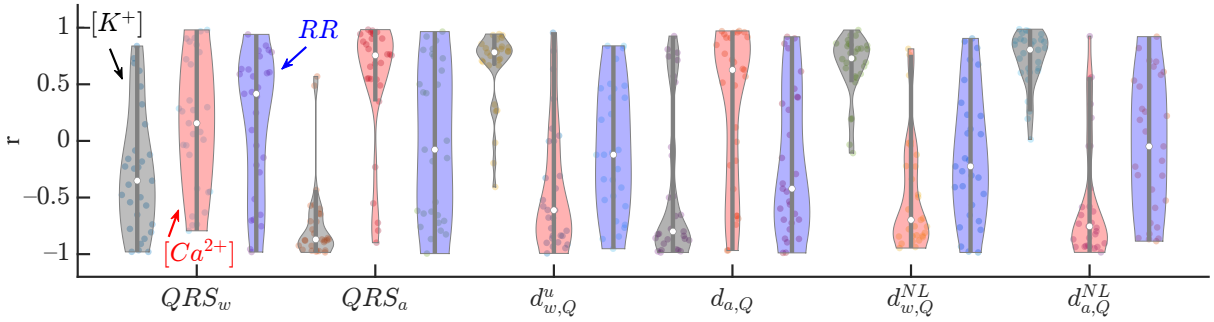

Figure 5.5: Pearson correlation coefficients between QRS markers (QRS_{w}, QRS_{a}, $d^{\mathrm{u}}_{\mathrm{w,Q}}$, $d_{\mathrm{a,Q}}$, $d^{\mathrm{NL}}_{\mathrm{w,Q}}$ and $d^{\mathrm{NL}}_{\mathrm{a,Q}}$) and $[\mathrm{K}^+]$ (black), $[\mathrm{Ca}^{2+}]$ (red) and RR (blue) for all patients at all HD points. The central white dot indicates the median. Each dot corresponds to an individual patient.

5.4.3 Uni- and multivariable estimation of $[\mathrm{K}^+]$ and $[\mathrm{Ca}^{2+}]$

Figure 5.6 shows an illustrative example of the comparison between measured and estimated $[\mathrm{K}^+]$ and $[\mathrm{Ca}^{2+}]$ using stage-specific (S), patient-specific (P) and global (G) approaches during (h_0, h_1, h_2, h_3, h_4^-) and after (h_{48}) HD for a particular patient, for both univariable (panels a–b) and multivariable (panel c) estimators. The patient-specific approach provided better results in terms of reduced errors, particularly using multivariable estimation (mean e_v over HD points being 0.071 (S), −0.008 (P), 0.001 (G) for $[\mathrm{K}^+]$ and 0.019 (S), 0.001 (P), 0.031 (G) for $[\mathrm{Ca}^{2+}]$).

Figure 5.7 shows the relative errors, e_v, for all patients and HD stages in the estimation of $[\mathrm{K}^+]$ and $[\mathrm{Ca}^{2+}]$ using stage-specific (top panel), patient-specific (middle panel) and global (bottom panel) approaches.

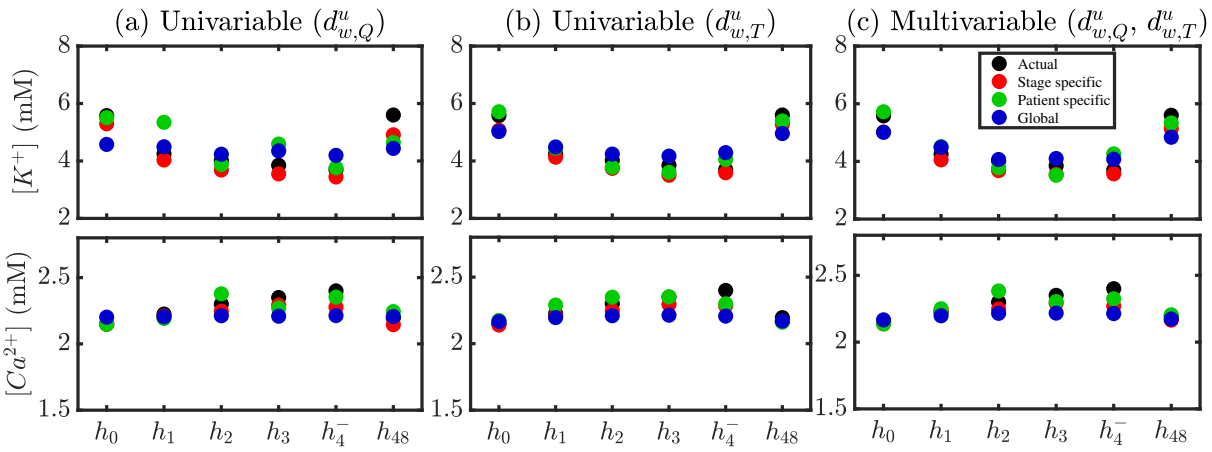

Figure 5.6: Actual (black) and estimated [K^+] and [Ca^{2+}] for a patient using stage-specific (red), patient-specific (green) and global (blue) approaches. Univariable $d^{u}_{w,Q}$-based estimation is shown in panel a, $d^{u}_{w,T}$-based in panel b and multivariable $d^{u}_{w,Q}$-$d^{u}_{w,T}$-based in panel c.

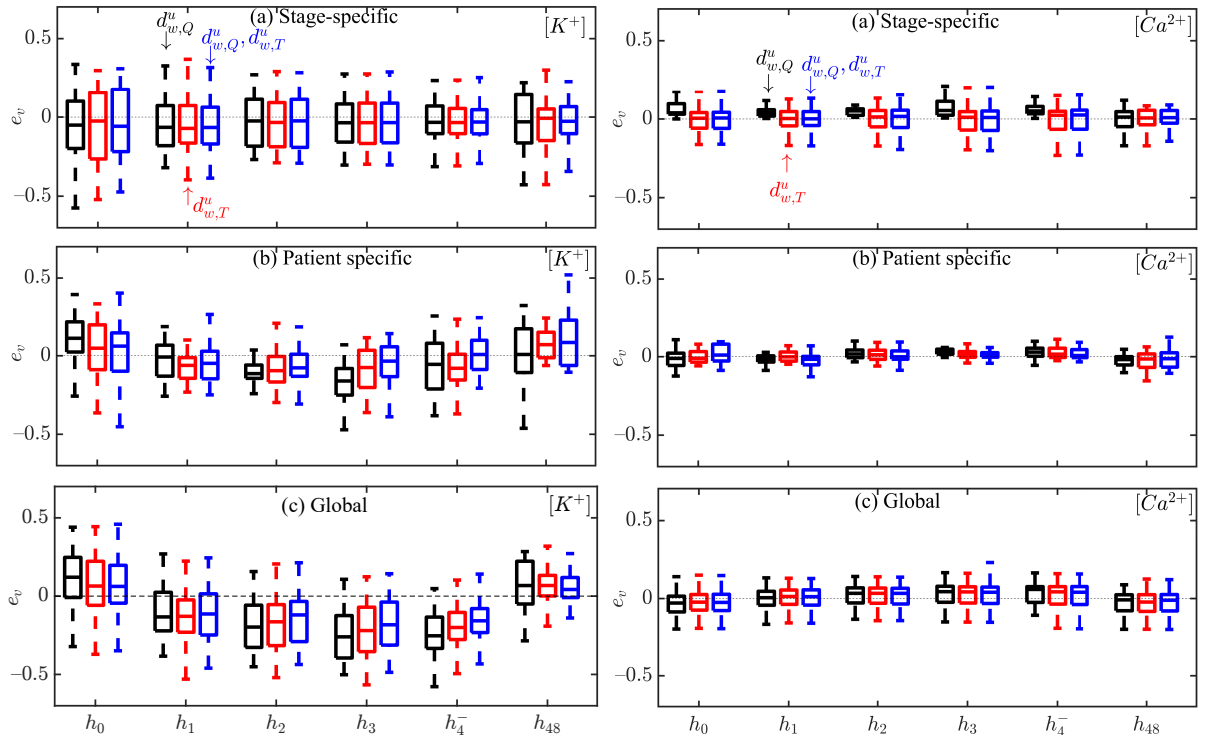

Figure 5.7: Box plots of [K^+] and [Ca^{2+}] estimation errors e_v during HD stages for all patients using $d^{u}_{w,Q}$(black), $d^{u}_{w,T}$(red) and the combination of $d^{u}_{w,Q}$ and $d^{u}_{w,T}$ (blue) for stage-specific (**top**), patient-specific (**middle**) and global (**bottom**) approaches. The central line indicates the median, whereas top and bottom edges show the 25th and 75th percentiles.

Table 5.2 shows actual and estimated [K^+] and [Ca^{2+}] values over the study population at each HD stage. Multivariable estimation results using stage-specific, patient-specific and global approaches are presented.

Tables 5.3 and 5.4 show the median and IQR values of intra-patient Pearson correla-

Table 5.2: Actual and estimated $[K^+]$ and $[Ca^{2+}]$ values over the study population at each HD stage using multivariable (m) estimation and stage-specific (S), patient-specific (P) and global (G) approaches. Values are expressed as median (IQR) and the units are mM.

	$\boldsymbol{h_0}$	$\boldsymbol{h_1}$	$\boldsymbol{h_2}$	$\boldsymbol{h_3}$	$\boldsymbol{h_4^-}$	$\boldsymbol{h_{48}}$
$[K^+]$	5.10 (1.30)	3.90 (0.86)	3.64 (0.81)	3.40 (0.71)	3.40 (0.56)	5.08 (1.53)
$[\hat{K}^+]_m^S$	5.31 (0.43)	4.03 (0.18)	3.70 (0.08)	3.49 (0.09)	3.43 (0.05)	4.56 (1.21)
$[\hat{K}^+]_m^P$	4.76 (1.90)	4.01 (1.33)	3.84 (1.16)	3.46 (0.97)	3.28 (0.44)	4.43 (1.46)
$[\hat{K}^+]_m^G$	4.50 (0.71)	4.33 (0.40)	4.07 (0.33)	3.97 (0.26)	3.84 (0.19)	4.57 (0.75)
$[Ca^{2+}]$	2.15 (0.20)	2.23 (0.20)	2.29 (0.19)	2.31 (0.23)	2.36 (0.21)	2.17 (0.20)
$[\hat{Ca}^{2+}]_m^S$	2.13 (0.02)	2.21 (0.05)	2.25 (0.02)	2.31 (0.05)	2.28 (0.03)	2.07 (0.13)
$[\hat{Ca}^{2+}]_m^P$	2.06 (0.29)	2.27 (0.23)	2.21 (0.26)	2.29 (0.20)	2.25 (0.23)	2.18 (0.20)
$[\hat{Ca}^{2+}]_m^G$	2.19 (0.04)	2.20 (0.02)	2.22 (0.02)	2.23 (0.01)	2.23 (0.01)	2.19 (0.04)

Table 5.3: Intra-patient Pearson correlation coefficient r between actual and estimated $[K^+]$ using univariable and multivariable estimators, with stage-specific (S), patient-specific (P) and global (G) approaches. Values are expressed as median (IQR).

$\boldsymbol{r_{[K^+],[\hat{K}^+]}}$	$\boldsymbol{d^u_{w,Q}}$	$\boldsymbol{d^u_{w,T}}$	$\boldsymbol{d^u_{w,Q}}$, $\boldsymbol{d^u_{w,T}}$
S	0.98 (0.08)	0.96 (0.06)	0.93 (0.30)
P	0.56 (0.75)	0.55 (0.90)	0.75 (0.51)
G	0.75 (0.15)	0.82 (0.35)	0.86 (0.32)

tion coefficients between actual and estimated $[K^+]$ ($[Ca^{2+}]$, respectively) using univariable and multivariable estimators.

Tables 5.5 and 5.6 show a comparison between estimation errors obtained for the

Table 5.4: Intra-patient Pearson correlation coefficient r between actual and estimated $[Ca^{2+}]$ using univariable and multivariable estimators, with stage-specific (S), patient-specific (P) and global (G) approaches. Values are expressed as median (IQR).

$\boldsymbol{r_{[Ca^{2+}],[\hat{Ca}^{2+}]}}$	$\boldsymbol{d^u_{w,Q}}$	$\boldsymbol{d^u_{w,T}}$	$\boldsymbol{d^u_{w,Q}}$, $\boldsymbol{d^u_{w,T}}$
S	0.88 (0.38)	0.88 (0.22)	0.80 (0.78)
P	0.88 (0.22)	0.63 (0.59)	0.63 (0.37)
G	0.64 (0.73)	0.64 (0.49)	0.70 (0.55)

Table 5.5: Estimation errors (e) using stage-specific (S), patient-specific (P) and global (G) approach based [K^+] estimators, from all patients at all HD time points.

e	S	P	G
$d^{\mathrm{u}}_{\mathrm{w,Q}}$	-0.041 ± 0.831	-0.091 ± 1.419	-0.204 ± 0.971
$d^{\mathrm{u}}_{\mathrm{w,T}}$	0.004 ± 0.806	-0.147 ± 0.809	-0.169 ± 0.959
$T_{\mathrm{S/A}}$	0.005 ± 0.792	-0.157 ± 1.120	-0.213 ± 0.996
$T_{\mathrm{S}/\sqrt{A}}$	0.003 ± 0.811	-0.149 ± 1.422	-0.238 ± 1.048
$d^{\mathrm{u}}_{\mathrm{w,Q}}$ & $d^{\mathrm{u}}_{\mathrm{w,T}}$	0.073 ± 0.808	-0.035 ± 1.113	-0.144 ± 0.883

*Values are expressed as mean ± standard deviation and the units are mM

Table 5.6: Estimation errors (e) using stage-specific (S), patient-specific (P) and global (G) approach based [Ca^{2+}] estimators, from all patients at all HD time points.

e	S	P	G
$d^{\mathrm{u}}_{\mathrm{w,Q}}$	0.117 ± 0.134	-0.007 ± 0.300	0.018 ± 0.175
$d^{\mathrm{u}}_{\mathrm{w,T}}$	0.0003 ± 0.170	0.024 ± 0.178	0.018 ± 0.172
$T_{\mathrm{S/A}}$	-0.002 ± 0.179	0.025 ± 0.191	0.023 ± 0.180
$T_{\mathrm{S}/\sqrt{A}}$	-0.002 ± 0.183	0.027 ± 0.201	0.020 ± 0.183
$d^{\mathrm{u}}_{\mathrm{w,Q}}$&$d^{\mathrm{u}}_{\mathrm{w,T}}$	0.023 ± 0.180	0.010 ± 0.125	0.016 ± 0.174

*Values are expressed as mean ± standard deviation and the units are mM

markers analyzed in this study and in previous studies. Tables 5.7–5.10 show mean absolute and root mean square errors for the analyzed markers.

Bland–Altman plots in Figures 5.8–5.13 show the difference vs the mean of actual and estimated [K^+] and [Ca^{2+}] for $d^{\mathrm{u}}_{\mathrm{w,Q}}$, $d^{\mathrm{u}}_{\mathrm{w,T}}$ and their combination using stage-specific,

Table 5.7: Mean absolute errors (MAE) using stage-specific (S), patient-specific (P) and global (G) approach-based [K^+] estimators, from all patients at all HD time points. Values are expressed as mean absolute error and the units are mM.

MAE	S	P	G
$d^{\mathrm{u}}_{\mathrm{w,Q}}$	0.649	0.910	0.821
$d^{\mathrm{u}}_{\mathrm{w,T}}$	0.631	0.579	0.763
$T_{\mathrm{S/A}}$	0.607	0.770	0.819
$T_{\mathrm{S}/\sqrt{A}}$	0.643	0.899	0.895
$d^{\mathrm{u}}_{\mathrm{w,Q}}$ & $d^{\mathrm{u}}_{\mathrm{w,T}}$	0.539	0.721	0.687

Table 5.8: Mean absolute errors (MAE) using stage-specific (S), patient-specific (P) and global (G) approach-based [Ca^{2+}] estimators, from all patients at all HD time points. Values are expressed as mean absolute error and the units are mM.

MAE	S	P	G
$d^{\mathrm{u}}_{\mathrm{w,Q}}$	0.138	0.127	0.141
$d^{\mathrm{u}}_{\mathrm{w,T}}$	0.133	0.098	0.138
$T_{\mathrm{S/A}}$	0.135	0.115	0.141
$T_{\mathrm{S}/\sqrt{A}}$	0.139	0.130	0.142
$d^{\mathrm{u}}_{\mathrm{w,Q}}$ & $d^{\mathrm{u}}_{\mathrm{w,T}}$	0.124	0.094	0.139

Table 5.9: Root mean square errors ($RMSE$) using stage-specific (S), patient-specific (P) and global (G) approach-based [K^{+}] estimators, from all patients at all HD time points. Values are expressed as root mean square error and the units are mM

$RMSE$	S	P	G
$d^{\mathrm{u}}_{\mathrm{w,Q}}$	0.723	1.363	0.961
$d^{\mathrm{u}}_{\mathrm{w,T}}$	0.783	0.794	0.946
$T_{\mathrm{S/A}}$	0.776	1.108	0.997
$T_{\mathrm{S}/\sqrt{A}}$	0.794	1.400	1.053
$d^{\mathrm{u}}_{\mathrm{w,Q}}$ & $d^{\mathrm{u}}_{\mathrm{w,T}}$	0.771	1.010	0.853

Table 5.10: Root mean square errors ($RMSE$) using stage-specific (S), patient-specific (P) and global (G) approach-based [Ca^{2+}] estimators, from all patients at all HD time points. Values are expressed as root mean square error and the units are mM.

$RMSE$	S	P	G
$d^{\mathrm{u}}_{\mathrm{w,Q}}$	0.173	0.283	0.171
$d^{\mathrm{u}}_{\mathrm{w,T}}$	0.164	0.172	0.167
$T_{\mathrm{S/A}}$	0.175	0.189	0.178
$T_{\mathrm{S}/\sqrt{A}}$	0.180	0.199	0.180
$d^{\mathrm{u}}_{\mathrm{w,Q}}$ & $d^{\mathrm{u}}_{\mathrm{w,T}}$	0.172	0.116	0.166

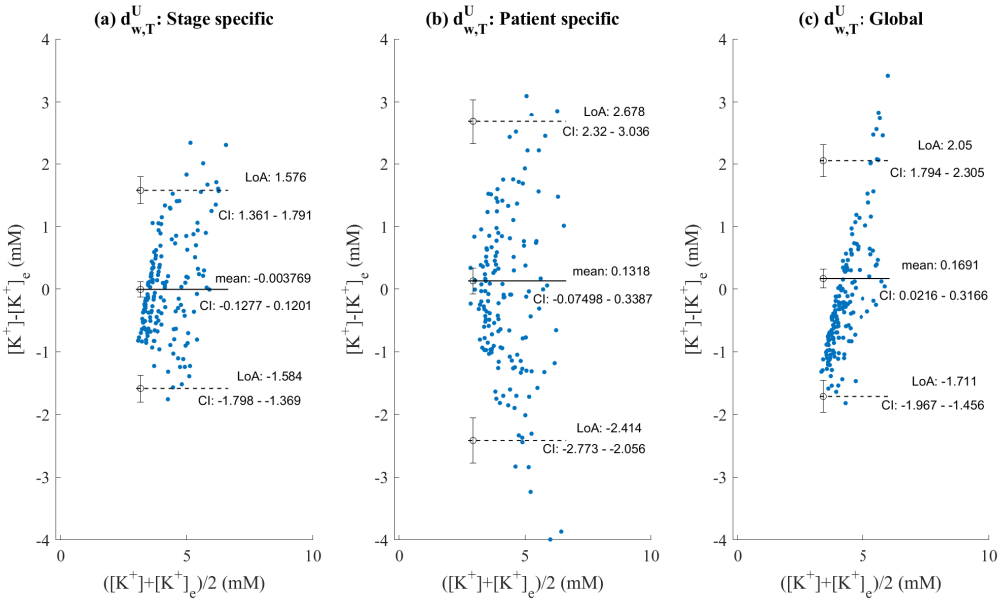

Figure 5.8: Left Panel: Bland-Altman plot between actual and estimated $[K^+]$ for $d^{u}_{w,T}$ using stage-specific approach. Middle Panel: Bland-Altman plot using patient-specific approach. Right Panel: Bland-Altman plot using global approach.

patient-specific and global approaches. In addition to that, Bland-Altman plots in Figures 5.14-5.17 show the difference vs the mean of actual and estimated $[K^+]$ and $[Ca^{2+}]$ for previously proposed T wave markers from other authors $T_{S/A}$ [9,31], and $T_{S/\sqrt{A}}$ [32], using stage-specific, patient-specific and global approach. Multivariable estimators combining information from $d^{u}_{w,Q}$ and $d^{u}_{w,T}$ outperformed univariable estimators (the ones proposed by us and other authors).

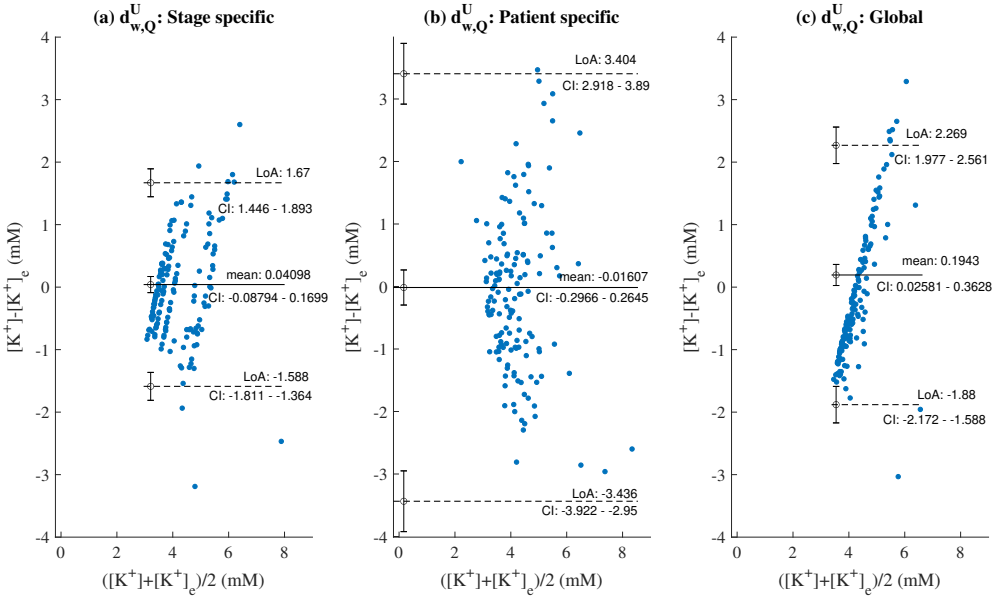

Figure 5.9: Left Panel: Bland-Altman plot between actual and estimated $[K^+]$ for $d^u_{w,Q}$ using stage-specific approach. Middle Panel: Bland-Altman plot using patient-specific approach. Right Panel: Bland-Altman plot using global approach.

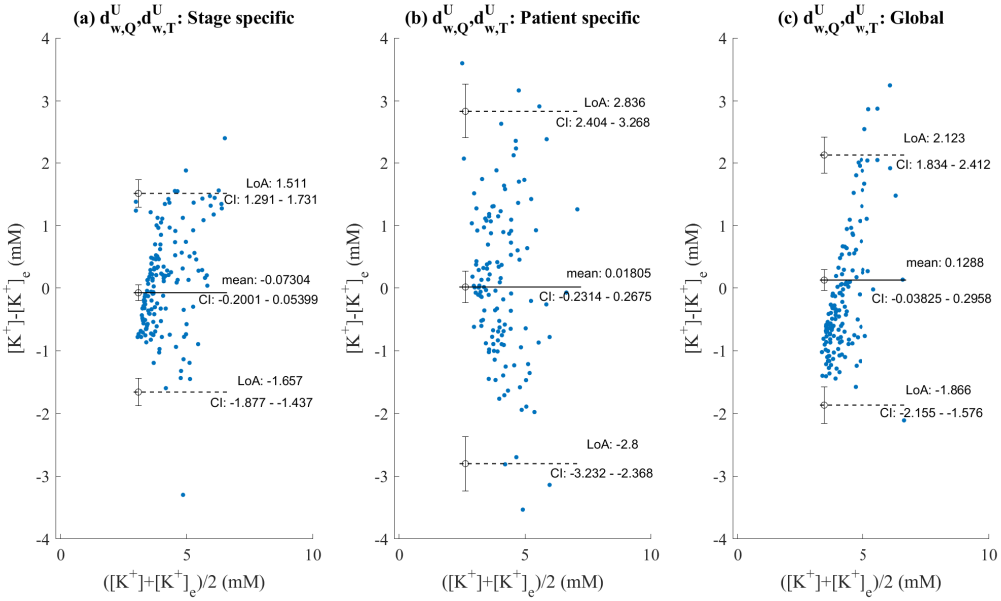

Figure 5.10: Left Panel: Bland-Altman plot between actual and estimated $[K^+]$ for the combined $d^u_{w,Q}$ and $d^u_{w,T}$ using stage-specific approach. Middle Panel: Bland-Altman plot using patient-specific approach. Right Panel: Bland-Altman plot using global approach.

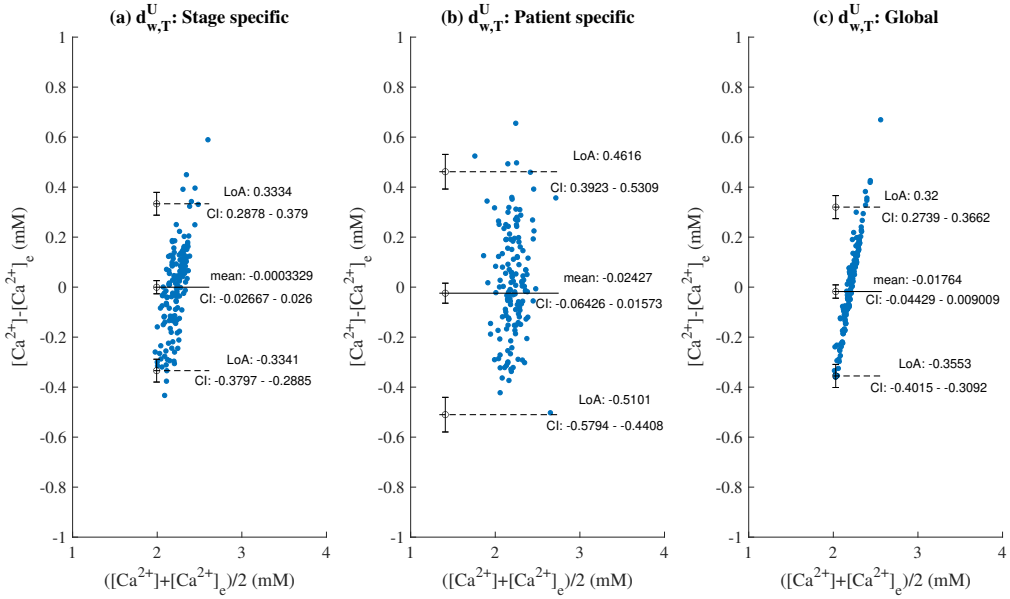

Figure 5.11: Left Panel: Bland-Altman plot between actual and estimated $[Ca^{2+}]$ for $d^{u}_{w,T}$ using stage-specific approach. Middle Panel: Bland-Altman plot using patient-specific approach. Right Panel: Bland-Altman plot using global approach.

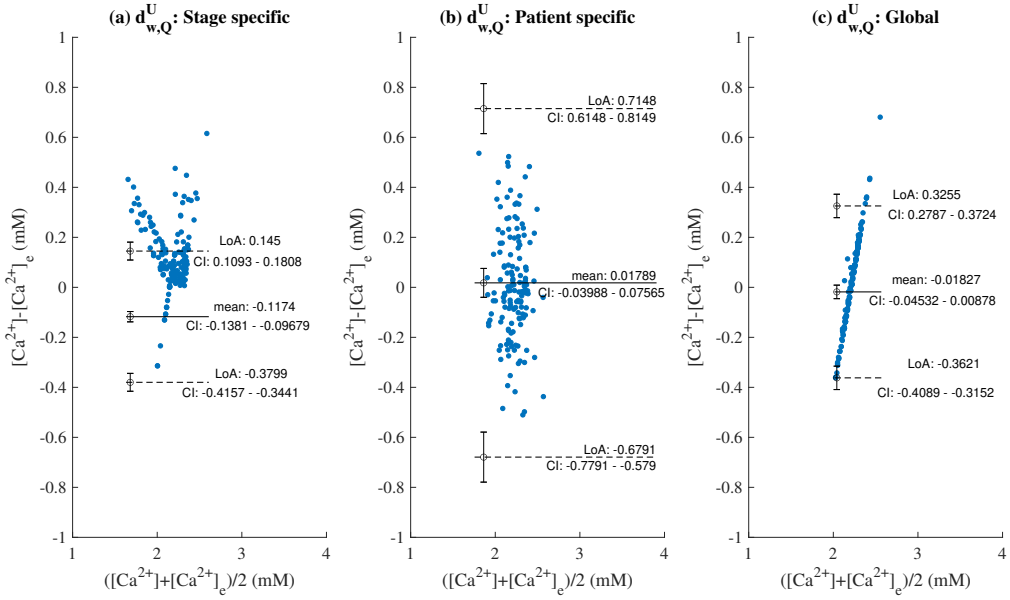

Figure 5.12: Left Panel: Bland-Altman plot between actual and estimated $[Ca^{2+}]$ for $d^{u}_{w,Q}$ using stage-specific approach. Middle Panel: Bland-Altman plot using patient-specific approach. Right Panel: Bland-Altman plot using global approach.

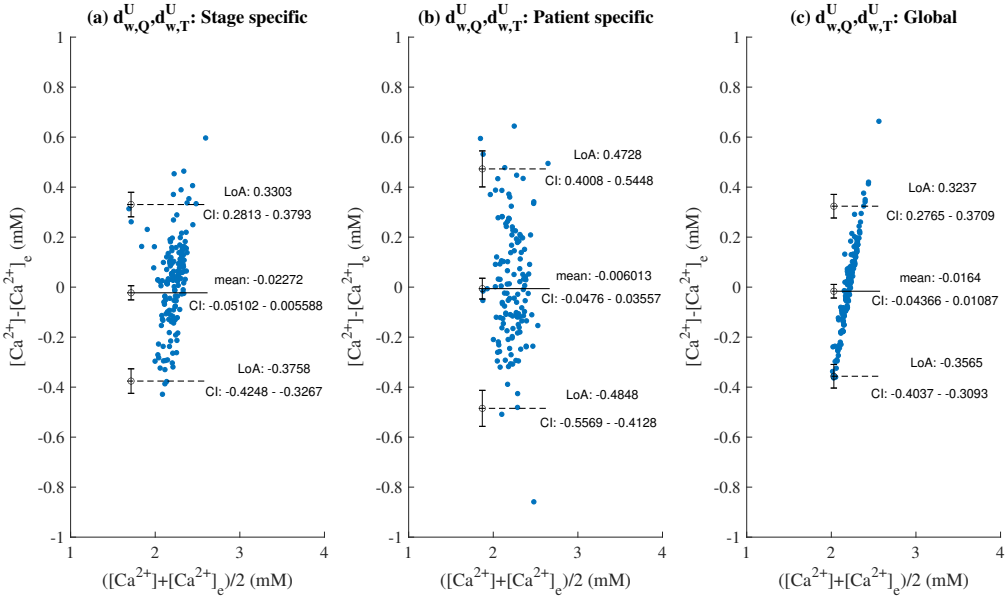

Figure 5.13: Left Panel: Bland-Altman plot between actual and estimated $[Ca^{2+}]$ for the combined $d^u_{w,Q}$ and $d^u_{w,T}$ using stage-specific approach. Middle Panel: Bland-Altman plot using patient-specific approach. Right Panel: Bland-Altman plot using global approach.

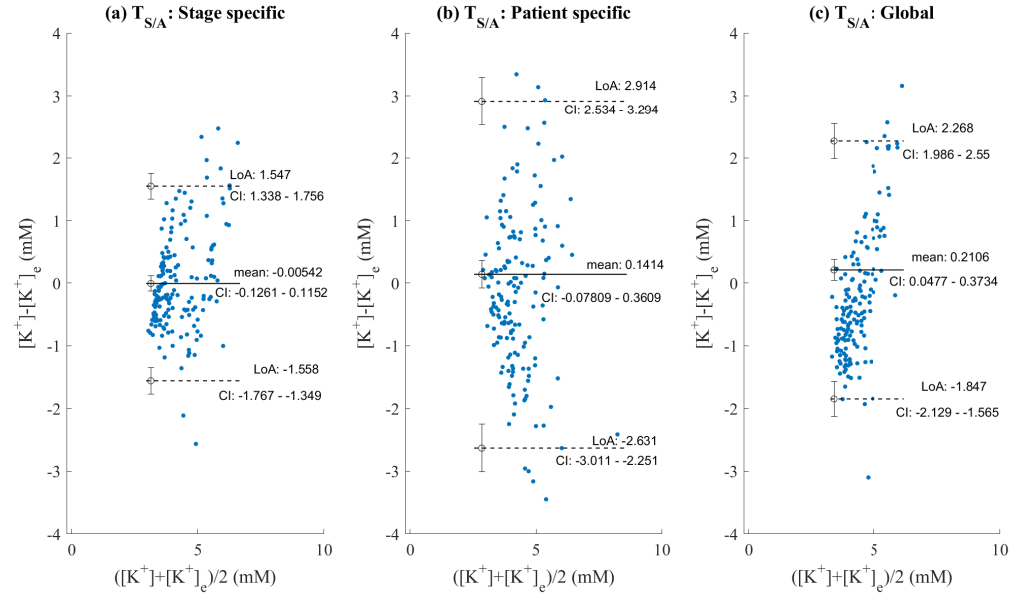

Figure 5.14: Left Panel: Bland-Altman plot between actual and estimated $[K^+]$ for $T_{S/A}$ using stage-specific approach. Middle Panel: Bland-Altman plot using patient-specific approach. Right Panel: Bland-Altman plot using global approach.

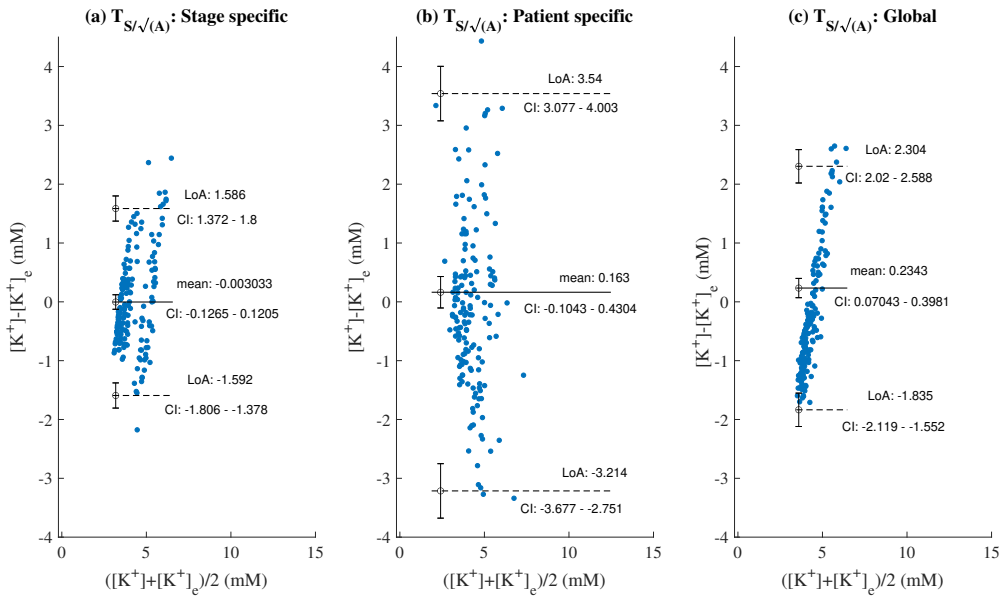

Figure 5.15: Left Panel: Bland-Altman plot between actual and estimated $[K^+]$ for $T_{S/\sqrt{A}}$ using stage-specific approach. Middle Panel: Bland-Altman plot using patient-specific approach. Right Panel: Bland-Altman plot using global approach.

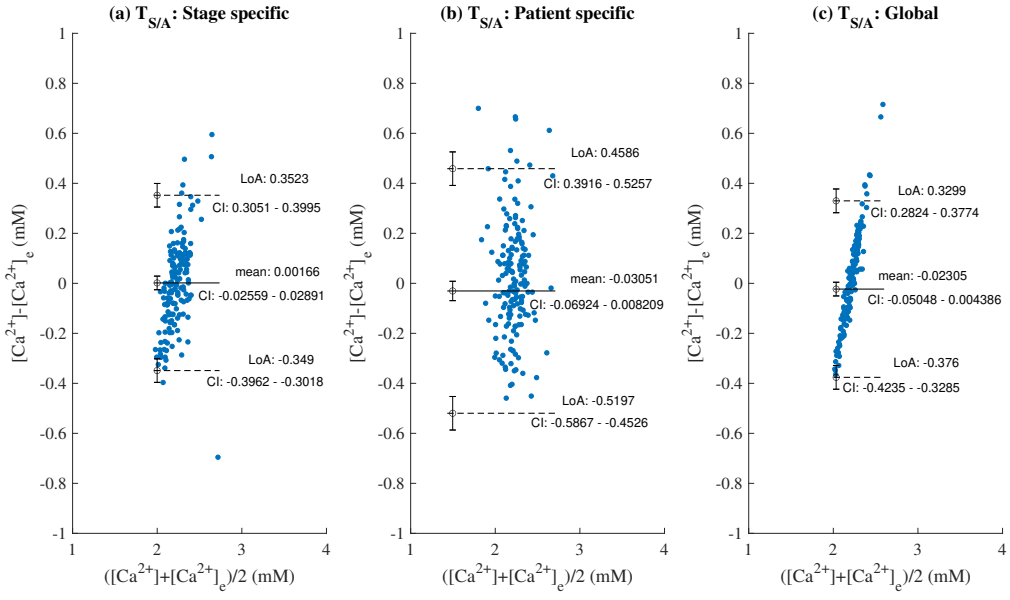

Figure 5.16: Left Panel: Bland-Altman plot between actual and estimated $[Ca^{2+}]$ for $T_{S/A}$ using stage-specific approach. Middle Panel: Bland-Altman plot using patient-specific approach. Right Panel: Bland-Altman plot using global approach.

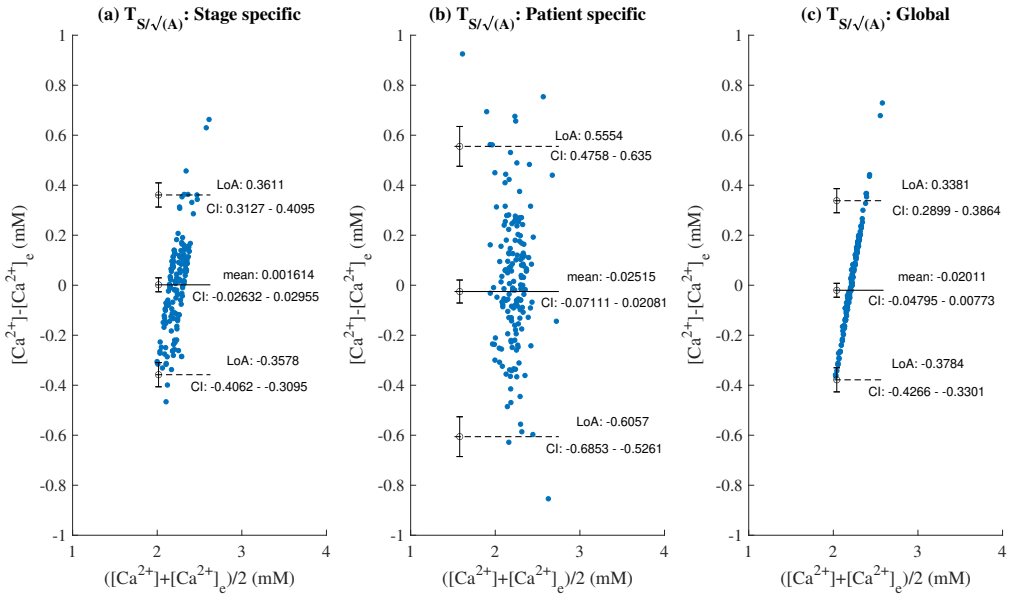

Figure 5.17: Left Panel: Bland-Altman plot between actual and estimated $[Ca^{2+}]$ for $T_{S/\sqrt{A}}$ using stage-specific approach. Middle Panel: Bland-Altman plot using patient-specific approach. Right Panel: Bland-Altman plot using global approach.

5.5 Discussion

In this chapter, we investigated changes in QRS duration, amplitude and morphology at varying $[K^+]$, $[Ca^{2+}]$ and HR in ESRD patients. We designed $[K^+]$ and $[Ca^{2+}]$ estimators based on our proposed QRS morphological characteristics, taken both individually and in combination with T wave morphology markers. We showed the accuracy of our proposed estimators using three different approaches: stage-specific, patient-specific and global estimation, which outperformed previously proposed methods. Our results offer new non-invasive tools to monitor serum $[K^+]$ and $[Ca^{2+}]$, which could have a significant role in clinical practice and could contribute to reduce the mortality risk associated with abnormal electrolyte levels in ESRD patients.

5.5.1 Characterization of QRS complex slope, amplitude, duration and morphology in ESRD patients during and after HD

In ECG recordings of ESRD patients, we evaluated QRS slopes, duration and amplitude, measured by markers I_{US}, I_{DS}, QRS_{w} and QRS_{a}, and QRS morphological characteristics, measured by markers $d^{\mathrm{u}}_{\mathrm{w,Q}}$, $d_{\mathrm{a,Q}}$, $d^{\mathrm{NL}}_{\mathrm{w,Q}}$ and $d^{\mathrm{NL}}_{\mathrm{a,Q}}$, which was proposed here for the first time. All markers except for QRS_{w} presented significant changes during and after HD. These changes were strongly associated with variations in $[K^+]$ and $[Ca^{2+}]$ but not in HR. The inconsistent relationship between QRS markers, such as QRS_{w}, and HR has been investigated in previous works, including the study by Hnatkova et al. [141], who reported increases in QRS duration with increasing HR in 35% of their patients and decreases in QRS duration in the remaining 65%. In line with these results, we found that QRS became markedly wider at higher RR intervals for 34% of the patients; it became markedly narrower for 21% of the patients; its width moderately changed with RR for 21% of the patients; and it showed poor association with RR for the remaining 24% of the patients (see Table 5.11 as following). This led to a median r value of 0.42 between QRS_{w} and RR over the 29 ESRD patients, reflecting a notably weaker relationship between QRS_{w} and RR as compared to other depolarization markers.

Regarding QRS amplitude, even if we found QRS_{a} to remarkably change during HD, this marker depended on ECG amplitudes at specific time points, which, in noisy ambu-

Table 5.11: Pearson correlation coefficient (r) between QRS complex width and RR interval in 29 ESRD patients. Values are expressed as median (interquartile range) over patients.

QRS_{w}	P1–10	P11–16	P17–P22	P23–P29	P1–P29 (overall)
r	0.77 (0.17)	−0.73 (0.21)	0.45 (0.13)	−0.04 (0.35)	0.42 (0.91)

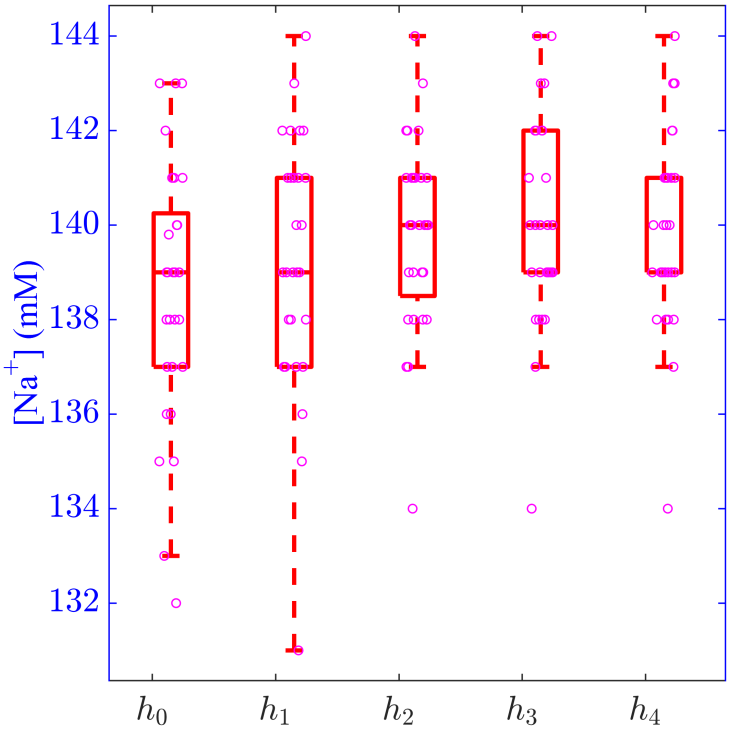

Figure 5.18: Changes in sodium levels ($[Na^+]$) along HD stages

latory recordings, could lead to large changes not associated with variations in electrolyte levels. On the other hand, changes in QRS slopes and warping-based markers accounted for deviations in the whole QRS waveform and could thus be better suited for ambulatory monitoring. In particular, if QRS duration on top of amplitude changes occurred in the inter-dialytic interval, as, e.g., reported during advanced ischemia [39, 40], these changes could be reflected in our proposed QRS warping markers.

On top of investigating the relationship between QRS markers and $[K^+]$ or $[Ca^{2+}]$, we also investigated the relationship between these markers and sodium concentration ($[Na^+]$). $[Na^+]$ variations were less remarkable than those of $[K^+]$ and $[Ca^{2+}]$ during HD in our patients (see Figure 5.18 and Table 5.12 as shown below). Importantly, none of the markers were strongly associated with $[Na^+]$ (see Table 5.13 as shown below). $[Na^+]$ could have been expected to play a more important role in modulating depolarization markers because the fast sodium current was primarily responsible for phase 0 of the action potential and its changes might have manifested in QRS complex alterations. However, we found that the QRS complex became markedly wider at higher $[Na^+]$ for 43% of the patients; it became markedly narrower for 7% of the patients; its width moderately changed with $[Na^+]$ for 14% of the patients; and it showed poor association with $[Na^+]$ for the remaining 36% of the patients (see Table 5.14 as shown below).

High inter-individual variability was found in the relationship between the analyzed QRS markers and $[K^+]$ or $[Ca^{2+}]$. This was especially remarkable in the case of $d_{a,Q}$, which presented high IQR in the intra-patient correlation coefficients with $[K^+]$ and $[Ca^{2+}]$. Such high dispersion could be explained by QRS polarity effects, as a reduction

Table 5.12: P-values from the Wilcoxon signed-rank test to assess differences in $[Na^+]$ between consecutive time stages.

p-value	h_0–h_1	h_1–h_2	h_2–h_3	h_3–h_4
$[Na^+]$	0.17	0.06	0.39	0.16

Table 5.13: Pearson (r) and Spearman (ρ) correlation coefficients between QRS complex markers and $[Na^+]$ in 29 ESRD patients along HD. Values are expressed as median (interquartile range) over patients.

	QRS_{w}	QRS_{a}	$d^{\mathrm{u}}_{\mathrm{w,Q}}$	$d_{\mathrm{a,Q}}$	$d^{\mathrm{NL}}_{\mathrm{w,Q}}$	$d^{\mathrm{NL}}_{\mathrm{a,Q}}$
r	0.24 (1.01)	0.30 (0.97)	−0.31 (1.00)	−0.37 (1.18)	−0.33 (1.05)	−0.18 (1.13)
ρ	0.23 (0.84)	0.24 (0.99)	0.00 (0.98)	−0.29 (0.90)	−0.10 (0.96)	−0.11 (0.95)

(increase, respectively) in the absolute amplitude could be reflected as either positive or negative $d_{\mathrm{a,Q}}$, depending on QRS being predominantly positive or negative.

Changes in ECG characteristics induced by variations in $[K^+]$ and $[Ca^{2+}]$ have been extensively investigated in terms of ventricular repolarization. A number of studies have characterized changes in T wave width, amplitude, slope or slope-to-amplitude ratio [7–9, 31, 113]. We have recently quantified changes in T wave nonlinear dynamics and morphology and have shown their relationship with $[K^+]$ and $[Ca^{2+}]$ variations [29, 129, 134, 140, 142].

The analysis of electrolyte-induced alterations in ventricular depolarization remains, however, much more limited. In a study including 923 patients with severe hyperkalemia, sine wave-shaped QRS complexes were observed in almost 36.7% of patients [60]. In the present study, we could observe such behavior in most of the patients (Figure 5.3). Inconsistent results have been reported in relation to the effects of $[K^+]$ on QRS duration, with a larger proportion of studies reporting QRS widening [23, 37, 143–147] and others reporting QRS narrowing [6, 38] with increased $[K^+]$. Here, we observed no significant changes in QRS width during and after HD. Regarding QRS amplitude, we found QRS_{a} to be strongly negatively correlated with $[K^+]$ and positively correlated with $[Ca^{2+}]$, in accordance with the increase in QRS_{a} with decreasing $[K^+]$, as described by Astan et al. [38]. We observed similar results for the QRS morphology-based amplitude marker $d_{\mathrm{a,Q}}$. Our study characterized additional QRS morphological changes by the warping markers

Table 5.14: Pearson correlation coefficient (r) between QRS complex width and $[Na^+]$ in 29 ESRD patients. Values are expressed as median (interquartile range) over patients.

QRS_{w}	P1–12	P13–14	P15–P18	P19–P29	P1–P29 (overall)
r	0.88 (0.13)	−0.72 (0.05)	−0.40 (0.23)	−0.05 (0.22)	0.24 (1.01)

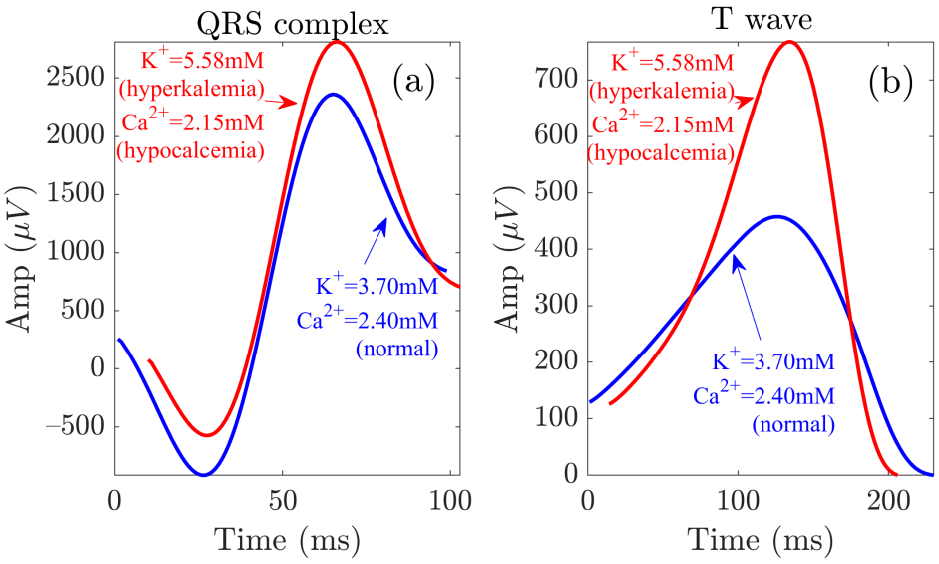

Figure 5.19: QRS and T wave variations at the start (red) and end (blue) of the HD session. Panels (**a**,**b**) show the waveforms related to the QRS complex and the T wave, respectively.

$d^{u}_{w,Q}$, $d^{NL}_{w,Q}$ and $d^{NL}_{a,Q}$ further extended these results to provide a robust characterization of QRS changes during and after HD in ESRD patients. Figure 5.19 illustrates QRS complexes and T waves at the start and end of HD.

5.5.2 Multivariable predictors of $[K^+]$ and $[Ca^{2+}]$ based on depolarization and repolarization characteristics

Based on the novel QRS morphology markers of this study and on already proposed T wave markers [29, 89, 93], we designed linear univariable and multivariable $[K^+]$ and $[Ca^{2+}]$ estimators. In particular, we used $d^{u}_{w,Q}$ (QRS marker) and $d^{u}_{w,T}$ (T wave marker), as these were strongly correlated with $[K^+]$ and $[Ca^{2+}]$ and poorly related to each other, thus potentially providing complementary information to monitor electrolyte variations.

For each of the constructed $[K^+]$ and $[Ca^{2+}]$ linear estimators, we used stage-specific, patient-specific and global estimation approaches. Overall, the stage-specific approach rendered results with both mean and median estimation errors very close to zero but with higher dispersion than in the patient-specific approach. The latter approach would be suitable for clinical application, as electrolyte levels could be predicted in each patient based on a short ECG recording of the same patient.

Multivariable estimators combining information from $d^{u}_{w,Q}$ and $d^{u}_{w,T}$ outperformed univariable estimators (the ones proposed by us and other authors [9,31,32]). The estimation errors for the multivariable estimators were lower (Figure 5.7, Figures 5.8–5.17, Tables 5.5 and 5.6) and the correlation coefficients r between actual and estimated electrolyte levels were higher than for univariable estimators, both for the patient-specific and global

estimation approaches (see Tables 5.3 and 5.4). In particular, for the patient-specific approach, median r in $[K^+]$ estimation was 0.75 for the combination of $d^{u}_{w,Q}$ and $d^{u}_{w,T}$, while it was 0.56 for $d^{u}_{w,Q}$ and 0.55 for $d^{u}_{w,T}$. Similarly, for the global approach, median r in $[Ca^{2+}]$ estimation was 0.70 for the combination compared to 0.64 for $d^{u}_{w,Q}$ and 0.64 for $d^{u}_{w,T}$. It should be noted that these correlation coefficient values were computed between actual $[K^+]$ and estimated $[\hat{K}^+]$ while the correlation between each of the tested markers and $[K^+]$ was higher, both for the QRS marker $d^{u}_{w,Q}$ proposed here and for the T wave marker $d^{u}_{w,T}$ analyzed in our previous studies [29, 89].

These results supported the use of our proposed QRS markers to improve prediction of $[K^+]$ and $[Ca^{2+}]$ by ECG repolarization markers. ECG depolarization-based estimators have been scarcely investigated in the literature for serum electrolyte monitoring. In [54], an ECG-based $[K^+]$ estimator was designed using QRS duration in addition to T wave markers, but QRS duration was found not to be highly correlated with $[K^+]$, in agreement with our present results for QRS_w. Pilia et al. [27] reviewed studies evaluating QRS amplitude and width features, but no improved serum electrolyte prediction by incorporating these features into repolarization-based estimators was provided. Here, we proposed univariable and multivariable $[K^+]$ and $[Ca^{2+}]$ estimators that included information from the whole morphology of the QRS complex. By accounting for characteristics beyond QRS amplitude and width, these estimators could offer more robust performance for ambulatory monitoring of ESRD patients and overcome some limitations of previously proposed markers, such as their dependence on blood volume [58, 59].

For all the estimators we built, we found that the values of $[K^+]$ and $[Ca^{2+}]$ at the beginning of each of the two HD sessions, i.e., time points h_0 and h_{48}, were the most challenging to estimate, as could be observed from the large estimation errors at those time points (Figure 5.3). Here, we duplicated the values of the ECG markers at h_0 and h_{48} to give them more weight in the training step, as all other measures corresponding to h_1, h_2, h_3 and h_4^- were more similar to one another and the learning could otherwise be biased towards such measures.

5.5.3 Study limitations and future research

For each patient, six blood samples were available, five of them taken during an HD session and the sixth one at the beginning of the following HD session. Future studies could be designed to have more frequent $[K^+]$ and $[Ca^{2+}]$ measurements, especially during the first HD hour, when electrolyte levels vary most remarkably. This could help to improve the learning of the estimators.

We used linear estimators due to the small number of samples, particularly when using a patient-specific approach. Future work could investigate the use of nonlinear estimators [9, 132], which could prove to be particularly relevant for estimation of $[K^+]$ and $[Ca^{2+}]$ at the start of HD sessions when these take values far from those at other HD

stages.

We did not have access to measurements of blood volume or of other variables that could be used to infer them. Studies on other data sets where such measurements were available could test the relationship between the markers $d^{u}_{w,Q}$ and $d^{u}_{w,T}$ used in our $[K^+]$ and $[Ca^{2+}]$ estimators and the blood volume. Also, some of the patients analyzed in the study had diseases like diabetes mellitus. We did not find significant differences in the analyzed markers between diabetic and non-diabetic patients. Nevertheless, future studies addressing larger patient cohorts could investigate the impact of diseases additional to ESRD on the relationship between QRS markers and electrolytes.

We focused our research on $[K^+]$ and $[Ca^{2+}]$ estimation. $[Na^+]$ was found to present less notable variations during HD and none of our analyzed QRS markers showed significant association with it in the reduced data set analyzed in this study, which should be further tested in larger patient cohorts. Although variations in other electrolytes, like magnesium ($[Mg^{2+}]$), have also been shown to alter the ECG to some extent [6, 50, 135–137], $[Mg^{2+}]$ measurements were not available for the present study.

5.6 Conclusions

Our proposed QRS morphology markers presented remarkable changes during and after HD, which were strongly associated with $[K^+]$ and $[Ca^{2+}]$ in the ESRD patients. Multivariable estimators based on combined QRS and T wave morphological variability allowed accurate prediction of $[K^+]$ and $[Ca^{2+}]$, outperforming estimators based on only ECG depolarization or repolarization. These results could pave the way to ambulatory, non-invasive monitoring of electrolyte levels, which could help to prevent fatal ventricular arrhythmias in ESRD patients.

Chapter 6

Investigation of Inter-Patient Variability in ECG Response to Serum Potassium and Calcium Variations using 3D and Torso Models

This chapter is partially based on a paper that is currently under Review in Frontiers in Physiology, 2022.

6.1 Introduction

In previous chapters 3, 4 and 5, we have used nonlinear dynamics and time-warping techniques to characterize changes in the whole T wave and QRS complex at varying $[K^+]$ and $[Ca^{2+}]$ in patients [29,89,92,129,132,134,140]. We found a strong relationship between $[K^+]$ (or $[Ca^{2+}]$) and T wave and QRS complex linear and nonlinear features in patients. Previous attempts have been published to assess the effects of changes in $[K^+]$ and $[Ca^{2+}]$ on simulated APs and ECGs using computational modeling [7, 84, 85]. However, all these *in silico* studies were based only on a single ventricular model and not accounting for potential inter-individual variability as observed in the patients [89, 92, 129, 132, 140].

A common weakness of all the proposed markers is that their relationships with electrolyte concentrations vary strongly between patients [27,132,148–152]. The cause of this variability is presently unknown. In this chapter, we hypothesized that inter-individual differences in cell type distribution across the ventricular wall could help to explain such variability between patients. We tested this hypothesis using a population of realistic computational models, based on the anatomy of a real subject. We characterized ECG

features, including several proposed markers for $[K^+]$ and $[Ca^{2+}]$, in models with different proportions of endocardial, midmyocardial and epicardial myocytes at varying $[K^+]$ and $[Ca^{2+}]$, and compared the results to measurements in 29 ESRD patients.

We found that the relationships between electrolyte concentrations in the models were similar to those in patients and that the variability in the relationships could indeed be explained, partly, by differences in ventricular wall composition.

6.2 Materials and Methods

6.2.1 *In silico* population of human heart-torso models

A population of coupled whole-ventricle and torso models was built taking as a basis the computed tomography (CT) data of a patient [153], as shown in Figure 6.1. The model included the ventricular wall, ventricular and atrial cavities, torso surface, lungs and an approximate anisotropic skeletal muscle layer, which were segmented from the CT data. A hexahedral mesh of the heart with 200 µm resolution and a torso mesh with 1 mm resolution were created.

Ventricular electrical propagation was simulated with a monodomain reaction-diffusion model as fully described in section 1.6.2.3 (equation 1.9). The fiber orientations used to compute the conductivity tensors were assigned with a rule-based method [154, 155]. Temporal integration was done with a forward Euler scheme with a time step of 0.01 ms. For accuracy, gating variables in the membrane model were integrated with the Rush-Larsen method [156]. The simulations were performed using a recent version of the Propag-5 software [157].

Cellular electrophysiology was represented by the human ventricular myocyte model of Ten Tusscher and Panfilov [69]. The updates to the Ten Tusscher-Panfilov model published by Severi et al. [82] were incorporated to adequately represent the relationship between APD and $[Ca^{2+}]$ as fully described in section 3.2.4.

The initial state for each simulation was pre-calculated from single cell simulations, one for each cell type: endocardial, midmyocardial and epicardial. The values of the

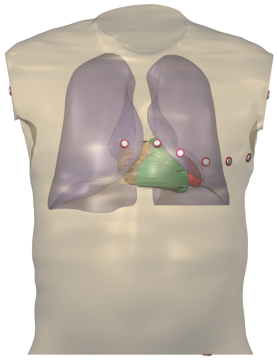

Figure 6.1: 3D heart-torso model used for ECG simulations.

model state variables after 1000 paced beats were considered as representative of the cell at steady state.

A total of 7 whole-ventricle models with variations in the proportions of endocardial, midmyocardial and epicardial cells were simulated, with the thickness of endocardial and midmyocardial layers ranging from 10% to 50% and the epicardial layer from 20% to 60%. We used the notation Cuvw, where C stands for the word "case" and u, v and w denote the thicknesses of the endocardial, midmyocardial, and epicardial layers in tenths of the total wall thickness, respectively, as described in section 3.2.4. The population of ventricular models included the following combinations of transmural heterogeneities: $C136$, $C154$, $C316$, $C334$, $C352$, $C514$, $C532$.

6.2.2 ECG simulation and processing

The extracellular potential, ϕ_e, was computed by solving

$$\nabla \cdot ((\sigma_i + \sigma_e)\nabla\phi_\mathrm{e}) = -\nabla \cdot (\sigma_i \nabla V_\mathrm{m}) \tag{6.1}$$

in the torso model, with V_m simulated by the monodomain reaction-diffusion model (1.9) [158]. Since we needed to know ϕ_e only at a few locations for the computation of the ECG we used a Green's function of the operator $\nabla \cdot ((\sigma_i + \sigma_e)\nabla .)$ for each of these locations to solve this equation efficiently. ECG leads can be represented by a linear combination of Green's functions because ECG lead is a linear combination of ϕ_e at two or more points. These linear combinations of Green's functions are termed lead fields [159,160]. Our lead fields were computed by solving an equation similar to (6.1) but as a lead field needs to be computed only once for each ECG lead this approach is much more efficient than solving (6.1) for each time step in each simulation [158]. Five-beat ECGs were simulated at a sampling frequency of 1 kHz.

A wavelet-based single-lead delineation method was used for QRS detection and wave delineation of each of the 12 leads [28]. PC analysis was spatially applied to the T waves (or QRS complexes) of the eight independent leads [90] to enhance the T wave (or QRS complex) energy as fully described in section 2.2.3. The T waves and QRS complexes in the first PC were delineated using the same single-lead delineation algorithm [28]. The onset, peak and end of the T waves and QRS complexes were determined and used for subsequent computation of T wave and QRS complex markers.

Simulation results were compared with the results obtained by applying the same analysis to ECG recordings from patients. The study population included 29 ESRD patients from Hospital Clínico Universitario de Zaragoza, Spain, from which 48-hour 12-lead ECGs were acquired. T waves and QRS complexes, respectively, in the first PC were obtained and delineated to compute the markers described below [89, 92, 140] as fully described in chapters 3 and 5.

6.2.3 Duration, amplitude and morphology-based ECG markers

Time- and amplitude-based T wave and QRS complex markers, T_{w}, $T_{\mathrm{s/a}}$, QRS_{w}, QRS_{a}, were computed from the last T wave and QRS complex of each simulated ECG projected onto the first PC, at varying $[K^+]$, $[Ca^{2+}]$ and their combinations, as fully described in section 2.2.4.1.

Morphology-based T wave and QRS complex markers, $d^{\mathrm{u}}_{\mathrm{w,T}}$, $d_{\mathrm{a,T}}$, $d^{\mathrm{NL}}_{\mathrm{w,T}}$, $d^{\mathrm{NL}}_{\mathrm{a,T}}$, $d^{\mathrm{u}}_{\mathrm{w,Q}}$, $d_{\mathrm{a,Q}}$, $d^{\mathrm{NL}}_{\mathrm{w,Q}}$ and $d^{\mathrm{NL}}_{\mathrm{a,Q}}$, were computed using the time-warping methodology described previously in section 2.2.4.1 [92, 93]. For each model in the population, reference T waves and QRS complexes were calculated from the last beat of the PC-transformed ECG at minimum $[K^+]$ (3 mM) and maximum $[Ca^{2+}]$ (3.2 mM).

6.2.4 Effects of $[K^+]$, $[Ca^{2+}]$ and their combination on simulated T waves and QRS complexes

To assess the relationship between $[K^+]$, $[Ca^{2+}]$ and their combination with T wave and QRS complex characteristics in each model of the population, simulations were conducted under varying values of the electrolytes. The range of simulated $[K^+]$ values included the default level in the Ten Tusscher-Panfilov model, i.e. $[K^+] = 5.4$ mM, as well as other levels below and above it: $[K^+] \in \{3, 4, 5.4, 6.2\}$ mM. In the case of $[Ca^{2+}]$, the range of simulated values included the default level of 2 mM and values around it: $[Ca^{2+}] \in \{1.4, 2, 2.6, 3.2\}$ mM. The combinations of $[K^+]$ and $[Ca^{2+}]$ included: [3,3.2], [4,2.6], [5.4,2.0] and [6.2,1.4] mM. The simulated ranges are similar to those observed in patients during HD [29, 89, 140].

Linear Pearson correlation analysis was also performed to assess the effects of $[K^+]$ and $[Ca^{2+}]$ on each investigated T wave and QRS complex marker.

6.2.5 Sensitivity analysis for assessment of inter-individual variability sources

Sensitivity analysis was performed to quantify how the proportion of endocardial, midmyocardial and epicardial cell layers modulated inter-individual variability in simulated T wave and QRS complex morphology markers at different $[K^+]$, $[Ca^{2+}]$ or their combination levels.

For each T wave and QRS complex marker at each given concentration of $[K^+]$ ($[Ca^{2+}]$ or both $[K^+]$ and $[Ca^{2+}]$, respectively), the percentage of change $D_{Y;c;a_{\mathrm{i}}}$ in marker Y and its sensitivity $S_{Y;c;a1,a2}$ to changes in the proportion of cells was computed as fully described in section 3.2.6 [29, 104, 134]. In this chapter, $C532$ was used as a reference, having similar ECG morphology as that of the patient used as a basis for building the heart-torso models.

6.3 Results

6.3.1 Evaluation of T wave and QRS complex changes induced by $[K^+]$ and $[Ca^{2+}]$ variations in heart-torso simulations

T wave markers (T_{w}, $T_{\mathrm{S/A}}$, $d^{\mathrm{u}}_{\mathrm{w,T}}$, $d_{\mathrm{a,T}}$, $d^{\mathrm{NL}}_{\mathrm{w,T}}$, $d^{\mathrm{NL}}_{\mathrm{a,T}}$) computed from simulated ECGs at varying $[K^+]$, $[Ca^{2+}]$ and their combinations are shown in Fig. 6.2. The morphological markers $d^{\mathrm{u}}_{\mathrm{w,T}}$, $d_{\mathrm{a,T}}$, $d^{\mathrm{NL}}_{\mathrm{w,T}}$ and $d^{\mathrm{NL}}_{\mathrm{a,T}}$ changed markedly at varying $[K^+]$ and $[Ca^{2+}]$. Large differences between models in the population could be observed for all analyzed T wave markers. Analogously, Fig. 6.3 shows changes in QRS complex markers (QRS_{w}, QRS_{a}, $d^{\mathrm{u}}_{\mathrm{w,Q}}$, $d_{\mathrm{a,Q}}$, $d^{\mathrm{NL}}_{\mathrm{w,Q}}$, $d^{\mathrm{NL}}_{\mathrm{a,Q}}$) at varying $[K^+]$ and $[Ca^{2+}]$ and their combinations, with high variability between models for all markers.

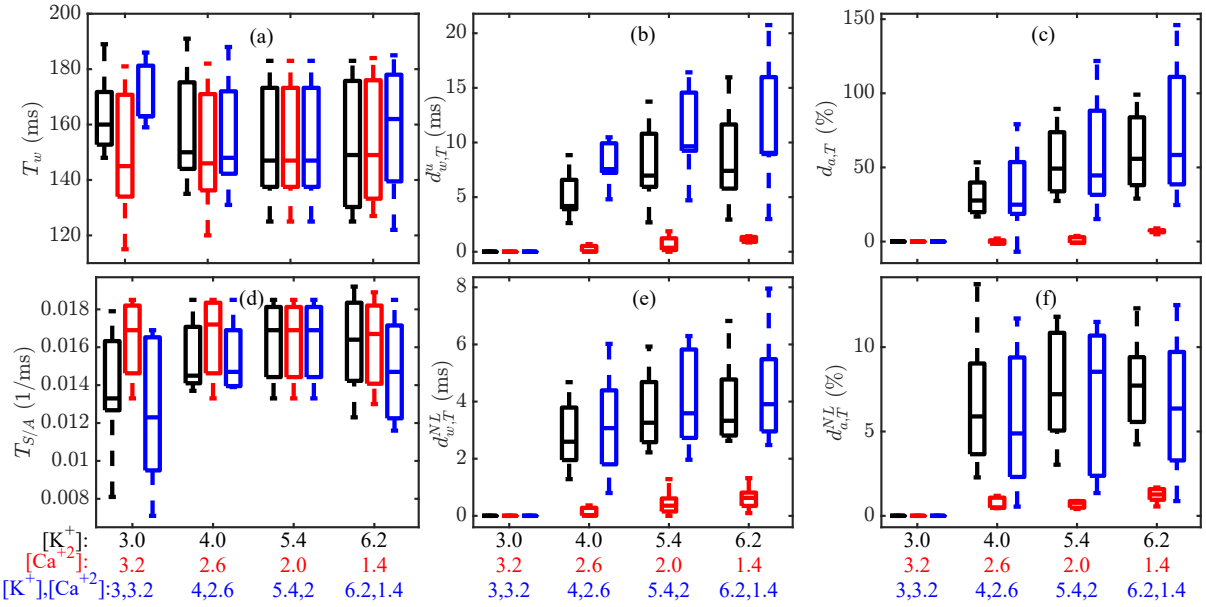

Figure 6.2: Panels a–f: Changes in T_{w}, $T_{\mathrm{S/A}}$, $d^{\mathrm{u}}_{\mathrm{w,T}}$, $d_{\mathrm{a,T}}$, $d^{\mathrm{NL}}_{\mathrm{w,T}}$ and $d^{\mathrm{NL}}_{\mathrm{a,T}}$ for varying $[K^+]$ at fixed $[Ca^{2+}]$=2.0 mM (black), varying $[Ca^{2+}]$ at fixed $[K^+]$ =5.4mM (red) and the combination of $[K^+]$ and $[Ca^{2+}]$ (blue), for ECGs simulated from the population of models. Central lines indicate the median, whereas bottom and top edges show the 25th and 75th percentiles, respectively.

6.3.2 Comparison of $[K^+]$- and $[Ca^{2+}]$-induced changes in T wave and QRS complex characteristics in simulations and patients

Fig. 6.4 shows T waves and the analyzed markers T_{w}, $T_{\mathrm{S/A}}$, $d^{\mathrm{u}}_{\mathrm{w,T}}$, $d_{\mathrm{a,T}}$, $d^{\mathrm{NL}}_{\mathrm{w,T}}$ and $d^{\mathrm{NL}}_{\mathrm{a,T}}$, computed from the ECGs of a particular model, $C514$, and a particular patient, P10, when concomitantly varying $[K^+]$ and $[Ca^{2+}]$. More peaked T waves can be observed with increasing $[K^+]$ and decreasing $[Ca^{2+}]$ in both the model and the patient. Analogously,

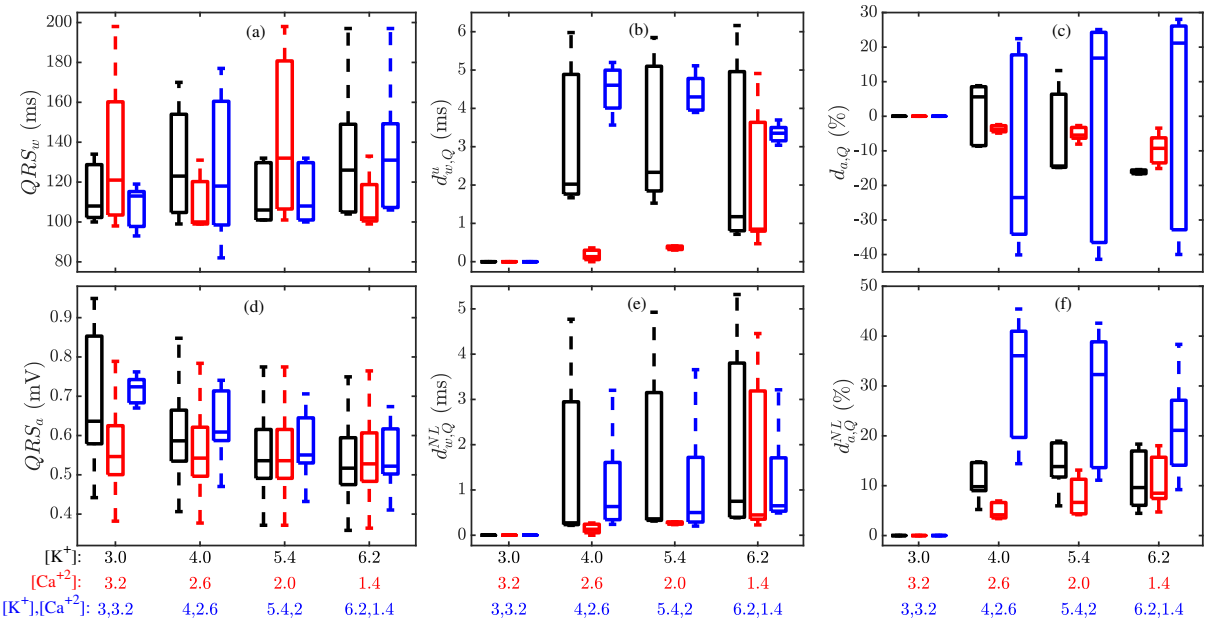

Figure 6.3: Panels a–f: Changes in QRS_{w}, QRS_{a}, $d^{\mathrm{u}}_{\mathrm{w,Q}}$, $d_{\mathrm{a,Q}}$, $d^{\mathrm{NL}}_{\mathrm{w,Q}}$ and $d^{\mathrm{NL}}_{\mathrm{a,Q}}$ for varying $[\mathrm{K}^+]$ at fixed $[\mathrm{Ca}^{2+}]$=2.0 mM (black), varying $[\mathrm{Ca}^{2+}]$ at fixed $[\mathrm{K}^+]$ =5.4mM (red), and the combination of $[\mathrm{K}^+]$ and $[\mathrm{Ca}^{2+}]$ (blue), for ECGs simulated from the population of models. Central lines indicate the median, whereas bottom and top edges show the 25th and 75th percentiles, respectively.

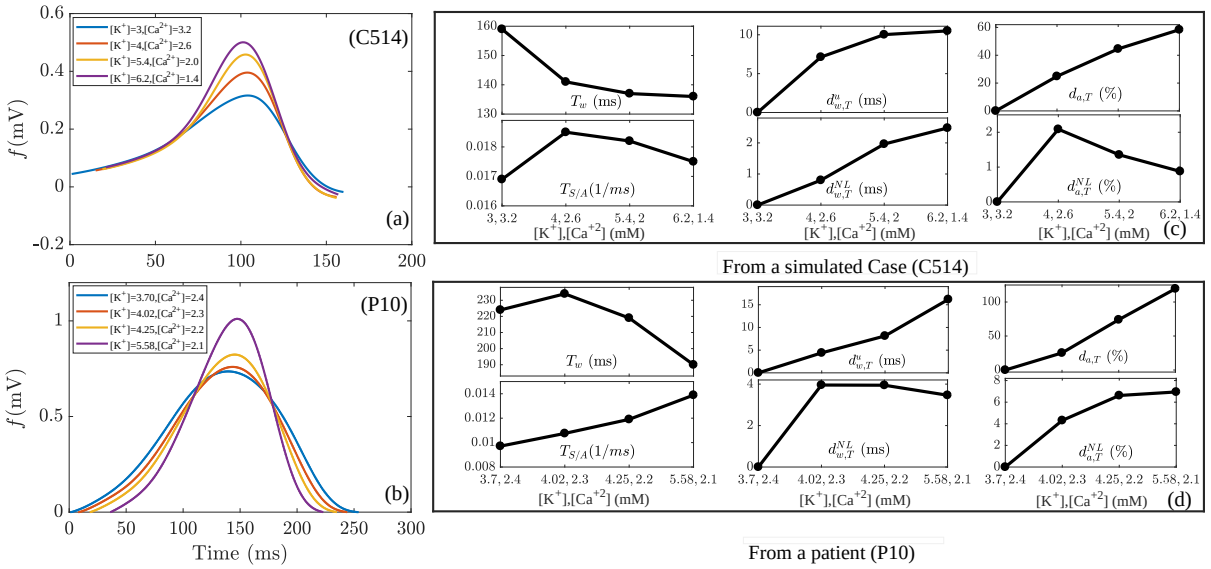

Figure 6.4: Panels a–b: T waves at varying $[\mathrm{K}^+]$ and $[\mathrm{Ca}^{2+}]$, for a simulated case ($C514$) and for a patient (P10). Panels c–d: Changes in T wave markers T_{w}, $T_{\mathrm{S/A}}$, $d^{\mathrm{u}}_{\mathrm{w,T}}$, $d_{\mathrm{a,T}}$, $d^{\mathrm{NL}}_{\mathrm{w,T}}$ and $d^{\mathrm{NL}}_{\mathrm{a,T}}$ for the same simulated case and patient, respectively.

Fig. 6.5 shows QRS complexes and analyzed QRS markers QRS_{w}, QRS_{a}, $d^{\mathrm{u}}_{\mathrm{w,Q}}$, $d_{\mathrm{a,Q}}$, $d^{\mathrm{NL}}_{\mathrm{w,Q}}$ and $d^{\mathrm{NL}}_{\mathrm{a,Q}}$, for a simulated case ($C154$) and a patient (P10) for simultaneous variations in $[\mathrm{K}^+]$ and $[\mathrm{Ca}^{2+}]$.

Fig. 6.6 shows a comparison of the changes in the marker $d^{\mathrm{NL}}_{\mathrm{w,T}}$ when varying both $[\mathrm{K}^+]$ and $[\mathrm{Ca}^{2+}]$ in the simulated cases and the patients. As can be observed by comparing

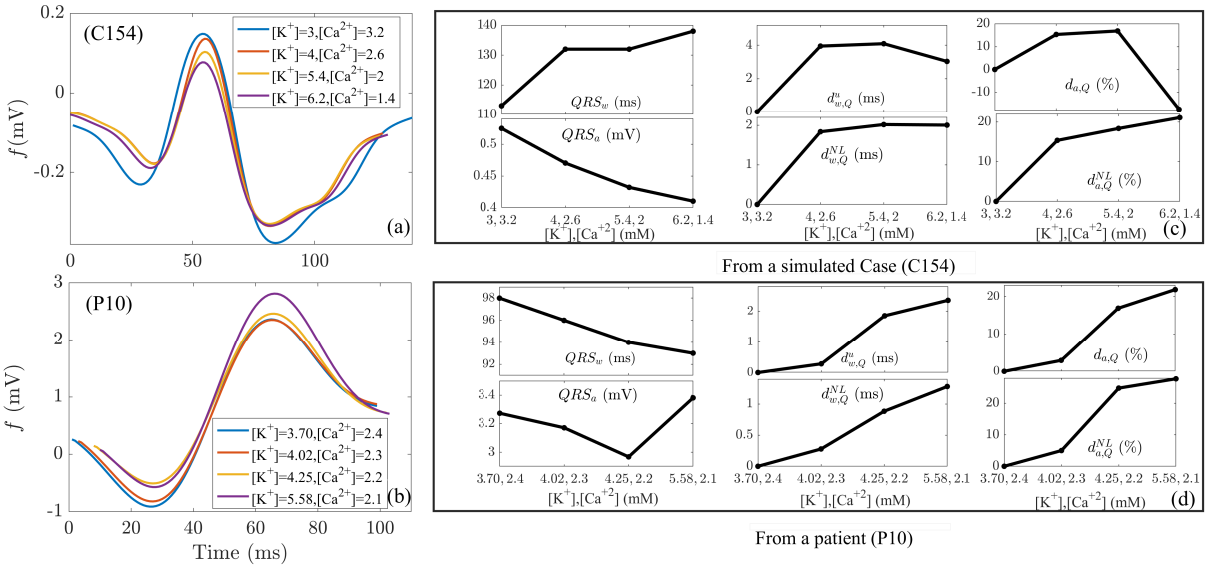

Figure 6.5: Panels a–b: QRS complexes at varying $[K^+]$ and $[Ca^{2+}]$, for a simulated case ($C154$) and for a patient (P10). Panels c–d: Changes in QRS complex markers QRS_w, QRS_a, $d^u_{w,Q}$, $d_{a,Q}$, $d^{NL}_{w,Q}$ and $d^{NL}_{a,Q}$ for the same simulated case and patient.

panels a and b, panels d and e and panels g and h, the models in the population reproduced some specific patterns of change of $d^{NL}_{w,T}$ in the patients, albeit with some quantitative differences. These results were confirmed by computation of correlation coefficients, as shown in panels c, f and i of the same figure. The ability of our *in silico* population to reproduce $d^{NL}_{w,T}$ trends measured in some of the patients was equally valid for other T wave markers even if they did not present as remarkable changes as $d^{NL}_{w,T}$ when varying $[K^+]$ and $[Ca^{2+}]$. Analogous results in simulated and patients' ECGs are depicted in Fig. 6.7 for the QRS-based $d^{NL}_{a,Q}$, which was the one showing the largest changes in response to electrolyte variations.

To assess the extent to which our population of models could reproduce the inter-patient variability in T wave markers at concomitantly varying electrolyte levels, a correlation analysis was performed. Fig. 6.8 shows the Pearson correlation coefficient r between each T wave marker and $[K^+]$, or $[Ca^{2+}]$, in the simulated and the patients' ECGs. T_w, $d^u_{w,T}$ and $d^{NL}_{a,T}$ were the markers most strongly correlated with $[K^+]$ (median r being -0.70, 0.87, 0.91 in simulations and -0.92, 0.93, 0.75 in patients, respectively) and $[Ca^{2+}]$ (median r being 0.70, -0.85, -0.91 in simulations and 0.79, -0.84, -0.75 in patients, respectively). Inter-individual variability in the correlation coefficients associated with T_w and $T_{S/A}$ was high in both simulations and patients. For all other T wave morphology markers, the variability between models only partly reproduced the differences between patients. Table 6.1 provides the results for the quantitative comparison between simulated and patients' T wave markers, in terms of median and interquartile range of r with $[K^+]$ and $[Ca^{2+}]$. As can be seen from the table, all the analyzed morphology-based T wave markers correlated strongly with $[K^+]$ and $[Ca^{2+}]$ in simulations and patients,

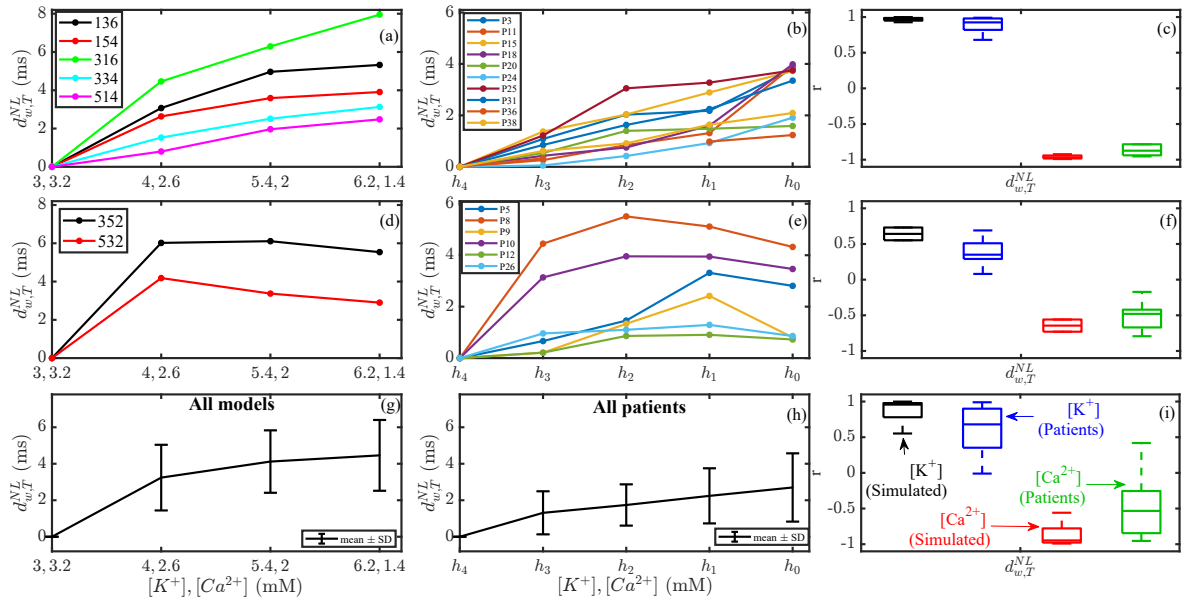

Figure 6.6: Panels a–b, d–e, g–h: Changes in $d^{\mathrm{NL}}_{\mathrm{w,T}}$ at varying [K$^+$] and [Ca^{2+}], in simulated cases and patients. Panel c: Pearson correlation coefficients, r, of $d^{\mathrm{NL}}_{\mathrm{w,T}}$ with [K$^+$] and [Ca^{2+}] for the simulated cases shown in a and the patients shown in b. Panel f: Pearson correlation coefficient r for the simulated cases shown in d and the patients shown in e. Panel i: correlation coefficient r for all the simulated cases and all the patients. h_0–h_4 are the HD time points corresponding to the onset and end of HD (h_4 with lowest [K$^+$] and highest [Ca^{2+}] and h_0 with highest [K$^+$] and lowest [Ca^{2+}].

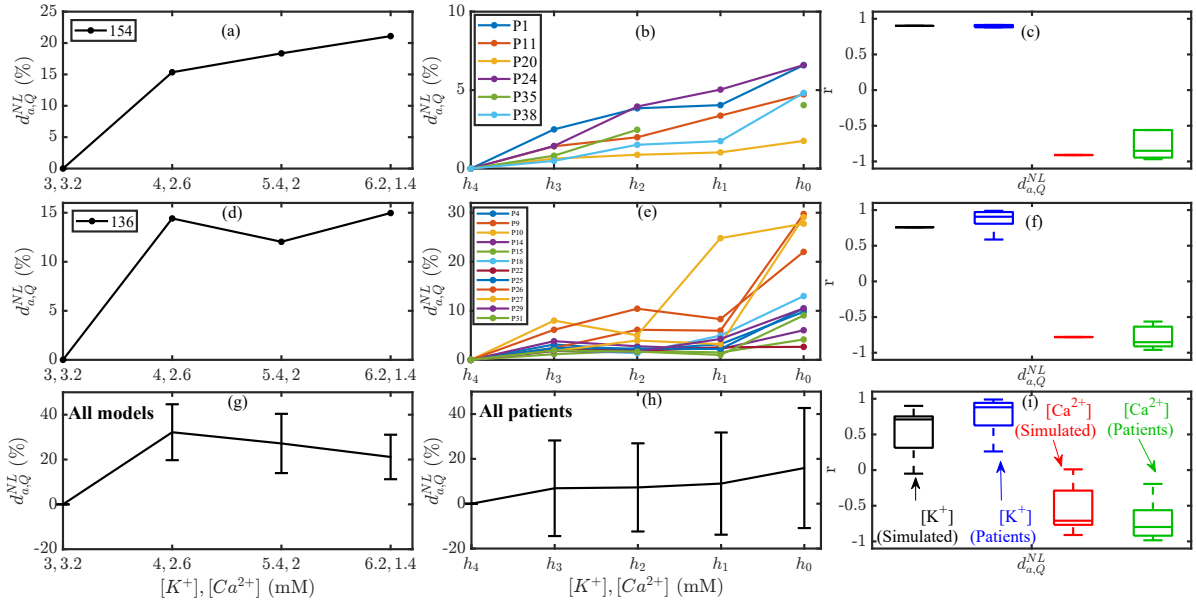

Figure 6.7: Panels a–b, d–e, g–h: Changes in $d^{\mathrm{NL}}_{\mathrm{a,Q}}$ at varying [K$^+$] and [Ca^{2+}], in simulated cases and patients. Panel c: Pearson correlation coefficients, r, of $d^{\mathrm{NL}}_{\mathrm{a,Q}}$ with [K$^+$] and [Ca^{2+}] for the simulated cases shown in a and the patients shown in b. Panel f: Pearson correlation coefficient r for the simulated cases shown in d and the patients shown in e. Panel i: correlation coefficient r for all the simulated cases and all the patients. h_0–h_4 are the HD time points corresponding to the onset and end of HD (h_4 with lowest [K$^+$] and highest [Ca^{2+}] and h_0 with highest [K$^+$] and lowest [Ca^{2+}].

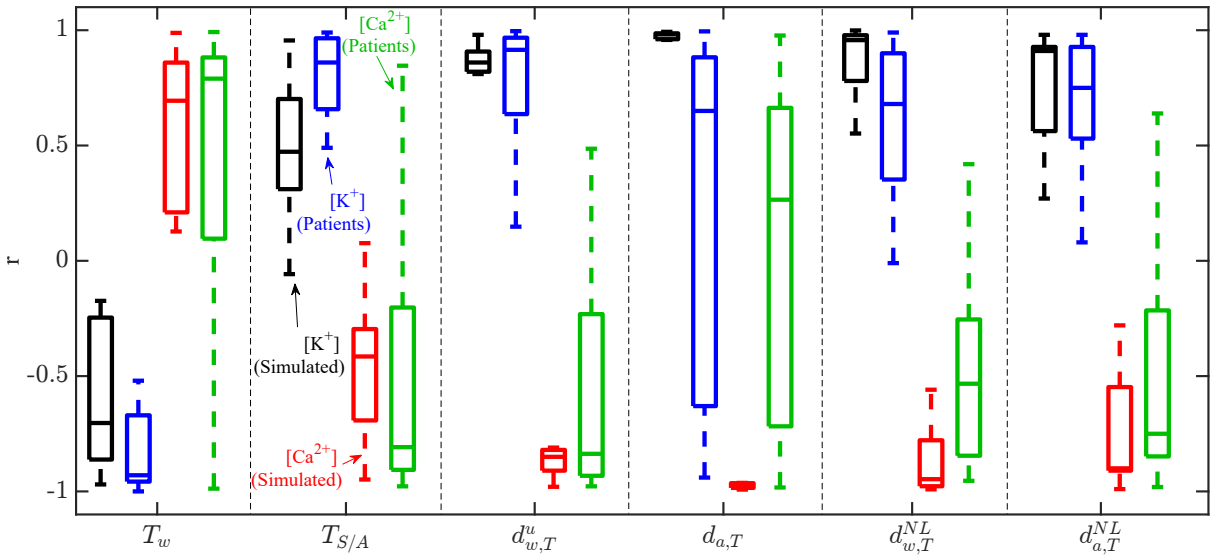

Figure 6.8: Pearson correlation coefficients, r, between each T wave marker (T_{w}, $T_{\mathrm{S/A}}$, $d_{\mathrm{w,T}}$, $d_{\mathrm{a,T}}$, $d^{\mathrm{NL}}_{\mathrm{w,T}}$ and $d^{\mathrm{NL}}_{\mathrm{a,T}}$) and [$K^+$] (black for simulated cases and blue for patients) or [Ca^{2+}] (red for simulated cases and green for patients), for simultaneous variations in [K^+] and [Ca^{2+}].

with part of the inter-patient variability being reproduced by the models.

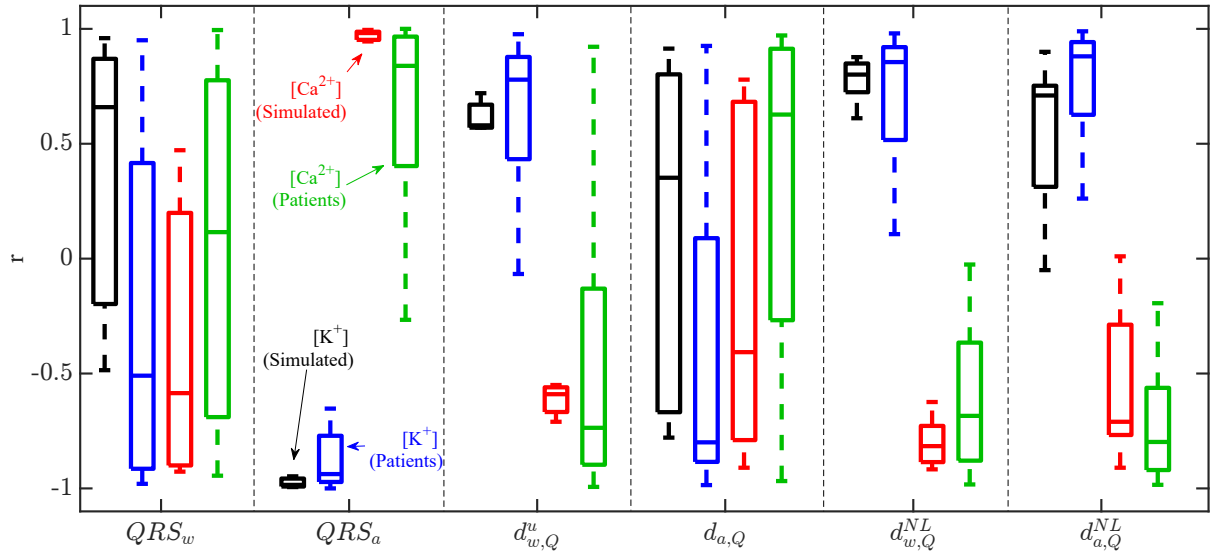

Figure 6.9: Pearson correlation coefficients, r, between each QRS complex marker (QRS_{w}, QRS_{a}, $d^{\mathrm{u}}_{\mathrm{w,Q}}$, $d_{\mathrm{a,Q}}$, $d^{\mathrm{NL}}_{\mathrm{w,Q}}$ and $d^{\mathrm{NL}}_{\mathrm{a,Q}}$) and [$K^+$] (black for simulated cases and blue for patients) or [Ca^{2+}] (red for simulated cases and green for patients), for simultaneous variations in [K^+] and [Ca^{2+}].

Fig. 6.9 and Table 6.2 show correlation coefficients between QRS complex markers and electrolyte levels in simulated and patients' ECGs.

Table 6.1: Median (interquartile range) of Pearson correlation coefficient between T wave markers and each of $[K^+]$ and $[Ca^{2+}]$ in the simulated cases and in the patients at varying $[K^+]$, $[Ca^{2+}]$ and their combination.

	T_{w}	$T_{\mathrm{S/A}}$	$d^{\mathrm{u}}_{\mathrm{w,T}}$	$d_{\mathrm{a,T}}$	$d^{\mathrm{NL}}_{\mathrm{w,T}}$	$d^{\mathrm{NL}}_{\mathrm{a,T}}$
$[K^+]$ (Simul. $[K^+]$ only)	−0.86(0.56)	0.64(0.91)	0.92(0.04)	0.97(0.02)	0.92(0.11)	0.89(0.05)
$[K^+]$ (Simul. $[K^+]$ & $[Ca^{2+}]$)	−0.70(0.52)	0.47(0.29)	0.86(0.07)	0.98(0.02)	0.96(0.14)	0.91(0.26)
$[K^+]$ (Patients)	−0.92(0.28)	0.84(0.30)	0.93(0.31)	0.65(1.50)	0.68(0.53)	0.75(0.38)
$[Ca^{2+}]$ (Simul. $[Ca^{2+}]$ only)	−0.98(0.16)	0.56(0.71)	−0.89(0.06)	−0.72(0.22)	−0.94(0.02)	−0.89(0.14)
$[Ca^{2+}]$ (Simul. $[K^+]$ & $[Ca^{2+}]$)	0.70(0.55)	−0.42(0.29)	−0.86(0.07)	−0.98(0.02)	−0.95(0.15)	−0.91(0.25)
$[Ca^{2+}]$ (Patients)	0.79(0.76)	−0.81(0.68)	−0.84(0.68)	0.27(1.28)	−0.53(0.59)	−0.75(0.58)

Table 6.2: Median (interquartile range) of Pearson correlation coefficient between QRS complex markers and each of $[K^+]$ and $[Ca^{2+}]$ in the simulated cases and in the patients at varying $[K^+]$, $[Ca^{2+}]$ and their combination.

	QRS_{w}	QRS_{a}	$d^{\mathrm{u}}_{\mathrm{w,Q}}$	$d_{\mathrm{a,Q}}$	$d^{\mathrm{NL}}_{\mathrm{w,Q}}$	$d^{\mathrm{NL}}_{\mathrm{a,Q}}$
$[K^+]$ (Simul. $[K^+]$ only)	−0.05(0.71)	−0.99(0.00)	0.46(0.32)	−0.82(0.34)	0.82(0.18)	0.76(0.17)
$[K^+]$ (Simul. $[K^+]$ & $[Ca^{2+}]$)	0.66(0.86)	−0.98(0.03)	0.58(0.09)	0.35(1.33)	0.80(0.10)	0.71(0.37)
$[K^+]$ (Patients)	−0.51(1.24)	−0.86(0.25)	0.82(0.33)	−0.81(1.49)	0.86(0.27)	0.87(0.28)
$[Ca^{2+}]$ (Simul. $[Ca^{2+}]$ only)	−0.66(1.31)	0.99(0.01)	−0.87(0.14)	0.97(0.02)	−0.91(0.12)	−0.98(0.24)
$[Ca^{2+}]$ (Simul. $[K^+]$ & $[Ca^{2+}]$)	−0.59(0.90)	0.98(0.03)	−0.59(0.09)	−0.41(1.34)	−0.82(0.12)	−0.71(0.40)
$[Ca^{2+}]$ (Patients)	0.12(1.47)	0.82(0.48)	−0.74(0.76)	0.78(1.45)	−0.71(0.49)	−0.80(0.36)

*Values are expressed as median (IQR)

6.3.3 Contribution of ventricular wall composition to inter-individual variability in T wave and QRS complex response to $[K^+]$ and $[Ca^{2+}]$ variations

The results of the sensitivity analysis performed to investigate how different proportions of endocardial, midmyocardial and epicardial cells contribute to explain individual T wave responses when varying both $[K^+]$ and $[Ca^{2+}]$ are presented in Table 6.3 for all the analyzed simulated T wave markers. The highest sensitivity values were observed for morphology-based T wave markers, particularly $d^{\mathrm{u}}_{\mathrm{w,T}}$ and $d^{\mathrm{NL}}_{\mathrm{w,T}}$, when varying the proportion of epicardial cells. Table 6.4 shows sensitivity results for QRS complex markers.

Table 6.3: Results of the sensitivity analysis, $S_{Y;c;a_1,a_2}$, for different values of combined $[K^+]$ and $[Ca^{2+}]$ for T wave markers, when varying cell proportions in layer c from a_1 to a_2 for human-specific Torso model.

$S_{Y;c;a_1,a_2}$	Y	T_{w}	$T_{\mathrm{S/A}}$	$d^{\mathrm{u}}_{\mathrm{w,T}}$	$d_{\mathrm{a,T}}$	$d^{\mathrm{NL}}_{\mathrm{w,T}}$	$d^{\mathrm{NL}}_{\mathrm{a,T}}$
c, a_1, a_2	$[K^+]$,$[Ca^{2+}]$	%	%	%	%	%	%
Endo, 10, 50	4,2.6	−0.36	1.26	−17.77	14.87	−2.16	5.32
	6.2,1.4	0.98	−2.52	−67.62	12.45	−16.62	1.17
Mid, 10, 50	4,2.6	6.40	−3.24	−14.32	1.06	10.13	−4.19
	6.2,1.4	4.56	−1.16	−43.50	2.22	−4.26	7.42
Epi, 20, 60	4,2.6	−6.03	1.98	32.09	−15.93	−7.98	−1.13
	6.2,1.4	−5.55	3.68	111.13	−14.67	20.88	−8.59

Table 6.4: Results of the sensitivity analysis, $S_{Y;c;a_1,a_2}$, for different values of combined $[K^+]$ and $[Ca^{2+}]$ for QRS complex markers, when varying cell proportions in layer c from a_1 to a_2 for human-specific Torso model.

$S_{Y;c;a_1,a_2}$	Y	QRS_{w}	QRS_{a}	$d^{\mathrm{u}}_{\mathrm{w,Q}}$	$d_{\mathrm{a,Q}}$	$d^{\mathrm{NL}}_{\mathrm{w,Q}}$	$d^{\mathrm{NL}}_{\mathrm{a,Q}}$
c, a_1, a_2	$[K^+]$,$[Ca^{2+}]$	%	%	%	%	%	%
Endo, 10, 50	4,2.6	−3.20	1.05	−1.24	49.99	−193.31	13.51
	6.2,1.4	−6.60	−0.06	−0.70	−8.31	−107.61	8.39
Mid, 10, 50	4,2.6	5.37	−7.22	3.59	−60.56	23.96	−6.48
	6.2,1.4	3.89	−7.30	−0.52	38.35	33.54	−21.50
Epi, 20, 60	4,2.6	−2.17	6.17	−2.35	10.57	169.35	−7.02
	6.2, 1.4	2.71	7.37	1.23	−30.04	74.07	13.11

6.4 Discussion

In our whole-heart and torso simulations, T wave and QRS complex duration, amplitude and morphology changed with $[K^+]$ and $[Ca^{2+}]$ in the same direction and with similar averaged magnitude as in ECGs from ESRD patients undergoing HD. In both simulations and patients, high inter-individual ECG variability was observed, which was accentuated at high $[K^+]$ and low $[Ca^{2+}]$. Differences in cell type distribution, particularly in the proportion of epicardial cells, partially explained inter-patient variability in T wave and QRS complex response to electrolyte variations.

6.4.1 *In silico* heart-torso models reproduce $[K^+]$- and $[Ca^{2+}]$-induced changes in T wave and QRS complex measured in ESRD patients

We measured commonly used QRS complex and T wave markers describing characteristics related to their duration and amplitude, including T wave and QRS complex widths (T_{w}, QRS_{w}), QRS complex amplitude (QRS_{a}) and T wave slope-to-amplitude ratio ($T_{\mathrm{S/A}}$), as well as our recently proposed morphological variability-based markers ($d^{\mathrm{u}}_{\mathrm{w,T}}$, $d^{\mathrm{u}}_{\mathrm{w,Q}}$, $d_{\mathrm{a,T}}$, $d_{\mathrm{a,Q}}$, $d^{\mathrm{NL}}_{\mathrm{w,T}}$, $d^{\mathrm{NL}}_{\mathrm{w,Q}}$, $d^{\mathrm{NL}}_{\mathrm{a,T}}$, $d^{\mathrm{NL}}_{\mathrm{a,Q}}$) [29,89,92,93]. We evaluated these markers in simulated ECGs derived from coupled heart-torso models with different proportions of endocardial, mid-myocardial and epicardial cells, at varying $[K^+]$ (3–6.2 mM), $[Ca^{2+}]$ (1.4–3.2 mM) and their combinations. We found that most of our simulated QRS and T wave markers (all except for QRS_{w}, $d_{\mathrm{a,T}}$ and $d_{\mathrm{a,Q}}$) presented a diversity of patterns in their relationships with $[K^+]$ and $[Ca^{2+}]$ that were in line with our observations in ESRD patients during and after HD [29,89,92,140]. Overall, the T wave morphology markers $d^{\mathrm{u}}_{\mathrm{w,T}}$, $d^{\mathrm{NL}}_{\mathrm{w,T}}$ and $d^{\mathrm{NL}}_{\mathrm{a,T}}$ were the ones that most notably changed with $[K^+]$, somewhat less notably with $[Ca^{2+}]$ and very remarkably with their combination, in average over the population of *in silico* models (Fig. 6.2). These results were in line with averaged changes presented by these markers in ESRD patients, as shown here and in previous studies where the markers were first evaluated during HD [29,89,140]. This generally corresponded to more peaked T waves, with lower amplitude and/or longer duration, which presented increasingly larger morphological differences with respect to a reference T wave (calculated at physiological electrolyte levels) when $[K^+]$ was increased and $[Ca^{2+}]$ was decreased (Fig. 6.4) [29, 89, 140]. Regarding the QRS complex, markers describing amplitude characteristics, like QRS_{a} and $d^{\mathrm{NL}}_{\mathrm{a,Q}}$, also varied appreciably with $[K^+]$, $[Ca^{2+}]$ and, particularly, with their combination, in both the simulations and the patients. Typically, the averaged QRS complex in the simulated and patient populations became lower in amplitude and had larger nonlinear amplitude morphological variations than a reference physiological QRS complex when evaluated in response to increasing $[K^+]$ and decreasing $[Ca^{2+}]$ (Fig. 6.5) [92].

For confirmation of the ability of our *in silico* population to describe averaged trends

of T wave and QRS complex changes with electrolyte variations in patients, a correlation analysis was performed. Among the analyzed T wave markers, $d^{\mathrm{u}}_{\mathrm{w,T}}$ and $d^{\mathrm{NL}}_{\mathrm{a,T}}$ were the most strongly correlated with $[K^+]$ and $[Ca^{2+}]$ in both the simulations and the patients (absolute median correlation coefficient ranging from 0.75 to 0.93). In the case of QRS complex markers, QRS_{a}, $d^{\mathrm{NL}}_{\mathrm{w,Q}}$ and $d^{\mathrm{NL}}_{\mathrm{a,Q}}$ were the ones most strongly associated with $[K^+]$ and $[Ca^{2+}]$ in the simulations and the patients (absolute median correlation coefficient ranging from 0.71 to 0.98). These results support the use of our *in silico* population of models to describe the average response of T wave and QRS complex to variations in electrolyte levels like those seen in ESRD patients during and after HD.

6.4.2 Differences in ventricular wall composition contribute to explain inter-individual variability in $[K^+]$- and $[Ca^{2+}]$-induced changes in T wave and QRS complex

After assessing how our population of *in silico* models could reproduce the general trends of electrolyte-induced changes in ECG markers observed in ESRD patients, we investigated how it could contribute to explain the high inter-patient variability in such changes. In agreement with the diversity of patterns of QRS complex and T wave changes in response to $[K^+]$ and $[Ca^{2+}]$ variations measured in the patients, we found different ventricular models presenting largely distinct behaviors that covered some of the patterns described in the patients. Models with thin epicardial layers were mainly related with a non-monotonic behavior of the evaluated ECG markers similar to that presented by some ESRD patients. This was particularly clear for the T wave morphology marker $d^{\mathrm{NL}}_{\mathrm{w,T}}$, illustrated in Fig. 6.6. Most models with thick epicardial layers reproduced the increasing linear trend of $d^{\mathrm{NL}}_{\mathrm{w,T}}$ observed in many patients (Fig. 6.6). For the QRS complex, we found that models with thick midmyocardial layers could replicate the increasing linear trend in the marker $d^{\mathrm{NL}}_{\mathrm{a,Q}}$ measured in some patients (Fig. 6.7). Also, the non-monotonic behavior of $d^{\mathrm{NL}}_{\mathrm{a,Q}}$ in many other patients was obtained for models with thick epicardial layers (Fig. 6.7). Therefore, we may conclude that the different transmural heterogeneities simulated in this study could reproduce part of the inter-patient variability in the ECG response to $[K^+]$ and $[Ca^{2+}]$ variations.

To quantify how different ventricular wall compositions could contribute to explain individual ECG responses at a range of $[K^+]$ and $[Ca^{2+}]$, we computed QRS and T wave marker sensitivities to variations in the thickness of the endocardial, midmyocardial and epicardial cell layers. The highest sensitivity values were observed for T wave morphology markers $d^{\mathrm{u}}_{\mathrm{w,T}}$, $d^{\mathrm{NL}}_{\mathrm{w,T}}$ and $d^{\mathrm{NL}}_{\mathrm{a,T}}$ and for QRS morphology markers $d^{\mathrm{NL}}_{\mathrm{w,Q}}$, $d_{\mathrm{a,Q}}$ and $d^{\mathrm{NL}}_{\mathrm{a,Q}}$. Extremely high sensitivities were found for some of these T wave markers at abnormally high levels of $[K^+]$ and low levels of $[Ca^{2+}]$, which could at least partially explain the remarkably large inter-patient variability observed at the beginning of the HD, when $[K^+]$ was enhanced and $[Ca^{2+}]$ was reduced. In particular, $d^{\mathrm{u}}_{\mathrm{w,T}}$ very notably increased

for progressively larger proportions of epicardial cells and it decreased for progressively larger proportions of endocardial or midmyocardial cells. The largest sensitivity of $d^{\mathrm{u}}_{\mathrm{w,T}}$ to variations in the proportion of epicardial cells within the ventricular wall agrees with previous reports showing the contribution of epicardial cells to other forms of repolarization variability like T wave alternans [120]. For $[K^+]$ = 6.2 mM and $[Ca^{2+}]$ = 1.4 mM, sensitivity values above 110% were found, which corresponded to a coefficient of determination of 0.93 for the relationship between $d^{\mathrm{u}}_{\mathrm{w,T}}$ and the proportion of epicardial cells. Previous experimental and theoretical studies have described how cell type distributions influence ECG characteristics [93, 120, 121, 123–125]. In particular, [120] reported that the contribution of epicardial cells to T wave alternans was significantly higher than that of mid-myocardial cells, which would be in line with our results for T wave morphological variability. In [121], cell type distributions were shown to highly affect both repolarization and T wave morphology parameters, in concordance with our findings on the impact of ventricular wall composition on T wave characteristics, particularly at abnormal $[K^+]$ and $[Ca^{2+}]$ values.

Our *in silico* analysis could pave the path to understand how patients with different ventricular wall compositions may present largely different responses to serum electrolyte variations, even if other factors could contribute to inter-patient variability. These results could help to improve monitoring and prediction of arrhythmic events in ESRD patients based on investigations combining *in silico* modeling and simulation with signal processing of the ECG.

6.4.3 Related work

Several previous studies have characterized ECG features in relation to electrolyte concentrations. [84] and [85] computed ECGs at different $[Ca^{2+}]$ from the ventricular electrophysiology and a torso model. No changes with $[Ca^{2+}]$ were found in QRS duration, while the R wave amplitude and energy diminished with decreasing $[Ca^{2+}]$ [84], which would agree with our observations of reduced QRS_{a} and $d^{\mathrm{NL}}_{\mathrm{a,Q}}$. Also, the T wave slopes were reported to increase with decreasing $[Ca^{2+}]$ [84] and increasing $[K^+]$ [85], which is in line with our observations of more peaked T waves at low $[Ca^{2+}]$ and high $[K^+]$.

Other studies have simulated human ventricular electrophysiology in a one-dimensional transmural model and have derived pseudo-ECGs at varying $[K^+]$ [7, 9]. Increases in T wave slope were reported in association with hyperkalemia, which is in agreement with our results.

Inter-patient variability in the relation between electrolytes and ECG markers has been reported by several authors [9,27,53,132,148–152,161]. We are not aware of previous work explaining this variability in terms of variations in ventricular wall composition.

6.4.4 Study limitations and future research

Our simulations were performed with the most realistic available techniques to model the electrophysiology of the heart and the resulting ECGs. The electrophysiology was represented by a widely-used and detailed model of the human ventricular myocyte [69] that is thoroughly rooted in experimental data. The ECG was simulated using a detailed torso model accounting for the major inhomogeneities in electrical conduction and for the anisotropic conductivity of cardiac and skeletal muscle [158]. Yet, our finding that variations in wall composition can help to explain inter-patient variability in the ECG response to electrolyte changes remains a theoretical prediction, and based on the theoretical concept of endocardial, mid-myocardial, and epicardial myocyte types that would be present as layers in the ventricles. While we have shown that variability in the thickness of such layers can be a cause, we cannot exclude that the main cause in real patients be entirely different.

Our *in silico* population included 7 whole-ventricle models with different cell type distributions across the ventricular wall, which we used to simulate variations in $[K^+]$ from 3 to 6.2 mM and in $[Ca^{2+}]$ from 1.4 to 3.2 mM. Future studies could extend the methods proposed here to add larger numbers of coupled ventricle-torso models and simulate a wider range of $[K^+]$ and $[Ca^{2+}]$.

The effects of other electrolyte concentrations such as magnesium, $[Mg^{2+}]$, which has been reported to be possibly involved in observed alterations in the ECG [6, 135–137], could be accounted for in the simulations if information on the variation of these electrolytes during and after HD were available. In the present study, we did not investigate $[Mg^{2+}]$ variations because serum $[Mg^{2+}]$ levels were not measured in our patients.

To investigate other sources of inter-individual variability in the ECG response to serum electrolyte variations, future studies could include other ventricular heterogeneities on top of transmural ones, like interventricular, apicobasal or anteroposterior [162, 163], which might play a relevant role in determining ECG characteristics under normal and abnormal electrolyte concentrations.

6.5 Conclusions

Our *in silico* population of coupled ventricle-torso models with different ventricular wall compositions allows to determine patient-dependent responses of T wave and QRS complex to variations in $[K^+]$ and $[Ca^{2+}]$. Differences in the proportion of ventricular cell types, particularly of epicardial cells, partly explain the inter-subject variability in such responses. These findings can pave a path to design better tools for non-invasive serum electrolyte monitoring and prediction of arrhythmic events in the patients.

Chapter 7

Study Limitations, Future Work and Conclusions

7.1 Main achievements

The main objective of this PhD thesis was to propose novel estimates of serum $[K^+]$ and $[Ca^{2+}]$ by combining novel ECG signal processing techniques with *in silico* modeling and simulation of cardiac electrophysiology. We processed ECGs of ESRD patients and we quantified ECG characteristics identified as being related to extracellular $[K^+]$ and $[Ca^{2+}]$ in simulations. The extracted ECG features were then used to propose novel noninvasive methods for the estimation of serum electrolyte levels. Clinically, this investigation can help to improve current therapies and to provide risk stratification tools.

Time-warping analysis can more robustly characterize hypo- or hyperkalemia and hypo- or hypercalcemia-induced changes in ventricular repolarization from ECGs. This thesis started by the characterization of hypo- or hyperkalemia and hypo- or hypercalcemia-induced changes in ventricular repolarization from ECGs (T wave) of ESRD patients. We described how T waves were extracted from ECGs and how we characterized changes in T waves at varying $[K^+]$, $[Ca^{2+}]$ and HR using time-warping analysis.

We confirmed our hypothesis that time-warping based markers, accounting for the whole T wave morphology, can more robustly characterize repolarization changes associated with different $[K^+]$ and $[Ca^{2+}]$ and be better suited for non-invasive electrolyte estimation as compared to local features.

Nonlinear dynamics markers can assess repolarization instabilities and temporal inter-beat variability. Next, T wave nonlinear dynamics markers were evaluated to assess the extent to which they provided complementary information to the already evaluated T wave morphology markers.

We confirmed our hypothesis that elevated $[K^+]$ at the start of HD and 48 hours later was associated with higher variability in the form of dynamical instabilities, which was reflected in larger values of the quantified nonlinear dynamics markers. Nonlinear dynamics markers assessed repolarization instabilities, temporal inter-beat variability and intra-beat differences.

Univariable and multivariable regression models including markers of T wave nonlinear dynamics in combination with warping-based markers of T wave morphology were built and their performance for $[K^+]$ estimation was assessed, which confirmed that combined markers can be a valuable tool for noninvasive monitoring of $[K^+]$ during inter-dialytic periods in ESRD patients.

Time-warping analysis can more robustly characterize hypo- or hyperkalemia and hypo- or hypercalcemia-induced changes in ventricular depolarization from ECGs and improve estimation of electrolytes. After successfully evaluating the performance of whole T wave morphology in response to varying $[K^+]$, $[Ca^{2+}]$ and HR, we characterized hypo- or hyperkalemia and hypo- or hypercalcemia-induced changes in ventricular depolarization from ECGs (QRS complex) of ESRD patients.

We confirmed our hypothesis that QRS morphology provided complementary information on $[K^+]$ and $[Ca^{2+}]$, additional to that provided by repolarization. This was done by performing univariate and multivariate regression analyses including novel QRS morphological markers in combination with T wave morphological markers to assess the contribution of depolarization and repolarization features for electrolyte monitoring in ESRD patients.

Inter-patient variability can be well reproduced using our *in silico* investigations. After investigating variations in the T wave and QRS complex morphology in ESRD patients, we characterized changes in the T wave and QRS complex markers in relation to $[K^+]$ and $[Ca^{2+}]$ variations in human heart-torso simulations to uncover potential mechanisms underlying differential ECG responses to variations in electrolytes.

This *in silico* study confirmed our hypothesis that inter-individual differences in cell type distribution across the ventricular wall can well reproduce inter-patient variability.

7.2 Study Limitations and Future Work

Study limitations and possible future work are discussed below:

- We focused our research on $[K^+]$ and $[Ca^{2+}]$ estimation. Sodium, $[Na^+]$, was found to present less notable variations during HD and none of our analyzed markers showed significant association with it in the dataset analyzed in this study, which should be further tested in larger patient cohorts. Although variations in other

electrolytes, such as magnesium [Mg^{2+}], have also been shown to alter the ECG to some extent [6, 135–137], in this thesis, [Mg^{2+}] was not investigated due to the unavailability of serum [Mg^{2+}] levels. Future studies using different data sets could investigate [Mg^{2+}] effects on ECG waveforms.

- In this thesis 48-hour ECG recordings of 29 ESRD patients were analyzed. Although the dataset was originally planned to include a larger number of patients, ECG acquisition had to be stopped due to the situation generated by the COVID-19 pandemic. Future studies including a larger number of patients and more frequent blood sampling during the inter-dialytic period would allow to confirm the present findings and extend the investigation to ECG-based linear and nonlinear estimators of [K^+], [Ca^{2+}] and [Mg^{2+}].

- In this thesis, we used linear estimators due to the small number of samples, particularly when using a patient-specific approach. Future work could investigate the use of nonlinear estimators [9, 132], which could prove to be particularly relevant for the estimation of [K^+] and [Ca^{2+}] at the start of HD sessions when these take values far from those at other HD stages.

- We did not have access to measurements of blood volume or of other variables that could be used to infer them. Studies on other data sets where such measurements were available could test the relationship between blood volume and the ECG-derived markers proposed in our study to monitor [K^+] and [Ca^{2+}]. In addition, some of the patients analyzed in the study had diseases, such as diabetes mellitus. We did not find significant differences in the analyzed markers between diabetic and non-diabetic patients. Nevertheless, future studies addressing larger patient cohorts could investigate the impact of diseases additional to ESRD on the relationship between analyzed ECG markers and electrolytes.

- Our electrophysiological simulations considered human biventricular models embedded in a patient-specific torso model, from which realistic ECGs were computed. This research and future investigations on patient-specific ventricular models will additionally allow exploring the role of other types of ventricular heterogeneities, on top of transmural ones, on the QRS and T wave response to electrolyte and HR variations.

- The present work could be extended to include deep learning-based approaches for serum electrolyte estimation provided large data sets of ECG recordings and concomitant blood samples were available for the analysis, in line with studies already addressing hypo- and hyperkalemia screening from the ECG using deep learning methods [55, 138, 139].

7.3 Conclusions

ECG signal processing and *in silico* electrophysiological modeling and simulation are used in my PhD thesis to investigate inter-individual differences in the T wave and QRS complex responses to $[K^+]$, $[Ca^{2+}]$ and HR changes. Novel T wave nonlinear dynamics markers and QRS morphological variability markers present remarkable variations with varying $[K^+]$, $[Ca^{2+}]$ and HR, but a wide range of patterns are observed for such relationships, both in simulated ventricular tissues and in patients' ECGs. The proportion of endocardial, midmyocardial and epicardial cells within the simulated ventricular tissues is shown to have a large impact on ECG derived markers, particularly for serum electrolyte concentrations and HR above and below their physiological levels. This suggests that transmural heterogeneities can play a relevant role in determining patient-dependent responses of the T wave and QRS complex in ESRD patients, which can have major relevance for non-invasive monitoring and prediction of arrhythmic events in these patients. Our results offer new non-invasive tools to monitor serum $[K^+]$ and $[Ca^{2+}]$, which could have a significant role in clinical practice by contributing to reduce the mortality risk associated with abnormal electrolyte levels in ESRD patients.

Honors and Publications

Awards and grants:

During my PhD, I have been awarded with:

PhD contract in the framework of Grant PID2019-105674RB-I00 awarded by Ministry of Science and Innovation of Spain to financially cover the fourth year of my PhD (June 2021 - September 2022).

IberCaja-CAI Mobility Grant awarded by IBERCAJA and CAI foundation, to cover reasonable living costs for the secondment at Inria, Bordeaux (March - April 2022).

IberCaja-CAI Mobility Grant awarded by IBERCAJA and CAI foundation, to cover reasonable living costs for the secondment at Inria, Bordeaux (March - May 2020).

Mortara Fellowship awarded by Welch Allyn, Inc., to attend the *Computing in Cardiology* meeting in Singapore (September 2019).

Clinical Needs Translational Award granted by the European Society of Cardiology and Computing in Cardiology (September 2019, in a team).

Free participation at the *Cardiac Electrophysiology Summer School*, IHU Liryc, Bordeaux (July 2019).

Travel and registration grant to attend the *Uncertainty Quantification for Cardiac Models* workshop at Cambridge University, Cambridge, (June 2019).

Marie Sklodowska-Curie grant awarded by European Union's Horizon 2020 research and Innovation programme under the Marie Sklodowska-Curie grant agreement No 764738, to cover first three year living expenses of the PhD (June 2018 - May 2021).

Publications:

During my PhD, thirteen papers were submitted to high impact journals and conference proceedings.

In eight of these papers, I am the first author:

- Bukhari et al, Transmural ventricular heterogeneities play a major role in determining T-wave morphology at different serum potassium levels, Proceedings of the XLVI International Conference on Computing in Cardiology, 2019 (conference paper, published, doi:10.22489/CinC.2019.404).
- Bukhari et al, Characterization of T Wave amplitude, duration and morphology changes during hemodialysis: Relationship with serum electrolyte levels and heart rate, IEEE Transactions on Biomedical Engineering, 2020 (journal paper, published, doi: 10.1109/TBME.2020.3043844).
- Bukhari et al, QRS slopes for potassium and calcium monitoring in end-stage renal disease patients, Computing in Cardiology, 2021 (conference paper, published, doi:10.22489/CinC.2021.221).
- Bukhari et al, Accelerating stabilization of whole-heart models after changes in cycle length, Computing in Cardiology, 2022 (conference paper, published).
- Bukhari et al, Inter-individual differences in cell composition across the ventricular wall may explain variability in ECG response to serum potassium and calcium Variations, Computing in Cardiology, 2022 (conference paper, published).
- Bukhari et al, Estimation of potassium levels in hemodialysis patients by T wave nonlinear dynamics and morphology markers, Computers in Biology and Control, 2022 (journal paper, published, doi: 10.1016/j.compbiomed.2022.105304).
- Bukhari et al, Monitoring of serum potassium and calcium levels in end-stage renal disease patients by ECG depolarization morphology analysis, Sensors, 2022 (journal paper, published, doi: 10.3390/s22082951).
- Bukhari et al, Differences in ventricular wall composition contribute to explain inter-patient variability in the ECG response to variations in serum potassium and calcium, Frontiers in Physiology, 2023 (journal paper, under review).

Five more papers were submitted in which I was a contributing author:

- Palmieri et al, T-Wave morphology changes as surrogate for blood potassium concentration in HD patients, Proceedings of the XLVI International Conference on Computing in Cardiology, 2019 (conference paper, published, doi:10.22489/CinC.2019.109).
- Palmieri et al, Estudio de los cambios en la morfología de las ondas T como sustituto de la concentración de potasio en sangre en pacientes de hemodiálisis, Proceedings of the XXXVII Congreso Anual de la Sociedad Española de Ingeniería, 2019 (conference paper, published, ISBN: 978-84-09-16707-4).

- Acero et al., The “digital twin” to enable the vision of precision cardiology, European Heart Journal, 2020 (journal paper, in print, doi:10.1093/eurheartj/ehaa159).
- Palmieri et al., Monitoring blood potassium concentration in HD patients by quantifying T-wave morphology dynamics, Scientific Reports, 2020 (journal paper, published, doi: 10.1038/s41598-021-82935-5).
- Srinivasan et al, Analysis of T wave nonlinear dynamics for serum potassium monitoring in end-stage renal disease patients. Computing in Cardiology, 2020 (conference paper, published, doi: 10.22489/CinC.2020.461).

Acknowledgment

I will always remember my first weeks at University of Zaragoza, particularly Biomedical Signal Interpretation and Computational Simulation (BSICoS) group, even it was also my starting days in Europe, particularly Spain. I was so nervous but motivated as well to learn new things among great people. My supervisors and all the other BSICoSian (BSICoS members) were really helpful, kind and polite in nature. I came from a culture which was entirely different from here but here all of them helped me a lot, in order to accept and adapt with the atmosphere. I am really thankful and grateful to all of them. I really found all this journey so amazing, interesting and meaningful both for the research and personal development.

First, I would like to thank my Ph.D. advisers, Prof. Esther Pueyo, Dr. Carlos Sánchez and Dr. Mark Potse, for offering me the opportunity of doing this thesis, and for always listening what I had to say. Thank you for all your support, thank you for all your encouragement, thank you for all your knowledge, thank you for creating the novel researcher I am now and thank you for always treating me as part of the family, for making me to feel at home, for being my friends. Honestly speaking, you people are great!

I am thankful and grateful to Prof. Pablo Laguna because you guide me, advise me and help me in technical and non-technical aspects. You are a great person!

Thanks to my mom, dad, sister, brother and all my teachers for relying so much on me. Thanks to my beloved wife, who helps and supports me during these years and is my strength in all situations.

I would love to thank Prof. Pablo Lamata and his team for starting this great Personalized In-silico Cardiology (PIC) project. I would like to thank all my PIC fellows because all of you are awesome. Also, thanks to Ms. Elena Portero, Ms. Pilar Borrajo, Ms. Arantxa Trigo, Ms. María Salinas, Ms. Susana Perez, Ms. Yolanda Velicias and especially Ms. Dorse Martínez for the administrative work because you helped me a lot throughout this journey. I am thankful to all of my BSICoS team members especially Prof. Juan Pablo, Prof. Pedro, Dr. David Sampedro, Saul, Chiara, Jennifer, Neurys, Maxi, Dr. David, Dr. Ana, Dr. Alba, Dr. Jesus and Mr. Joaquín Chivite (IT manager). I am also thankful to all of my CARMEN, INRIA team members especially Prof. Yves Coudière, Dr. Nejib Zemzemi, Ms. Nathalie Robin, Dr. Malal, Dr. Amel, Dr. Oumayama, Andony, Dr. Bachar, Mehdi, Pauline, Narimane and Niami. Also, thankful to the progress review monitoring members especially Prof. Blanca Rodriguez, Prof. Jean-Marc Couveignes and

Dr. Afaf Bouharguane.

Dr. Julia Ramírez, this thesis started as the continuation of your thesis, I am also thankful to you and also thankful to Dr. Flavio Palmieri because Flavio is also working on the same topic and is a good friend of mine. Both of you are really nice and helpful.

This work was supported by projects ERC-StG 638284 (ERC), PID2019-105674RB-I00 and PID2019-104881RB-I00 (Ministerio de Ciencia e Innovación), Marie Skłodowska-Curie grants 764738 (European Commission) and by European Social Fund (EU) and Aragón Government through BSICoS group T39_20R and project LMP94_21. Computations were performed by the ICTS NANBIOSIS (HPC Unit at University of Zaragoza) and the French national supercomputing center IDRIS. I acknowledge all the support received from above mentioned grants because it would not have been possible for me to continue my Ph.D. without these grants.

Last but not least, I am wholeheartedly thankful and grateful to all my supervisors, particularly Esther, who has supported me a lot throughout this journey.

Bibliography

[1] N. R. Hill, S. T. Fatoba, J. L. Oke, J. A. Hirst, C. A. O'Callaghan, D. S. Lasserson, and F. D. R. Hobbs, "Global prevalence of chronic kidney disease - a systematic review and meta-analysis," *PloS One*, vol. 11, no. 7, p. e0158765, 2016.

[2] H. Bozbas, I. Atar, A. Yildirir, A. Ozgul, M. Uyar, N. Ozdemir, H. Muderrisoglu, and B. Ozin, "Prevalence and predictors of arrhythmia in end stage renal disease patients on hemodialysis," *Renal Failure*, vol. 29, no. 3, pp. 331–339, 2007.

[3] A. Lanari, L. O. Chait, and C. Capurro, "Electrocardiographic effects of potassium. I. Perfusion through the coronary bed," *American Heart Journal*, vol. 67, no. 3, pp. 357–363, 1964.

[4] N. El-Sherif and G. Turitto, "Electrolyte disorders and arrhythmogenesis," *Cardiology Journal*, vol. 18, no. 3, pp. 233–245, 2011.

[5] C. Van Mieghem, M. Sabbe, and D. Knockaert, "The clinical value of the ECG in noncardiac conditions," *Chest*, vol. 125, no. 4, pp. 1561–1576, 2004.

[6] R. Noordam, W. J. Young, R. Salman, J. K. Kanters, M. E. van den Berg, D. van Heemst, H. J. Lin, S. M. Barreto, M. L. Biggs, G. Biino, E. Catamo, M. P. Concas, J. Ding, D. S. Evans, L. Foco, N. Grarup, L.-P. Lyytikäinen, M. Mangino, H. Mei, P. J. van der Most, M. Müller-Nurasyid, C. P. Nelson, Y. Qian, L. Repetto, M. A. Said, N. Shah, K. Schramm, P. G. Vidigal, S. Weiss, J. Yao, N. R. Zilhao, J. A. Brody, P. S. Braund, M. Brumat, E. Campana, P. Christofidou, M. J. Caulfield, A. De Grandi, A. F. Dominiczak, A. S. F. Doney, G. Eiriksdottir, C. Ellervik, L. Giatti, M. Gögele, C. Graff, X. Guo, P. van der Harst, P. K. Joshi, M. Kähönen, B. Kestenbaum, M. F. Lima-Costa, A. Linneberg, A. C. Maan, T. Meitinger, S. Padmanabhan, C. Pattaro, A. Peters, A. Petersmann, P. Sever, M. F. Sinner, X. Shen, A. Stanton, K. Strauch, E. Z. Soliman, K. V. Tarasov, K. D. Taylor, C. H. L. Thio, A. G. Uitterlinden, S. Vaccargiu, M. Waldenberger, A. Robino, A. Correa, F. Cucca, S. R. Cummings, M. D örr, G. Girotto, V. Gudnason, T. Hansen, S. R. Heckbert, C. R. Juhl, S. Kääb, T. Lehtimäki, Y. Liu, P. A. Lotufo, C. N. A. Palmer, M. Pirastu, P. P. Pramstaller, A. L. P. Ribeiro, J. I. Rotter, N. J. Samani,

H. Snieder, T. D. Spector, B. H. Stricker, N. Verweij, J. F. Wilson, J. G. Wilson, J. W. Jukema, A. Tinker, C. H. Newton-Cheh, N. Sotoodehnia, D. O. Mook-Kanamori, P. B. Munroe, and H. R. Warren, "Effects of calcium, magnesium, and potassium concentrations on ventricular repolarization in unselected individuals," *Journal of the American College of Cardiology*, vol. 73, no. 24, pp. 3118–3131, 2019.

[7] S. Kharche, G. Callisesi, T. Stary, A. Bracci, and S. Severi, "Simulating the effects of serum potassium on the ECG," in *2012 Computing in Cardiology*, 2012, pp. 225–228.

[8] J. J. Dillon, C. V. DeSimone, Y. Sapir, V. K. Somers, J. L. Dugan, C. J. Bruce, M. J. Ackerman, S. J. Asirvatham, B. L. Striemer, J. Bukartyk, C. G. Scott, K. E. Bennet, S. B. Mikell, D. J. Ladewig, E. J. Gilles, A. Geva, D. Sadot, and P. A. Friedman, "Noninvasive potassium determination using a mathematically processed ECG: proof of concept for a novel "blood-less, blood test"," *Journal of Electrocardiology*, vol. 48, no. 1, pp. 12–18, 2015.

[9] C. Corsi, M. Cortesi, G. Callisesi, J. De Bie, C. Napolitano, A. Santoro, D. Mortara, and S. Severi, "Noninvasive quantification of blood potassium concentration from ECG in hemodialysis patients," *Scientific Reports*, vol. 7, p. 42492, 2017.

[10] M. Kanbay, B. Afsar, D. Goldsmith, and A. Covic, "Sudden death in hemodialysis: an update," *Blood Purification*, vol. 30, no. 2, pp. 135–145, 2010.

[11] "Cleveland clinic. heart. (https://my.clevelandclinic.org/health/body/21704-heart) Accessed 5/16/2022."

[12] "Heart foundation. how the heart works. (https://www.heartfoundation.org.nz/your-heart/how-the-heart-works) Accessed 5/16/2022."

[13] L. Sörnmo and P. Laguna, *Bioelectrical signal processing in cardiac and neurological applications*. Academic Press, 2005.

[14] E. Pueyo, "Lecture notes in electrophysiology of the heart," 2017.

[15] D. E. Becker, "Fundamentals of electrocardiography interpretation," *Anesthesia Progress*, vol. 53, no. 2, pp. 53–63, 2006.

[16] "CKD Stages | The UK Kidney Association," https://ukkidney.org/health-professionals/information-resources/uk-eckd-guide/ckd-stages, accessed: 2022-07-10.

[17] J.-C. Lv and L.-X. Zhang, "Prevalence and Disease Burden of Chronic Kidney Disease," *Advances in Experimental Medicine and Biology*, vol. 1165, pp. 3–15, 2019.

[18] C. P. Kovesdy, "Epidemiology of chronic kidney disease: an update 2022," *Kidney International Supplements*, vol. 12, no. 1, pp. 7–11, 2022.

[19] "Chronic Kidney Disease," https://www.kidney.org/atoz/content/about-chronic-kidney-disease, accessed: 2021-05-04.

[20] KDOQI, "KDOQI Clinical Practice Guidelines and Clinical Practice Recommendations for Diabetes and Chronic Kidney Disease," *American Journal of Kidney Diseases: The Official Journal of the National Kidney Foundation*, vol. 49, no. 2 Suppl 2, pp. S12–154, 2007.

[21] K. Hebert, A. Dias, M. C. Delgado, E. Franco, L. Tamariz, D. Steen, P. Trahan, B. Major, and L. M. Arcement, "Epidemiology and survival of the five stages of chronic kidney disease in a systolic heart failure population," *European Journal of Heart Failure*, vol. 12, no. 8, pp. 861–865, 2010.

[22] "Hemodialysis | NIDDK," https://www.niddk.nih.gov/health-information/kidney-disease/kidney-failure/hemodialysis, accessed: 2022-05-27.

[23] J. N. Weiss, Z. Qu, and K. Shivkumar, "Electrophysiology of hypokalemia and hyperkalemia," *Circulation. Arrhythmia and Electrophysiology*, vol. 10, no. 3, 2017.

[24] J. Soar, G. D. Perkins, G. Abbas, A. Alfonzo, A. Barelli, J. J. L. M. Bierens, H. Brugger, C. D. Deakin, J. Dunning, M. Georgiou, A. J. Handley, D. J. Lockey, P. Paal, C. Sandroni, K.-C. Thies, D. A. Zideman, and J. P. Nolan, "European Resuscitation Council Guidelines for Resuscitation 2010 Section 8. cardiac arrest in special circumstances: electrolyte abnormalities, poisoning, drowning, accidental hypothermia, hyperthermia, asthma, anaphylaxis, cardiac surgery, trauma, pregnancy, electrocution," *Resuscitation*, vol. 81, no. 10, pp. 1400–1433, 2010.

[25] J. T. Levis, "ECG diagnosis: hypokalemia," *The Permanente Journal*, vol. 16, no. 2, p. 57, 2012.

[26] D. Poulikakos, D. Banerjee, and M. Malik, "Risk of sudden cardiac death in chronic kidney disease," *Journal of Cardiovascular Electrophysiology*, vol. 25, no. 2, pp. 222–231, 2014.

[27] N. Pilia, S. Severi, J. G. Raimann, S. Genovesi, O. Dössel, P. Kotanko, C. Corsi, and A. Loewe, "Quantification and classification of potassium and calcium disorders with the electrocardiogram: What do clinical studies, modeling, and reconstruction tell us?" *APL Bioengineering*, vol. 4, no. 4, p. 041501, 2020.

[28] J. P. Martínez, R. Almeida, S. Olmos, A. P. Rocha, and P. Laguna, "A wavelet-based ECG delineator: evaluation on standard databases," *IEEE transactions on bio-medical engineering*, vol. 51, no. 4, pp. 570–581, 2004.

[29] H. A. Bukhari, F. Palmieri, J. Ramirez, P. Laguna, J. E. Ruiz, D. Ferreira, M. Potse, C. Sanchez, and E. Pueyo, "Characterization of T wave amplitude, duration and morphology changes during hemodialysis: Relationship with serum electrolyte levels and heart rate," *IEEE Transactions on Biomedical Engineering*, pp. 1–1, 2020.

[30] C. Slovis and R. Jenkins, "ABC of clinical electrocardiography: Conditions not primarily affecting the heart," *BMJ (Clinical research ed.)*, vol. 324, no. 7349, pp. 1320–1323, 2002.

[31] C. Corsi, J. DeBie, C. Napolitano, S. Priori, D. Mortara, and S. Severi, "Validation of a novel method for non-invasive blood potassium quantification from the ECG," in *2012 Computing in Cardiology*, 2012, pp. 105–108.

[32] Z. I. Attia, C. V. DeSimone, J. J. Dillon, Y. Sapir, V. K. Somers, J. L. Dugan, C. J. Bruce, M. J. Ackerman, S. J. Asirvatham, B. L. Striemer, J. Bukartyk, C. G. Scott, K. E. Bennet, D. J. Ladewig, E. J. Gilles, D. Sadot, A. B. Geva, and P. A. Friedman, "Novel bloodless potassium determination using a signal-processed single-lead ECG," *Journal of the American Heart Association: Cardiovascular and Cerebrovascular Disease*, vol. 5, no. 1, 2016.

[33] M. Andersen, J. Xue, C. Graff, T. Hardahl, E. Toft, J. Kanters, M. Christiansen, H. Jensen, and J. Struijk, "A robust method for quantification of IKr-related T-wave morphology abnormalities," in *2007 Computers in Cardiology*, 2007, pp. 341–344.

[34] L. Hong, L. J. Andersen, C. Graff, E. Vedel-Larsen, F. Wang, J. J. Struijk, P. Sogaard, P. R. Hansen, Y. Z. Yang, M. Christiansen, E. Toft, and J. K. Kanters, "T-wave morphology analysis of competitive athletes," *Journal of Electrocardiology*, vol. 48, no. 1, pp. 35–42, 2015.

[35] S. G. Tischer, C. Graff, C. Ellervik, E. Prescott, J. K. Kanters, and H. K. Rasmusen, "Influence of type of sport on cardiac repolarization assessed by electrocardiographic T-wave morphology combination score," *Journal of Electrocardiology*, vol. 51, no. 2, pp. 296–302, 2018.

[36] M. L. Krogager, K. Kragholm, R. K. Skals, R. N. Mortensen, C. Polcwiartek, C. Graff, J. B. Nielsen, J. K. Kanters, A. G. Holst, P. Søgaard, A. Pietersen, C. Torp-Pedersen, and S. M. Hansen, "The relationship between serum potassium concentrations and electrocardiographic characteristics in 163,547 individuals from primary care," *Journal of Electrocardiology*, vol. 57, pp. 104–111, 2019.

[37] W. A. Parham, A. A. Mehdirad, K. M. Biermann, and C. S. Fredman, "Hyperkalemia Revisited," *Texas Heart Institute Journal*, vol. 33, no. 1, pp. 40–47, 2006.

[38] R. Astan, I. Akpinar, A. Karan, F. Kacmaz, E. Sokmen, E. Baysal, O. Ozeke, and M. T. Selçuk, "The Effect of Hemodialysis on Electrocardiographic Parameters," *Annals of Noninvasive Electrocardiology*, vol. 20, no. 3, pp. 253–257, 2015.

[39] E. Pueyo and *et al.*, "QRS slopes for detection and characterization of myocardial ischemia," *IEEE transactions on bio-medical engineering*, vol. 55, no. 2, pp. 468–477, 2008.

[40] M. Ringborn and *et al.*, "Evaluation of depolarization changes during acute myocardial ischemia by analysis of QRS slopes," *Journal of Electrocardiology*, vol. 44, no. 4, pp. 416–424, 2011.

[41] H. A. Bukhari, P. Laguna, M. Potse, C. Sánchez, and E. Pueyo, "QRS slopes for potassium and calcium monitoring in end-stage renal disease patients," in *2021 Computing in Cardiology (CinC)*, vol. 48, 2021, pp. 1–4.

[42] B. Di Iorio and A. Bellasi, "QT interval in CKD and haemodialysis patients," *Clin. Kidney J.*, vol. 6, no. 2, pp. 137–143, 2013.

[43] M. R. Khosoosi Niaki, M. Saravi, F. Oliaee, R. Akbari, S. Noorkhomami, S. H. Bozorgi Rad, K. Fallahpoor, and M. S. Ramezani, "Changes in QT interval before and after hemodialysis," *Caspian J. Intern. Med.*, vol. 4, no. 1, pp. 590–594, 2013.

[44] P. M. Sohal, A. Goel, D. Gupta, N. Aslam, J. Sandhu, J. S. Sandhu, E. E. John, and D. Sharma, "Effect of hemodialysis on corrected QT interval and QTc dispersion," *Indian J. Nephrol.*, vol. 28, no. 5, pp. 335–338, 2018.

[45] Y. Matsumoto, Y. Mori, S. Kageyama, K. Arihara, H. Sato, K. Nagata, Y. Shimada, Y. Nojima, K. Iguchi, and T. Sugiyama, "Changes in QTc interval in long-term hemodialysis patients," *PLOS ONE*, vol. 14, no. 1, p. e0209297, 2019.

[46] M. Malhis, S. Al-Bitar, S. Farhood, and K. A.-D. Zaiat, "Changes in QT intervals in patients with end-stage renal disease before and after hemodialysis," *Saudi J. Kidney Dis. Transpl.*, vol. 21, no. 3, pp. 460–465, 2010.

[47] E. D. Kim, J. Watt, L. G. Tereshchenko, B. G. Jaar, S. M. Sozio, W. H. L. Kao, M. M. Estrella, and R. S. Parekh, "Associations of serum and dialysate electrolytes with QT interval and prolongation in incident hemodialysis: The predictors of arrhythmic and cardiovascular risk in end-stage renal disease (PACE) study," *BMC Nephrol.*, vol. 20, no. 1, p. 133, 2019.

[48] I. Lorincz, J. Mátyus, Z. Zilahi, C. Kun, Z. Karányi, and G. Kakuk, "QT dispersion in patients with end-stage renal failure and during hemodialysis," *J. Am. Soc. Nephrol.*, vol. 10, no. 6, pp. 1297–1302, 1999.

[49] A. Covic, M. Diaconita, P. Gusbeth-Tatomir, M. Covic, A. Botezan, G. Ungureanu, and D. J. Goldsmith, "Haemodialysis increases QTc interval but not QTc dispersion in ESRD patients without manifest cardiac disease," *Nephrol. Dial. Transplant.*, vol. 17, no. 12, pp. 2170–2177, 2002.

[50] H. Ozportakal, A. Ozkok, O. Alkan, A. S. Bulut, M. Boyraz, M. Inanir, G. Acar, and A. R. Odabas, "Hemodialysis-induced repolarization abnormalities on ECG are influenced by serum calcium levels and ultrafiltration volumes," *International Urology and Nephrology*, vol. 49, no. 3, pp. 509–515, 2017.

[51] F. Floccari, E. Aloisi, L. Nostro, C. Caccamo, A. Crisafulli, A. Barillà, C. Aloisi, A. Romeo, F. Corica, R. Ientile, N. Frisina, and M. Buemi, "QTc interval and QTc dispersion during haemodiafiltration," *Nephrology (Carlton)*, vol. 9, no. 6, pp. 335–340, 2004.

[52] O. Z. Yasin, Z. Attia, J. J. Dillon, C. V. DeSimone, Y. Sapir, J. Dugan, V. K. Somers, M. J. Ackerman, S. J. Asirvatham, C. G. Scott, K. E. Bennet, D. J. Ladewig, D. Sadot, A. B. Geva, and P. A. Friedman, "Noninvasive blood potassium measurement using signal-processed, single-lead ecg acquired from a handheld smartphone," *Journal of electrocardiology*, vol. 50, no. 5, pp. 620–625, 2017.

[53] S. Severi, C. Corsi, M. Haigney, J. DeBie, and D. Mortara, "Noninvasive potassium measurements from ECG analysis during hemodialysis sessions," in *2009 36th Annual Computers in Cardiology Conference (CinC)*, 2009, pp. 821–824.

[54] V. Velagapudi, J. C. O'Horo, A. Vellanki, S. P. Baker, R. Pidikiti, J. S. Stoff, and D. A. Tighe, "Computer-assisted image processing 12 lead ECG model to diagnose hyperkalemia," *Journal of Electrocardiology*, vol. 50, no. 1, pp. 131–138, 2017.

[55] C.-S. Lin, C. Lin, W.-H. Fang, C.-J. Hsu, S.-J. Chen, K.-H. Huang, W.-S. Lin, C.-S. Tsai, C.-C. Kuo, T. Chau, S. J. Yang, and S.-H. Lin, "A deep-learning algorithm (ECG12Net) for detecting hypokalemia and hyperkalemia by electrocardiography: Algorithm development," *JMIR Med. Inform.*, vol. 8, no. 3, 2020.

[56] D. Schüttler, U. Schönermarck, F. Wenner, M. Toepfer, K. D. Rizas, A. Bauer, S. Brunner, and W. Hamm, "Large potassium shifts during dialysis enhance cardiac repolarization instability," *Journal of Nephrology*, 2020.

[57] A. S. Rodrigues, A. Petrėnas, B. Paliakaitė, N. Kušleikaitė-Pere, G. Jaruševičius, I. A. Bumblytė, P. Laguna, and V. Marozas, "Noninvasive Monitoring of Potassium Fluctuations During the Long Interdialytic Interval," *IEEE Access*, vol. 8, pp. 188 488–188 502, 2020.

[58] M. Curione, C. Castro, C. Cammarota, G. Tonnarini, and M. Pasquali, "Progressive loss in circulating volume during haemodialysis can be monitored by time voltage integral area of QRS complex: Pilot study," *Archives of medical science: AMS*, vol. 9, no. 3, pp. 544–547, 2013.

[59] S. Ojanen, T. Kööbi, P. Korhonen, J. Mustonen, and A. Pasternack, "QRS amplitude and volume changes during hemodialysis," *American Journal of Nephrology*, vol. 19, no. 3, pp. 423–427, 1999.

[60] J. N. An, J. P. Lee, H. J. Jeon, D. H. Kim, Y. K. Oh, Y. S. Kim, and C. S. Lim, "Severe hyperkalemia requiring hospitalization: predictors of mortality," *Critical Care (London, England)*, vol. 16, no. 6, p. R225, 2012.

[61] "Cardiovascular diseases (CVDs)." [Online]. Available: https://www.who.int/news-room/fact-sheets/detail/cardiovascular-diseases-(cvds)

[62] S. A. Niederer, J. Lumens, and N. A. Trayanova, "Computational models in cardiology," *Nature Reviews Cardiology*, vol. 16, no. 2, pp. 100–111, 2019.

[63] A. L. Hodgkin and A. F. Huxley, "A quantitative description of membrane current and its application to conduction and excitation in nerve," *The Journal of Physiology*, vol. 117, no. 4, p. 500, 1952.

[64] D. A. S. Puente, "Theoretical analysis of autonomic nervous system effects on cardiac electrophysiology and its relationship with arrhythmic risk," Ph.D. dissertation, Universidad de Zaragoza, 2020.

[65] J. C. Fernández, "New methodologies for the development and validation of electrophysiological models," Ph.D. dissertation, Universidad de Zaragoza, 2018.

[66] C. S. Tapia, "Multiscale Analysis of Atrial Fibrillation Mechanisms," Ph.D. dissertation, Universidad de Zaragoza, 2014.

[67] M. Potse, "Integrated electrocardiographic mapping. Combined analysis of multichannel endocardial and body surface ECG data," Ph.D. dissertation, Universiteit van Amsterdam, 2001.

[68] J. P. Whiteley, "An efficient numerical technique for the solution of the monodomain and bidomain equations," *IEEE transactions on bio-medical engineering*, vol. 53, no. 11, pp. 2139–2147, 2006.

[69] K. H. W. J. Ten Tusscher and A. V. Panfilov, "Alternans and spiral breakup in a human ventricular tissue model," *American Journal of Physiology-Heart and Circulatory Physiology*, vol. 291, no. 3, pp. H1088–H1100, 2006.

[70] K. H. W. J. ten Tusscher, D. Noble, P. J. Noble, and A. V. Panfilov, "A model for human ventricular tissue," *American Journal of Physiology. Heart and Circulatory Physiology*, vol. 286, no. 4, pp. H1573–1589, 2004.

[71] V. Iyer, R. Mazhari, and R. L. Winslow, "A Computational Model of the Human Left-Ventricular Epicardial Myocyte," *Biophysical Journal*, vol. 87, no. 3, pp. 1507–1525, 2004.

[72] E. Grandi, F. S. Pasqualini, and D. M. Bers, "A novel computational model of the human ventricular action potential and Ca transient," *Journal of Molecular and Cellular Cardiology*, vol. 48, no. 1, pp. 112–121, 2010.

[73] T. R. Shannon, F. Wang, J. Puglisi, C. Weber, and D. M. Bers, "A mathematical treatment of integrated Ca dynamics within the ventricular myocyte," *Biophysical Journal*, vol. 87, no. 5, pp. 3351–3371, 2004.

[74] J. Carro, J. F. Rodríguez, P. Laguna, and E. Pueyo, "A human ventricular cell model for investigation of cardiac arrhythmias under hyperkalaemic conditions," *Philosophical Transactions. Series A, Mathematical, Physical, and Engineering Sciences*, vol. 369, no. 1954, pp. 4205–4232, 2011.

[75] T. O'Hara, L. Virág, A. Varró, and Y. Rudy, "Simulation of the undiseased human cardiac ventricular action potential: model formulation and experimental validation," *PLoS computational biology*, vol. 7, no. 5, p. e1002061, 2011.

[76] Y. Himeno, K. Asakura, C. Y. Cha, H. Memida, T. Powell, A. Amano, and A. Noma, "A human ventricular myocyte model with a refined representation of excitation-contraction coupling," *Biophysical Journal*, vol. 109, no. 2, pp. 415–427, 2015.

[77] S. Dutta, A. Mincholé, T. A. Quinn, and B. Rodriguez, "Electrophysiological properties of computational human ventricular cell action potential models under acute ischemic conditions," *Progress in Biophysics and Molecular Biology*, vol. 129, pp. 40–52, 2017.

[78] J. V. Temte and L. D. Davis, "Effect of calcium concentration on the transmembrane potentials of Purkinje fibers," *Circulation Research*, vol. 20, no. 1, pp. 32–44, 1967.

[79] B. Cx, N. I, K. J, T. H, S. K, and F. T, "Role of nitric oxide in Ca2+ sensitivity of the slowly activating delayed rectifier K+ current in cardiac myocytes," *Circulation research*, vol. 96, no. 1, 2005.

[80] S. P. Leitch and H. F. Brown, "Effect of raised extracellular calcium on characteristics of the guinea-pig ventricular action potential," *Journal of Molecular and Cellular Cardiology*, vol. 28, no. 3, pp. 541–551, 1996.

[81] J. Tomek, A. Bueno-Orovio, E. Passini, X. Zhou, A. Minchole, O. Britton, C. Bartolucci, S. Severi, A. Shrier, L. Virag, A. Varro, and B. Rodriguez, "Development, calibration, and validation of a novel human ventricular myocyte model in health, disease, and drug block," *eLife*, vol. 8, p. e48890, 2019.

[82] S. Severi, C. Corsi, and E. Cerbai, "From in vivo plasma composition to in vitro cardiac electrophysiology and in silico virtual heart: the extracellular calcium enigma," *Philosophical Transactions. Series A, Mathematical, Physical, and Engineering Sciences*, vol. 367, no. 1896, pp. 2203–2223, 2009.

[83] C. Bartolucci, E. Passini, J. Hyttinen, M. Paci, and S. Severi, "Simulation of the effects of extracellular calcium changes leads to a novel computational model of human ventricular action potential with a revised calcium handling," *Frontiers in Physiology*, vol. 11, 2020.

[84] M. Hernández Mesa, N. Pilia, O. Dössel, S. Severi, and A. Loewe, "Effects of serum calcium changes on the cardiac action potential and the ECG in a computational model," *Current Directions in Biomedical Engineering*, vol. 4, no. 1, pp. 251–254, 2018.

[85] N. Pilia, O. Dössel, G. Lenis, and A. Loewe, "ECG as a tool to estimate potassium and calcium concentrations in the extracellular space," in *2017 Computing in Cardiology (CinC)*, 2017, pp. 1–4.

[86] N. Pilia, M. H. Mesa, O. Dössel, and A. Loewe, "ECG-based estimation of potassium and calcium concentrations: proof of concept with simulated data," in *2019 41st Annual International Conference of the IEEE Engineering in Medicine and Biology Society (EMBC)*, 2019, pp. 2610–2613.

[87] A. Loewe, M. Hernández Mesa, N. Pilia, S. Severi, and O. Dössel, "A heterogeneous formulation of the Himeno et al human ventricular myocyte model for simulation of body surface ECGs," in *2018 Computing in Cardiology Conference (CinC)*, vol. 45, 2018, pp. 1–4.

[88] L. Sörnmo and P. Laguna, "Electrocardiogram (ECG) signal processing," in *Wiley Encyclopedia of Biomedical Engineering*. American Cancer Society, 2006.

[89] F. Palmieri, P. Gomis, D. Ferreira, J. E. Ruiz, B. Bergasa, A. Martín-Yebra, H. A. Bukhari, E. Pueyo, J. P. Martínez, J. Ramírez, and P. Laguna, "Monitoring blood potassium concentration in hemodialysis patients by quantifying T-wave morphology dynamics," *Scientific Reports*, vol. 11, no. 1, p. 3883, 2021.

[90] F. Castells, P. Laguna, L. Sörnmo, A. Bollmann, and J. M. Roig, "Principal component analysis in ECG signal processing," *EURASIP Journal on Advances in Signal Processing*, vol. 2007, no. 1, pp. 1–21, 2007.

[91] F. Palmieri, P. Gomis, D. Ferreira, J. E. Ruiz, B. Bergasa, A. Martín-Yebra, H. A. Bukhari, E. Pueyo, J. P. Martínez, J. Ramírez, and P. Laguna, "Monitoring blood potassium concentration in hemodialysis patients by quantifying T-wave morphology dynamics," *Scientific Reports*, vol. 11, no. 1, p. 3883, 2021.

[92] H. A. Bukhari, C. Sánchez, J. E. Ruiz, M. Potse, P. Laguna, and E. Pueyo, "Monitoring of Serum Potassium and Calcium Levels in End-Stage Renal Disease Patients by ECG Depolarization Morphology Analysis," *Sensors*, vol. 22, no. 8, p. 2951, 2022.

[93] J. Ramírez, M. Orini, J. D. Tucker, E. Pueyo, and P. Laguna, "Variability of ventricular repolarization dispersion quantified by time-warping the morphology of the T-waves," *IEEE transactions on bio-medical engineering*, vol. 64, no. 7, pp. 1619–1630, 2017.

[94] M. T. Rosenstein, J. J. Collins, and C. J. De Luca, "A practical method for calculating largest Lyapunov exponents from small data sets," *Physica D.*, vol. 65, no. 1, pp. 117–134, 1993.

[95] R. Killick, P. Fearnhead, and I. A. Eckley, "Optimal Detection of Changepoints With a Linear Computational Cost," *Journal of the American Statistical Association*, vol. 107, no. 500, pp. 1590–1598, 2012.

[96] D. Freedman, R. Pisani, and R. Purves, "Statistics (international student edition)," *Pisani, R. Purves, 4th edn. WW Norton & Company, New York*, 2007.

[97] J. Benesty, J. Chen, Y. Huang, and I. Cohen, "Pearson correlation coefficient," in *Noise reduction in speech processing*. Springer, 2009, pp. 37–40.

[98] Y. Zuo, G. Yu, M. G. Tadesse, and H. W. Ressom, "Biological network inference using low order partial correlation," *Methods (San Diego, Calif.)*, vol. 69, no. 3, pp. 266–273, 2014.

[99] J. L. Fleiss and J. M. Tanur, "A note on the partial correlation coefficient," *The American Statistician*, vol. 25, no. 1, pp. 43–45, 1971.

[100] J. D. Gibbons and S. Chakraborti, "Nonparametric statistical inference," in *International Encyclopedia of Statistical Science*, M. Lovric, Ed. Berlin, Heidelberg: Springer Berlin Heidelberg, 2011, pp. 977–979.

[101] R. A. Fisher, "Statistical methods for research workers," in *Breakthroughs in Statistics: Methodology and Distribution*, ser. Springer Series in Statistics, S. Kotz and N. L. Johnson, Eds. New York, NY: Springer, 1992, pp. 66–70.

[102] K. Gima and Y. Rudy, "Ionic current basis of electrocardiographic waveforms: a model study," *Circulation Research*, vol. 90, no. 8, pp. 889–896, 2002.

[103] E. A. Heidenreich, J. M. Ferrero, M. Doblaré, and J. F. Rodríguez, "Adaptive macro finite elements for the numerical solution of monodomain equations in cardiac electrophysiology," *Annals of Biomedical Engineering*, vol. 38, no. 7, pp. 2331–2345, 2010.

[104] L. Romero, E. Pueyo, M. Fink, and B. Rodríguez, "Impact of ionic current variability on human ventricular cellular electrophysiology," *American Journal of Physiology. Heart and Circulatory Physiology*, vol. 297, no. 4, pp. H1436–1445, 2009.

[105] E. Pueyo, Z. Husti, T. Hornyik, I. Baczkó, P. Laguna, A. Varró, and B. Rodríguez, "Mechanisms of ventricular rate adaptation as a predictor of arrhythmic risk," *American Journal of Physiology-Heart and Circulatory Physiology*, vol. 298, no. 5, pp. H1577–H1587, 2010.

[106] J. H. Brown, L. P. Hunt, N. P. Vites, C. D. Short, R. Gokal, and N. P. Mallick, "Comparative mortality from cardiovascular disease in patients with chronic renal failure," *Nephrology, Dialysis, Transplantation: Official Publication of the European Dialysis and Transplant Association - European Renal Association*, vol. 9, no. 8, pp. 1136–1142, 1994.

[107] M. L. Krogager, C. Torp-Pedersen, R. N. Mortensen, L. Køber, G. Gislason, P. Søgaard, and K. Aasbjerg, "Short-term mortality risk of serum potassium levels in hypertension: a retrospective analysis of nationwide registry data," *European Heart Journal*, vol. 38, no. 2, pp. 104–112, 2017.

[108] B. Pitt and P. Rossignol, "The association between serum potassium and mortality in patients with hypertension: 'a wake-up call'," *European Heart Journal*, vol. 38, no. 2, pp. 113–115, 2017.

[109] A. Loewe, Y. Lutz, A. Fabbri, and S. Severi, "Sinus bradycardia due to electrolyte changes as a potential pathomechanism of sudden cardiac death in hemodialysis patients," *Biophysical Journal*, vol. 116, no. 3, p. 231a, 2019.

[110] F. Ajam, "Cardiac arrhythmias in patients with end stage renal disease (ESRD) on hemodialysis; recent update and brief literature review," *American Journal of Internal Medicine*, vol. 7, no. 1, p. 22, 2019.

[111] J. D. Gardner, J. B. Calkins, and G. E. Garrison, "ECG diagnosis: the effect of ionized serum calcium levels on electrocardiogram," *The Permanente Journal*, vol. 18, no. 1, pp. e119–e120, 2014.

[112] E. Chorin, R. Rosso, and S. Viskin, "Electrocardiographic manifestations of calcium abnormalities," *Annals of Noninvasive Electrocardiology : The Official Journal of the International Society for Holter and Noninvasive Electrocardiology, Inc*, vol. 21, no. 1, pp. 7–9, 2015.

[113] P. P. Frohnert, E. R. Giuliani, M. Friedberg, W. J. Johnson, and W. N. Tauxe, "Statistical investigation of correlations between serum potassium levels and electrocardiographic findings in patients on intermittent hemodialysis therapy," *Circulation*, vol. 41, no. 4, pp. 667–676, 1970.

[114] N. Akter, A. Nessa, S. Israt, A. Sharmin, M. I. Dipa, S. Firoz, and R. Chowdhury, "Study on Serum Calcium Level in Patients with Chronic Kidney Disease," *Mymensingh medical journal: MMJ*, vol. 31, no. 4, pp. 920–924, 2022.

[115] C. J. Janmaat, M. van Diepen, A. Gasparini, M. Evans, A. R. Qureshi, J. Ärnlöv, P. Barany, C.-G. Elinder, J. I. Rotmans, M. Vervloet, F. W. Dekker, and J. J. Carrero, "Lower serum calcium is independently associated with CKD progression," *Scientific Reports*, vol. 8, no. 1, p. 5148, 2018.

[116] F. F. Siyam and D. M. Klachko, "What Is Hypercalcemia? The Importance of Fasting Samples," *Cardiorenal Medicine*, vol. 3, no. 4, pp. 232–238, 2013.

[117] O. Edafe, R. Antakia, N. Laskar, L. Uttley, and S. P. Balasubramanian, "Systematic review and meta-analysis of predictors of post-thyroidectomy hypocalcaemia," *British Journal of Surgery*, vol. 101, no. 4, pp. 307–320, 2014.

[118] E. Pueyo, A. Corrias, L. Virág, N. Jost, T. Szél, A. Varró, N. Szentandrássy, P. P. Nánási, K. Burrage, and B. Rodríguez, "A multiscale investigation of repolarization variability and its role in cardiac arrhythmogenesis," *Biophysical Journal*, vol. 101, no. 12, pp. 2892–2902, 2011.

[119] L. Priebe and D. J. Beuckelmann, "Simulation study of cellular electric properties in heart failure," vol. 82, no. 11, pp. 1206–1223.

[120] D. Janusek, J. Svehlikova, J. Zelinka, W. Weigl, R. Zaczek, G. Opolski, M. Tysler, and R. Maniewski, "The roles of mid-myocardial and epicardial cells in T-wave alternans development: a simulation study," *Biomedical Engineering Online*, vol. 17, no. 1, p. 57, 2018.

[121] M. W. Rivolta, G. H. Bevan, V. Gurev, J. J. Rice, C. M. Lopes, and J.-P. Couderc, "T-wave morphology depends on transmural heterogeneity in a high-resolution human left-ventricular wedge model," in *2015 Computing in Cardiology Conference (CinC)*, 2015, pp. 433–436.

[122] P. K. Priya and S. Jayaraman, "Do M-cells contribute significantly in T-wave morphology during normal and arrhythmogenesis conditions like short QT Syndrome?" *bioRxiv*, p. 2020.05.28.121079, 2020.

[123] J.-I. Okada, T. Washio, A. Maehara, S.-I. Momomura, S. Sugiura, and T. Hisada, "Transmural and apicobasal gradients in repolarization contribute to T-wave genesis in human surface ECG," *American Journal of Physiology. Heart and Circulatory Physiology*, vol. 301, no. 1, pp. H200–208, 2011.

[124] N. T. Srinivasan, M. Orini, R. Providencia, R. Simon, M. Lowe, O. R. Segal, A. W. Chow, R. J. Schilling, R. J. Hunter, P. Taggart, and P. D. Lambiase, "Differences in the upslope of the precordial body surface ECG T wave reflect right to left dispersion of repolarization in the intact human heart," *Heart Rhythm*, vol. 16, no. 6, pp. 943–951, 2019.

[125] B. Hooft van Huysduynen, C. A. Swenne, H. H. M. Draisma, M. L. Antoni, H. Van De Vooren, E. E. Van Der Wall, and M. J. Schalij, "Validation of ECG indices of ventricular repolarization heterogeneity: a computer simulation study," *Journal of Cardiovascular Electrophysiology*, vol. 16, no. 10, pp. 1097–1103, 2005.

[126] A. J. Izenman, *Modern multivariate statistical techniques: regression, classification, and manifold learning*, ser. Springer texts in statistics. New York ; London: Springer, 2008.

[127] N. R. Draper and H. Smith, *Applied regression analysis*, 3rd ed., ser. Wiley series in probability and statistics. New York: Wiley, 1998.

[128] L. Li, C. Liu, C. Liu, Q. Zhang, and B. Li, "Physiological signal variability analysis based on the largest Lyapunov exponent," in *2009 2nd International Conference on Biomedical Engineering and Informatics*, 2009, pp. 1–5.

[129] S. Srinivasan, H. A. Bukhari, P. Laguna, C. Sánchez, and E. Pueyo, "Analysis of T Wave Nonlinear Dynamics for Serum Potassium Monitoring in End-Stage Renal Disease Patients," in *2020 Computing in Cardiology*, 2020, pp. 1–4.

[130] J. M. Bland and D. G. Altman, "Statistical methods for assessing agreement between two methods of clinical measurement," *Lancet (London, England)*, vol. 1, no. 8476, pp. 307–310, 1986.

[131] E. A. Secemsky, R. L. Verrier, G. Cooke, C. Ghossein, H. Subacius, A. Manuchehry, C. A. Herzog, and R. Passman, "High prevalence of cardiac autonomic dysfunction and T-wave alternans in dialysis patients," *Heart Rhythm*, vol. 8, no. 4, pp. 592–598, 2011.

[132] F. Palmieri, P. Gomis, J. E. Ruiz, D. Ferreira, A. Martín-Yebra, E. Pueyo, J. P. Martínez, J. Ramírez, and P. Laguna, "Nonlinear T-wave time warping-based sensing model for non-invasive personalized blood potassium monitoring in hemodialysis patients," *Sensors*, vol. 21, no. 2710, pp. 1–13, 2021.

[133] S. Severi, E. Grandi, C. Pes, F. Badiali, F. Grandi, and A. Santoro, "Calcium and potassium changes during haemodialysis alter ventricular repolarization duration: in vivo and in silico analysis," *Nephrology, Dialysis, Transplantation: Official Publication of the European Dialysis and Transplant Association - European Renal Association*, vol. 23, no. 4, pp. 1378–1386, 2008.

[134] H. A. Bukhari, F. Palmieri, D. Ferreira, M. Potse, J. Ramírez, P. Laguna, C. Sánchez, and E. Pueyo, "Transmural ventricular heterogeneities play a major role in determining T-wave morphology at different extracellular potassium levels," in *2019 Computing in Cardiology (CinC)*, 2019, pp. 1–4.

[135] N. Naksuk, T. Hu, C. Krittanawong, C. Thongprayoon, S. Sharma, J. Y. Park, A. N. Rosenbaum, P. Gaba, A. M. Killu, A. M. Sugrue, T. Peeraphatdit, V. Herasevich, M. R. Bell, P. A. Brady, S. Kapa, and S. J. Asirvatham, "Association of serum magnesium on mortality in patients admitted to the intensive cardiac care unit," *The American Journal of Medicine*, vol. 130, no. 2, pp. 229.e5–229.e13, 2017.

[136] W. K. Jhang, Y. J. Lee, Y. A. Kim, S. J. Park, and Y. S. Park, "Severe hypermagnesemia presenting with abnormal electrocardiographic findings similar to those of hyperkalemia in a child undergoing peritoneal dialysis," *Korean Journal of Pediatrics*, vol. 56, no. 7, pp. 308–311, 2013.

[137] W. M. van den Bergh, A. Algra, and G. J. E. Rinkel, "Electrocardiographic abnormalities and serum magnesium in patients with subarachnoid hemorrhage," *Stroke*, vol. 35, no. 3, pp. 644–648, 2004.

[138] C. D. Galloway, A. V. Valys, J. B. Shreibati, D. L. Treiman, F. L. Petterson, V. P. Gundotra, D. E. Albert, Z. I. Attia, R. E. Carter, S. J. Asirvatham, M. J. Ackerman, P. A. Noseworthy, J. J. Dillon, and P. A. Friedman, "Development and validation of a deep-learning model to screen for hyperkalemia from the electrocardiogram," *JAMA Cardiol.*, vol. 4, no. 5, pp. 428–436, 2019.

[139] J. Kwon, M. Jung, K. Kim, Y. Jo, J. Shin, Y. Cho, Y. Lee, J. Ban, K. Jeon, S. Y. Lee, J. Park, and B. Oh, "Artificial intelligence for detecting electrolyte imbalance

using electrocardiography," *Annals of Noninvasive Electrocardiology*, vol. 26, no. 3, p. e12839, 2021.

[140] H. A. Bukhari, C. Sánchez, S. Srinivasan, F. Palmieri, M. Potse, P. Laguna, and E. Pueyo, "Estimation of potassium levels in hemodialysis patients by T wave nonlinear dynamics and morphology markers," *Computers in Biology and Medicine*, vol. 143, p. 105304, 2022.

[141] K. Hnatkova, P. Smetana, O. Toman, G. Schmidt, and M. Malik, "Sex and race differences in QRS duration," *Europace: European Pacing, Arrhythmias, and Cardiac Electrophysiology: Journal of the Working Groups on Cardiac Pacing, Arrhythmias, and Cardiac Cellular Electrophysiology of the European Society of Cardiology*, vol. 18, no. 12, pp. 1842–1849, 2016.

[142] F. Palmieri, P. Gomis, D. Ferreira, J. E. Ruiz, B. Bergasa, A. Martín-Yebra, H. A. Bukhari, E. Pueyo, J. P. Martínez, J. Ramírez, and P. Laguna, "T-Wave Morphology Changes as Surrogate for Blood Potassium Concentration in Hemodialysis Patients," in *2019 Computing in Cardiology (CinC)*, 2019, pp. Page 1–Page 4.

[143] P. O. Ettinger, T. J. Regan, and H. A. Oldewurtel, "Hyperkalemia, cardiac conduction, and the electrocardiogram: A review," *American Heart Journal*, vol. 88, no. 3, pp. 360–371, 1974.

[144] S. Aslam, E. A. Friedman, and O. Ifudu, "Electrocardiography is unreliable in detecting potentially lethal hyperkalaemia in haemodialysis patients," *Nephrology Dialysis Transplantation*, vol. 17, no. 9, pp. 1639–1642, 2002.

[145] B. T. Montague, J. R. Ouellette, and G. K. Buller, "Retrospective Review of the Frequency of ECG Changes in Hyperkalemia," *Clinical Journal of the American Society of Nephrology : CJASN*, vol. 3, no. 2, pp. 324–330, 2008.

[146] A. Martinez-Vea, A. Bardají, C. Garcia, and J. A. Oliver, "Severe hyperkalemia with minimal electrocardiographic manifestations: A report of seven cases," *Journal of Electrocardiology*, vol. 32, no. 1, pp. 45–49, 1999.

[147] Fisch Charles, "Relation of Electrolyte Disturbances to Cardiac Arrhythmias," *Circulation*, vol. 47, no. 2, pp. 408–419, 1973.

[148] M. A. Alabd, W. El-Hammady, A. Shawky, W. Nammas, and M. El-Tayeb, "QT Interval and QT Dispersion in Patients Undergoing Hemodialysis: Revisiting the Old Theory," *Nephron Extra*, vol. 1, no. 1, pp. 1–8, 2011.

[149] D. Green, H. D. Green, D. I. New, and P. A. Kalra, "The clinical significance of hyperkalaemia-associated repolarization abnormalities in end-stage renal disease," *Nephrology Dialysis Transplantation*, vol. 28, no. 1, pp. 99–105, 2013.

[150] M. Buemi, E. Aloisi, G. Coppolino, S. Loddo, E. Crascì, C. Aloisi, A. Barillà, V. Cosentini, L. Nostro, C. Caccamo, F. Floccari, A. Romeo, N. Frisina, and D. Teti, "The effect of two different protocols of potassium haemodiafiltration on QT dispersion," *Nephrology Dialysis Transplantation*, vol. 20, no. 6, pp. 1148–1154, 2005.

[151] B. T. Montague, J. R. Ouellette, and G. K. Buller, "Retrospective review of the frequency of ECG changes in hyperkalemia," *Clinical journal of the American Society of Nephrology: CJASN*, vol. 3, no. 2, pp. 324–330, 2008.

[152] F. Palmieri, P. Gomis, D. Ferreira, E. Pueyo, J. P. Martinez, P. Laguna, and J. Ramirez, "Weighted time warping improves T-wave morphology markers clinical significance," *IEEE transactions on bio-medical engineering*, vol. 69, no. 9, pp. 2787–2796, 2022.

[153] M. Kania, Y. Coudière, H. Cochet, M. Haïssaguerre, P. Jais, and M. Potse, "Prediction of the exit site of ventricular tachycardia based on different ECG lead systems," in *2017 Computing in Cardiology (CinC)*, 2017, pp. 1–4.

[154] M. Potse, B. Dubé, J. Richer, A. Vinet, and R. M. Gulrajani, "A comparison of monodomain and bidomain reaction-diffusion models for action potential propagation in the human heart," *IEEE transactions on bio-medical engineering*, vol. 53, no. 12 Pt 1, pp. 2425–2435, 2006.

[155] D. D. Streeter, H. M. Spotnitz, D. P. Patel, J. Ross, and E. H. Sonnenblick, "Fiber orientation in the canine left ventricle during diastole and systole," *Circulation Research*, vol. 24, no. 3, pp. 339–347, 1969.

[156] S. Rush and H. Larsen, "A practical algorithm for solving dynamic membrane equations," *IEEE Trans. Biomed. Eng.*, vol. 25, no. 4, pp. 389–392, 1978.

[157] D. Krause and *et al.*, "Hybrid parallelization of a large-scale heart model," in *Facing the Multicore-Challenge II*, ser. Lecture Notes in Computer Science, R. Keller, D. Kramer, and J.-P. Weiss, Eds., vol. 7174. Berlin: Springer, 2012, pp. 120–132.

[158] M. Potse, "Scalable and Accurate ECG Simulation for Reaction-Diffusion Models of the Human Heart," *Frontiers in Physiology*, vol. 9, 2018.

[159] R. McFee and F. D. Johnston, "Electrocardiographic Leads," *Circulation*, vol. 9, no. 6, pp. 868–880, 1954.

[160] P. Colli-Franzone, M. Pennacchio, and L. Guerri, "Accurate computation of electrograms in the left ventricular wall," *Mathematical Models and Methods in Applied Sciences*, vol. 10, no. 04, pp. 507–538, 2000.

[161] D. Yoon, H. S. Lim, J. C. Jeong, T. Y. Kim, J.-g. Choi, J.-H. Jang, E. Jeong, and C. M. Park, "Quantitative Evaluation of the Relationship between T-Wave-Based Features and Serum Potassium Level in Real-World Clinical Practice," *BioMed Research International*, vol. 2018, p. e3054316, 2018.

[162] M. J. Janse, R. Coronel, T. Opthof, E. A. Sosunov, E. P. Anyukhovsky, and M. R. Rosen, "Repolarization gradients in the intact heart: Transmural or apico-basal?" *Prog. Biophys. Mol. Biol.*, vol. 109, pp. 6–15, 2012.

[163] T. Opthof, C. A. Remme, E. Jorge, F. Noriega, R. F. Wiegerinck, A. Tasiam, L. Beekman, J. Alvarez-Garcia, C. Munoz-Guijosa, R. Coronel, and J. Cinca, "Cardiac activation-repolarization patterns and ion channel expression mapping in intact isolated normal human hearts," *Heart Rhythm*, vol. 14, pp. 265–272, 2017.

Ph.D. Thesis

Estimation of Serum Potassium and Calcium Concentrations from Electrocardiographic Depolarization and Repolarization Waveforms

Syed Hassaan Ahmed Bukhari

Supervisors:

Prof. Esther Pueyo, Dr. Mark Potse, Dr. Carlos Sánchez

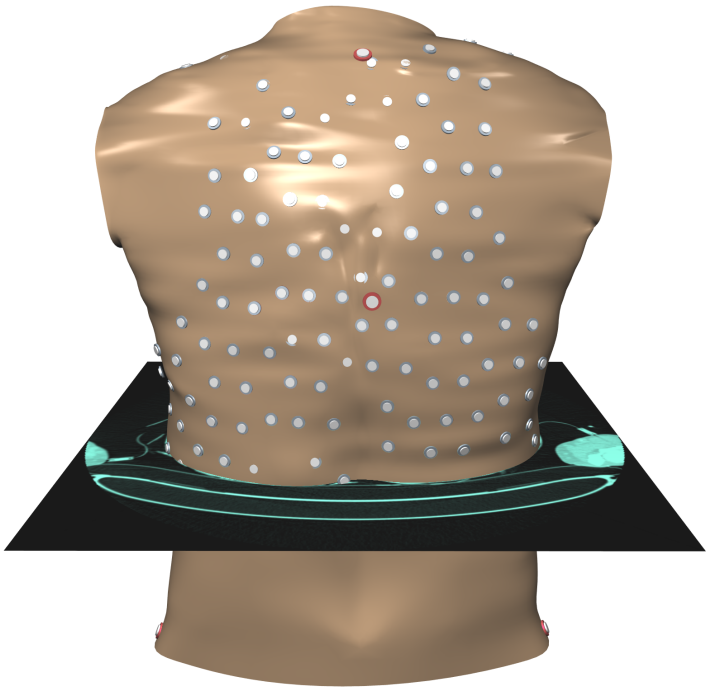

University of Zaragoza, Spain & University of Bordeaux, France